

Probing Environment of AGNs based on their feedback processes

A THESIS SUBMITTED TO THE UNIVERSITY OF DELHI
FOR THE DEGREE OF
DOCTOR OF PHILOSOPHY

By
Sapna Mishra

Aryabhata Research Institute of observational sciences
(ARIES), Manora Peak, Nainital-263002
And
Department of Physics & Astrophysics
University of Delhi, Delhi-110 007



DEPARTMENT OF PHYSICS & ASTROPHYSICS
UNIVERSITY OF DELHI
DELHI-110 007, INDIA

September 2020

Declaration

I, Sapna Mishra, hereby declare that the thesis entitled “**Probing Environment of AGNs based on their feedback processes**” is an authentic record of the research carried out by me under the joint supervision of Prof. T. R. Seshadri, Department of Physics & Astrophysics, University of Delhi and Prof. Hum Chand, Department of Physics and Astronomical Sciences, Central University of Himachal Pradesh. This work is original and has not been submitted for the award of any other degree in this university or any other university. The assistance received from various sources during the course of study has been acknowledged.

Prof. T. R. Seshadri

(Supervisor)

Sapna Mishra

(PhD Candidate)

Prof. Hum Chand

(Co-supervisor)

Brajesh Chandra Choudhary

Head, Department of Physics & Astrophysics

University of Delhi, Delhi - 110 007

September 2020



Department of Physics & Astrophysics

University of Delhi

Delhi - 110 007, India

Date : _____

Certificate of Originality

The research work embodied in this thesis entitled “**Probing Environment of AGNs based on their feedback processes**” has been carried out by me at the **Department of Physics & Astrophysics**, University of Delhi, Delhi, India. The manuscript has been subjected to plagiarism check by **Urkund** software. The work submitted for consideration of award of Ph.D. is original.

Sapna Mishra

Name and signature of the Candidate

Student Approval Form

Name of the Author	<i>Sapna Mishra</i>
Department	<i>Physics and Astrophysics</i>
Degree	<i>Doctor of Philosophy</i>
University	<i>University of Delhi</i>
Guide	<i>Prof. T. R. Seshadri and Prof. Hum Chand</i>
Thesis Title	<i>Probing Environment of AGNs based on their feedback processes</i>
Year of Award	

Agreement

1. I hereby certify that if appropriate, I have obtained and attached hereto a written permission/statement from the owner(s) of each third party copyrighted matter to be included in my thesis/dissertation, allowing distribution as specified below.
2. I hereby grant to the university and its agents the non-exclusive license to archive and make accessible, under the conditions specified below, my thesis/dissertation, in whole or in part in all forms of media, now or hereafter known. I retain all other ownership rights to the copyright of the thesis/dissertation. I also retain the right to use in future works (such as articles or books) all or part of this thesis, dissertation, or project report.

Conditions:

1. Release the entire work for access worldwide	
2. Release the entire work for 'My University' only for 1 Year 2 Year 3 Year and after this time release the work for access worldwide.	
3. Release the entire work for 'My University' only while at the same time releasing the	

<p>following parts of the work (e.g. because other parts relate to publications) for worldwide access.</p> <p>a) Bibliographic details and Synopsis only.</p> <p>b) Bibliographic details, synopsis and the following chapters only.</p> <p>c) Preview/Table of Contents/24 page only.</p>	
<p>4. View Only (No Downloads) (worldwide)</p>	

Signature of the Scholar

Signature and seal of the Guide

Place: _____

Date: _____

Dedicated to My Mother....

Acknowledgements

I am wholeheartedly grateful to my mother for adding value to my life. She has consistently supported me ever since my childhood. I would never be able to come up with sufficient words to be thankful to you, no matter how hard I try.

I am incredibly thankful to my Supervisor cum a genius mentor, Prof. T. R. Seshadri, for providing me with his valuable guidance. His positive attitude and energetic personality have inspired me a lot. I am extremely thankful to my Co-supervisor Prof. Hum Chand. He has always been very helpful to me with his selfless valuable suggestions, be it related to work or personal life. The scientific discussions with him have not only strengthened my theoretical and computational background but also have generated an eagerness to explore more and more research problems. Thank you so much, Sir, for believing in me, and this wouldn't have been possible without your encouragement.

I would also like to acknowledge Prof. Gopal-Krishna. It is my honor to work under his collaboration. I am also extremely grateful to Prof. Jean Surdej for introducing me to the new exciting problems of gravitational lensing and modeling. I have learned a lot in his precious direction. I am thankful to Dr. Ravi Joshi and Dr. M. Vivek, for their valuable help and discussions.

I am exceedingly obliged to Delhi University and specially ARIES for providing me this platform.

Special thanks to all the exceptionally supportive and crazy friends namely, Amit Kumar, Parveen Kumar, Raya Dastidar¹. I personally thank all my family members: Raya Dastidar (my friend cum sister), Shalu Mishra, Shikha Mishra, Vagmi Dubey, Jija ji, and Shailendra Sir, for their love and affection. I thank Piyali Saha, Rakesh Pandey, Krishan Chand, Harsh Verma, and Vibhore Negi for providing me a pleasant environment.

–Sapna

¹Do I really need to acknowledge you all?? Naaaaa..... I don't think so!!!

LIST OF PUBLICATIONS

Refereed Journal

1. On the incidence of MgII absorbers along the blazar sightlines.
Mishra, Sapna, Chand H., Gopal-Krishna, Joshi R., Shchekinov Y. A., Fatkhullin T. A., *MNRAS*, 2018,473, 5154.
2. Are there broad absorption-line blazars?
Mishra, Sapna, Gopal-Krishna, Chand H., Chand K., Ojha V., *MNRAS Letters*, 2019, 489, L42
3. Comparative intra-night optical variability of X-ray and γ -ray detected narrow-line Seyfert 1 galaxies.
Ojha, V., Chand H., Gopal-Krishna, **Mishra, Sapna**, Chand K. *MNRAS*, 2020, 493, 3642.
4. Photoionization-driven appearance/disappearance of broad absorption line quasars.
Mishra, Sapna, M Vivek, Chand H., Joshi R. 2020 (submitted to *MNRAS*)
5. Intranight optical variability of blazar counter parts of BAL–blazars.
Mishra, Sapna, et al. 2020 (to be submitted)

Conference Proceedings & GCN Circular

1. Revisiting the incidence of Mg II absorbers along the blazar sightlines.
Mishra, Sapna; Chand H., Gopal-Krishna, Joshi R., *BSRSL*, 2018, 87, 325
2. Probing the central engine and environment of AGN using ARIES 1.3-m and 3.6-m telescopes.
Chand H., Rakshit S., Jalan P., Ojha V., Srianand R., Vivek M., **Mishra, Sapna** et al., *BSRSL*, 2018, 87, 291
3. GRB 200412B: Optical afterglow detection with 1.3m DFOT.
Kumar A., Aryan, A., Pandey S.B., **Mishra, Sapna**; et al. 2020GCN.27564....1K

Abstract

It is broadly accepted that the presence of a supermassive black hole (SMBH) at the center of an active galaxy is not merely triggering the mass accretion onto it but may play a crucial role in predicting the final evolution of its host galaxy. The generation of energy via accretion of surrounding matter onto the SMBH, known as Active Galactic Nucleus (AGN) feedback, in the form of winds/outflows or jets, can interact with the stellar environment of its host and may set off the heating, compression or expulsion of the gases residing in the host galaxy. The two main modes of the AGN feedbacks are the radiative mode and kinetic mode. The radiative mode occurs in highly luminous sources, delivering high radiation pressure and hence resulting in the ejection of gases in the form of strong outflows. On the other hand, the kinetic mode scenario is perhaps due to the radio jets mainly occurring in low luminous AGNs. In this thesis, we study these modes of the AGN feedback to understand the dynamics of the gases in the central region of the AGN as well as the metal enrichment of the IGM. We have performed a detailed photometric and spectroscopic analysis for the continuum variability and absorption/emission line study of the AGNs to address some serious questions in this field.

It is widely believed that the cool gas clouds traced by Mg II absorption, within a velocity offset of 5000 km s^{-1} relative to the background quasar are mostly associated with the quasar itself, whereas the absorbers seen at larger velocity offsets towards us are intervening absorber systems and hence their existence is completely independent of the background quasar. This paradigm has been recently questioned based on an analysis of 45 blazars, showing that the number density of intervening Mg II absorbers (dN/dz) towards them is nearly 2 times higher in comparison to the normal quasar sightlines. Given its serious implications, it becomes important to revisit this finding, by enlarging the blazar sample and subjecting it to an independent analysis. In this thesis, we have assembled a ~ 3 times larger sample of blazars (191 blazars), albeit with moderately sensitive optical spectra. Our analysis with this enlarged sample shows that the dN/dz of the Mg II

absorbers statistically matches with results known for normal quasars sightlines. However, our analysis revealed that associated Mg II absorbers remain a significant contributor to dN/dz up to a velocity offset of $0.2c$ measured relative to the blazars in contrast to the commonly used upper limit of 5000kms^{-1} .

We extend our study of associated systems using the high ionization absorption lines, such as C IV. In this study, we mainly focus on the appearance and disappearance of C IV absorption troughs in broad absorption line (BAL) quasars to explore for the leading cause responsible for their extreme variation. We have derived a new set of 94 BAL quasars ($1.7 < z_{\text{em}} < 4.4$) exhibiting an appearance of C IV BAL troughs over 0.3–4.8 rest-frame years by comparing the Sloan Digital Sky Survey Data Release (SDSSDR)-7, SDSSDR-12, and SDSSDR-14 quasar catalogs. We have compared the quasar's intrinsic, BAL trough, and continuum parameters of this new appearing BAL quasar sample with a disappearing BAL quasar sample from the literature. We have found that the appearing BAL quasars are brighter compared to the disappearing BAL quasars. The appearing BAL sample is also found to have shallower BAL troughs compared to the disappearing BAL sample. The distribution of quasar continuum variability parameters between the two samples is clearly separated with the appearance of the BAL troughs being accompanied by the dimming of the continuum and vice versa. Spectral index variations in the two samples also point to the anti-correlation between the BAL trough and continuum variations consistent with the "bluer when brighter" trend in quasars. We found that the intrinsic dust model is less likely to be a favorable scenario in explaining BAL appearance/disappearance. Our analysis suggests that the extreme variations of BAL troughs like BAL appearance/disappearance are mainly driven by changes in the ionization conditions of the absorbing gas.

In this thesis, we have also accomplished a first systematic search for blazar-like BAL quasars to inquire if a blazar subset exists even among the BAL quasars. We have carried out intra-night optical variability (INOV) study of a well-defined sample of 10 BAL–blazar candidates selected based on a flat spectrum and high linear polarization at radio wavelengths. A small population of BAL–blazars can be expected in the 'polar model' of BAL quasars. However, no such case was found, since none of our 30 monitoring sessions devoted to the 10 BAL–blazar candidates yielded a positive detection of INOV, which is highly abnormal in blazars. This suggests that the physical conditions in the relativistic jets of BAL–blazars are less conducive for strong INOV. An evidence in support of this scenario has also been inferred in this thesis based on the INOV DC of 11% for a comparison sample of 9 blazars (non-BAL) matching in magnitude and redshift with that of

BAL–blazars.

In summary, our study rule out the puzzling excess of the dN/dz of intervening Mg II galaxies towards the blazars in contrast to the normal quasars. Our analysis suggests that fluctuating ionizing continuum mainly drive BAL trough’s appearance and disappearance. At last, our INOV study of BAL–blazar candidates hints that the physical conditions in the relativistic jets of the BAL quasars differ from the blazars.

Notations and Abbreviations

The most commonly used notations and abbreviations in the thesis are given below. If a symbol has been used in a different connection than listed here, it has been explained at the appropriate place.

Notations

\AA	Angstrom
α , RA	right ascension
χ^2	chi-square value
$^\circ$, deg	degree
c	velocity of light
δ , Dec	declination
dN/dz	absorber number density
ℓ	Eddington ratio
$g(z)$	Redshift path density
h	hour/hours
H_0	Hubble constant
$J2000$	epoch of observation
Jy	Jansky
keV	Kiloelectronvolt
kpc	kiloparsec(unit of distance)
λ	wavelength
m	apparent visual magnitude
M_{BH}	black hole mass
M_\odot	Mass of Sun
M_V	absolute visual magnitude

Myr	million Years
N_H	H_I column densities
Ω_Λ	Vacuum density of the Universe
Ω_m	Matter density of the Universe
pc	parsec (unit of distance)
$'$, arcmin	arc minute
$''$, arcsec	arc second
ψ	INOV amplitudes
sr	Steradian
τ	optical depth
W_r , EW	equivalent width
yr	year/years
z_{abs}	Absorption-redshift
z_{em}	Emission-redshift
z	redshift

Abbreviations

AGN	Active Galactic Nuclei
ARIES	Aryabhata Research Institute of observational SciencES
BAL	Broad Absorption Line
BBM	Bergeron et al. (2011)
BI	Balnicity Indices
BLR	Broad-Line Region
BOSS	Baryon Oscillation Spectroscopic Survey
CCD	Charge Coupled Device
CDQ	core-dominated quasar
CGM	circum-galactic medium
DAOPHOT	Dominion Astronomical Observatory Photometry
DC	Duty Cycle
DFOT	1.3-m Devasthal Fast Optical Telescope
DLC	Differential Light Curve

ESO	European Southern Observatory
FORS	FOcal Reducer/low dispersion Spectrograph
FWHM	Full Width at Half Maximum
GHz	Giga Hertz
HCT	2.01-m Himalayan Chandra Telescope
HFOSC	Himalaya Faint Object Spectrograph and Camera
HiBAL	High-ionization BAL quasars
IAO	Indian Astronomical Observatory
IGM	Intergalactic medium
IIA	Indian Institute of Astrophysics
INOV	Intranight Optical Variability
IRAF	Image Reduction and Analysis Facility
KDE	Kernel Density Estimation
K-S	Kolmogorov-Smirnov
LDQ	lobe-dominated quasar
LoBAL	Low-ionization BAL quasars
LOS	line-of-sight
LRIS	Low Resolution Imaging Spectrograph
MJD	Modified Julian Date
NED	Nasa Extragalactic Database
NLR	Narrow-line Region
QSO	Quasi Stellar Object
RL	radio-loud
RQ	radio-quiet
RRM	Residual Rotation Measure
SAO	Special Astrophysical Observatory
SCORPIO	Spectral Camera with Optical Reducer for Photometrical and Interferometrical Observations
SDSS	Sloan Digital Sky Survey
SDSSDR	Sloan Digital Sky Survey Data Release
SNR	signal-to-noise ratio
ST	1.04-m Sampunanand Telescope

UV	ultraviolet
UVES	UV-Visual Echelle Spectrograph
VLT	Very Large Telescope

Contents

Declaration	iii
Acknowledgements	vii
Abstract	ix
Notations and Abbreviations	xiii
List of Tables	xxi
List of Figures	xxiii
1 Introduction	1
1.1 Active galactic Nuclei	1
1.2 AGN unification model	3
1.3 AGN feedbacks and Types	4
1.3.1 Kinetic mode of feedback: Blazars	5
1.3.2 Radiative mode of feedback: Broad absorption line quasars	6
1.4 Thesis motivation	8
1.5 Thesis Outline	9
2 Data acquisition and reduction	11
2.1 Spectroscopy	11
2.1.1 Data sourcing	13
2.1.2 Data Reduction	14
2.1.2.1 Pre-processing	16

2.1.2.2	Spectrum extraction	17
2.1.2.3	Dispersion correction	18
2.1.2.4	Flux calibration	19
2.2	Photometry	19
2.2.1	Data sourcing	20
2.2.2	Data reduction	21
2.2.2.1	Pre-processing	21
2.2.2.2	Aperture Photometry	22
2.3	Catalogs	23
3	Probing AGN environment using the kinetic-mode feedback	25
3.1	On the incidence of Mg II absorbers along the blazar sightlines	25
3.1.1	The Sample	27
3.1.2	Analysis	31
3.1.2.1	Data Reduction	31
3.1.2.2	Computation of the EW detection limit and the corresponding useful redshift path	32
3.1.2.3	Mg II absorption-line identification	33
3.1.2.4	Computation of dN/dz	34
3.1.3	Results	35
3.1.3.1	Incidence of Mg II absorbers in the present enlarged sample	35
3.1.3.2	Re-analysis of the BBM sample	37
3.1.4	Discussion and Conclusion	40
4	Probing AGN environment using the radiative-mode feedback	45
4.1	Photoionization-driven appearance/disappearance of broad absorption line quasars	46
4.1.1	The Sample	48
4.1.2	Data Analysis	50
4.1.2.1	Continuum fitting	51
4.1.2.2	BAL identification	52
4.1.2.3	BAL trough properties measurement	54
4.1.2.4	BAL Variability Measurement	55
4.1.3	Results	58

4.1.3.1	Comparison of quasar intrinsic properties	59
4.1.3.2	Comparison of BAL-profile Properties	60
4.1.3.3	Comparison of continuum properties	61
4.1.3.4	Comparison of reddening parameters	66
4.1.4	Discussion	68
4.1.5	Conclusions	70
5	The relative role of kinetic-mode and radiative-mode of AGN feedback	73
5.1	Are there broad absorption-line blazars?	74
5.1.1	The sample of BAL-blazar candidates	75
5.1.2	Intranight photometric monitoring	76
5.1.3	The Data Reduction	77
5.1.4	Statistical analysis and results	81
5.1.5	Discussion and Conclusion	83
5.2	Intra-night optical monitoring of blazar counter parts of BAL quasars	86
5.2.1	Sample	87
5.2.2	Photometric observation	89
5.2.3	The Data Reduction	91
5.2.4	Statistical analysis and Result	91
5.2.5	Estimation of INOV DC	95
5.2.6	Discussion and Conclusion	95
6	Summary, Conclusions and Future Prospects	97
6.1	Summary and Conclusions	97
6.2	Future Prospects	100
A		103
B		107
	Bibliography	121

List of Tables

2.1	Properties of telescopes, detectors, spectrographs utilized in spectral data sourcing.	14
2.2	Parameters of telescopes, detectors and filters used in the photometric data sourcing.	20
3.1	The spectral data sourcing for our enlarged sample of blazars.	27
3.2	Basic properties of our sample of 191 blazars.	30
3.3	The detected 43 Mg II absorption systems and their rest-frame equivalent widths, $W_r(\text{Mg II } \lambda 2796 \text{ \AA})$, as identified in 34 blazars belonging to our sample of 191 blazars.	34
3.4	Incidence of Mg II absorbers for the present sample and its various subsets. . . .	36
3.5	Incidence of strong Mg II absorption systems towards the low SNR (SNR<15) and high SNR (>15) spectra in our sample of 191 blazars. The last column shows the same relative to normal QSOs.	37
3.6	Re-analysis of the (high sensitivity) spectra of the 42 southern blazars in the BBM sample.	40
3.7	The results for the present sample and its various subsets, after excluding the Mg II absorption systems with $\Delta v < 60000 \text{ km s}^{-1}$	41
4.1	Summary of sample selection that resulted in the compilation of appearing BAL sample.	50
4.2	Physical parameters of <i>Preliminary</i> sample of 379 BAL quasars with 517 MJD pairs.	51
4.3	Summary of various subsamples involved in the present study.	57
4.4	Details of the <i>Appearing</i> , <i>Appearing pristine</i> , and <i>Disappearing</i> samples of C IV BAL absorption complexes.	58

5.1	The sample of 10 BAL–blazar candidates monitored for intranight optical variability (INOV).	76
5.2	Parameters of comparison stars selected for the 10 BAL–blazars.	78
5.3	Observation log of the 30 monitoring sessions of the 10 BAL–blazar.	82
5.4	Properties of our $m-z$ matched blazar sample.	87
5.5	Parameters of comparison stars selected for the 9 $m-z$ matched blazars.	90
5.6	Observation log and INOV results for the sample of 9 $m-z$ matched blazars.	94
A.1	Basic properties of our sample of 191 blazars.	103
A.1	(continued)	104
A.2	The detected 43 Mg II absorption systems and their rest-frame equivalent widths, $W_r(\text{Mg II } \lambda 2796 \text{ \AA})$, as identified in 34 blazars belonging to our sample of 191 blazars.	105
B.1	Physical parameters of <i>Preliminary</i> sample of 379 BAL quasars with 517 MJD pairs.	107
B.1	(continued)	108
B.1	(continued)	109
B.1	(continued)	110
B.1	(continued)	111
B.1	(continued)	112
B.1	(continued)	113
B.1	(continued)	114
B.1	(continued)	115
B.1	(continued)	116
B.1	(continued)	117
B.2	Details of the <i>Appearing</i> , <i>Appearing pristine</i> , and <i>Disappearing</i> samples of CIV BAL absorption complexes.	118
B.2	(continued)	119
B.2	(continued)	120

List of Figures

1.1	Image credit: Brooks/Cole Thomson Learning.	2
1.2	A representation of the unified AGN model presented by Urry & Padovani (1995).	4
2.1	Basic spectrograph layout.	12
2.2	Raw CCD image of the spectrum of J145127+635426 recorded on the CCD in a rectangular window of 2068×1046 pixels. The image is taken with SCORPIO spectrograph mounted on SAO 6-m telescope with an integration time of 1200 seconds. A bright narrow horizontal strip is obtained when a light beam passing through the source at the center of the slit (with a width of 1.2'') gets dispersed via GRISM-VPHG1200G. This horizontal strip is called the dispersion axis covering a wavelength range of 3900-5700 Å. The width of dispersion axis is limited by the atmospheric seeing conditions. The vertical lines in the image are the night sky emission lines prevailing in the entire region of the slit opening. The uneven background illumination pattern across the image are produced by (i) the varying QE of CCD pixels, and (ii) nonuniformity of illuminated sky from the slit. The random circular patches are caused by the high energetic cosmic-ray hits.	15
2.3	Raw CCD frame acquired for the INOV monitoring of J115944.82+011206.9 (encircled in green) with DFOT within a CCD window of 2048×2048 pixel in sdss-r filter over an exposure time of 420 seconds.	21

3.1	Representative normalized blazar spectra: J001937+202146 (<i>top</i>), J191816-411154 (<i>middle</i>), J073346+411120 (<i>bottom</i>). In each case, the most redshifted Mg II absorption system (thick blue arrow) detected was used as the lower limit to the blazar's emission redshift. Thin blue lines in <i>top panel</i> mark the Fe II (λ 2344, 2374, 2383, 2585, 2600) lines associated with the Mg II absorption line system at $z_{\text{abs}} = 0.85840$	29
3.2	Distributions of emission redshift (<i>left</i>) and SNR (<i>right</i>) for our full sample of 262 blazars (including the 71 blazars which are subsequently excluded from the Mg II strong systems analysis; see Section 3.1.2.2. For 58 blazars without exact z_{em} , we have used their lower limit on z_{em} , derived based on the most redshifted absorption system seen in their spectra).	31
3.3	The distributions of redshift path density ($g(z)$) for the intervening Mg II systems towards blazars, for the strong ($W_r(2796) \geq 1.0 \text{ \AA}$: red dashed curve) and the weak absorption systems ($0.3 \leq W_r(2796) < 1.0 \text{ \AA}$: blue solid curve).	33
3.4	Cumulative number of weak (<i>left</i>) and strong (<i>right</i>) intervening Mg II absorption systems detected towards blazars (blue solid line) and QSOs (red dashed line), after excluding the systems with offset velocity ($\Delta v < 5000 \text{ km s}^{-1}$ (<i>top panel</i>), $\Delta v < 30000 \text{ km s}^{-1}$ (<i>middle panel</i>) and $\Delta v < 60000 \text{ km s}^{-1}$ (<i>bottom panel</i>). For QSOs the estimates for weak Mg II systems are taken from Nestor et al. (2005) (see text), and for strong systems these are adopted from Prochter et al. (2006).	38
3.5	Number density evolution of strong ($W_r(2796) \geq 1.0 \text{ \AA}$) Mg II absorption systems (averaged over redshift bins of 0.5) towards our 191 blazar sightlines (black triangles), and the sightlines towards the QSOs in the SDSS (blue solid line). The absorption systems with $\Delta v < 5000 \text{ km s}^{-1}$ have been excluded. The solid line for the SDSS QSOs has been computed from the analytical expression given by Zhu & Ménard (2013) for strong Mg II absorption systems towards QSOs. The two distributions show an excellent agreement with a P_{null} of ~ 0.99 based on the K-S and χ^2 tests.	39

-
- 4.1 The continuum fit (red dashed curve) for the spectrum of SDSS-J072134.30+413108.8 modeled by a combination of a reddened power law, double Gaussians for C iv and Si iv emission lines and a single Gaussian for C iii] emission line. Three vertical lines (black dotted) correspond to the quasar's S iv $\lambda\lambda$ 1393,1403, C iv $\lambda\lambda$ 1548,1550, and C iii] λ 1909 emission lines. 52
- 4.2 Demonstration of determining the lower (v_{min}) and upper (v_{max}) limits of an absorption complex using the multi-epoch spectra of SDSS J124312.93+144812.0. Two vertical dashed lines indicate the lower and upper limit of velocity region used for the BAL trough, while two horizontal dashed lines represent the normalized continuum level at 1.0 and 0.9. 53
- 4.3 Distribution of rest-frame timescale between the two epochs for *Appearing* (*blue*), *Appearing pristine* (*red*) and *Disappearing* (*green*) samples. Overlaid on the data are the PDFs derived with KDE using Gaussian kernel of fixed bandwidth for *Appearing* (*solid blue*), *Appearing pristine* (*dashed red*) and *Disappearing* (*dotted green*) samples. The p-values computed using the K-S test between *Appearing* and *Disappearing* ($P_{1\rightarrow3}$), and *Appearing pristine* and *Disappearing* ($P_{2\rightarrow3}$) are given in top right corner. 58
- 4.4 Distribution of (a) bolometric luminosity, (b) black hole mass, (c) Eddington ratio and (d) *i*-band absolute magnitude for *Appearing* (*blue*), *Appearing pristine* (*red*) and *Disappearing* (*green*) samples are drawn. The PDFs over the data sets generated using Gaussian KDEs for *Appearing* (*solid blue*), *Appearing pristine* (*dashed red*) and *Disappearing* (*dotted green*) samples are shown in each panel. The estimated p-values of the K-S test between *Appearing* and *Disappearing* ($P_{1\rightarrow3}$), and *Appearing pristine* and *Disappearing* ($P_{2\rightarrow3}$) are shown in the top right corner of each panel. 60

-
- 4.5 Distribution of (a) absolute change in EW, (b) absolute fractional change in EW, (c) average EW, (d) average normalized BAL depth, (e) absolute change in normalized BAL depth, (f) minimum outflow velocity, (g) maximum outflow velocity, and (h) width of BAL trough for *Appearing (blue)*, *Appearing pristine (red)* and *Disappearing (green)* BAL complexes. On top of each distribution in each panel are the PDFs derived with Gaussian kernel KDE of similar bandwidth for *Appearing (solid blue)*, *Appearing pristine (dashed red)* and *Disappearing (dotted green)* samples. The p-values derived from the K-S test between *Appearing* and *Disappearing* ($P_{1\rightarrow3}$), and *Appearing pristine* and *Disappearing* ($P_{2\rightarrow3}$) are mentioned at the top right corner of each panel. 62
- 4.6 Distribution of (a) change in continuum flux at 1700 Å (b) median of change in V-band magnitudes, (c) standard deviation of change in V-band magnitudes and (d) slope of change in V-band magnitude with time for *Appearing (blue)*, *Appearing pristine (red)* and *Disappearing (green)* samples. Overlaid on the three distributions are the PDFs constructed with KDE using Gaussian kernels of same bandwidth for *Appearing (solid blue)*, *Appearing pristine (dashed red)* and *Disappearing (dotted green)* samples. The p-values of the K-S test applied on *Appearing* and *Disappearing* ($P_{1\rightarrow3}$), and *Appearing pristine* and *Disappearing* ($P_{2\rightarrow3}$) are labeled at the top right corner of each panel. 63
- 4.7 Distribution of change in spectral index for *Appearing (blue)*, *Appearing pristine (red)* and *Disappearing (green)* samples. On top of these three distributions in each panel are the PDFs generated with KDE taking Gaussian kernels of similar bandwidth for *Appearing (solid blue)*, *Appearing pristine (dashed red)* and *Disappearing (dotted green)* samples. The p-values of the K-S test estimated for *Appearing* and *Disappearing* ($P_{1\rightarrow3}$), and *Appearing pristine* and *Disappearing* ($P_{2\rightarrow3}$) are given at the top right corner. 66

4.8	Distribution of slope of IR continuum for <i>Appearing</i> (blue), <i>Appearing pristine</i> (red) and <i>Disappearing</i> (green) samples. On top of these three distributions in each panel are the PDFs generated with KDE taking Gaussian kernels of similar bandwidth for <i>Appearing</i> (solid blue), <i>Appearing pristine</i> (dashed red) and <i>Disappearing</i> (dotted green) samples. The p-values derived from the K-S test between <i>Appearing</i> and <i>Disappearing</i> ($P_{1\rightarrow3}$), and <i>Appearing pristine</i> and <i>Disappearing</i> ($P_{2\rightarrow3}$) are mentioned at the top right corner.	67
5.1	DLCs for the 10 BAL–blazar candidates (30 monitoring sessions). The name of the AGN, date, duration, and the telescope used are mentioned at the top of the panels for individual sessions. In each panel, the upper curve in blue is the DLC of the chosen two comparison stars ("star-star" DLC). The two middle blue curves display the DLCs of the target AGN relative to the two comparison stars, as defined in the labels on the right side. The lowest profile in each panel (black stars) shows the variation of the FWHM through the monitoring session.	79
5.2	Same as Fig.5.1	80
5.3	Distribution of absolute magnitude in B-band (M_B , upper panel) and emission redshift (lower panel) for the present sample of 10 BAL–blazar candidates (cyan filled) and for the sample of 24 normal blazars from Goyal et al. (2013) (black dotted). The dotted vertical in the upper panel corresponds to $M_B = -25.0$	84
5.4	Distribution of INOV amplitude (ψ) for the 4 bins of T_{int} , derived using the comparison sample of 24 normal blazars monitored in 85 sessions (see text).	85
5.5	Distribution of R-band magnitude (left) and redshift (right) for BAL–blazar sample of M19 (red-filled) and our $m-z$ matched blazar sample (black-hatched). The p-value of the K-S test is mentioned at the top right corner of each panel. The two vertical lines in each panel correspond to the parameters' median values in BAL–blazar sample (red dashed) and $m-z$ matched blazar sample (black dashed).	88
5.6	Distribution of the intrinsic duration of 27 monitoring sessions devoted to 9 BAL–blazars of M19 (red filled) and 18 sessions dedicated to 9 $m-z$ matched blazars in the present study (black hatched). The two dashed vertical lines in red and black show the median value of T_{int} of the BAL–blazar and $m-z$ matched blazar samples, respectively. The p-value of the K-S test estimated for these two samples is mentioned at the top right corner.	89

5.7 Same as Fig. 5.1 but for the *m-z* matched blazar sample. 92

5.8 Same as Figure 5.7 93

Chapter 1

Introduction

1.1 Active galactic Nuclei

It is well established that the center of most, if not all, galaxies harbors a supermassive black hole (SMBH). In case of few galaxies, accretion onto SMBH ($\sim 10^8 M_{\odot}$) yields an enormous amount of radiation and giving rise to luminosities of the order of $10^{46} - 10^{48} \text{ erg-s}^{-1}$. Such galaxies are referred to as active galactic nuclei (AGNs). Typical features of these galaxies that distinguish them from the normal galaxies are the following:

- Tremendously luminous compact nuclear region that outshines the entire host galaxy.
- Presence of both thermal and/or non-thermal continuum emission spanning almost the entire range of the electromagnetic spectrum.
- Signature of very broad and forbidden narrow emission lines in the typical spectra of these objects.
- Rapid variability of the continuum and/or emission lines. The variability time scale ranges from minutes to years depending on the compactness of the central region.

The standard model of AGN is shown in Fig. 1.1, which depicts the presence of a SMBH at the center as the main element of the accretion process. Infalling material around the SMBH spirals inward and loses its potential energy which gets converted to thermal energy and is released in the form of radiation. As the infalling gas has finite initial angular momentum, it cannot fall straight into the black hole. Rather through friction with other materials and momentum transportation, the gas will form a disk-like structure normal to the direction of angular momentum vector. This

disk-like structure, known as accretion disk (AD), extends up to a distance of 10^{-3} pc from the core of the SMBH. It is mainly comprised of the optically thick hot plasma ($n_{e^-} \sim 10^{15} \text{cm}^{-3}$) therefore emits its radiation in the form of black body emission. Above the AD there exists a region of extremely hot relativistic particles known as hot corona and is capable of producing X-rays through inverse Comptonization of optical/UV photons coming from the AD. At a distance between 0.01 – 1 pc from the core, we have broad line region (BLR) which contains the clumpy clouds of very high density ($\sim 10^{8-11} \text{cm}^{-3}$). Being closer to the BH, these clouds are under the high influence of its gravity. Thus, these clouds have very large velocities of the order of $> 1000 \text{ km s}^{-1}$, thereby producing emission line typically of same velocity widths due to Doppler effect. The region between 1-100 pc is surrounded by optically thick molecular dust that form the dusty torus. This region is completely opaque to BLR emission and it mainly emits in infrared by reprocessing the optical/UV photon and re-emit in longer wavelengths. Going further out from the core up to a distance of 10^{2-3} pc, there are clouds of low column density ($\sim 10^{2-4} \text{ cm}^{-3}$) having velocities of the order of $< 1000 \text{ km s}^{-1}$ being farther away from the BH. This region is known as narrow line region (NLR) and because of the low density of clouds, NLR mainly gives rise to the forbidden emission lines of narrow widths. In about 10% of AGNs, depending on the AD nature and BH spin, the infalling material gets ejected in the form of collimated relativistic jets. The exact physical phenomena behind these jets extending to very far distance ($\sim 10 \text{ kpc}$) while being collimated is uncertain.

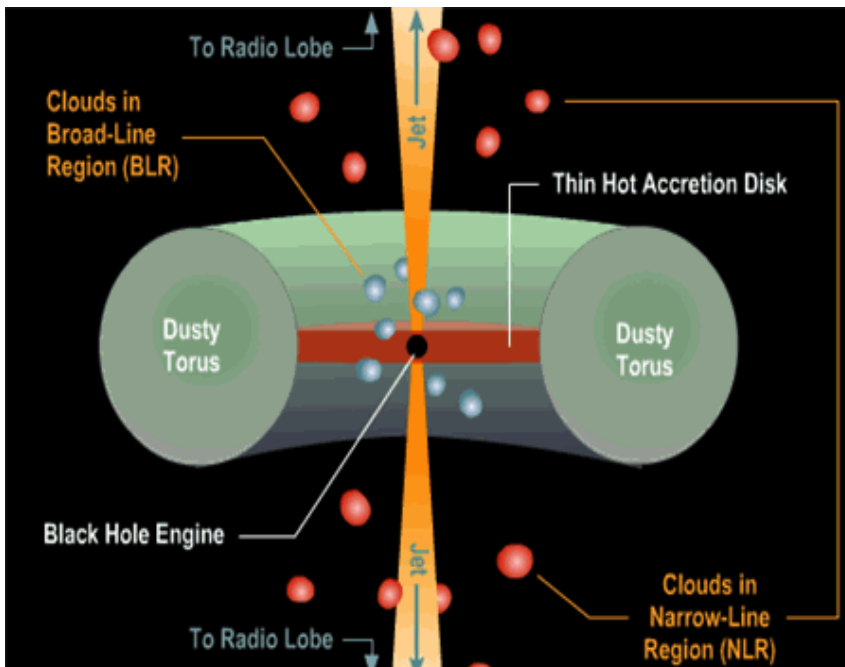


Figure 1.1: Image credit: Brooks/Cole Thomson Learning.

1.2 AGN unification model

The standard model outlined above illustrate a simple picture of AGNs. However the miscellanies of the observational features found in variety of AGNs do not seem to support directly the aforementioned AGN model in spite of having a common powering mechanism. Historically AGNs were first classified based on their luminosities. AGNs with higher luminosities completely outshining the host galaxies formed one class and were known as quasars (with absolute magnitude $M_B < -23$ mag; rarer in the local universe), while low luminous AGNs with resolved host galaxies were tagged as Seyfert galaxies ($M_B > -23$ mag; more common locally). Further, the evidence of anisotropy observed in the radio emission and the occurrence/non-occurrence of broad emission lines in the spectral feature of many AGNs implies that the appearance of the AGNs strongly depend on the observer's position relative to the torus axis which gave rise to unification model (Urry & Padovani 1995). Based on this model the variety of AGN properties explained above have been reconciled and hence divided AGNs into two types, type1 and type2 AGNs (see Antonucci 1993; Urry & Padovani 1995). The basis of this classification mainly relies on the difference seen in the spectral feature of different types of AGNs.

In type-1 AGNs (e.g., Seyfert1, QSOs), observer's LOS passes along the jet axis (face-on perspective, see Fig. 1.2) and hence intercept the direct view of both BLR and NLR, as well as the AD emission. Therefore type-1 AGN spectra will have both broad and narrow permitted emission lines coming from NLR and BLR. Type-1 AGNs also show strong UV/optical continuum. On the other hand, on viewing through the torus (edge-on perspective, Fig. 1.2), the AD (optical-UV and soft X-ray continuum) and the BLR clouds get obstructed by the intercepting material and one can see only emission (both permitted and forbidden) coming from the NLR. These AGNs are classified as type-2 (e.g., Seyfert2). In type-2 AGNs, the UV/optical continuum is highly suppressed, while an excess of IR continuum is noticeable.

AGNs are further sub-classified on the basis of the radio emission. The sources viewed along the jet axis will have dominance of emission in radio regime (due to non-thermal synchrotron emission) and are called radio-loud (RL, eg. Seyfert 1, blazars, quasars, broad line radio galaxies). The sources viewed at a larger angle relative to the jet axis will contribute less in the radio regime and classified as radio-quiet (RQ, e.g., narrow-line radio galaxies, Seyfert 2).

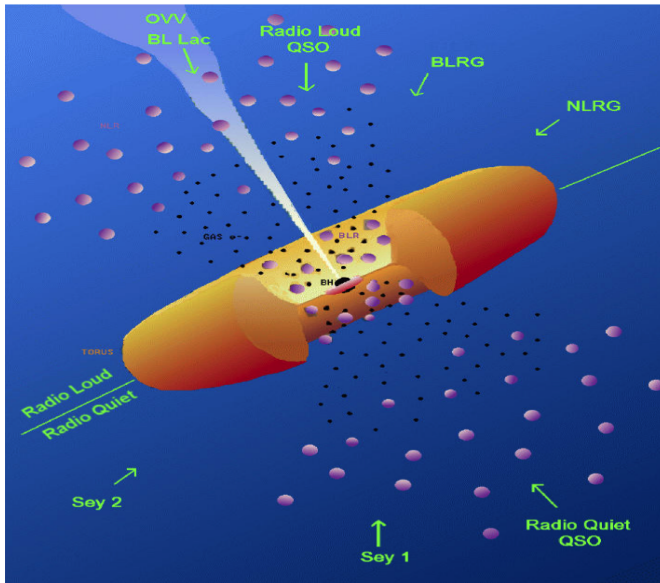


Figure 1.2: A representation of the unified AGN model presented by Urry & Padovani (1995).

1.3 AGN feedbacks and Types

A tremendous amount of energy released from the accretion of surrounding matter onto the SMBH may severely affect the host galaxy environment. The binding energy of the host galaxy bulge of mass M_{gal} is defined as $E_{\text{gal}} \approx M_{\text{gal}}\sigma^2$; where σ is the stellar velocity dispersion in the bulge. However, the radiative energy produced in black hole growth via accretion is given as $E_{\text{BH}} = \epsilon M_{\text{BH}}c^2$; where ϵ is the efficiency of the accretion and M_{BH} is the black hole mass. From the studies of Kormendy & Gebhardt (2001); Merritt et al. (2001); Häring & Rix (2004) it is often found that $M_{\text{BH}} \approx 1.4 \times 10^{-3} M_{\text{gal}}$. Typically the maximum stellar dispersion velocity of the galaxies is of the order of 400 km s^{-1} and assuming $\epsilon = 0.1$, the value of $E_{\text{BH}}/E_{\text{gal}}$ will be of the order of 80. Consequently, the black hole growth energies via accretion are generally very large compared to the binding energies of the host galaxies. Therefore, the interaction of the accretion-generated immense amount of energy and radiation with the gases residing in the host galaxies may decide the final fate of the AGN host galaxies. The process with which such interactions take place is termed as ‘AGN feedback’.

The AGN feedback affects the galaxy environment in two ways: one negatively by quenching the star formation and second positively by triggering the star formation in the host galaxy. In the former case, the energy and radiation produced via accretion heats up the gases within the galaxy. This deters the cooling of the gas and disperses off the galaxy material, thereby quenching star formation and AGN activities. However, in the latter scenario, the intense flow of energy

and momentum compresses the material around the galaxy and triggers the star forming activities. These processes get materialized through two major modes of the AGN feedback which are described in subsequent section.

Based on the powering mechanism and the energy outcome, AGN feedbacks are classified into two modes. The first mode is known as *kinetic mode* alias jet mode or maintenance mode. The AGNs which are believed to exhibit this mode have a low accretion rate and possess powerful jets of relativistic plasma. This mode often sets off when AGN resides in the massive galaxies with a hot halo. The second mode is called *radiative mode* a.k.a. wind mode or quasar mode. This mode is triggered when the AGNs have strong outflows. Such AGNs are believed to have an accretion rate nearly equal to or more than the Eddington limit.

The objective of the thesis is to study the environment of the AGNs and their surroundings employing the fact that they are known to harbor the aforementioned forms of energy outcome i.e., either in the form of jets or outflows/winds. In the following sections, the characteristic properties of two subclasses of AGNs are discussed: (i) blazar having powerful jets closely aligned with the LOS of the observer, (ii) broad absorption line (BAL) quasars with the strong observational signature of outflows/inflows.

1.3.1 Kinetic mode of feedback: Blazars

Blazars are among the RL population of AGNs in which the jet axis makes an angle $< 10^\circ$ relative to the LOS of the observer. The extent of these jets traces a distance of \sim Mpc in some cases, therefore, they have an extreme impact on the intergalactic medium (IGM). The high energy particles in the magnetized relativistic plasma interact with the photons and give rise to both optical and radio non-thermal synchrotron radiations. As a result, the radiations are highly polarized in radio and optical regimes (Fugmann 1988; Lister & Smith 2000). Since the jets are highly aligned, the particles emitting radiations acquire a very high bulk motion giving rise to what we call Doppler boosting of the radiations (Begelman et al. 1984). Consequently, blazars are among the highly variable extragalactic objects which show variations on the time scales ranging from a few hours to years (Gopal-Krishna et al. 1995; Sagar et al. 2004; Stalin et al. 2005; Gopal-Krishna et al. 2011) and hence also known as the optically violent variable (OVV). Combining the variability time scale with the causality argument hints that the emitting regions are very compact. Depending on whether the emitting jet particles are approaching or receding the observer, the Doppler effect can enhance or undermine the strength of the radiations. The amount by which the intensity

of the approaching object gets modified is the same by which the intensity of the receding object gets attenuated. That is why in the case of the highly aligned sources the receding jets are not noticeable. These sources because of relativistic bulk motion of particles, are sometimes subjected to the apparent superluminal motion of jet components which can be observed with high angular resolutions. Even though rigorously studied some phenomena such as jet launching mechanism, the exact location of the high energy emitting region are still unclear.

Blazars are sub-divided into two classes: BL Lacertae objects (BL Lacs) and flat-spectrum radio quasars (FSRQs). The former class shows no or very weak emission lines ($EW < 5 \text{ \AA}$) in the optical spectrum due to the boosted continuum. The latter class possesses strong emission lines in the optical spectrum. The BL Lacs are generally found at low redshift precisely due to the featureless spectra and have low luminosity ($< 10^{46} \text{ erg s}^{-1}$) while FSRQs are found at high redshifts and are extremely luminous ($\sim 10^{46-48} \text{ erg s}^{-1}$).

1.3.2 Radiative mode of feedback: Broad absorption line quasars

Strong outflows are ubiquitous feature of the AGNs (Laor & Brandt 2002). These outflows extend to large distance relative to the central SMBH enriching the metal content in the circumgalactic medium (CGM) and the IGM of nearby galaxies (Kormendy & Ho 2013). Their existence strongly hints that the mass ejection of AGNs is correlated with the mass accretion onto the SMBH. As a consequence, the expelling angular momentum from the accreting material (e.g., Emmering et al. 1992) could drive away the matter content from the host galaxy, quenching the star formation. Therefore, their studies are essential to understand the renowned AGN feedback (Fabian 2012) for a better comprehension of the black hole growth and host galaxy evolution.

The most spectacular manifestation of quasar outflows is the broad absorption lines seen in the blue wings of the prominent emission lines like C iv and Mg II, in the rest-frame UV spectra of 15–20% of optically selected quasars (Hewett & Foltz 2003). These absorption troughs trace outflows of thermal plasma with speeds from $\sim 2000 \text{ km s}^{-1}$ to $\sim 0.2c$. The presence of broad absorption is thought to be arising from the co-existing optically thick material in the winds generated near the accretion disk and accelerated radially outward (Murray et al. 1995; Elvis 2000). These winds often carry a large amount of energy and momentum along their way and are hence the potential contributor to the AGN feedback (Fabian 2012).

The first BAL signature was reported by Lynds (1967) in the ionization of C iv and Si iv towards the blue side of the quasar emission. The conventional definition of BALs demands the

absorption feature to be wider than 2000 km s^{-1} and at least 10% below the continuum level (Weymann et al. 1991). Additionally, absorption troughs with a width between $500\text{--}2000 \text{ km s}^{-1}$ are known as mini-BALs, while those with widths less than 500 km s^{-1} are termed as narrow absorption lines (NALs). Further, BALs are divided into three sub-classes based on the ionization states of absorption troughs. BAL troughs resulting from the high ionization transitions of the species such as C IV, Si IV, N V, P V are referred to as HiBALs (Weymann et al. 1991). They contribute to the majority of the BAL population. Around $\sim 10\%$ of BALs arise from the transition of lower ionization species such as Al II, Al III, Mg II and are known as LoBALs (Voit et al. 1993). Very few BAL populations show absorption troughs of the transitions from the excited states of Fe II or Fe III and are called FeLoBALs (Becker et al. 2000). In order to illustrate the origin of BAL outflows, two main models have been propounded i.e., orientation model and evolution model.

Under the orientation scenario, all quasars are believed to have BAL winds. However, the existence of slightly redder continuum (Reichard et al. 2003) and high optical polarisation distinguishes the BAL quasars from the normal quasars. This observational signature is dictated by the preferential alignment of BALQSO's as compared to normal quasars. It has been suggested that BAL outflows originate from small radii of rotating AD of AGN, along the equatorial direction and are accelerated to high speed via radiative and/or magneto-centrifugal forces, in the form of thin funnel-shaped outflows having a width of $\sim 6^\circ\text{--}12^\circ$ diverging outward (Murray et al. 1995; Proga et al. 1998; Elvis 2000).

The bipolar wind model on the other hand, (Punsly 1999a,b) predicts that the BAL outflow would be gradually aligned along the polar axis (normal to the accretion disc), such that the relativistic jet would be nested inside it. Clearly, this model is more relevant for the BALs exhibited by RL quasars. This also raises the question about the role of the jets in accelerating the BAL clouds. Some support for this possibility comes from (i) the discovery of rapid radio variability, or bright nuclear radio jets in some RL BAL quasars, revealing very high brightness temperatures of the jets which are understood in terms of a relativistic jet roughly pointed towards us (e.g., Zhou et al. 2006; Ghosh & Punsly 2007; Doi et al. 2009). Likewise, Becker et al. (2000) found that (ii) about one-third of the radio-selected BAL quasars show flat radio spectra (due to the dominance of a Doppler boosted nuclear synchrotron jet), which again favors a pole-on orientation for the accretion discs in these quasars.

In the evolutionary scenario, BAL outflow is believed to exist for a short duration of quasar lifetime such that their reported BAL fraction is derived from the fraction of quasar's lifetime for

which these outflows appear. Alternatively, these BAL outflows may also result during evolutionary stages when QSOs expel thick shrouds of gas and dust (Voit et al. 1993; Gregg et al. 2006).

1.4 Thesis motivation

Although the broader picture of AGN and its environment is well constrained from the unification scheme (Padovani & Giommi 1995), several bemusing scenarios have been reported where the existing scheme of AGN unification and its circumgalactic environment is challenged. For instance, varying estimates of the incidence rates of intervening absorption systems (i.e., with offset velocity $\geq 5000 \text{ km s}^{-1}$ and gravitationally unbound to the background source) have been detected towards different types of background sources, such as normal QSOs, gamma-ray bursts (GRBs) and blazars (Stocke & Rector 1997; Prochter et al. 2006; Tejos et al. 2009; Bergeron et al. 2011, hereinafter BBM). It has challenged the conventional wisdom of the intervening systems and hence has raised several interesting questions such as: can the presence of relativistic jets alter the occurrence rate of the intervening absorption systems? Up to what distance relative to the background source the impact of the relativistic jets can be witnessed? On the other hand, in case of BAL quasars with strong outflows, extreme variabilities seen in their broad absorption troughs on multi-year timescales are comprehended from (i) change in the covering fraction of the QSOs by the absorbing gas due to its transverse motion across our LOS, (ii) change in the ionizing conditions of the radiation field giving rise to the change in optical depth of the absorbers. Yet proper validation and precise implications of these exciting physical scenarios demand their detailed manifestation on a statistically larger number of BAL quasars, especially where the variability results in the complete emergence or disappearance of the BAL troughs. To illustrate the low observed BAL quasar fraction (i.e., 10–20%) among the quasar population, primarily two models have been proposed viz., orientation model and evolution model, however, both hitherto lack concrete consensus. If BAL quasars with flat/inverted radio spectra and a large radio polarization are described under the bipolar wind model, where BAL outflows are aligned along the axis of the relativistic jet, then can these BAL quasars be regarded as manifestations of blazars?

Therefore, a detailed study of the aforementioned interesting problems would play a crucial role in understanding the environment of various subclasses of AGNs where different modes of feedback mechanism (e.g., radiative/wind mode or kinetic/radio mode) could be at play. In this thesis, we intend to answer the following question regarding the objectives mentioned above:

-
- Does the incidence rate of intervening absorbers depend on the type of background AGNs? Can the presence of relativistic jets alter the demarcating limits between the jet-accelerated associated and the intervening absorption systems? This will be important to study the environments of AGNs when viewed differently.
 - What drives the extreme variation of absorption troughs in emerging BAL quasars? This will be important for understanding the location and physical state of the absorbing gas (e.g., quasar wind lifetimes, size, and geometries) and hence the physical processes that give rise to such outflows.
 - Is there any resemblance of BAL quasars with flat/inverted spectra and high radio polarisation with the blazar population of AGNs? In other words, does the blazar subset exist even among BAL quasars? If yes, then what impact do these strong outflows have onto the strong continuum variabilities predominantly visible in the blazars? Whenever the cause behind the observed low fraction of BAL quasar populations is concerned, discernment of such questions is vital. Hence, this will be of utmost importance to confirm/refute among the evolutionary and/or orientational models of the BAL quasars.

1.5 Thesis Outline

The work presented in the thesis adopts the modes of AGN feedbacks to address the above stated interesting problems pertaining to the various AGN environments and is arranged in six chapters as outlined below:

Chapter 1: The basic introduction of the AGNs and their unification scheme are discussed in this chapter. This chapter also provides a brief prologue to the AGN feedbacks, their types, and modes with a comprehensive description of AGNs contributing to the feedback mechanisms. In addition, the underlying thesis motivation is explicitly stated in this chapter.

Chapter 2: In this chapter, detailed illustrations of data sourcing and telescope properties are given for both spectroscopic and photometric observations. It also provides a comprehensive description of various backend instruments mounted on respective telescopes during our monitoring sessions. Furthermore, basic pre-processing steps and calibration tasks involved in removing the instrumental defects from the data are explained in detail.

Chapter 3: In this chapter, we probe whether the presence of relativistic jets can alter the demarcating limits between the jet-accelerated associated and the intervening absorption systems.

It compares the incident rates of intervening Mg II absorbers towards the background sources with and without jets. The details of sample making, analysis and the conclusion drawn are presented in this chapter and are published in [Mishra et al. \(2018\)](#).

Chapter 4: In this chapter, based on the extensive literature search, we isolate a new catalog of appearing C IV BAL quasars and present their detailed properties. The chapter aims to examine the cause behind the extreme variation of their broad absorption troughs and seeks for the comprehensive explanation of such variations to understand the physical condition near the outflowing region. The work of this chapter is submitted for publication in MNRAS.

Chapter 5: This chapter probes for the resemblance of BAL quasars with flat/inverted spectra and high radio polarisation with the blazar population of AGNs based on the rigorous photometric monitoring. It aims to enquire if the blazar subset exists even among BAL quasars. If yes, then what impact do these strong outflows have onto the strong continuum variabilities predominantly visible in the blazars is discussed here and also presented in [Mishra et al. \(2019\)](#).

Chapter 6: In this last chapter, we compile the outcomes of the problems addressed in the thesis along with elaborated discussions and conclusions. We also describe a comprehensive future aspects which can be pursued as an extension of this research contribution.

Chapter 2

Data acquisition and reduction

The main aim of this thesis is to study the environment of various subclasses of AGNs through their feedback effects onto its surroundings. Absorption line studies via spectroscopic monitoring of desired sources are among the best tools to probe the impact of associated jets or strong radiative winds around its nearby environment. On the other hand, photometric studies of the continuum variations arising from the central region of AGNs on diverse time scales would provide a clue about the physical mechanism responsible for these variations. Therefore, we have employed the spectroscopic as well as photometric techniques to constrain the properties of circumgalactic domains and continuum variation of AGNs respectively. For optical spectroscopic studies, observations have been performed with 2-6 m class national and international telescopes. In addition, we have extensively utilized optical spectroscopic archival data accessible from various databases. The optical photometric monitorings presented here were carried out using 1-2 m class national telescopes. In this chapter, detailed illustrations of data sourcing and telescope properties are given for both spectroscopic and photometric observations. It also provides a comprehensive description of various backend instruments such as detectors and spectrographs mounted on respective telescopes during our monitoring sessions. Furthermore, basic pre-processing steps and calibrating tasks involved in data preparations are explained in detail.

2.1 Spectroscopy

Spectroscopy is a tool to study the interaction between electromagnetic radiation and matter (e.g., atoms and molecules) in a graphical representation of the intensity of radiation against the frequency

or wavelength known as a spectrum. In observational astronomy, these spectra are generated through an instrumental setup commonly known as a spectrograph.

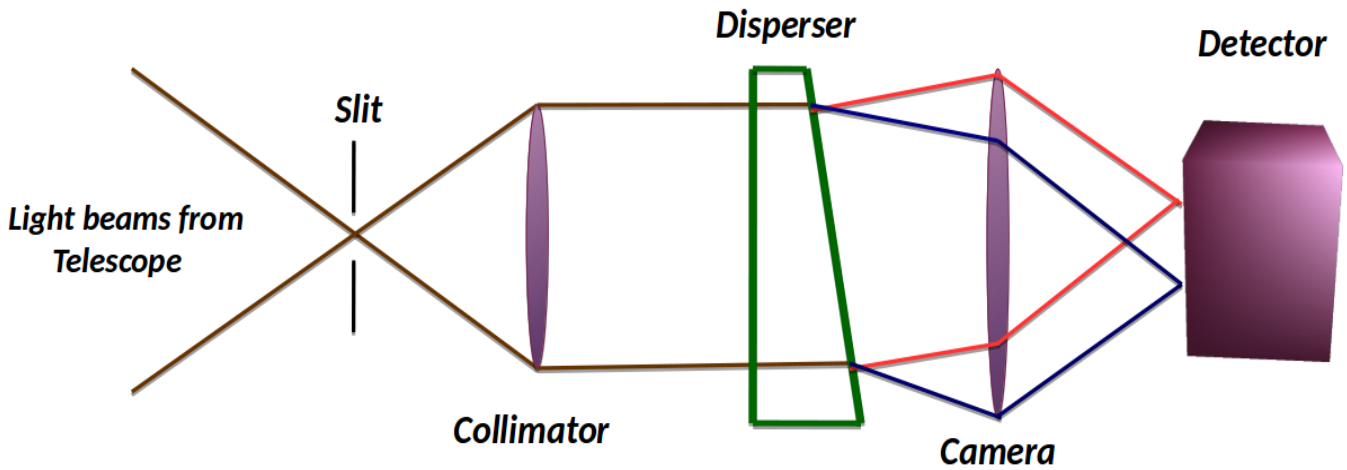


Figure 2.1: Basic spectrograph layout.

The primary layout of the spectrograph is presented in Fig. 2.1. The instrumental setup of the spectrograph consists of an opening known as slit which allows the diverging light beams from an object to pass through the subsequent elements of the setup. Besides, it blocks the unwanted light from the background enhancing the spectral resolution ($R = \lambda/\Delta\lambda$, where λ is the operating wavelength, $\Delta\lambda$ is the tiniest separable wavelength interval). The diverging beams are then allowed to pass through a collimator making the beams to fall parallelly on to the dispersive elements such as prisms, gratings or the combination of both (grisms). The collimator is also used as a focal reducer in some setups to enlarge the field of view of the detectors. Thereafter, the disperser placed between the collimator and the camera disperses the parallel beams into its multiple wavelength components. These spectrally-dispersed wavelength components are further allowed to pass through the camera which converges the beams onto the detector imaging the characteristic spectrum of the object.

The detector utilized in the present study is a Charge Coupled Device (CCD). A CCD is mainly an array of a huge number of coupled metal oxide semiconductors such as Silicon. The principle of the CCD is based on the photoelectric effect where electron-hole pairs are generated when photons of the adequate energies strike on the aforementioned arrays. The electrical setup of the CCD contains two or more electrodes (i.e., gates) per isolated picture elements (i.e., pixels).

The electrons get confined between these electrodes, however the holes are forced to diffuse away to avoid the recombination. The photo-electrons stored in the 2-D array modes are emptied and readout pixel by pixel and converted to the digital units (also known as Analog-to-Digital-Unit, ADU) through an on-chip Analog-to-digital converter. The large peak quantum efficiency ($> 70\%$), high dynamical range (i.e., $> 10^4$), nearly linear response to the incident photons and operational band-pass of $3000\text{--}10,000 \text{ \AA}$ of the CCDs make them an ideal detector for the imaging, especially in the optical regime.

Based on the spectral resolution provided by the dispersive elements, the spectrographs are predominantly divided into three categories (i) low-resolution spectrographs ($R = \sim 1000\text{--}3000$), (ii) moderate-resolution spectrographs ($R = \sim 5000\text{--}18000$), and (iii) high-resolution spectrographs ($R > \sim 40,000$). The present study utilizes spectral data from low-resolution to high-resolution spectrographs as can be elucidated from the resolution values of various spectrographs listed in Table 2.1.

2.1.1 Data sourcing

The spectroscopic data used in the present study are assembled both (i) from the new observations of the sources with various national and international facilities and (ii) extensively from the archival databases devoted to the optical studies as available in either processed or unprocessed forms. Table 2.1 lists the detailed parameters of the telescopes and instruments utilized in the acquisition of the spectral data along with the softwares employed in their pre-processing.

The optical spectra of the northern sky sources used in the present study are mainly gathered from the SDSS archive¹. The SDSS employs the low-resolution spectrographs i.e., SDSS and BOSS to obtain the spectral data. However, the spectra of southern sky sources are predominantly retrieved from the archive of the European Southern Observatory². The ESO observatory incorporates several spectrographs from low-resolution to high-resolution for the spectroscopic monitoring which are used in the present work. For two sources, we have utilized their optical spectra from the archive of KECK³ Observatory. The archival KECK spectra used here were observed with LRIS which is a low-resolution spectrograph. In addition, newly observed spectra obtained from the SCORPIO and HFOSC spectrographs are also introduced in the present study (see Table 2.1

¹<https://dr14.sdss.org/optical/spectrum/search>

²http://archive.eso.org/eso/eso_archive_main.html

³<https://koa.ipac.caltech.edu/cgi-bin/KOA/nph-KOAllogin>

Table 2.1: *Properties of telescopes, detectors, spectrographs utilized in spectral data sourcing.*

Telescope	Special Astronomical Observatory (SAO)	Himalayan Chandra Telescope (HCT)	Sloan Digital Sky Survey (SDSS)		W. M. Keck Observatory (KECK)	Very Large Telescope (VLT)		
Spectrograph	SCORPIO ^a	HFOSC ^b	SDSS ^c	BOSS ^d	LRIS ^e	FORS ^f -1/2	UVES ^g	X-SHOOTER
Data Type	New	New	Archival	Archival	Archival	Archival	Archival	Archival
Place	Russian Academy of Science, Russia	IAO, Hanle, India	Apache Point Observatory New Mexico, United States		Mauna Kea, Hawaii	European Southern Observatory (ESO) Cerro Paranal, Chile		
Longitude	41° 26' 30" E	78° 57' 51" E	105° 49' 13" W		155° 28' 24" W	70° 24' 18" W (UT1)		70° 24' 17" W (UT2)
Latitude	43° 39' 12" N	32° 46' 46" N	32° 46' 49" N		19° 49' 36" N	24° 37' 39" S (UT1)		24° 37' 37" S (UT2)
System	Ritchey-Chrétien	Ritchey-Chrétien	Ritchey-Chrétien		Ritchey-Chrétien	Ritchey-Chrétien		
Diameter	6 meters	2 meters	2.5 meters		10 meters	8 meters		
Focal ratio	f/2.6 with SCORPIO	f/9	f/5		f/15 on KECK I	f/3.13, UT1		f/15
Chip dimension	2048×2048	2048×4096	2048×2048	4096×4096	2048×4096	2048×4096	2048×4096	4k×2k, 2k×1k
Pixel Scale (''/pixel)	0.18	0.29	-	-	0.14	0.25	0.215 B, 0.155 R	0.176
Field of View (arcmin ²)	6.1×6.1	10×10	16.5×16.5	-	6×8	6.8×6.8	-	1.5×1.5
Pixel size (μm)	13.5	15	24	15	15 B	15	15	15,15,18
Gain (e ⁻ /ADU)	0.46	1.22	-	-	1.6	2.24	1.84B, 1.5R	~1.23,1.14,2.29
Readout (e ⁻)	4	4.8	-	-	4	5	4.1B, 4.2R	~3.5,5
Grism	VPHG1200 B,G	Gr7	-	-	300 B, 150 R	GRIS_1200B,V,R	Blue, Red	-
Resolution	818, 970	1330	~1850-2200	1560-2270 B 1850-2650 R	5678 B, 9800 R	1420, 2100, 2140	58000, 62,000	5400 UVB, 8900 VIS 5600 NIR
Spectral-Coverage	3600–5400 Å, 3800–6840 Å	4000–5700 Å	3800–9200 Å	3600–10400 Å	3000–10000 Å	3660–5110 Å, 4560–5860 Å 5750–7310 Å	3000–5000 Å B 4200–1100 Å R	3000–25000 Å UVB, VIS, NIR
Pre-processing software	IRAF	IRAF	Processed Data		LPipe	Esorex- Gargano FORS pipeline version 5.1.4	Processed Data	
Number of sources used	3	>20	> 50,000	> 70,000	2	90	>10	17

^a SCORPIO: Spectral Camera with Optical Reducer for Photometrical and Interferometrical Observations; ^b HFOSC: Himalaya Faint Object Spectrograph and Camera

^c SDSS: Sloan Digital Sky Survey; ^d BOSS: Baryon Oscillation Spectroscopic Survey; ^e LRIS: Low Resolution Imaging Spectrograph

^f FORS: FOcal Reducer/low dispersion Spectrograph; ^g UVES: UV-Visual Echelle Spectrograph

for details).

2.1.2 Data Reduction

Retrieval of a standard intensity versus the wavelength plot (i.e., a spectrum) requires a precise background subtraction on science frames, master flat-fielding, rejection of cosmic-ray impacts, employing an optimal extraction technique and then application of calibration tasks for wavelength and flux standardization. Data reduction for the FORS spectra was performed using the ESO-FORS pipeline (version 5.1.4), by executing it using the ESOREX ⁴ algorithm. The pipeline performs all the aforementioned tasks involved in the spectrum extraction. The Keck/LRIS data

⁴<http://www.eso.org/sci/software/cpl/esorex.html>

were reduced using a publicly available Lris automated reduction Pipeline⁵ (lpipe) written in IDL. However, the spectral data obtained with SCORPIO and HFOSC spectrographs were reduced manually using the standard IRAF⁶ software tasks.

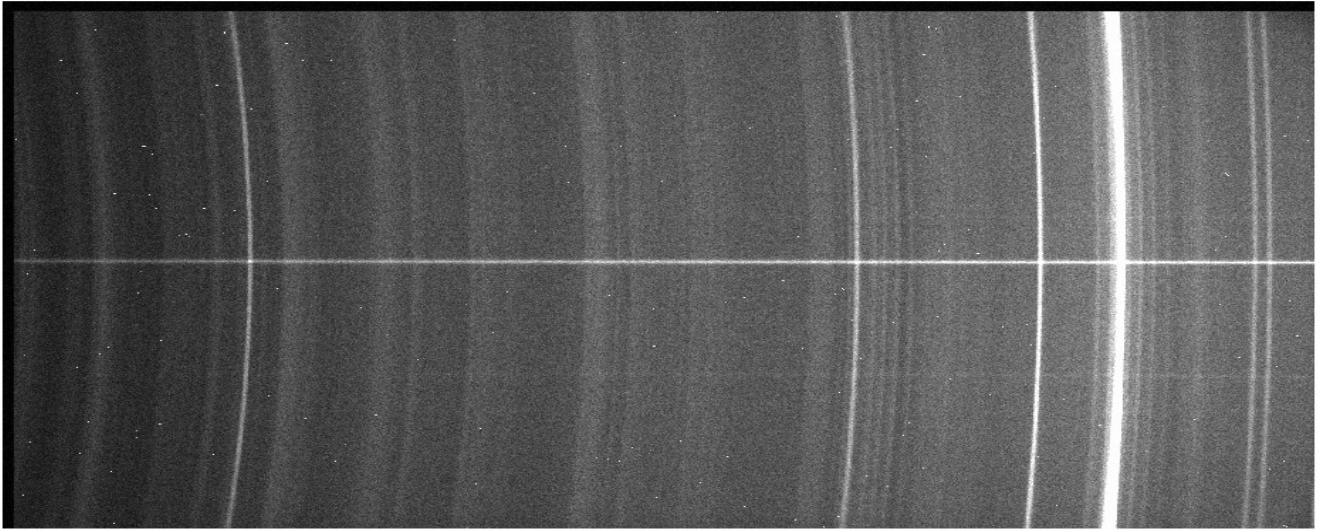


Figure 2.2: Raw CCD image of the spectrum of J145127+635426 recorded on the CCD in a rectangular window of 2068×1046 pixels. The image is taken with SCORPIO spectrograph mounted on SAO 6-m telescope with an integration time of 1200 seconds. A bright narrow horizontal strip is obtained when a light beam passing through the source at the center of the slit (with a width of 1.2'') gets dispersed via GRISM-VPHG1200G. This horizontal strip is called the dispersion axis covering a wavelength range of 3900-5700 Å. The width of dispersion axis is limited by the atmospheric seeing conditions. The vertical lines in the image are the night sky emission lines prevailing in the entire region of the slit opening. The uneven background illumination pattern across the image are produced by (i) the varying QE of CCD pixels, and (ii) nonuniformity of illuminated sky from the slit. The random circular patches are caused by the high energetic cosmic-ray hits.

A typical spectral image as returned by any detector after the observation is presented in Fig. 2.2. In the slit spectroscopy, the target source is placed at the center of a thin opening called the slit and the light passing through the dispersive element (i.e., grating or grism) gets dispersed and recorded in a linear strip of pixels known as dispersion axis. In Fig. 2.2 it is evident that the dispersion axis is along the horizontal direction. An axis perpendicular to the dispersion axis is perceived as a spatial axis. The steps involved in the pre-processing and the calibration of the spectral data are comprehensively discussed in the subsequent sections.

⁵<http://www.astro.caltech.edu/~dperley/programs/lpipe.html>

⁶Image Reduction and Analysis Facility, distributed by NOAO, operated by AURA, Inc. under agreement with the US NSF.

2.1.2.1 Pre-processing

The astronomical signals gathered from the CCD are the amalgamation of the signals arriving directly from the astronomical objects and the signals arising due to the imperfection of the electronics (such as in telescopes, detectors, and spectrographs). The process of elimination of these imperfections from the astronomical signals is called the pre-processing. The steps for the pre-processing of the CCD data involve the bias subtraction, flat fielding, and cosmic ray removal and are outlined below in detail.

1. **Bias Subtraction:** Due to the limitation of the CCD electronics (including A/D converter and amplifier), unrepeatable analog to digital numbers are generated during the readout of a pixel even if hypothetically the same pixel gets readout again. A/D converter produces a rather statistical distribution of possible results with center at mean value. Therefore, in the case of readout of a pixel with nearly zero photoelectrons, the A/D converter may give rise to negative counts. To avoid the negative result from the A/D converter, an offset voltage is applied to all the CCD pixels to set the electron level of each pixel more than a certain value. This voltage is independent of the integrated exposure time of the CCD. Hence even if the CCD is not exposed to the sky, certain positive counts which are additive in nature always remain in the CCD frame. Such CCD frames with zero time exposure with camera shutter closed are called the bias frames. Ideally an equal number of counts are generated in each pixel from the offset voltage, however, some pixel to pixel variations in the number of the bias counts persist due to the introduction of random thermal noises arising from the long-time exposure of the CCD camera. To avoid such variations from the bias frames, generally, at least three bias frames are observed. A task named "zerocombine" under IRAF package median combines the multiple bias frames and gives the master bias frame. Further, this master bias frame is subtracted from all the remaining CCD image frames using "ccdproc" task in IRAF.
2. **Flat Fielding:** The term flat-fielding refers to the smoothening of the CCD pixel-to-pixel sensitivity variation. The non-uniformity in the CCD pixels stems from (i) the optical vignetting of the telescope, (ii) varying quantum efficiency (QE) or gain of the CCD pixels either due to the uneven coating and/or presence of dust on the CCD. As a result, the response of

the pixels may differ. Hence even if the CCD is exposed to the perfectly uniform sky with an equal number of photons striking on each CCD pixel, the pixel-to-pixel generation of photo-electrons would be intermittent. A twilight sky is commonly used as the uniformly illuminated light source to flatten out the CCD pixel response. However, in spectroscopy, the spatial sensitivity variation of the CCD pixels gets translated into the spectral variation of the sensitivity of CCD pixels. Therefore inbuilt halogen lamps inside the spectrographs are used as a flat-field calibrator as they have an intrinsic featureless continuum spectrum. The "flatcombine" task is used to median combine the multiple bias subtracted flat frames of the flat-field calibrators to generate a master flat frame. A task named "response" evaluates the response of each horizontal layer of the master flat frame. Besides, it generates a polynomial fit over the median response of the master flat frame along the dispersion axis and returns the departure from the fit. It further produces a normalized flat frame which is defined as the ratio of master flat frame to the aforementioned polynomial fit. Again using the "ccdproc" task, the remaining frames (such as source, arc lamp calibrator, flux calibrator) involved in the observation are divided by the normalized flat frame.

3. **Cosmic ray removal:** Apart from the defects originating from the internal instrumental and electrical imperfections, there exists an additional source of unwanted counts stemming from the extraterrestrial cosmic ray hits (see Fig. 2.2). The cosmic rays are comprised of very high energy particles therefore, their arrival on the CCD pixels, results in the sudden rise of single-pixel counts. The point spread function (PSF) of these hits are of the form of Dirac delta function which is entirely different from the typical stellar PSF (having Gaussian form). A task named "lacos" developed by [van Dokkum \(2001\)](#) under "stsdas" package is incorporated in the present work to clean the bias subtracted and flat corrected frames from the cosmic rays. The task robustly separates the point sources and the cosmic rays on the basis of the sharpness of the edges irrespective of the shape and size of the cosmic rays. The sharpness of the edges is computed based on the Laplacian Edge detection method.

2.1.2.2 Spectrum extraction

Successful execution of the preprocessing steps produces clean 2-D images of the spectral data. The process of getting a 1-D spectrum from the 2-D image can be sub-divided into the steps described below:

- 1). Identifying the spectrum: Identification of the spectrum involves manual intervention and

requires the pre-knowledge of the source location. Generally, in the narrow slit observation, the location of the object is at the center of the CCD window (see Fig. 2.2). The accurate pixel-wise location of the object, however, can be obtained by placing a cut along the spatial axis and noting the peak position of the Gaussian profile whose full width at half maximum (FWHM) is limited by the atmospheric seeing.

2). Defining the extraction and background window: Once the location of the source is identified, an extraction window along the spatial axis is defined around base to base Gaussian profile of the source. Similarly, small background region is also selected on either side of the central Gaussian profile along the spatial direction to ensure the proper sky background subtraction.

3). Tracing the peak of spatial profiles: Practically the spectrum of the object is not exactly perpendicular to the spatial axis due to (i) the distortion produced by the optics of the instruments involved and the grating alignment, (ii) the gradient of the atmospheric refraction with the wavelength. Therefore the spectrum along the dispersion axis is generated by tracing the peak of the spatial profiles. Further at each point along the dispersion axis, the counts within the extraction window across the identified trace at that point are summed up to fold the 2-D spectrum into the 1-D spectrum.

The "apall" task under IRAF performs all the aforementioned jobs involved in the spectrum extraction. The final 1-D spectrum has a form of pixels versus the count values. To convert pixels into the wavelengths, arc-lamps (such as Fe-Ar, Fe-Ne, and Neon) are observed. Likewise, to convert counts to standard flux unit, standard stars are observed on the same observing night. The spectrum of the standard star is produced in a similar way using "apall". However, the spectrum extraction of the arc lamps separately observed for both object and the standard star for wavelength calibration is done at the identical trace and centering location as of the object (or standard star).

2.1.2.3 Dispersion correction

As mentioned earlier, the spectrum obtained after "apall" task has a form of pixel versus the counts. Therefore to map the pixels to the wavelengths, the 1-D spectrum of arc lamps extracted using the same set-up as of the object are used. These arc lamps are known to possess the various characteristic emission lines in their spectrum. Using a task called "identify" in the IRAF, the emission lines of the arc-lamp spectrum are manually identified. Besides, the pixel-to-wavelength mapping of these emission lines is improved further based on their conventional values available in the Arc-atlas line list of that particular lamp. This yields two linear dispersion solutions between

the pixel and the wavelength values of the arc-lamp spectra observed independently at the setting of the object as well as the standard star. Further "hedit" and "dispcor" tasks are used to incorporate these linear solutions explicitly onto the extracted 1-D spectra of the object and the standard star. Besides to examine the accuracy of the pixel to wavelength conversion, standard atmospheric emission lines at 5577 Å, 6300 Å and 6364 Å are appropriated. Small deviations (if any) between the observed and actual values of these atmospheric wavelengths are refined by applying the required offsets in the wavelength axis using "specshift" task.

2.1.2.4 Flux calibration

The flux calibration task involves the transformation of the instrumental intensity values (in counts) into the absolute flux values (in $\text{erg s}^{-1} \text{cm}^{-2} \text{Å}^{-1}$) in the wavelength calibrated 1-D spectrum of the object. For this purpose, spectra of non-varying, bright spectrophotometric standard stars are acquired on the same observing night. The standard flux values of these flux calibrators are available in the IRAF library. The tasks called "standard" and "sensfunc" are employed to generate a sensitivity curve defined as the ratio of the standard flux to the observed flux (corrected for atmospheric extinction and time) of the flux calibrator. The "calibrate" task is used to apply this sensitivity curve over the wavelength corrected 1-D spectrum of the object. Hence the final 1-D spectrum obtained after the flux calibration represents the object spectrum in wavelength versus the flux.

2.2 Photometry

Astronomical photometry/imaging concerns with the measurement of the amount of electromagnetic radiation (i.e., brightness) received from the celestial objects. Photometry is a low-resolution spectroscopy where the flux measurement is performed over the broadbands of radiation. The instrumental setup for the imaging observation requires the placement of filters in front of the CCD camera. The filters have a particular response function, enabling the radiation from specific wavelength region (bandpass) to pass through while constraining the transmission of radiations of other wavelengths. In the present study, we have utilized sdss-r filter having bandpass window ($\Delta\lambda$) of 1388 Å with a maximum response at wavelength (λ_{peak}) of 6254 Å and Cousins-R filter with $\Delta\lambda = 1066 \text{ Å}$ and $\lambda_{peak} = 6888 \text{ Å}$. The purpose of performing the observations using the aforementioned filters is that the optical detectors (such as CCD) generally have peak QE nearly

at $\sim 6000 \text{ \AA}$.

The aim of acquiring the photometric observations in present work is to estimate the temporal fluctuation of the continuum emission originating from the blazar type BAL quasars in this study. The plots concerning the temporal variation of the fluxes are known as the light curves (LCs). Therefore, to derive the LCs of our target sources, continuous intra-night optical monitoring was performed for a minimum duration of 3 hours. Typically, the exposure time for each data sample was between 7–9 min. The FWHM of the seeing disk during our monitoring sessions was typically between 2–2.5 arcsec.

2.2.1 Data sourcing

In order to examine the continuum variation, the photometric data of our sources were collected using three national telescopes viz (i) Devasthal Fast Optical Telescope (DFOT), (ii) Sampurnanand Telescope (ST) both managed by Aryabhata Research Institute of observational sciencES (ARIES), Nainital, India, and (iii) Himalayan Chandra Telescope (HCT) functioned by the Indian Astronomical Observatory (IAO) at Hanle operated by Indian Institute of Astrophysics (IIA), Bangalore, India. The useful parameters of the telescopes, detectors and the filters employed in the photometric monitoring are tabulated in Table 2.2. The majority of the photometric data used in the thesis are collected from the DFOT, ARIES.

Table 2.2: *Parameters of telescopes, detectors and filters used in the photometric data sourcing.*

Telescope	Devasthal Fast Optical Telescope (DFOT)	Sampurnanand Telescope (ST)	Himalayan Chandra Telescope (HCT)
Location	ARIES, Nainital, India	ARIES, Nainital, India	IAO, Hanle, India, Operated by IIA
Latitude	29° 21' 40" N	29° 21' 42" N	32° 46' 46" N
Longitude	79° 41' 04" E	79° 27' 24" E	78° 57' 51" E
Configuration	Ritchey-Chrétien, Cassegrain	Ritchey-Chrétien, Cassegrain	Ritchey-Chrétien, Cassegrain
Mounting	Equatorial fork mount	Equatorial 2-pier mount	Alt-Azimuth mount
Diameter	1.30	1.04	2.01
Focal ratio	f/4	f/13	f/9
Plate Scale	40.05"/mm	15.5"/mm	11.5"/mm
Chip dimension (pixel ²)	2048×2048	2048×2048	2048×4096
Saturation Limit(counts)	~ 65000	32768	65536
Field of view (arcmin ²)	~18×18	~13×13	~10×10
Pixel size ("/pixel)	0.53	0.37	0.29
Gain (e ⁻ /ADU)	2	10	1.22
Readout noise (e ⁻)	7	5.3	4.8
Filters/ $\lambda(\mu\text{m})/\Delta(\mu\text{m})$	SDSS-r/0.63/0.18	R/0.70/0.22	R/0.64/0.16
Number of light curves	25	3	2

2.2.2 Data reduction

Akin to spectroscopy, here also counts from the celestial objects get recorded in the form of a 2-D array. However, to retrieve an amount of energy in terms of magnitudes entails detailed prescriptions. A raw image captured from the photometric observation is shown in Fig. 2.3. The light beams are not dispersed along any preferential direction as they are allowed to fall on the camera from all the directions, unlike spectroscopy, where narrow slits are used to constrain them. The steps involved in extracting the magnitude information from the objects existing in the raw CCD frame are described hereinafter.

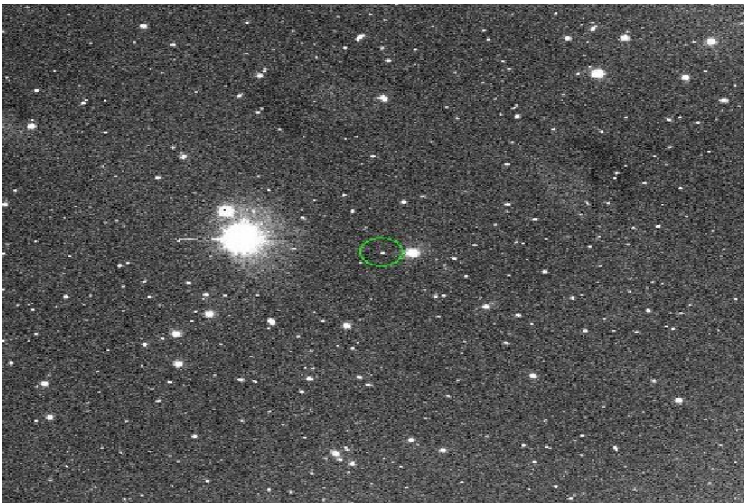


Figure 2.3: Raw CCD frame acquired for the INOV monitoring of $J115944.82+011206.9$ (encircled in green) with DFOT within a CCD window of 2048×2048 pixel in *sdss-r* filter over an exposure time of 420 seconds.

2.2.2.1 Pre-processing

Similar to spectroscopy, the raw images consist of unwanted counts arising from the instrumental as well as electrical defects such as an additional offset voltage counts or bias counts and extraterrestrial cosmic hit counts. Besides, here also uneven CCD pixel response may give rise to the nonuniform ejection of photoelectrons even in the case of uniform exposure of background photons. Therefore, here too we perform the bias subtraction, flat-field correction, and cosmic ray removal as a part of the pre-processing of photometric data before extracting the magnitude information. However, unlike spectroscopy, we do not use "response" task to remove the spectral variation of the response of CCD pixels. Rest all the steps involved in the pre-processing of raw imaging data are similar to the as of aforementioned spectroscopic data (see Section 2.1.2.1). The cleaned images thus obtained from the pre-processing are further used to extract the magnitude information of the various sources in the CCD frame and are outlined in the subsequent section.

2.2.2.2 Aperture Photometry

Aperture photometry is a simple tool which merely adds up the number of counts (and hence magnitude) observed within an aperture (e.g., circular, rectangular, etc.) with a source at the center, irrespective of any underlying assumption concerning the exact shape of the stellar profile (PSF) of that source. Generally, for the point source observations as in the present work, the apertures are assumed to be circular in nature. The optimal radius of the aperture employed in the magnitude measurements is compromised by a quantity known as signal-to-noise ratio (SNR) which typically provides the goodness of the astrophysical data, and is estimated as:

$$\frac{S}{N} = \frac{Nt}{\sqrt{Nt + n_{\text{pix}}(N_{\text{S}} + N_{\text{D}}t + N_{\text{R}}^2)}} \quad (2.1)$$

where N is the number of photons per second received from an object in n_{pix} number of pixels, t is the exposure time of the CCD camera, N_{S} is the number of background/sky photons per second per pixel, N_{D} is the number of thermally agitated dark current electrons per second per pixel, and N_{R} is the number of electrons per second per pixel coming from the readout noise of the CCD.

Thus aperture photometry predominately requires the application of two steps viz. (i) determination of centroid of the PSF, (ii) extraction of magnitude information within a circular region around the centroid of multiple objects present in the image. We have employed the general tasks under DAOPHOT⁷ II (Stetson 1987) to perform these two tasks and are described below:

1). To find the location of all the objects present in a CCD frame, a task named "find" under DAOPHOT II is used. This task automatically identifies the objects with counts more than the user-defined threshold value (generally 3 times the local background fluctuation) within a circular aperture. The optimal radius of the aperture is taken to be 2 times the average FWHM of the stellar profiles of 5 bright stars present in the frame. This aperture radius renders the maximum SNR from Eq. 2.1 by not including the unnecessary pixels of the background sky. The exact coordinates of the centroid of the PSF of these detected objects are obtained and listed in a file by fitting a Gaussian profile of similar FWHM around them.

2). The x and y coordinate as returned by the "find" task are used by the "phot" task of DAOPHOT II to locate the objects present in the single CCD frame. This task adds up the number of photons around each x and y coordinate in the aperture of radius defined above. Similarly, it estimates the number of photons in the local background (free from the stars) region and subtracts

⁷Dominion Astrophysical Observatory Photometry

it from the photons within the aperture. Further, the conversion of the number of background-subtracted photons inside the aperture into the instrumental magnitude is performed using the equation; $m_{inst} = -2.5\log(C)$; where m_{inst} is the instrumental magnitude and C is the sum of number of background-subtracted photons/counts within the aperture. Since in the present study, we have employed differential photometry to generate the LCs of our objects, we have omitted the flux calibration of the magnitudes as returned after the aperture photometry.

2.3 Catalogs

The present work is supplemented by the various catalogs. We have extensively used quasar catalogs derived for the quasars of SDSSDR-7 (Schneider et al. 2007), SDSSDR-10 (Shen et al. 2011), SDSSDR-12 (Pâris et al. 2017) and SDSSDR-14 (Pâris et al. 2018). The absorption line properties of large quasar sample employed in the present work are obtained from the Zhu & Ménard (2013), Raghunathan et al. (2016) and Gibson et al. (2009). However, the useful parameters of blazars are adopted from the blazar catalogs given by Massaro et al. (2009) and Véron-Cetty & Véron (2010). The radio properties of the sources used in the thesis are compiled from the Faint Images Radio Sky at Twenty centimeters (FIRST, Becker et al. 2000), NRAO VLA Sky Survey (NVSS, Condon et al. 1998) catalogs.

Chapter 3

Probing AGN environment using the kinetic-mode feedback

Powerful extragalactic relativistic jets can efficiently distribute or rearrange the matter and energy from small to \sim Mpc scales, and hence, can hugely affect the host galaxy environment as well as the intergalactic medium. A subclass of AGNs known as blazar, hosts such powerful jets within an opening angle of $< 10^\circ$ relative to our sightline (see Section 1.3.1). In this chapter, we have used high redshift blazars as background sources to examine the physical conditions of the gaseous medium around the galaxies as well as the relative role of relativistic jets onto the jet-accelerated associated and the intervening absorption systems. This chapter presents the analysis of the narrow absorption-line systems (in the spectra of blazars) lying at extremely large distances and hence are too faint for direct imaging/spectroscopy even with the largest telescopes (Bahcall & Salpeter 1966; Wolfe et al. 2005; Kulkarni et al. 2012). The work of this chapter is based on the paper published in MNRAS (Mishra et al. 2018).

3.1 On the incidence of Mg II absorbers along the blazar sight-lines

It is widely held that the cool gas clouds (e.g., Mg II absorption systems) with velocities offsets βc up to $\sim 5000 \text{ km s}^{-1}$ relative to the background quasar are gravitationally bound to the quasar itself (i.e., ‘associated systems’, see Anderson et al. 1987; Khare et al. 1989; Møller et al. 1994, and

references therein), whereas absorbers showing larger velocity offsets directed towards us are intervening systems probably associated with foreground galaxies and, consequently, their existence should be totally independent of the background quasar. A few recent studies, however, seem to question this canonical view, based on the differing estimates for the incidence rates of intervening systems (like Mg II absorption having $\beta c \geq 5000 \text{ km s}^{-1}$) detected towards different types of background sources, such as normal QSOs, gamma-ray bursters (GRBs) and blazars (Stocke & Rector 1997; Prochter et al. 2006; Sudilovsky et al. 2007; Vergani et al. 2009; Tejos et al. 2009; Bergeron et al. 2011, hereinafter BBM). It has been also claimed by BBM and Cucchiara et al. (2009) that associated systems having a significantly relativistic speed relative to the quasar may also be present (BBM), e.g., when the quasar is undergoing powerful jet activity and/or ejecting high speed accretion-disk outflows. A possible way to differentiate between these possibilities would be to check if the incidence rates, dN/dz , of intervening absorbers differ depending on whether the background sources are non-blazars, or blazars whose powerful relativistic jets are therefore expected to be pointed close to our direction and, consequently the jet-accelerated potential absorbers would lie along the LOS. Indeed, this expectation is echoed in the unexpected finding of BBM that the dN/dz of Mg II absorption systems (for strong absorbers having a rest-frame equivalent width $W_r \geq 1 \text{ \AA}$) towards blazars is ~ 2 times larger (at 3σ confidence) than the value established for the sightlines to normal quasars (QSOs). An even greater excess had earlier been reported by Stocke & Rector (1997), albeit using a much smaller sample of blazars. On the other hand, a recent analysis by Chand & Gopal-Krishna (2012) of the existing high-resolution spectra of a sample of about 115 flat-spectrum RL quasars (FSRQs, of non-blazar type) did not show any excess in the incidence of Mg II absorption systems, as compared to QSOs. They reconciled the two seemingly discrepant results by appealing to the jet orientation scenario which lies at the heart of the Unified Scheme for powerful extragalactic radio sources (e.g., see, Antonucci 1993). In their explanation, since the jets in FSRQs are thought to be less closely aligned to the LOS, any gas clouds accelerated outward by the powerful jets are unlikely to appear in the foreground of the quasar's nucleus and hence escape being detected in absorption against its bright optical emission. Later, Joshi et al. (2013) extended this probe by analyzing a large set of redshift-matched sightlines to 3975 radio core-dominated (CDQs, i.e., FSRQs) and 1583 radio lobe-dominated (LDQs) quasars. While, overall, only a marginal (9% at 1.5σ significance) excess of dN/dz was found towards the FSRQ sightlines, as compared to the sightlines to normal QSOs, they showed that the excess becomes quite significant (3.75σ) when the comparison is restricted to the absorbers having offset

speeds i.e., $\beta < 0.1c$ relative to the background quasar. Similarly, Tombesi et al. (2011) have used observations of Fe XXV/XXVI K-shell resonance lines in the X-ray band and found their outflow velocity distribution spans from $\sim 10,000 \text{ km s}^{-1}$ up to $\sim 100,000 \text{ km s}^{-1}$ ($\sim 0.3c$), with a peak and mean value of $\sim 42,000 \text{ km s}^{-1}$ ($\sim 0.14c$), for highly ionised gas clouds with column densities of $N_H \approx 10^{23} \text{ cm}^{-2}$ located within the central parsec of the AGN.

In this context, it is important to emphasize that even though BBM’s analysis has employed very high-sensitivity spectral data, their result rests on just 45 blazars, due to which small number statistics might be at work. It is worthwhile recalling that the 4-fold excess of dN/dz along the GRB sightlines, inferred by Prochter et al. (2006) using just 14 GRBs, has subsequently been pronounced as a possible statistical fluke, on the basis of a 3 times larger set of sightlines (Cucchiara et al. 2013). Given its potentially deep ramifications, it is therefore desirable to revisit the BBM claim of excess dN/dz towards blazars, by enlarging the blazar sample and carrying out an independent analysis. The present study is motivated by this objective.

3.1.1 The Sample

The blazar sample employed in our analysis is an amalgamation of 3 sets of blazars extracted from the catalogues published by Massaro et al. (2009, hereafter ROMA-BZCAT), Véron-Cetty & Véron (2010, hereafter VV), and Padovani & Giommi (1995, hereafter, Padovani-Catalogue). From the ROMA-BZCAT we selected sources classified as BZB (implying confirmed BL Lac), resulting in a set of 1059 blazars. From the VV catalogue we selected the sources classified either as ‘BL’ (i.e., confirmed BL Lac), or ‘HP’ (a confirmed highly polarized quasar). This res-

sulted in a set of 729 confirmed blazars from this catalogue. Accounting for the 480 sources that are common to these two sets, led to a list of 1308 confirmed blazars. The Padovani-catalogue also classifies BL Lacs objects using homogeneous criteria. It contains a total of 233 blazars, of which 189 were already in the above two sets (among them 169 blazars of the Padovani-catalogue

Table 3.1: *The spectral data sourcing for our enlarged sample of blazars.*

Archive	Instrument	Content	Resolution
ESO	FORS-1/2	48 blazars found (10 taken ¹)	900
ESO	X-SHOOTER	17 found(8 taken ²)	3600
ESO	UVES	1 found (taken)	40000
SAO	SCORPIO	3 new observations (3 taken)	818
KECK	LRIS	2 (both taken)	9800
SDSS	BOSS	622 found (196 taken ³)	2500
BBM	FORS-1	42 (all 42 taken)	900

¹Ten blazars do not have useful redshift path (i.e., not satisfying our selection criteria-ii), another 28 lack emission redshift ($48 - 10 - 28 = 10$).

²Two blazars do not have useful redshift path (i.e., not satisfying the selection criteria-ii), another 7 lack emission redshift ($17 - 2 - 7 = 8$).

³Excluded 69 sources with $\text{SNR} < 5$ (i.e., not satisfying the selection criteria-i, 207 lack emission redshift, and 138 sources were excluded for not meeting the selection criteria-ii), 12 sources were excluded since their spectra had been already taken from the other archives listed in this table ($622 - 69 - 207 - 138 - 12 = 196$).

are in BZ-ROMA, while 20 in the VV catalogue). Their exclusion left us with 44 blazars solely contributed by the Padovani-catalogue. Merging these 3 sets resulted in our final ‘parent sample’ of 1352 confirmed blazars.

We then performed an extensive search for optical spectra of our parent sample of blazars, in the archives of the SDSS⁴, the ESO and the KECK Observatory. We applied two main selection filters: (i) median SNR of the entire spectrum should be more than 5, so that false detections of Mg II line are minimized, and (ii) the blazar’s redshift should allow at least $10 \times (1 + z_{em}) \text{ \AA}$ wide coverage in the available spectrum, of the region between the Ly α and Mg II emission lines; this would ensure that the observed spectrum can be used to search for the Mg II doublet due to at least one absorber (given that the two components of the doublet Mg II λ 2796, 2803, are separated by 8 \AA in the rest frame).

In the ESO archive, after excluding the spectra of the 42 BBM blazars, which had been taken using the FOcal Reducer and the low-dispersion Spectrograph (FORS1) at the ESO observatory, we found that for 66 of our blazars (within 1 arcmin search radius) a spectrum with SNR > 5 was available either in the reduced form, from the ESO-advanced data product⁵ (17 observed using X-shooter spectrograph, 1 observed using the Ultraviolet and the Visual Echelle Spectrograph (UVES)), or we were at least able to extract the spectra based on their raw images using associated calibration files (48 observed using FORS-1,2). Among these 66 blazars, emission redshift was available for only 31, out of which just 16 were found useful for Mg II absorber search after applying our emission redshift constraint mentioned above. For the remaining 35 blazars with unknown emission redshifts we could establish a lower redshift limit for 4 blazars using the redshift of the observed most redshifted Mg II absorption doublet. One of these 4 had to be excluded as the Mg II derived redshift was not yielding adequate redshift path (i.e., not satisfying the selection criteria-ii). Here, it is also important to clarify that the spectral region containing this most redshifted absorption doublet was excluded for the purpose of computing dN/dz , in order to keep the estimate free of bias resulting from exclusion of those blazars with unknown redshift, for which even a lower limit to redshift could not be established (using the Mg II absorption doublet).

For another three blazars from our ‘parent-sample’, viz, J145127+635426, J165248+363212, J182406+565100, we have newly obtained spectra in VPHG1200 grism using the SCORPIO spectrograph mounted on the 6-m telescope at the SAO. Inclusion of another 2 blazars viz, J001937+202146, J043337+290555, became possible due to the availability of their spectra in the KECK archive,

⁴<https://dr12.sdss.org/bulkSpectra>

⁵http://archive.eso.org/wdb/wdb/adp/phase3_main/form

taken with the Low Resolution Imaging Spectrometer (LRIS).

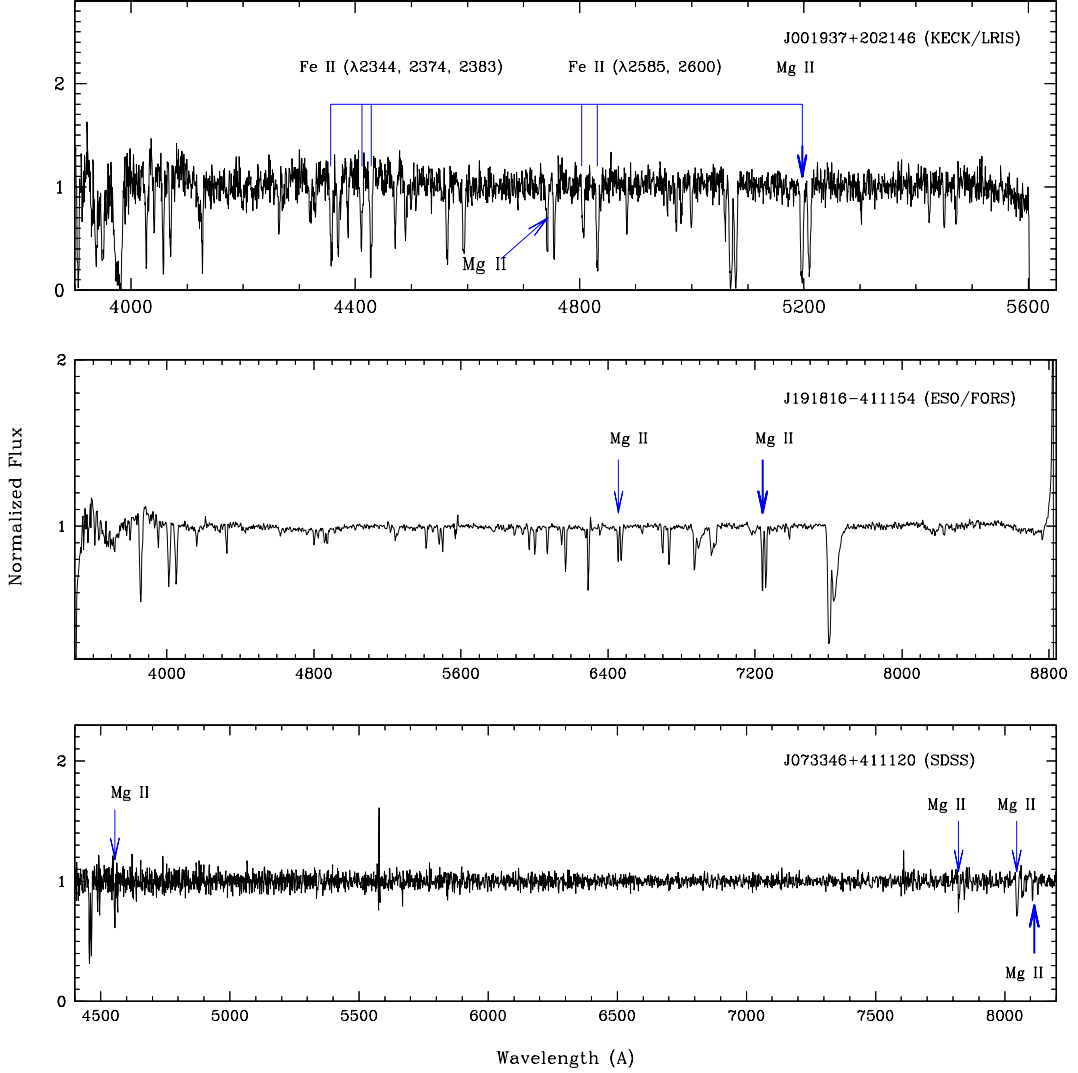


Figure 3.1: Representative normalized blazar spectra: J001937+202146 (top), J191816-411154 (middle), J073346+411120 (bottom). In each case, the most redshifted Mg II absorption system (thick blue arrow) detected was used as the lower limit to the blazar’s emission redshift. Thin blue lines in top panel mark the Fe II (λ 2344, 2374, 2383, 2585, 2600) lines associated with the Mg II absorption line system at $z_{\text{abs}} = 0.85840$.

For 622 blazars in our ‘parent sample’ we could find spectra in the SDSS archives (within a tolerance of 2 arcsec) in reduced form, covering a wavelength range 3800–10000 Å. Excluding the 69 spectra with $\text{SNR} < 5$, left us with good quality spectra for 553 blazars. Among these, emission redshifts were available for 277 blazars, out of which 150 sources were found useful for Mg II absorber search, after meeting our aforementioned emission redshift criterion (selection

criterion-ii). In addition, from among the 276 blazars with unknown emission redshift, a lower redshift limit could be set for 59 sources, using the detected Mg II absorption feature. However, one of these 59 sources (viz, J130008.5+175538) had to be excluded as it did not meet our criterion of useful minimum redshift path (i.e., the selection criterion-ii). In addition, after excluding another 12 blazars as they are already included in our above sample from other resources (ESO archive and SAO observations) we are left with 196 blazars solely contributed by the SDSS, which are found satisfactory for the purpose of our Mg II absorption-line search.

To recapitulate, we have assembled a sample of 220 blazars (SDSS: 196, ESO: 19, SAO: 3, KECK: 2) as summarized in Table 3.1, to make a search for intervening Mg II absorbers. Out of these, only a lower limit to z_{em} is available for 58 blazars (i.e., 54 SDSS, 3 ESO and 1 KECK). We have discussed three out of them in Fig. 3.1 where we have also shown their representative spectra as well.

Further, as mentioned above, we have also made use of the BBM blazar sample to revisit their conclusion (Section 3.1), by subjecting it to an independent data reduction and analysis procedure, as followed in the present work. The sample employed in their analysis consists of 45 blazars. For 42 of them, we could obtain the raw spectral data from the ESO archive based on their program ID 080:A-0276, 081:A-0193. The raw data used in the BBM analysis for the remaining 3 (northern sky) blazars were not accessible and hence they could not be included in our analysis.

The z_{em} and SNR distributions for our sample of 262 blazars (including 42 from the BBM sample) are shown in Fig. 3.2. However, as described in Section 3.1.2.2, among the 220 non-BBM blazars only 149 blazars were found to contribute to robust redshift path for the case of strong absorbers and only 58 of them have contributed to the robust redshift path for weak absorbers, as well. Thus, for the purpose of the present dN/dz analysis, we are led to a final sample of 191 blazars (149 ours plus 42 BBM blazars) for the strong absorber case. Only 100 out of them also contribute to the dN/dz analysis for weak absorbers. The sample of 191 blazars is listed in Table 3.2.

Table 3.2: Basic properties of our sample of 191 blazars.

Target	z_{em}	Data archive	Δz_{strong}^a	SNR
J001937+202146	0.858	KECK	0.417	6.4
J003514+151504	0.443	SDSS	0.123	55.0
J003808+001336	0.740	FORS/ESO	0.439	91.8
J004054-091525	5.030	FORS/ESO	0.891	66.2

Note. See Table A.1 for the full version.

^aThe redshift path contribution to the strong Mg II system ($W_r(2796) \geq 1.0 \text{ \AA}$) analysis.

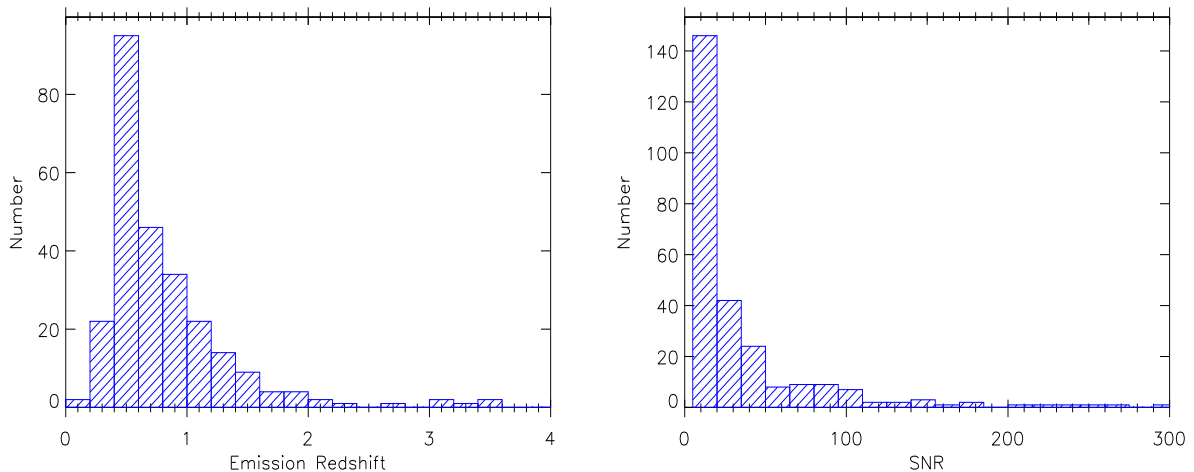


Figure 3.2: Distributions of emission redshift (left) and SNR (right) for our full sample of 262 blazars (including the 71 blazars which are subsequently excluded from the Mg II strong systems analysis; see Section 3.1.2.2. For 58 blazars without exact z_{em} , we have used their lower limit on z_{em} , derived based on the most redshifted absorption system seen in their spectra).

3.1.2 Analysis

3.1.2.1 Data Reduction

Data reduction for the FORS spectra available for our 53 blazars, including the 42 blazars from BBM, was performed using the ESO-FORS pipeline (version 5.1.4), by executing it using the ES-OREX algorithm. The pipeline performs a precise background subtraction on science frames, does master flat-fielding, rejects cosmic-ray impacts by employing an optimal extraction technique and then applies calibrations for wavelength and flux. The Keck/LRIS data were reduced using the lpipe routine (Section 2.1.2). The UVES and SDSS spectra (total 197 blazars) were already available in the reduced form. Finally, the spectra taken with the SAO 6-m telescope for 3 of our blazars (viz, J145127+635426, J165248+363212 and J182406+565100) were reduced using the standard IRAF tasks (see Section 2.1.2). For post-processing of each one-dimensional spectrum, which involves steps such as air-to-vacuum wavelength conversion, heliocentric correction, combining individual exposures for SNR enhancement and continuum fitting to determine the normalized spectrum, we have followed the procedure described in Chand et al. (2004).

3.1.2.2 Computation of the EW detection limit and the corresponding useful redshift path

For identifying absorption features in a given spectrum, proper evaluation of noise plays a crucial role as it defines the detection limit for the features. Therefore, to generate the distribution of rms noise along the spectrum we used the matched-filtering technique employed by [Zhu & Ménard \(2013\)](#), which involves the following main steps:

- (i) Subtracting unity from each point/pixel of the normalized spectrum (thus, the mean level of the spectrum becomes zero).
- (ii) Using this residual spectrum, generate its amplitude version, by plotting only the magnitude of the signal at each spectral pixel (i.e., setting the negative sign to positive).
- (iii) This ‘noise amplitude spectrum’ is then subjected to a top-hat smoothing over the ‘effective spectral resolution’, which is taken to be the quadratic sum of the instrumental resolution and the typical Mg II absorption line width. For instance, the typical FWHM of the QSOs absorption line convolved with the SDSS instrumental resolution lies in the range $\sim 100\text{--}400 \text{ km s}^{-1}$ ($\sim 2\text{--}6$ pixels). Thus, for the SDSS instrumental resolution of 120 km s^{-1} , we have taken an ‘effective spectral resolution’ of about 4 pixels (i.e., $\sim 276 \text{ km s}^{-1}$, e.g., see [Zhu & Ménard 2013](#)).
- (iv) This ‘smoothed noise amplitude spectrum’ was then sub-divided into a sequence of 100 \AA wide segments. Within each segment all points deviating by more than one σ were clipped (including any spectral lines) and substituted with interpolated values. In this smoothed noise amplitude spectrum the amplitude at a given spectral (i.e., wavelength) pixel ‘ i ’ is the representative noise, n_i , for that pixel.
- (v) For each spectral pixel, we then set the 3σ detection threshold of a spectral feature. To do this, we model the feature as a Gaussian having a FWHM equal to the afore-mentioned ‘effective spectral resolution’ and then subject it to the same ‘top-hat’ smoothing as mentioned in (iii) above, and finally, we optimize its amplitude to equal $3n_i$. Equivalent width of the Gaussian satisfying this criterion thus becomes the limiting equivalent width ($W_{i,det}$) of the Mg II absorption line that would be accepted as a significant (3σ) detection at that particular pixel in the spectrum. Only provided the pre-set restframe threshold value (W_{th}), which is 0.3 \AA for weak and 1.0 \AA for strong absorption systems, respectively, exceeds the computed $W_{i,det}$ for that pixel, would that spectral pixel be accepted as contributing to ‘useful’ redshift path, not otherwise. Note that this procedure is very similar to that adopted in [Mathes et al. \(2017\)](#).

As a result, for our blazar sample, the net useful redshift path at a given redshift z_i (so that the Mg II absorption line falls in the i^{th} spectral pixel) for detection of the Mg II doublet above a

designated rest-frame equivalent width threshold, W_{th} would be:

$$g(W_{th}, z_i) = \sum_{j=1}^{N_{blazar}} H(z_i - z_{j,min}) \times H(z_{j,max} - z_i) \times H(W_{th} - W_{j,det}(z_i)) \quad (3.1)$$

where H is the Heaviside step function, and the summation is taken over all the blazar spectra in our sample, $z_{j,min}$ and $z_{j,max}$ are, respectively, the minimum and maximum expected absorption redshift limits which were used in the search for the Mg II doublet for j^{th} quasar (see Section 3.1.2.3). W_{th} is the threshold rest-frame EW of the Mg II absorption line which we have set at 1 Å and 0.3 Å, for strong and weak absorption systems, respectively. $W_{j,det}(z_i)$ is the computed rest-frame EW detection limit at the i^{th} pixel in the spectrum of the j^{th} quasar, as discussed above. In the parent sample of 262 blazar, a non-zero $g(W_{th}, z_i)$ was found for only 191 blazars for the strong absorber case, and 100 out of them also contributed a non-zero $g(W_{th}, z_i)$ for the case of weak absorption system, as well. Hence only these two subsets have been used in the present dN/dz analysis.

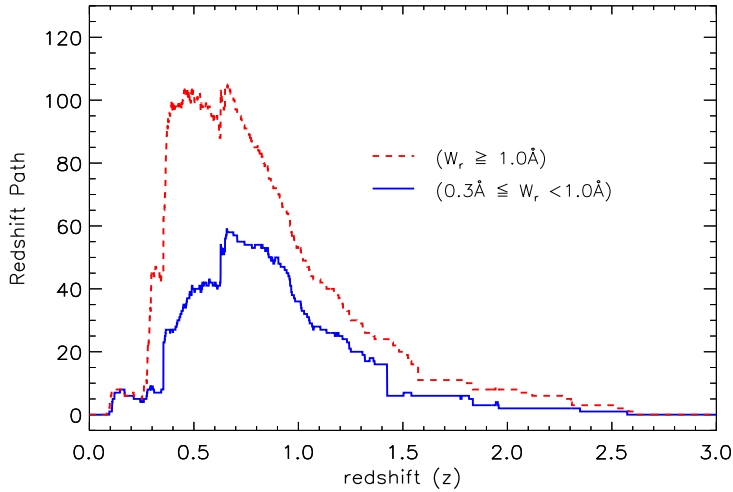


Figure 3.3: The distributions of redshift path density ($g(z)$) for the intervening Mg II systems towards blazars, for the strong ($W_r(2796) \geq 1.0 \text{ \AA}$: red dashed curve) and the weak absorption systems ($0.3 \leq W_r(2796) < 1.0 \text{ \AA}$: blue solid curve).

3.1.2.3 Mg II absorption-line identification

Normally, the wavelength coverage may differ from spectrum to spectrum, as it depends on the spectrograph's specifications and the instrumental settings used for the observations. Additionally, we place two constraints on the redshift path over which the search for the Mg II doublet was made. Firstly, the search was restricted to within the range $(1 + z_{em}) \times 1216 \text{ \AA} < \lambda < (1 + z_{em}) \times 2803$

Å. The lower limit is meant to avoid the Ly α forest, while the upper limit is dictated by the fact that any Mg II absorber with $\lambda \geq (1 + z_{em}) \times 2803$ Å has a strong likelihood of being an associated system falling into the background AGN. We performed the search for the Mg II doublet at z_{em} following the steps enumerated in section 3 of Chand & Gopal-Krishna (2012). Accordingly, a line profile matching technique was used, such that we first plotted the normalized spectrum of a given blazar and then overplotted the same spectrum by shifting the wavelength axis by a factor of $\lambda_{Mg II} 2796.3543 / \lambda_{Mg II} 2803.5315$ (i.e., 0.997). Then, about 50 Å wide spectral segments were manually examined. The location of perfect overlap between the absorption lines in the shifted and the original (unshifted) spectra were marked as a detected Mg II absorption system. As a further corroboration, we looked for the corresponding metal lines (e.g., Fe II, C IV, Si IV, etc.) in the spectrum. If the redshift/velocity of a Mg II absorption doublet was found to be consistent with that of the peak estimated for the metal line(s), this was taken as a further confirmation of the previously identified Mg II absorber. Note that the systems having a velocity offset within 5000 km s⁻¹ of z_{em} of the blazar were classified as associated systems, following the standard practice. For each detected Mg II absorption system, we also performed visually a quality check on the fit to the underlying continuum. If deemed desirable we carried out a local continuum fitting and this improved fit was then used to obtain a better estimate of $W_r(\text{Mg II})$. Detailed information on the 43 Mg II absorption systems thus identified in the spectra of 34 blazars, out of the total present sample of 191 blazars, is provided in Table 3.3.

3.1.2.4 Computation of dN/dz

The incidence rate of Mg II absorbers is defined as $\frac{dN}{dz} = N_{obs}/\Delta z$; where N_{obs} is the total number of the Mg II absorbers detected within the entire *useful* redshift path (Δz), defined as:

$$\Delta z = \int_0^\infty \sum_{j=1} g_j(W_{min}, z_i) dz_i \quad (3.2)$$

where $g_j(W_{min}, z_i) = 1$ if W_{th} (0.3 Å for weak systems and 1 Å for strong systems) is more than the (3σ) detection threshold $W_{j,det}(z_j)$ estimated for the i^{th} spectral pixel (see Eq. 3.1),

Table 3.3: *The detected 43 Mg II absorption systems and their rest-frame equivalent widths, $W_r(\text{Mg II } \lambda 2796 \text{ Å})$, as identified in 34 blazars belonging to our sample of 191 blazars.*

Blazar	z_{em}	z_{abs}	W_r	Associated absorptions
J001937+202146	0.858	0.69616	1.0969	Fe II
J010009-333730	0.875	0.67996	0.5110	Fe II
J014125-092843	0.730	0.50042	0.3641	Fe II
J021748+014449	1.715	1.34428	2.0130	Mg I, Fe II, Zn II, Mn II
J023838+163659	0.940	0.52379	2.3725	Mg I, Fe II, Mn II

Note. See Table A.2 for the full version.

otherwise $g(W_{min}, z_i) = 0$. The values of redshift path density for i^{th} redshift pixel, i.e., $g(W_{min}, z_i)$, were thus computed using the total 191 blazar sightlines for strong absorption systems and the 100 blazar sightlines for weak absorption systems (Fig. 3.3).

Table 3.2 lists the values of Δz calculated for the individual sightline in our entire blazar sample and in its various sub-sets. The errors in the computed dN/dz values were estimated assuming the Poisson small number statistics for $N_{obs} < 50$, within a limit of 1σ confidence level of a Gaussian distribution, using the tabulation given by Gehrels (1986).

3.1.3 Results

3.1.3.1 Incidence of Mg II absorbers in the present enlarged sample

As noted in Section 3.1, the BBM result is based on a sample of just 45 blazars and this has motivated us to build an enlarged sample. Our sample of 191 blazars provides nearly a factor of 3 increase in the redshift path (Table 3.2). Table 3.4 summarizes the results for this enlarged sample and its various subsets. Note that, as in BBM, the values of dN/dz for normal QSOs are calculated at the mean value of the redshift path for the corresponding blazar subset (column 1 of Table 3.4). This was done using equation 2 of BBM for the case of weak absorption systems, and equation 6 of BBM, for the case of strong absorption systems. From Table 3.4, no significant excess is evident in the dN/dz for the blazar sightlines, vis a vis normal QSOs, both for weak (column 5) and strong (column 9) Mg II absorbers. The same is apparent from Fig. 3.4, which displays the cumulative numbers of Mg II absorbers up to different values of absorption redshift. Although, when only the absorption systems having $\Delta v < 5000 \text{ km s}^{-1}$ are deemed as associated systems and therefore excluded, a mild excess may be present for blazar sightlines (Fig. 3.4 top panel). However, it vanishes for the strong systems if one excludes all absorbers having offset velocities up to $\Delta v < 30000 \text{ km s}^{-1}$ (Fig. 3.4 middle panel). The mild excess vanishes even for weak systems if the absorbers with offset velocities up to $\Delta v < 60000 \text{ km s}^{-1}$ are excluded (Fig. 3.4 bottom panel), suggesting the possibility of extension of Mg II intrinsic absorbers up to $\Delta v = 0.2c$ for blazars. In any case, our focus here is on the results for strong absorption systems, which are statistically more robust since the majority of our spectra (which have relatively low SNR) have contributed to the useful redshift path only for strong systems and not for weak systems.

In Fig. 3.5 we have displayed the redshift dependence of dN/dz for strong ($W_r(\lambda 2796) \geq 1.0 \text{ \AA}$) Mg II absorption systems detected in our blazar sample and compared it with that computed

Table 3.4: Incidence of Mg II absorbers for the present sample and its various subsets.

Sample type	Weak absorption systems				Strong absorption systems			
	N_{obs}	Δz	$\frac{N_{obs}}{\Delta z} \equiv dN/dz$	$\left(\frac{(N_{obs}/\Delta z)}{(dN/dz)_{qso}}\right)^\alpha$	N_{obs}	Δz	$\frac{N_{obs}}{\Delta z}$	$\left(\frac{(N_{obs}/\Delta z)}{(dN/dz)_{qso}}\right)^\beta$
Sample I ^a	23	44.21	$0.52^{0.13}_{0.11}$	$1.21^{0.31}_{0.25}$	20	86.08	$0.23^{0.06}_{0.05}$	$1.26^{0.35}_{0.28}$
Sample II ^b	20	40.06	$0.50^{0.14}_{0.11}$	$1.16^{0.32}_{0.26}$	16	81.41	$0.20^{0.06}_{0.05}$	$1.07^{0.34}_{0.26}$
Sample III ^c	17	32.69	$0.52^{0.16}_{0.12}$	$1.20^{0.37}_{0.29}$	13	60.10	$0.22^{0.08}_{0.06}$	$1.11^{0.40}_{0.30}$
Sample IV ^d	6	19.05	$0.31^{0.19}_{0.12}$	$0.74^{0.44}_{0.29}$	8	58.98	$0.14^{0.07}_{0.05}$	$0.80^{0.39}_{0.28}$
Sample V ^e	3	11.69	$0.26^{0.25}_{0.14}$	$0.57^{0.56}_{0.31}$	5	37.67	$0.13^{0.09}_{0.06}$	$0.72^{0.49}_{0.31}$
Sample VI ^f	4	15.48	$0.26^{0.20}_{0.12}$	$0.59^{0.47}_{0.28}$	7	52.21	$0.13^{0.07}_{0.05}$	$0.76^{0.41}_{0.28}$
Sample VII ^g	2	9.29	$0.22^{0.28}_{0.14}$	$0.46^{0.60}_{0.29}$	5	32.70	$0.15^{0.10}_{0.07}$	$0.76^{0.51}_{0.33}$
Sample VIII ^h	16	24.58	$0.65^{0.21}_{0.16}$	$1.52^{0.48}_{0.38}$	9	29.20	$0.31^{0.14}_{0.10}$	$1.61^{0.73}_{0.53}$
Sample IX ⁱ	15	23.41	$0.64^{0.21}_{0.16}$	$1.50^{0.50}_{0.38}$	8	27.41	$0.29^{0.14}_{0.10}$	$1.52^{0.75}_{0.52}$

^a dN/dz for QSOs is calculated at the mean value of the redshift path of the blazars, using equation 2 of BBM.

^b dN/dz for QSOs is calculated at the mean value of the redshift path of the blazars, using equation 6 of BBM.

^a Full sample of 191 blazars (also included are the sources with only a lower limit available for z_{em}).

^b 184 BL Lacs, i.e., Sample I (191 blazars) – 7 (BBM FSRQs).

^c 133 BL Lacs, i.e., Sample II (184 BL Lacs) – 51 (sources with only a lower limit on z_{em}).

^d 149 Non-BBM BL Lacs, i.e., Sample I (191 blazars) – 42 (BBM blazars).

^e 98 Non-BBM BL Lacs, i.e., Sample IV (149 Non-BBM BL Lacs) – 51 (Non-BBM BL Lacs with only lower limit on z_{em}).

^f 126 SDSS BL Lacs, i.e., Sample II (184 BL Lacs) – 58 (Non-SDSS BL Lacs).

^g 79 SDSS BL Lacs, i.e., Sample VI (126 SDSS BL Lacs) – 47 (SDSS BL Lacs with only lower limit on z_{em}).

^h 58 Non-SDSS BL Lacs, i.e., Sample II (184 BL Lacs) – 126 (SDSS BL Lacs).

ⁱ 54 Non-SDSS BL Lacs, i.e., Sample VIII (58 Non-SDSS BL Lacs) – 4 (Non-SDSS BL Lacs with only lower limit on z_{em}).

for the sightlines towards normal QSOs, using the analytical expression given by [Zhu & Ménard \(2013\)](#) for strong Mg II absorption systems. To quantify the similarity of these two distributions we have applied Kolmogorov-Smirnov (K-S) test, which resulted in $P_{null}=0.997$; where P_{null} is the null probability that two distributions are indistinguishable. Similarly a very good statistical agreement is found between the estimates of dN/dz for blazars and QSOs, with a χ^2 -test giving $P_{null} = 0.99$, leading us to infer that the distributions of dN/dz for blazars and QSOs are statistically indistinguishable. Recall that it is for the strong absorption systems that [BBM](#) had reported a significant excess of dN/dz (compared to QSOs sightlines), based on the high SNR spectroscopic data available for their sample of 45 blazars. To pursue this further, we present in the next section a re-analysis of their data following our data reduction and analysis procedure.

Since this has yielded results consistent with the [BBM](#) claim, could then the discrepant result we have found here using a much larger sample of blazars ([Table 3.1](#)) have its origin in the substantially lower SNR of the spectra available for most of the present enlarged sample? To check this possibility we divide our blazar sample into (i) a low SNR subset (spectra having SNR between 5 and 15) and (ii) a high SNR subset (SNR > 15). It is seen from [Table 3.5](#) that in neither case is a significant excess of dN/dz (vis a vis normal QSOs) detected for the strong Mg II absorption systems (the same is found to hold for the weak absorption systems as well). Thus, the discrepant result found here for the present blazar sample from the [BBM](#) sample is unlikely to be on account of the SNR contrast between the spectral data employed in the two studies. An alternative possibility is explored in the next section.

Table 3.5: *Incidence of strong Mg II absorption systems towards the low SNR (SNR<15) and high SNR (>15) spectra in our sample of 191 blazars. The last column shows the same relative to normal QSOs.*

Sample type	N_{obs}	Δz	$\frac{N_{obs}}{\Delta z}$	$\left(\frac{N_{obs}/\Delta z}{(dN/dz)_{qso}}\right)^\alpha$
Low SNR	7	28.74	$0.24_{0.09}^{0.13}$	$1.19_{0.44}^{0.64}$
High SNR	13	57.33	$0.23_{0.06}^{0.08}$	$1.29_{0.35}^{0.47}$

^{α} $(dN/dz)_{qso}$ for the strong systems ($W_r(2796) \geq 1.0 \text{ \AA}$) is calculated (as done in [BBM](#) analysis) based on [Prochter et al. \(2006\)](#).

3.1.3.2 Re-analysis of the [BBM](#) sample

As discussed in [Section 3.1](#), based on a sample of 45 blazars having high-sensitivity (ESO/FORS) spectra [BBM](#) found about a factor of 2 excess in the number density of Mg II absorbers on the blazar sightlines, as compared to the sightlines to normal QSOs. Since the present analysis of a sample of 191 blazars does not show such a trend, we have carried out a re-analysis of the [BBM](#)

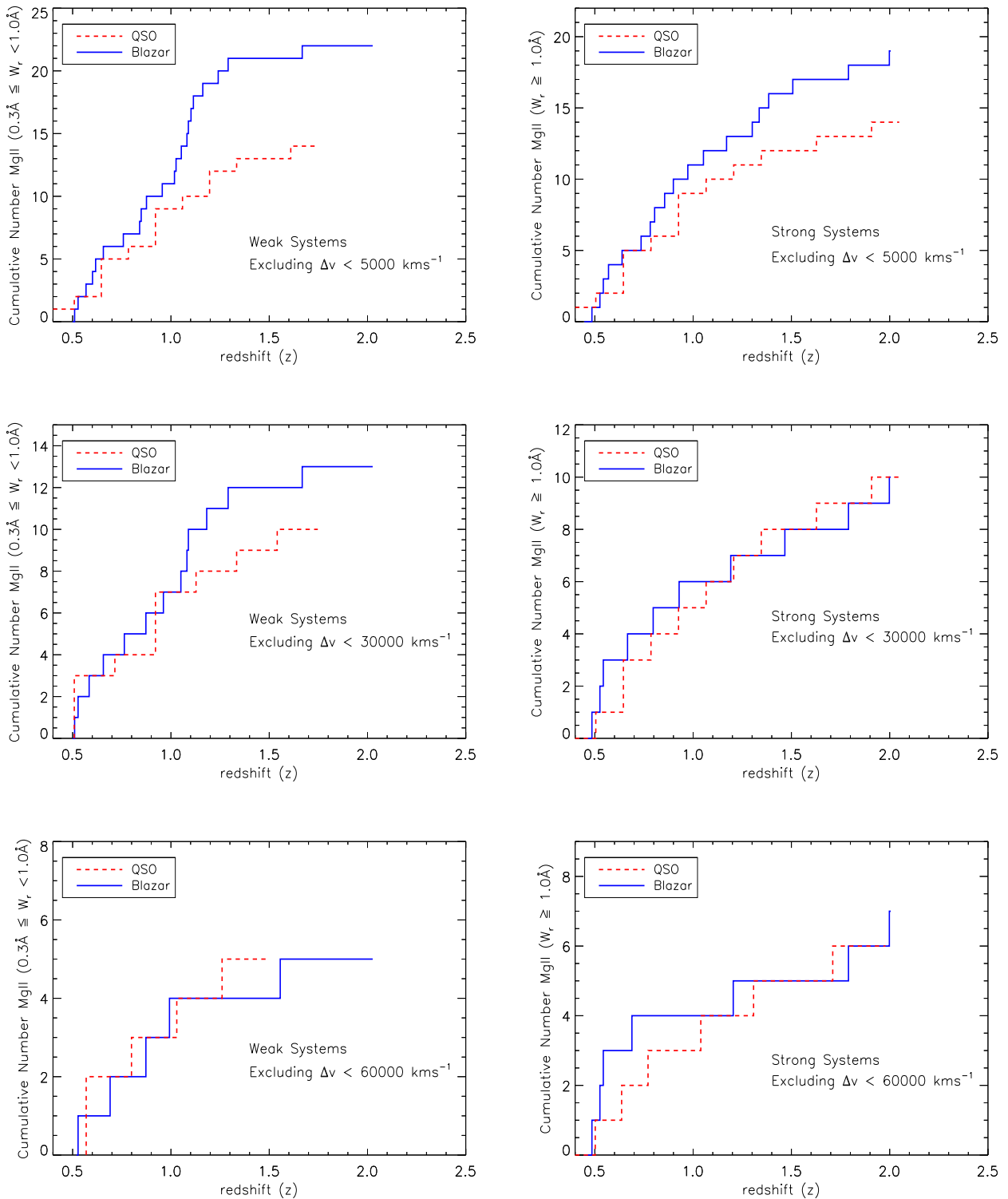


Figure 3.4: Cumulative number of weak (left) and strong (right) intervening Mg II absorption systems detected towards blazars (blue solid line) and QSOs (red dashed line), after excluding the systems with offset velocity (Δv) $< 5000 \text{ km s}^{-1}$ (top panel), $\Delta v < 30000 \text{ km s}^{-1}$ (middle panel) and $\Delta v < 60000 \text{ km s}^{-1}$ (bottom panel). For QSOs the estimates for weak Mg II systems are taken from *Nestor et al. (2005)* (see text), and for strong systems these are adopted from *Prochter et al. (2006)*.

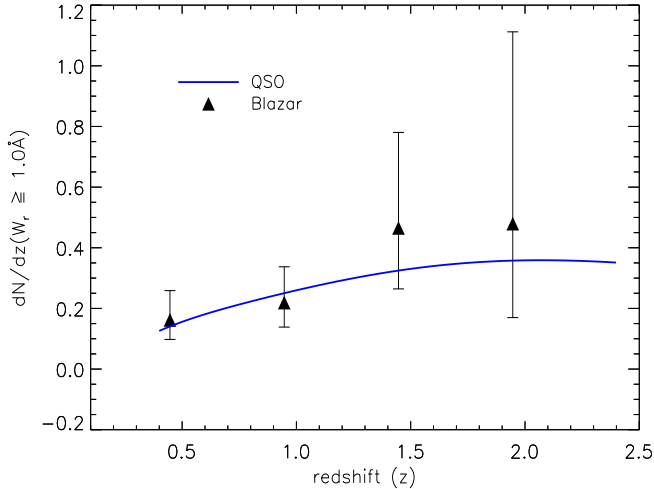


Figure 3.5: Number density evolution of strong ($W_r(2796) \geq 1.0 \text{ \AA}$) Mg II absorption systems (averaged over redshift bins of 0.5) towards our 191 blazar sightlines (black triangles), and the sightlines towards the QSOs in the SDSS (blue solid line). The absorption systems with $\Delta v < 5000 \text{ km s}^{-1}$ have been excluded. The solid line for the SDSS QSOs has been computed from the analytical expression given by Zhu & Ménard (2013) for strong Mg II absorption systems towards QSOs. The two distributions show an excellent agreement with a P_{null} of ~ 0.99 based on the K-S and χ^2 tests.

sample using the same procedure which we have followed here for our sample. As mentioned in Section 3.1.1, we have limited the re-analysis to 42 out of the 45 BBM blazars, since we could not access the requisite raw spectral data for the remaining 3 (northern) blazars. For both weak and strong absorption systems, Table 3.6 compares our results with the BBM estimates of N_{obs} , Δz and dN/dz . It is clear that the BBM estimates are reasonably well reproduced in our analysis; a few minor discrepancies are noted below.

For strong systems, there is a small difference in the redshift path, our value of 27.1 is slightly lower than the BBM estimate of 28.04. This small difference might be owing to the difference in the methods of determining ‘useful’ redshift path. We also compared the absorption redshifts and equivalent widths of the detected Mg II absorption systems and a good match was found, except in two cases: (i) the system at $z_{\text{abs}} = 0.5592$ towards the blazar J0428–3756 was classified as ‘weak’ in BBM ($W_r = 0.93$), but ‘strong’ ($W_r = 1.03$) in our analysis, and (ii) the $z_{\text{abs}} = 1.1158$ system towards J2031+1219 was classified as ‘strong’ ($W_r = 1.29$) in BBM, but ‘weak’ ($W_r = 0.94$) in our analysis. Coming to the weak systems, we detected a total of 17 Mg II absorbers, whereas BBM reported 19 Mg II absorbers, with the redshift path being 25.16 in our case, very close to their estimate of 25.11. Two systems, viz. (i) the $z_{\text{abs}} = 1.1039$ system towards J1419+0445 ($W_r = 0.52$) and (ii) the $z_{\text{abs}} = 0.6236$ system towards J1956–3225 (with $W_r = 0.95$), could not be included in our analysis. The former remained undetected and the latter system corresponds to a wavelength of 4539 Å which falls just below the starting wavelength of 4540 Å of the spectrum used in our analysis.

Table 3.6: *Re-analysis of the (high sensitivity) spectra of the 42 southern blazars in the BBM sample.*

Absorber type	$W_r(2796)$ -range	$N_{re-analysis}$	$\Delta z_{re-analysis}$	N_{BBM}	Δz_{BBM}	$\left(\frac{(dN/dz)_{re-analysis}}{(dN/dz)_{BBM}}\right)$
Strong ^{γ}	$W_r \geq 1.0 \text{ \AA}$	12	27.10	12	28.04	1.03 ± 0.48
Strong ^{β}	$W_r \geq 1.0 \text{ \AA}$	8	22.44	10	23.44	0.83 ± 0.46
Weak ^{γ}	$0.3 \text{ \AA} \leq W_r < 1.0$	17	25.16	19	25.11	0.89 ± 0.33
Weak ^{β}	$0.3 \text{ \AA} \leq W_r < 1.0$	14	21.01	15	20.55	0.91 ± 0.38

^{γ} For the 42 BBM blazars.

^{β} Analysis using 35 BL Lacs in BBM sample. It is to be noted that out of the 42 blazar in BBM sample, 32 were designated as BL Lacs. The other three included BL Lacs are those which in BBM sample were classified as non-BL Lac (i.e 'opt' class in BBM) viz, J023405–301519, J024156+004351, J221450–293225, but are reported as confirmed BL Lacs in VV catalogue and hence are included here in this sample of 35 BL Lacs.

3.1.4 Discussion and Conclusion

We have presented a new comparison of the incidence rates of Mg II absorption systems towards two different classes of AGNs, namely blazars and normal (optically selected) QSOs. A factor of two higher rate towards blazars has earlier been claimed by BBM (Section 3.1) and similar excess incidence of intervening Mg II absorbers has been reported in a few earlier studies of GRBs Prochter et al. (2006), Sudilovsky et al. (2007), Vergani et al. (2009) and Tejos et al. (2009). However, the physical cause of the purported excess relative to normal QSOs still remains to be understood. In fact, BBM have already discounted the possibilities of dust obscuration and gravitational lensing playing a significant role (see also Cucchiara et al. 2013).

On the other hand, no excess in the incidence rate of intervening Mg II absorbers towards flat-spectrum radio quasars has been reported in some recent studies based on large samples (Chand & Gopal-Krishna 2012; Joshi et al. 2013). Therefore, in order to take a fresh look into the BBM finding of excess incidence of Mg II absorbers along blazar sightlines, we have assembled a large sample of 191 blazars (including the BBM sample of blazars). An independent sample of sightlines is also intended to provide a check on the possible role of statistical fluctuation arising from small source sample, as indeed turned out to be the case for GRBs (Cucchiara et al. 2013, Section 3.1)

Table 3.7: *The results for the present sample and its various subsets, after excluding the Mg II absorption systems with $\Delta v < 60000 \text{ km s}^{-1}$.*

Sample type [†]	Weak systems				Strong systems			
	N_{obs}	Δz	$\frac{N_{obs}}{\Delta z}$	$\left(\frac{(N_{obs}/\Delta z)}{(dN/dz)_{qso}}\right)^\alpha$	N_{obs}	Δz	$\frac{N_{obs}}{\Delta z}$	$\left(\frac{(N_{obs}/\Delta z)}{(dN/dz)_{qso}}\right)^\beta$
Sample I	6	18.80	$0.32^{0.19}_{0.13}$	$0.76^{0.45}_{0.30}$	8	39.68	$0.20^{0.10}_{0.07}$	$1.10^{0.54}_{0.38}$
Sample II	5	16.87	$0.30^{0.20}_{0.13}$	$0.70^{0.47}_{0.30}$	7	37.56	$0.19^{0.10}_{0.07}$	$1.00^{0.54}_{0.37}$
Sample III	5	15.19	$0.33^{0.22}_{0.14}$	$0.77^{0.52}_{0.33}$	7	29.83	$0.23^{0.13}_{0.09}$	$1.16^{0.62}_{0.43}$
Sample IV	1	7.38	$0.14^{0.31}_{0.11}$	$0.29^{0.67}_{0.24}$	4	27.56	$0.15^{0.11}_{0.07}$	$0.74^{0.58}_{0.35}$
Sample V	1	5.69	$0.18^{0.40}_{0.15}$	$0.36^{0.84}_{0.30}$	4	19.83	$0.20^{0.16}_{0.10}$	$0.85^{0.67}_{0.41}$
Sample VI	1	6.37	$0.16^{0.36}_{0.13}$	$0.33^{0.75}_{0.27}$	4	25.12	$0.16^{0.13}_{0.08}$	$0.79^{0.63}_{0.38}$
Sample VII	1	5.19	$0.19^{0.44}_{0.16}$	$0.39^{0.90}_{0.32}$	4	18.19	$0.22^{0.17}_{0.11}$	$0.91^{0.72}_{0.44}$
Sample VIII	4	10.50	$0.38^{0.30}_{0.18}$	$0.92^{0.73}_{0.44}$	3	12.44	$0.24^{0.23}_{0.13}$	$1.38^{1.35}_{0.75}$
Sample IX	4	10.00	$0.40^{0.32}_{0.19}$	$0.97^{0.77}_{0.46}$	3	11.65	$0.26^{0.25}_{0.14}$	$1.48^{1.44}_{0.81}$
Sample X	5	11.42	$0.44^{0.30}_{0.19}$	$1.06^{0.72}_{0.46}$	4	12.12	$0.33^{0.26}_{0.16}$	$1.89^{1.50}_{0.91}$

^α dN/dz for QSOs is calculated at the mean value of the redshift path for the blazars, using equation 2 of BBM.

^β dN/dz for QSOs is calculated at the mean value of redshift path for the blazars, using equation 6 of BBM.

[†]The sample types are the same as in Table 3.4 except that the regions with $\Delta v < 60000 \text{ km s}^{-1}$ have been excluded here; The additional Sample X in the last row corresponds to the 42 BBM blazars.

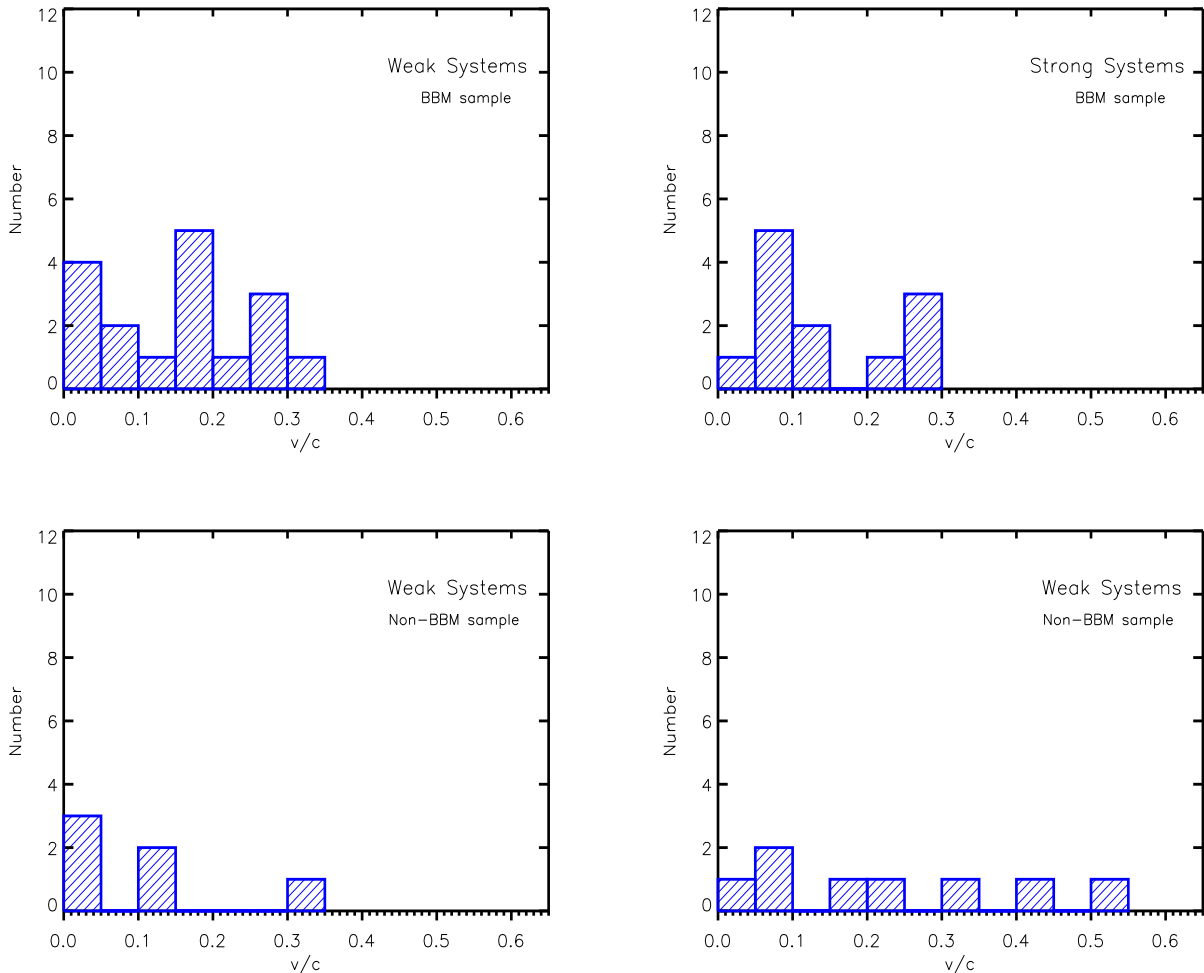


Figure 3.6: Top: Velocity distribution of the Mg II absorbers, relative to the background blazar (Eq. 3.3) for the 17 weak ($0.3 \text{ \AA} \leq W_r(2796) < 1.0 \text{ \AA}$; left) and 12 strong ($W_r(2796) \geq 1.0 \text{ \AA}$; right) ‘intervening’ Mg II absorbers seen towards the 42 BBM blazars, (see Section 3.1.3.2). Bottom: The same as the top panel for the 7 weak and 8 strong ‘intervening’ Mg II absorbers detected towards 160 blazars (among which only 64 have useful redshift path for weak systems) after excluding the BBM blazars. Note that the absorption systems with offset velocities $\Delta v < 5000 \text{ km s}^{-1}$, i.e., $\beta < 0.017$ have been excluded.

From the results of our analysis of the enlarged blazar sample (Table 3.4), no excess is evident in the dN/dz along the sightlines to blazars, as compared to the sightlines to normal QSOs. Recognizing that the spectral data for our blazar sample have mostly rather modest SNR in comparison to the BBM sample (see Fig. 3.2), we have sub-divided the spectra for our blazar sample into two ranges of SNR (SNR between 5 and 15, and SNR > 15). For neither of these SNR ranges did our analysis show a significant difference between the dN/dz estimates towards blazars and

normal QSOs (see Table 3.4 and Table 3.5). Conceivably, the discrepancy between our and BBM estimates of dN/dz may then be rooted in the use of different analysis procedures. However, this too seems unlikely since our independent re-analysis of the BBM blazar sample reproduces the dN/dz excess reported by them (Table 3.6).

To probe this issue further, we compare in Fig. 3.6, the β distributions of the Mg II absorbers for the BBM and our samples of blazars. Here $c\beta$ is the velocity of an absorber measured relative to the background blazar, where:

$$\beta \equiv \frac{v}{c} = \frac{(1 + z_{em})^2 - (1 + z_{abs})^2}{(1 + z_{em})^2 + (1 + z_{abs})^2} \quad (3.3)$$

with, z_{em} and z_{abs} are the redshifts of the background AGN and the Mg II absorber, respectively. The distributions shown in Fig.3.6 are useful for checking the extent of clustering, if any, of Mg II absorbers up to mildly relativistic β values, as was noted in some recent studies of other AGN samples (see below). The top two panels in Fig. 3.6 show the histograms of β values of Mg II absorbers for the BBM sample, both for weak (left panel of Fig. 3.6) and strong absorbers (right panel in Fig. 3.6). The lower two panels show the histograms for the Mg II absorbers for our blazar sample, after excluding the BBM blazars. For the strong absorbers in the BBM sample, a slight clustering at smaller β is hinted, which is consistent with the trend noticed in some earlier studies (Joshi et al. 2013; Chand & Gopal-Krishna 2012, also BBM), as well as from Fig. 3.4 (see above). This might indicate that associated Mg II absorbers may still contribute significantly to dN/dz up to offset velocities $\sim 0.2c$, especially for weak systems towards blazars (e.g., see Fig. 3.4, left panel). Table 3.7 summarizes the dN/dz estimates for the various subsets of our 191 blazar sample, after excluding the systems with $\Delta v < 60000 \text{ km s}^{-1}$ i.e., $\beta < 0.2c$.

There is a hint of discrepancy when the dN/dz excess for blazar (relative to QSO sightlines) is compared for strong and weak absorption systems, the excess being noticeable for weak absorbers (e.g., see the top and middle panels in Fig. 3.4). Attributing this marginally significant excess to gas clumps accelerated outwards by the powerful blazar jet, (e.g., up to $\Delta v < 60000 \text{ km s}^{-1}$), as also noted in BBM, the hinted excess in the case of weak absorbers could have its origin in a physical cause, or merely an observational bias. For instance, observationally the detection of gas clumps with higher column density (i.e., stronger systems) would be easier as compared to the lower column density clumps (i.e., weak absorbers). On the other hand, occurrence of lower column density clumps is more likely, intuitively. This seems to be the case as dynamical stability of the relativistic jets suggests that external perturbations do not disrupt the jets globally (see, e.g.,

Komissarov 2017). This means, in particular, that most of the clumps (or clouds) impinging on the jet, as it propagates through the mostly diffuse gas, are smaller than the jet radius. Assuming that clumps or clouds in the ambient medium have similar volume densities, those with lower column densities (hence weak systems) are likely to have a less disruption effect on the jets via a slower growth of global instabilities. Hence, lower column density clumps accelerated by the jets should be intuitively more abundant in comparison to higher column density clumps, consistent with the results shown in (Fig. 3.4, left panel). The reality of the discrepancy, however, remains to be confirmed using larger set of blazar sightlines.

In summary, we conclude that (i) our independent analysis of the spectral data used by BBM for their blazar sample has reproduced the factor two excess claimed by them in dN/dz for Mg II absorbers seen towards blazars, vis-a-vis normal QSO; (ii) by using a ~ 3 times larger blazar sample (albeit, mostly with a moderate SNR) which includes the BBM sample as well, we have arrived at a statistically more robust and independent estimate of dN/dz of Mg II absorbers along blazar sightlines and the present analysis does not show a significant difference from the dN/dz known for the sightlines to normal QSOs; (iii) the agreement improves further when we limit the comparison to offset velocities above 60000 km s^{-1} . This would be consistent with the possibility that associated Mg II absorbers remain a significant contributor to dN/dz up to $\beta = 0.2c$ measured relative to the background QSO (see Joshi et al. 2013, also BBM).

Finally, in order to firmly settle the issues raised in the present study a significant enlargement of the sample of Mg II absorbers towards blazars would be vital. This can be achieved, e.g., by extending the high sensitivity optical spectroscopic coverage to the 71 blazars which had to be excluded from the present analysis because the SNR of their currently available spectra falls below our adopted reasonable threshold ($\text{SNR} > 5$).

Chapter 4

Probing AGN environment using the radiative-mode feedback

In the Chapter 1, we have discussed in detail about the BALs seen in the blue wings of the prominent emission lines like C IV and Mg II, in the UV spectra of quasars (e.g., Hewett & Foltz 2003) subclassing them as BAL quasars. These absorption troughs are thought to be a signature of strong winds generated in the proximity of accretion disk, which are radially accelerated outwards (Murray et al. 1995; Elvis 2000) up to speeds from $\sim 2000 \text{ km s}^{-1}$ to $\sim 0.1c$. These strong outflows expel a tremendous amount of momentum and energy and hence largely contributing to the AGN feedback. Many BAL outflows are believed to be originated from the accretion disk at 10–100 light days from the SMBH (e.g., Murray et al. 1995; Proga et al. 1998), then the time required for outflowing clouds with a typical outflow velocity of 8000 km s^{-1} to cross the launching region will be about 1–10 years. Therefore, it is believed that fluctuations produced in the accretion disk can give rise to the variations of BAL outflows over the time-scales of 1–10 years. Thus, multi-year variability studies of BAL quasars are essential to understand the location and physical condition of the absorbing gas (e.g., quasar wind lifetimes, sizes, and geometries) and hence the physical mechanisms that give rise to such outflows. The exciting cases for the study of such outflows are where the variability of these BALs results in complete emergence or disappearance of the BAL troughs. In this chapter, we present the results of our new set of 94 BAL quasars ($1.7 < z_{\text{em}} < 4.4$) exhibiting an appearance of C IV BAL troughs over 0.3–4.8 rest-frame years by comparing the SDSSDR-7, SDSSDR-12, and SDSSDR-14 quasar catalogs. In addition, to explore the leading cause responsible for such extreme variations, a detailed comparison of this new appearing BAL

quasar sample with a disappearing BAL quasar sample studied in literature is also presented in this chapter. The work of this chapter is submitted for publication in MNRAS.

4.1 Photoionization-driven appearance/disappearance of broad absorption line quasars

Variations of BAL troughs such as changes in the absorption strength, e.g., equivalent width (EW), appearance or disappearance of BAL troughs, kinematic shifts in the absorption profiles, and changes in the shape of BAL profiles in C iv and Si iv BALs have been studied in several cases. Such variations in the BAL absorption profiles can be comprehended from (i) the changes in covering fraction of the quasar by the absorbing gas due to its transverse motions across our LOS (Lundgren et al. 2007; Gibson et al. 2008; Capellupo et al. 2011, 2013; Vivek et al. 2014; Yi et al. 2019), and/or (ii) changes in the ionizing radiation giving rise to changes in optical depth of the absorbers (Barlow 1994; Capellupo et al. 2012; He et al. 2015; Rogerson et al. 2018; Lu et al. 2018; Vivek 2019).

The first systematic spectral variability analysis of BAL quasar sample was carried out by Barlow (1994) using multiple epoch observations of 23 BAL quasars. They found BAL trough variations are correlated with the changes in the broadband continuum flux, hence identified the fluctuating ionizing source as the primary cause of BAL variability. The studies of Lundgren et al. (2007) and Gibson et al. (2008) found no evidence of variation in continuum flux with the BAL changes and support changing covering fraction of the BAL clouds as a major driver in causing BAL variations. Rigorous analysis of 24 luminous quasars at redshift $1.2 < z_{\text{em}} < 2.9$ by Capellupo et al. (2011, 2012, 2013) over the time scale of 8–10 days to 8.7 years¹ supports both cloud crossing and fluctuating ionizing radiation scenarios based on the variability found only in a portion of BAL troughs and coordinated variability of multiple BAL troughs respectively. Filiz Ak et al. (2013) performed the variability analysis in a sample of 291 quasars on a time scale of 1–3.7 years and similar to Gibson et al. (2010), they found BAL variation occurs in a portion of BAL troughs with more variation of the narrower regions. They have also reported coordinated BAL trough variabilities in BAL quasars with multiple troughs supporting the changing shielding cloud scenario of BAL variations. Simultaneous multi-epoch spectral and photometric analysis of 22 LoBAL quasars of Al III and Mg II absorption lines by Vivek et al. (2014) over a time scale of 10 days

¹All the timescales are in rest-frame of quasar

to 7.69 years reported no strong correlation between the varying continuum flux and absorption strength. Their analysis favors the line-of-sight cloud crossing scenario as the primary cause of BAL variations. Interestingly, with a sample of 2099 BAL quasars, [Zhang et al. \(2014\)](#) proposed a dust outflow scenario of BAL quasars where they used the slope of near-infrared (NIR) continuum as an indicator for the associated hot dust emissions. They found a moderate correlation between the absorption strength and velocity with slope of NIR continuum. Based on their dust outflow scenario, they suggested dust is intrinsic to the BAL outflows and may contribute to the acceleration provided to BAL clouds (also see [Scoville & Norman 1995](#)). Based on the multi-epoch spectroscopic data set of 6250 quasars from SDSSDR-10, [Wang et al. \(2015\)](#) found a high correlation among the variability of multiple BAL troughs associated with same ions or the same troughs of different ions. They also observed appearance and disappearance of BAL troughs co-occur with the dimming and brightening of the continuum flux, respectively, indicating varying ionizing radiation scenario as a major cause for driving these extreme variations of BAL troughs. [He et al. \(2015\)](#) presented the variability study of 188 SDSSDR-7 BAL quasar over a time scale ranging from 0.001–3 years and found a mild correlation between the variation in continuum luminosity at 1500 Å and variation in the spectral index. They also reported a mild negative correlation between the variation in EW and Mg II-based black hole mass and a strong positive correlation between the maximum velocity of outflow and Eddington ratio. Their findings suggest that variabilities are governed by the accretion onto the central engine. [McGraw et al. \(2017\)](#) explored the emerging and disappearing behavior in 471 SDSS BAL quasars covering a time range of 0.1–5.25 years. They reported 14 disappearing BALs with a BAL disappearance rate of $2.3^{+0.9}_{-0.7}$ within 1.73–4.62 years and 18 emerging BALs at a BAL emergence rate of $3.0^{+1.0}_{-0.8}$ in 1.46–3.66 years. Their variability analysis supports both the ionization change and the cloud crossing scenarios. Recent study of [De Cicco et al. \(2018\)](#) isolates a set of 73 disappearing C IV BAL troughs over the time scale of ~ 3.1 years. Their analysis indicates that the multiple BAL troughs in a BAL quasar vary in a coordinated manner, and the coordination persists over the larger radial distances and hence demands a global mechanism to explain such variations. [Rogerson et al. \(2018\)](#) presented a detailed analysis of 105 emerging BAL quasars. They found emerging BAL quasars can be represented as BALs of shallower depths, smaller balnicity indices, larger velocities, and smaller widths. They found a rate of coordinated variation of 68.3% in the multiple BAL troughs at different velocities in the same quasars facing the same fluctuating ionizing radiation. To probe the link between the continuum flux and C IV absorption line strength variation, [Vivek \(2019\)](#) utilized a multi-epoch

spectral data of 78 BAL quasars in the Stripe 82 regions. The author has discovered a strong correlation between the varying continuum and the absorption trough of shallower depths. On the other hand, no correlation between the continuum and the deeper absorption troughs indicates a significant role of line saturation effects.

BAL variability analysis has been performed with a variety of ions, on a range of time scales and different sample sizes. The cause of variability is possibly due to cloud crossing, fluctuating ionizing radiation, and/or a combination of both the scenario. Hitherto, the root cause for the extreme variation i.e., appearance and disappearance of BAL troughs is debated. In this chapter, we, for the first time, aim to contrast the properties of appearing and disappearing BAL quasars to explore for the leading cause responsible for such extreme variation of BAL troughs. With this motivation we, (i) provide a new catalog of appearing BAL quasars built up by comparing the data set of SDSSDR-7, SDSSDR-12, and SDSSDR-14, (ii) present a detailed variability study of this new appearing BAL catalog, (iii) establish a comprehensive comparison of this appearing BAL quasar sample with an existing large sample of disappearing BAL quasars presented by [De Cicco et al. \(2018\)](#).

4.1.1 The Sample

The initial emerging BAL quasar sample utilized in the present work is constructed based on the quasar properties presented in the quasar catalogs of SDSSDR-7 ([Schneider et al. 2010](#)), SDSSDR-12 ([Pâris et al. 2017](#)), and SDSSDR-14 ([Pâris et al. 2018](#)). The SDSSDR-7 catalog contains 1,05,783 quasars with their detailed properties presented in [Shen et al. \(2011\)](#). From the analysis of [Shen et al. \(2011\)](#), 99,569 SDSSDR-7 quasars (hereafter Q-DR7) were classified as non-BAL quasars with BAL flag 0. The SDSSDR-12 catalog comprises of 2,97,301 quasars, out of which 15,177 are BAL quasars (hereafter BQ-DR12) with a non-zero value of balnicity index (BI) of C iv BAL trough. The remaining 2,82,124 quasars have either BI = 0 or have BAL flag = 0 and constitute a non-BAL DR12 quasar catalog (hereafter Q-DR12). On the other hand, SDSSDR-14 quasar catalog has a total of 5,26,357 quasars out of which 21,877 quasars have been assigned a non-zero BI value of C iv BAL troughs (BQ-DR14).

The process of building the emerging BAL quasar sample can be split into two steps. In step one, we combined the BAL quasars of BQ-DR12 and BQ-DR14 catalogs after discounting the repeated entries in RA and DEC between these two catalogs, which have the same epoch of observation. This amalgamation resulted in 22,626 unique BAL quasars and is designated as the

BQ-DR12/14 catalog. We then cross-correlated the BQ-DR12/14 BAL quasar catalog with the non-BAL Q-DR7 catalog using a search radius of 2 arc-seconds. The cross-correlation resulted in a sample 834 emerging BAL sources uniquely designated as BAL quasars in later epoch SDSS-12/DR14 catalogs (hereinafter referred as DR7-DR12/14 emerging BAL sample).

In step two, we searched for the sources classified as non-BAL quasars in the SDSSDR-12 catalog but are BAL quasars in the SDSSDR-14 catalog. For this purpose, we cross-correlated the SDSSDR-12 non-BAL quasar (i.e., Q-DR12) catalog with the SDSSDR-14 BAL quasar (i.e., BQ-DR14) catalog within two arc-seconds of search radius. Our search resulted in a sample of 141 sources, which we refer to as the sample of DR12-DR14 emerging BAL quasars. Furthermore, we also noted that among them, seven sources are already members of our DR7-DR12/14 emerging sample of 834 sources (i.e., they remained as a non-BAL quasar in SDSSDR-12 data, and the BAL appeared in the SDSSDR-14 data), while 11 sources were BAL quasar in the SDSSDR-7 data. As a result, DR12-DR14 emerging sample adds new 123 sources (i.e., $141 - 7 - 11$), resulting in our total sample of 957 (i.e., $834 + 123$) emerging BAL quasars.

The spectral coverage of sources in SDSSDR-7 spans a range of 3800–9200 Å while the sources in SDSSDR-12/DR14 have spectral coverage of 3600–10,400 Å. Therefore, to ensure a proper spectral coverage allowing the detection of C IV BAL troughs for the sources common in the SDSSDR-7 and SDSSDR-12/14 catalogs, we applied a filter based on emission redshift (z_{em}), which excludes the sources beyond $1.68 < z_{em} < 4.39$ range. This constraint on the z_{em} reduces our sample from 957 to 901 quasars. Besides, we also excluded 37 sources overlapping with the previous BAL variability analysis focusing on the emerging/appearing nature of BAL troughs carried out by Rogerson et al. (2018). This yielded a sample of 864 BAL quasars with at least two epoch of observations available and that have undergone a non-BAL to BAL transition.

Further, to avoid the uncertainty in the analysis due to the inclusion of noisy spectra, we included only those sources with $SNR_{1700} > 6$ (see Gibson et al. 2009) in at least two epochs of observation. Out of the 864 sources, we found that 464 sources (with 1010 spectra) have $SNR_{1700} > 6$ spectral data available for at least two epochs. Among these 464 sources, 399 sources have 2 epochs, 54 sources have 3 epochs, 8 sources have 4 epochs, 1 source has 5 epochs, 1 source has 6 epochs while 1 source has 7 epochs of spectral data (i.e., a total of $2 \times 399 + 3 \times 54 + 4 \times 8 + 5 \times 1 + 6 \times 1 + 7 \times 1 = 1010$ spectra). For the sources with spectral data available for more than two epochs, we have treated each unique pair of MJD as a single source. For instance, J002028.34–002914.9 has three epochs of spectra available at MJDs 51816, 51900 and 56979;

therefore the combinations of MJDs 51816-51900, 51816-56979 and 51900-56979 are considered as three different measurements in our analysis equivalent to three sources.

Hence our final sample of 464 sources having 1010 spectra resulted in 655 MJD pairs with emerging BAL (i.e., $399 + 3 \times 54 + 6 \times 8 + 10 \times 1 + 15 \times 1 + 21 \times 1$). Based on our preliminary data analysis, discussed below in Section 4.1.2.2, this sample further reduced to 379 BAL quasars comprising of 517 MJD pairs, hereinafter referred as “*Preliminary*” sample. Our sample compilation procedure is summarised in Table 4.1. In Table 4.2 we have listed the physical properties of this *Preliminary* sample, where the values of bolometric luminosity ($\log L_{\text{bol}}$), black hole mass ($\log M_{\odot}$) and Eddington ratio ($\log \frac{L_{\text{bol}}}{L_{\text{Edd}}}$) are based on the study of Shen et al. (2011).

To draw a comparison of our appearing BAL quasar sample with the disappearing BAL quasars, we have used from literature the largest sample of 67 disappearing BAL quasars presented by De Cicco et al. (2018) for which spectral data is readily available from SDSS-I/II/III. Since this sample is derived from SDSS-I/II/III programs similar to our study, any bias arising in the comparison due to the intrinsic spectral properties (i.e., spectral coverage and resolution) can be neglected. The classification of their 67 disappearing BAL quasars was performed based on the two-sample χ^2 test on the flux value of the two available epochs of each BAL quasars. To minimize the random occurrence of the disappearance of BAL troughs, the authors required the probability of the test (P_{χ}^2) to be $P_{\chi}^2 \leq 10^{-4}$. Their analysis isolated 73 such BAL troughs in the spectra of 67 BAL quasars. They labeled it as P_4 . Among this P_4 , 52 BAL troughs had $P_{\chi}^2 \leq 10^{-8}$, and the authors labeled this sample as P_8 . However, 30 BAL troughs in P_8 had no residual absorption in their later epoch observations, and this sample was tagged as Pristine.

4.1.2 Data Analysis

Table 4.1: Summary of sample selection that resulted in the compilation of appearing BAL sample.

(1)	SDSSDR-7 quasars with BAL flag ^a = 0 (Q-DR7)	99569
(2)	SDSSDR-7 quasars with BAL flag ^a ≠ 0	6214
(3)	SDSSDR-12 quasars with BAL flag ^b = 0 or BI=0 (Q-DR12)	282124
(4)	SDSSDR-12 quasars with BI > ^b 0 (BQ-DR12)	15177
(5)	SDSSDR-14 quasars with BI ^c > 0 (BQ-DR14)	21877
Step-1		
(6)	(4) and (5) excluding repeated entries (BQ-DR12/14)	22626
(7)	(1) and (6) within 2 arc-seconds (DR7-DR12/14)	834
Step-2		
(8)	(3) and (5) within 2 arc-seconds (DR12-DR14)	141
(9)	(7) and (8) within 2 arc-seconds	7
(10)	(2) and (8) within 2 arc-seconds	11
(11)	(7) + (8) - (9) - (10)	957
(12)	(11) and $1.68 < z_{em} < 4.39$	901
(13)	(12) - 37 previously studied appearing BAL quasars ^d	864
(14)	(13) and multi-epoch SN ₁₇₀₀ ^{spectra} > 6 spectra	464
(15)	(14) + preliminary analysis of Section 4.1.2.2	379

^a Shen et al. (2011); ^b Pâris et al. (2017); ^c Pâris et al. (2018);

^d from Rogerson et al. (2018)

Table 4.2: *Physical parameters of Preliminary sample of 379 BAL quasars with 517 MJD pairs.*

BAL quasar	MJD-pair	z_{em}	M_i (mag)	$\log L_{bol}$ (erg s ⁻¹)	$\log M_{BH}$ (M_{\odot})	$\log \frac{L_{bol}}{L_{Edd}}$	Δt (years)
SDSS J000448.32+185635.8	56240-56945	2.48	-27.17	-	-	-	0.56
SDSS J002028.34-002914.9	51816-56979	1.94	-26.68	46.76±0.01	-0.82±9.48	0.05	4.82
SDSS J002028.34-002914.9	51816-56979	1.94	-26.68	46.76±0.01	-0.82±9.48	0.05	4.82
SDSS J002028.34-002914.9	51900-56979	1.94	-26.68	46.76±0.01	-0.82±9.48	0.05	4.74
SDSS J002028.34-002914.9	51900-56979	1.94	-26.68	46.76±0.01	-0.82±9.48	0.05	4.74
—	—	—	—	—	—	—	—

Note. See Table B.1 for the full version.

4.1.2.1 Continuum fitting

We used multi-epoch spectra that are normalized by an estimated continuum model to study the variations in BAL characteristics. To determine the proper continuum levels, we first corrected the main-sample spectra for Galactic extinction using a Milky Way extinction model (see Fitzpatrick 1999) for $R_V = 3.1$. The A_V values were taken from the Schlegel et al. (1998). The night-sky lines from the data were removed using the “BRIGHTSKY” mask flag provided by SDSS. We then translated observed wavelengths to the rest frame using redshifts from Hewett & Wild (2010). We constructed the underlying continuum by fitting a power-law model that is intrinsically reddened using the SMC-like reddening model from Gordon et al. (2003) to only relatively line-free (RLF) windows of the spectral regions: 1250-1350 Å, 1700-1800 Å, 1950-2200 Å, 2650-2910 Å, 3950-4050 Å. The RLF windows were selected to be relatively free from emission and absorption lines considering the composite quasar spectra of Vanden Berk et al. (2001). The three power-law continuum-model parameters are thus the power-law normalization, the power-law spectral index, and the intrinsic absorption coefficient. To exclude the data points that deviate from the fit by more than 3σ , we apply an iterative sigma-clipping algorithm using a non-linear least-squares fit.

Besides, we employed a double Gaussian function for the fitting of C iv and Si iv emission line doublets and a single Gaussian function for C iii] emission line. Here we have tied the width and redshift of the Gaussian components of these species. The continuum model generated after the simultaneous fitting of the reddened power-law, two double Gaussians for C iv and Si iv, and a single Gaussian C iii] for emission line is shown in Fig. 4.1 for the spectrum of SDSS-J072134.30+413108.8. To evaluate the uncertainties over the continuum fit, we performed the Monte Carlo simulations by randomizing the flux in each pixel with a random Gaussian deviate

associated with the uncertainty in the pixel for 100 realizations. We fit the continuum to these 100 realizations and adopted their standard deviation as the uncertainty of the continuum fit.

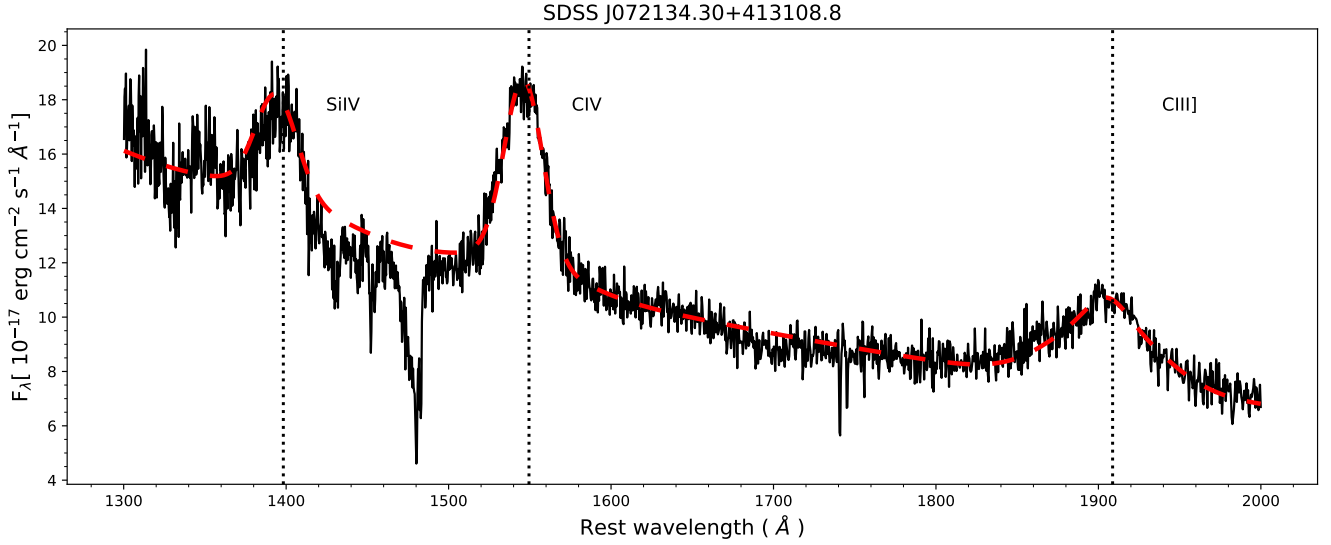


Figure 4.1: The continuum fit (red dashed curve) for the spectrum of SDSS-J072134.30+413108.8 modeled by a combination of a reddened power law, double Gaussians for C IV and Si IV emission lines and a single Gaussian for C III] emission line. Three vertical lines (black dotted) correspond to the quasar’s Si IV $\lambda\lambda 1393, 1403$, C IV $\lambda\lambda 1548, 1550$, and C III] $\lambda 1909$ emission lines.

4.1.2.2 BAL identification

To formally quantify a BAL trough, Weymann et al. (1991) defined the Balnicity Index (BI), which measures the strength of all the C IV absorption troughs in a spectrum over a velocity range of 3000 to 25,000 km s^{-1} blue-ward of the quasar C IV emission. According to this BI definition, the normalized flux of each absorption trough needs to be below 0.9 for at least 2000 km s^{-1} .

In this work, we have used spectral regions between 3000 to 30000 km s^{-1} blue-ward of the quasar C IV emission to exclude the regions which are prone to be affected by the variabilities caused in quasars C IV and Si IV emission lines (see Filiz Ak et al. 2012). To identify the multiple BAL troughs in each quasar spectrum, we have used a modified form of BI for each C IV BAL trough and defined as:

$$\text{BI}_{\text{trough}} \equiv \int_{v_{\text{max}}}^{v_{\text{min}}} \left[1 - \frac{f(v)}{0.9} \right] C \, dv \quad (4.1)$$

where $f(v)$ is the normalized flux density at velocity v , and C is a constant, which is 1 if the normalized flux is below 0.9 for at least 2000 km s^{-1} and 0 otherwise. The upper (v_{max}) and lower (v_{min}) limit on velocities are defined as the maximum and minimum velocity of the trough within which the normalized continuum level is continuously below 0.9 for at least 2000 km s^{-1} . An absorption trough with $BI_{\text{trough}} > 0$ is considered as BAL absorption trough.

Since the prime interest of this study is to report the multi-epoch variability of the BAL quasar spectra, v_{max} and v_{min} of each C iv BAL trough is derived using all the available spectra of each BAL quasar. A BAL trough may split into two small absorption troughs, or small troughs may merge to form a broad trough from one epoch to another epoch of observation. Therefore, to quantify the variability of absorption troughs between two epochs of BAL quasar spectra, we considered absorption complexes as presented in Filiz Ak et al. (2013) and Rogerson et al. (2018).

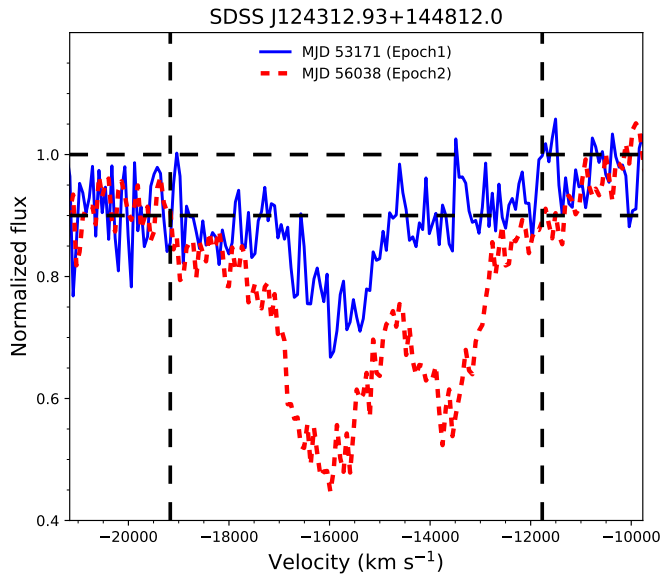


Figure 4.2: Demonstration of determining the lower (v_{min}) and upper (v_{max}) limits of an absorption complex using the multi-epoch spectra of SDSS J124312.93+144812.0. Two vertical dashed lines indicate the lower and upper limit of velocity region used for the BAL trough, while two horizontal dashed lines represent the normalized continuum level at 1.0 and 0.9.

If v_{min} and/or v_{max} of a BAL trough, detected in one epoch of a BAL quasar intercepts inside the BAL trough found in other epoch of the same BAL quasar, the minimum of the lower velocities of the BAL troughs from both the epochs is set as the v_{min} of the absorption complex. Similarly, the maximum of the higher velocities of the BAL troughs is taken as the v_{max} of the absorption complex. However, in the case of no BAL trough detection in one of the epochs, the lower and higher velocities of the BAL trough detected in the other epoch is taken as the v_{min} and v_{max} of absorption complexes respectively. In this way, each absorption complex contains all the

BAL troughs, which may have split into multiple small BAL troughs from one epoch to another epoch of observation for a BAL quasar. In Fig. 4.2, we show an example of absorption complex found in SDSS J124312.93+144812.0, where the BAL trough has increased in strength along with an emergence of a new component in the later epoch as compared to the earlier epoch. However, the variability measurement of this BAL trough has been performed between the v_{min} and v_{max} estimated from the later epoch. From among the 655 MJD pairs of 464 BAL quasars (see Section 4.1.1), we report no BAL detection in 138 MJD pairs of 85 BAL quasars in both the epochs of observation and hence excluded them from further analysis. In the remaining 517 MJD pairs of 379 BAL quasars, we found 614 absorption complexes and called it the *Preliminary* sample, as mentioned earlier in Section 4.1.1.

We note that in vast majority of complexes in the 614 *Preliminary* sample, i.e., 378 complexes in 341 MJD pairs of 249 BAL quasars, we identified BAL troughs with $BI \neq 0$ in both earlier and later epochs of the observations whereas the study of Shen et al. (2011) characterises them as non-BAL quasars from their earlier epoch observation (even to few visually obvious cases e.g., SDSS J141723.73+285522.6). This noted discrepancy between the analysis of Shen et al. (2011) and the present work may be emerging from the difference in the methods employed for fitting the continuum. Besides, the catalog presented by Shen et al. (2011) is not explicitly tuned for BAL detections. Since the present work mainly focuses on the appearing behaviors of C iv BAL complexes, we have excluded these BAL complexes in further analysis. The remaining 236 complexes in 213 MJD pairs of 174 BAL quasars have $BI \neq 0$ only in the later epochs. It is important to note that, out of these 174 BAL quasars, 130 BAL quasars only host the BAL complexes with $BI = 0$ from earlier epochs. While 44 BAL quasars also have BAL complexes with non-zero BI values from both earlier and later epochs hence we have not studied the nature of the variability of these BAL complexes. However, we have included these 44 BAL quasars as they host at least one BAL complex having $BI = 0$ from the earlier epochs.

4.1.2.3 BAL trough properties measurement

For quantifying the properties of BAL troughs associated with the absorption complexes in each BAL quasar spectrum, we measured the EW (in \AA), depth below the normalized continuum, centroid velocity (in km s^{-1}), and width (in km s^{-1}).

The EW in Å and its uncertainty was measured using equations 1 and 2 of Kaspi et al. (2002):

$$EW = \sum_i \left(1 - \frac{F_i}{F_c}\right) B_i, \quad (4.2)$$

and,

$$\sigma_{EW} = \sqrt{\left[\frac{\Delta F_c}{F_c} \sum_i \left(\frac{B_i F_i}{F_c}\right)\right]^2 + \sum_i \left(\frac{B_i \Delta F_i}{F_c}\right)^2}. \quad (4.3)$$

where F_i is the normalized flux with associated error ΔF_i at i th pixel and F_c is the mean of the continuum normalized flux and ΔF_c is the corresponding error on mean. B_i is the width of a wavelength bin measured in units of angstrom. The summation is carried out over the wavelength range set by v_{min} and v_{max} as explained in Section 4.1.2.2.

The centroid velocity, v_{cent} , of a BAL trough is defined as the mean of the normalized flux weighted velocities in the window within v_{min} and v_{max} . The width of a BAL trough, Δv , is taken as the difference between the v_{max} and the v_{min} . The normalized depth, d_{BAL} of each BAL trough is computed by taking the mean of the normalized fluxes inside the window over which BAL features are identified.

4.1.2.4 BAL Variability Measurement

To characterize the variability of BAL features from one epoch to another, we computed the change in the EW and the corresponding uncertainty as:

$$\Delta EW = EW_2 - EW_1 \quad \sigma_{\Delta EW} = \sqrt{\sigma_{EW_2}^2 + \sigma_{EW_1}^2}. \quad (4.4)$$

where the subscripts ‘1’ and ‘2’ correspond to the earlier and later epoch of observation, respectively. Similarly, we computed the fractional EW variations and the corresponding uncertainties using the following equations:

$$\frac{\Delta EW}{\langle EW \rangle} = \frac{EW_2 - EW_1}{(EW_2 + EW_1) \times 0.5} \quad (4.5)$$

$$\sigma_{\frac{\Delta EW}{\langle EW \rangle}} = \frac{4 \sqrt{EW_2^2 \sigma_{EW_1}^2 + EW_1^2 \sigma_{EW_2}^2}}{(EW_2 + EW_1)^2} \quad (4.6)$$

where $\langle EW \rangle$ is the average of the EWs measured between the two epochs; σ_{EW} is the associated uncertainty in the EW values. The fractional change in EW ($\Delta EW / \langle EW \rangle$) depicts the

significance of the change in the absorption compared to the size of changing feature.

Similar to the change in EW, the change in the normalized depths with associated uncertainties of the absorption complexes are also computed as:

$$\Delta d_{\text{BAL}} = d_{\text{BAL},2} - d_{\text{BAL},1} \quad (4.7)$$

$$\sigma_{\Delta d_{\text{BAL}}} = \sqrt{\sigma_{d_{\text{BAL},2}}^2 + \sigma_{d_{\text{BAL},1}}^2}. \quad (4.8)$$

To probe the role of ionizing source, we evaluated fractional flux variation of the line free continuum at 1700 Å ($\Delta F/\langle F \rangle_{1700}$), and corresponding uncertainty using the following equations:

$$\frac{\Delta F_{\text{cont},2}}{\langle F_{\text{cont},1} \rangle} = \frac{F_{\text{cont},2} - F_{\text{cont},1}}{(F_{\text{cont},2} + F_{\text{cont},1}) \times 0.5} \quad (4.9)$$

$$\sigma_{\frac{\Delta F_{\text{cont}}}{\langle F_{\text{cont}} \rangle}} = \frac{4 \sqrt{F_{\text{cont},2}^2 \sigma_{F_{\text{cont},1}}^2 + F_{\text{cont},1}^2 \sigma_{F_{\text{cont},2}}^2}}{(F_{\text{cont},2} + F_{\text{cont},1})^2} \quad (4.10)$$

where $F_{\text{cont}1}$ and $F_{\text{cont}2}$ represent the power-law continuum flux at 1700 Å for the two epochs respectively; $\sigma_{F_{\text{cont}}}$ is the associated flux uncertainty.

Among the set of 236 BAL complexes, 122 BAL complexes in 117 MJD pairs of 94 BAL quasars have shown the appearance of BAL troughs at 5σ and we refer this sample as “*Appearing*” sample. It is important to note that, even though our *Appearing* sample consists of BAL complexes transitioning from non-BAL to BAL at more than 5σ , residual absorption does not account for a non-zero $\text{BI}_{\text{trough}}$ that may exist in a few cases of the earlier epoch spectra. Therefore, to isolate the definite cases of appearing complexes with negligible residual absorption in the earlier epochs, we have performed a visual inspection of the BAL complexes from the *Appearing* sample. Based on this inspection from among the *Appearing* BAL sample, we have identified a pristine sample of 59 BAL complexes in 59 MJD pairs of 43 BAL quasars (hereafter “*Appearing pristine*”).

As discussed in Section 4.1.1, to perform a comparison of our appearing BAL quasars with the disappearing BAL quasars, we made use of the largest sample of 67 disappearing BAL quasars from De Cicco et al. (2018). Using the information provided in the Table A.1 of De Cicco et al. (2018), we assembled the multi-epoch spectra of their P₄ sample and subjected them to the same analysis of the present work (as of Section 4.1.2). In total, we identified 96 disappearing C IV BAL complexes in 65 MJD pairs of 65 BAL quasars. Out of these 96 BAL complexes, our analysis

yielded 63 C iv BAL troughs in 54 BAL quasars, which had undergone a disappearance of their BAL troughs at 5σ . It is important to note that among these 63 disappearing BAL troughs, only 55 BAL troughs in 53 BAL quasars are common with P₄ sample of 73 BAL troughs in 67 BAL quasars (see Table A.2 of De Cicco et al. 2018). Unlike De Cicco et al. (2018), we only included region between 3000–30000 km s⁻¹ blue-ward of quasar’s C iv emission line. In addition, we examined the disappearance of BAL absorption complexes as compared to the analysis of the disappearance of different BAL components considered in De Cicco et al. (2018).

As a result, few disappearing BAL troughs were included as single BAL troughs in our analysis while as multiple in the analysis of De Cicco et al. (2018). Besides, different continuum levels assessed in these two studies may introduce the expected inconsistency in BAL trough detection. Therefore, due to these differences in the analysis of De Cicco et al. (2018) and present work, the discrepancy of 18 BAL troughs from De Cicco et al. (2018)

study and the detection of 8 new BAL troughs in our analysis can be explained. However, to avoid any disagreement based on the difference in the analysis employed in the two studies, we only considered those 55 C iv BAL troughs in 53 BAL quasars which are common in P₄ sample of De Cicco et al. (2018). We refer to this sample as “Disappearing” sample. A summary of the various samples is presented in Table 4.3 and the details of the BAL absorption complexes is presented in Table 4.4.

In Fig. 4.3, we present the distribution of the rest-frame timescale of variability for *Appearing*, *Appearing pristine* and *Disappearing* samples. We used a non-parametric kernel density estimation (KDE, Silverman 1986) with Gaussian kernel of fixed bandwidth for the distributions mentioned above to derive probability density function (PDF) for each. We performed a two-sample K-S test in these distributions and the corresponding p-values of the K-S test are given in top right corner of Fig. 4.3; where the p-value of the K-S test gives the null probability for the two distributions being identical.

It is clear from Fig. 4.3 that the *Disappearing* sample and *Appearing pristine* sample (which is a reliable sub-sample of *Appearing* sample) are found on comparable rest-frame time scales of

Table 4.3: Summary of various subsamples involved in the present study.

Sample Type	Number of complexes	Number of MJD pairs	Number of BAL quasars
<i>Preliminary</i> ^a	614	517	379
<i>Appearing</i> ^b	122	117	94
<i>Appearing pristine</i> ^c	59	59	43
<i>Disappearing</i> ^d	55	53	53

^a BI=0 in Epoch-1 from Shen et al. (2011) or Pâris et al. (2017).

^b BI=0 in Epoch-1 from present analysis and $\Delta EW / \langle EW \rangle > 5 \times \sigma_{\Delta EW / \langle EW \rangle}$.

^c Subsample of *Appearing* BAL sample with definite appearing BAL trough from visual inspection

^d BI=0 in Epoch-2 from present analysis and $\Delta EW / \langle EW \rangle > 5 \times \sigma_{\Delta EW / \langle EW \rangle}$, and common in P₄ of De Cicco et al. (2018).

Table 4.4: Details of the Appearing, Appearing pristine, and Disappearing samples of C IV BAL absorption complexes.

BAL quasar	MJD pair	Δt year	$\Delta F/\langle F \rangle_{1700}$	Δv km s ⁻¹	v_{min} km s ⁻¹	v_{max} km s ⁻¹	ΔEW Å	$\Delta EW/\langle EW \rangle$	Type
SDSS J002028.34–002914.9	51816–56979	4.81	-0.08 ± 0.10	2462.49	-19579.23	-17116.73	1.68 ± 0.28	0.69 ± 0.14	Appearing
SDSS J002028.34–002914.9	51900–56979	4.73	-0.06 ± 0.07	2462.49	-19579.23	-17116.73	2.17 ± 0.19	0.99 ± 0.11	Appearing pristine
SDSS J004022.40+005939.6	52261–55182	2.24	0.15 ± 0.17	6453.83	-9535.71	-3081.88	-9.88 ± 0.63	-1.31 ± 0.06	Disappearing
SDSS J005157.24+000354.7	51812–52201	0.36	-0.18 ± 0.06	3483.76	-10579.55	-7095.78	1.38 ± 0.18	0.68 ± 0.08	Appearing
SDSS J005157.24+000354.7	51812–54800	2.77	-0.42 ± 0.05	3483.76	-10579.55	-7095.78	2.87 ± 0.14	1.03 ± 0.06	Appearing pristine
SDSS J005157.24+000354.7	51812–55451	3.38	-0.37 ± 0.05	3483.76	-10579.55	-7095.78	4.30 ± 0.13	1.23 ± 0.05	Appearing pristine

Note. See Table B.2 for the full version.

observation ($P_{2 \rightarrow 3} = 0.174$).

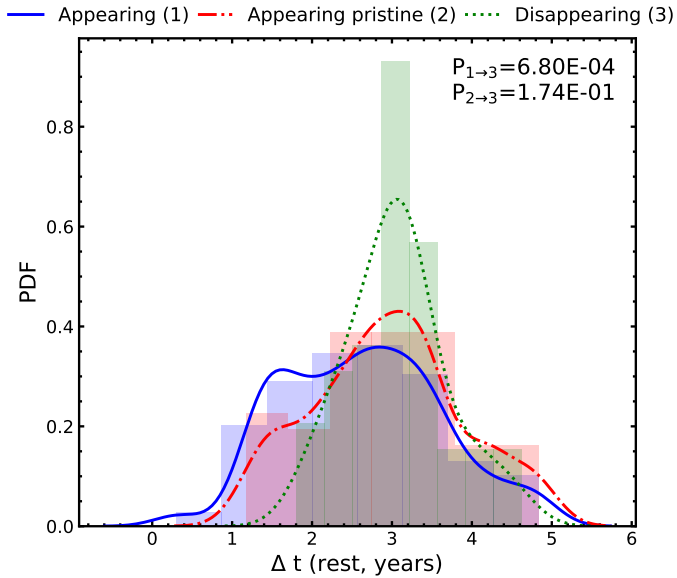


Figure 4.3: Distribution of rest-frame timescale between the two epochs for Appearing (blue), Appearing pristine (red) and Disappearing (green) samples. Overlaid on the data are the PDFs derived with KDE using Gaussian kernel of fixed bandwidth for Appearing (solid blue), Appearing pristine (dashed red) and Disappearing (dotted green) samples. The p -values computed using the K-S test between Appearing and Disappearing ($P_{1 \rightarrow 3}$), and Appearing pristine and Disappearing ($P_{2 \rightarrow 3}$) are given in top right corner.

4.1.3 Results

In this part, we present the comparison of quasar intrinsic parameters (Section 4.1.3.1), BAL trough parameters (Section 4.1.3.2), parameters associated with the continuum (Section 4.1.3.3), and reddening parameter (Section 4.1.3.4) among the 122 *Appearing*, 59 *Appearing pristine*, and 55 *Disappearing* C IV BAL complexes associated with 94, 43 and 53 BAL quasars respectively.

4.1.3.1 Comparison of quasar intrinsic properties

It is known that accretion disk winds are very much sensitive to the Eddington ratio, defined as the ratio of bolometric luminosity to the Eddington luminosity which further depends on the black hole (BH) mass (Proga & Kallman 2004). Therefore, the BAL quasar properties are expected to depend on these parameters (see Laor & Brandt 2002; Ganguly et al. 2007). To probe whether the nature of the ionizing sources in the appearing and disappearing BAL quasars are similar, we in Fig. 4.4 compare the quasar parameters such as (a) bolometric luminosity, (b) BH mass, (c) Eddington ratio and (d) i-band absolute magnitude for *Appearing*, *Appearing pristine*, and *Disappearing* BAL quasars. We adopt these quasar properties from the study of Shen et al. (2011). We wish to emphasize that as the quasar intrinsic parameters are adopted from the Shen et al. (2011) catalog, the intrinsic parameters are reflective of the physical conditions in the first epoch of spectroscopic observation.

From Fig. 4.4 (a, b and c), we note that the distributions of bolometric luminosity, BH mass, and absolute i-band magnitude for *Disappearing* BAL quasars differ significantly from the *Appearing* and *Appearing pristine* BAL quasars with p-values of K-S test for the *Appearing* and *Disappearing* ($P_{1\rightarrow3}$) and *Appearing pristine* and *Disappearing* ($P_{2\rightarrow3}$) BAL samples consistent with less than 5%. This implies that the *Disappearing* BAL quasars are low luminous, have lower BH mass, and fainter compared to the *Appearing* BAL quasars. However, Fig. 4.4 (c) shows no difference in the Eddington ratio distribution of *Appearing* and *Disappearing* ($P_{1\rightarrow3} \sim 0.05$) and *Appearing pristine* and *Disappearing* BAL quasars ($P_{1\rightarrow3} \sim 0.14$), suggesting that central environments of *Appearing* and *Disappearing* BAL quasars are alike.

It is worth noting that the Eddington ratio's calculations involve the measurements of black hole masses, which further requires the estimations of full width at half maximum (FWHM) of quasar emission lines. Since our sources are at high redshifts (with median $z_{em} \sim 2$), the BH mass estimates are predominately based on C iv emission line (see Shen et al. 2011). The C iv emission lines exhibit remarkable displacements towards the blue side (Gaskell 1982), possibly due to strong outflows; hence the measurements of FWHM and virialized velocity dispersion are inaccurate in such cases. As a result, C iv based BH mass estimations are systematically biased compared to the BH mass derived from other low-ionization quasar emission lines (such as H β and Mg II). Therefore, any conclusion inferred based on the Eddington ratio and BH mass needs to be handled with caution. To be conservative, we will not interpret the results based on the BH mass and Eddington ratio in this study.

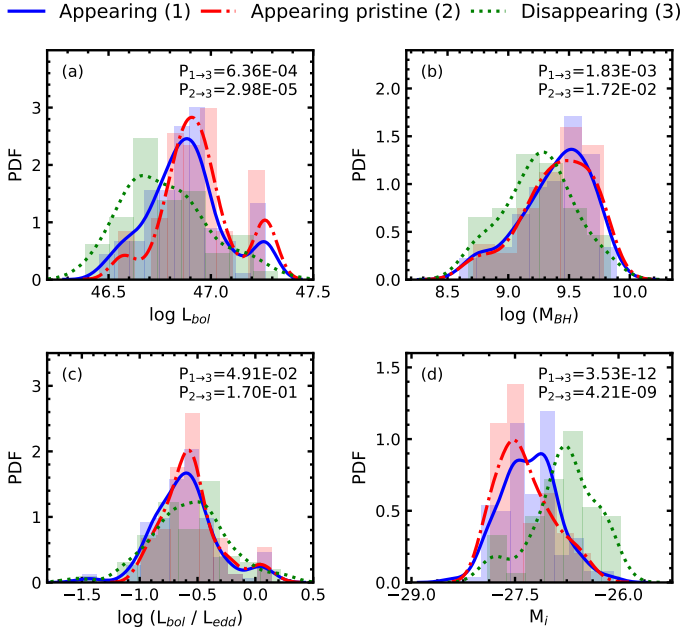


Figure 4.4: Distribution of (a) bolometric luminosity, (b) black hole mass, (c) Eddington ratio and (d) i-band absolute magnitude for Appearing (blue), Appearing pristine (red) and Disappearing (green) samples are drawn. The PDFs over the data sets generated using Gaussian KDEs for Appearing (solid blue), Appearing pristine (dashed red) and Disappearing (dotted green) samples are shown in each panel. The estimated p-values of the K-S test between Appearing and Disappearing ($P_{1 \rightarrow 3}$), and Appearing pristine and Disappearing ($P_{2 \rightarrow 3}$) are shown in the top right corner of each panel.

4.1.3.2 Comparison of BAL-profile Properties

In this section, we compare the BAL trough properties such as the average EW ($\langle EW \rangle$), average normalized trough depth ($\langle d_{BAL} \rangle$), change in normalized trough depth (Δd_{BAL}), maximum/minimum velocity of outflow, and trough width (Δv) among the *Appearing*, *Appearing pristine* and *Disappearing* samples. In Fig. 4.5, we show the distributions of these parameters. The PDFs to the distributions are derived by applying a Gaussian KDE and are shown in each panel of Fig. 4.5. The p-values computed using the K-S test for two pairs of distributions i.e., *Appearing* and *Disappearing* ($P_{1 \rightarrow 3}$) and *Appearing pristine* and *Disappearing* ($P_{2 \rightarrow 3}$) are also shown in each panel. From Fig. 4.5 (a, f, g, and h), it can be discerned that the distributions of $|\Delta EW|$, v_{min} , v_{max} and Δv are similar for *Appearing*, *Appearing pristine* and *Disappearing* samples as can also be concluded from the p-values mentioned in each panel.

We see in Fig. 4.5 (b and c), the distribution of $|\Delta EW / \langle EW \rangle|$ and $\langle EW \rangle$ are similar for *Appearing pristine* and *Disappearing* samples (with $P_{2 \rightarrow 3} < 5\%$ for both the distributions), while the distribution of $|\Delta EW / \langle EW \rangle|$ and $\langle EW \rangle$ differ in case of *Appearing* and *Disappearing* ($P_{1 \rightarrow 3} > 5\%$) samples. Since by definition, *Appearing pristine* BAL sample is the conservatively reliable subsample of *Appearing* BAL sample with systematically larger values of $|\Delta EW / \langle EW \rangle|$ of BAL complexes, we conclude from Fig. 4.5 (b and c) that the absolute fractional variation of EW and

average EW are similar in appearing and disappearing BAL quasars.

It is worth noting from Fig. 4.5 (d and e), the distributions of $\langle d_{\text{BAL}} \rangle$ and $|\Delta d_{\text{BAL}}|$ for *Disappearing* diverges substantially from both *Appearing* ($P_{1 \rightarrow 3}$) and *Appearing pristine* ($P_{2 \rightarrow 3}$) samples with *Disappearing* sample peaking towards the larger value of $\langle d_{\text{BAL}} \rangle$ and $|\Delta d_{\text{BAL}}|$, implying *Disappearing* BALs are narrower compared to *Appearing* and *Appearing pristine* BAL complexes.

Further, using Spearman correlation test, we searched for correlations between $\Delta \text{EW} / \langle \text{EW} \rangle$ and other BAL-trough parameters (i.e $\langle \text{EW} \rangle$, $\langle d_{\text{BAL}} \rangle$, Δd_{BAL} , v_{min} , v_{max} , and Δv) for the *Appearing*, *Appearing pristine* and *Disappearing* samples of BAL quasars (Lundgren et al. 2007; Gibson et al. 2008; Capellupo et al. 2011; Filiz Ak et al. 2013; Vivek et al. 2014; De Cicco et al. 2018). Our analysis shows no significant correlation between $\Delta \text{EW} / \langle \text{EW} \rangle$ and BAL-trough parameters, $\langle \text{EW} \rangle$, $\langle d_{\text{BAL}} \rangle$, v_{min} , v_{max} , and Δv for *Appearing*, *Appearing pristine*, and *Disappearing* samples. Although previous BAL variability studies have found significant correlations between $\Delta \text{EW} / \langle \text{EW} \rangle$ and BAL-trough parameters, the lack of significant correlation between these parameters in this study may be because this study focuses on the extreme cases of BAL variability, which only spans a narrow range of $\Delta \text{EW} / \langle \text{EW} \rangle$. However, we note that there is a very strong positive and highly significant ($> 99.9\%$) correlation between $\Delta \text{EW} / \langle \text{EW} \rangle$ and Δd_{BAL} for all the three BAL samples.

4.1.3.3 Comparison of continuum properties

As discussed in Section 4.1, change in the photo-ionizing conditions inside the central engine can cause the variation in the optical depths of ions in the BAL clouds and therefore, can contribute to the large change in the EW of BAL troughs. Previous studies based on the coordinated variabilities of BAL troughs of multiple ions at the same velocity (Filiz Ak et al. 2013; Wang et al. 2015; McGraw et al. 2017; Lu et al. 2018) and of the same ion at different velocities (Capellupo et al. 2012; De Cicco et al. 2018; Rogerson et al. 2018) confirmed that similar mechanism is accountable for such coordinated variations of the BAL troughs. The transverse motions of the BAL clouds across the LOS are less likely to explain such variation unless the BAL outflows are confined to smaller distances relative to the ionizing source. In addition, a significant correlation between the change in continuum and change in absorption strength of the BAL troughs (He et al. 2015; Lu et al. 2018; Vivek 2019; Lu & Lin 2019) supports the ionization driven scenario of BAL trough variations. He et al. (2015) found that in 60.5 percent of their BAL troughs, the decrease in EW is accompanied by the brightening of the continuum, and spectra turned bluer during this phase. The study of Wang et al. (2015) showed that the emergence and disappearance of BAL troughs

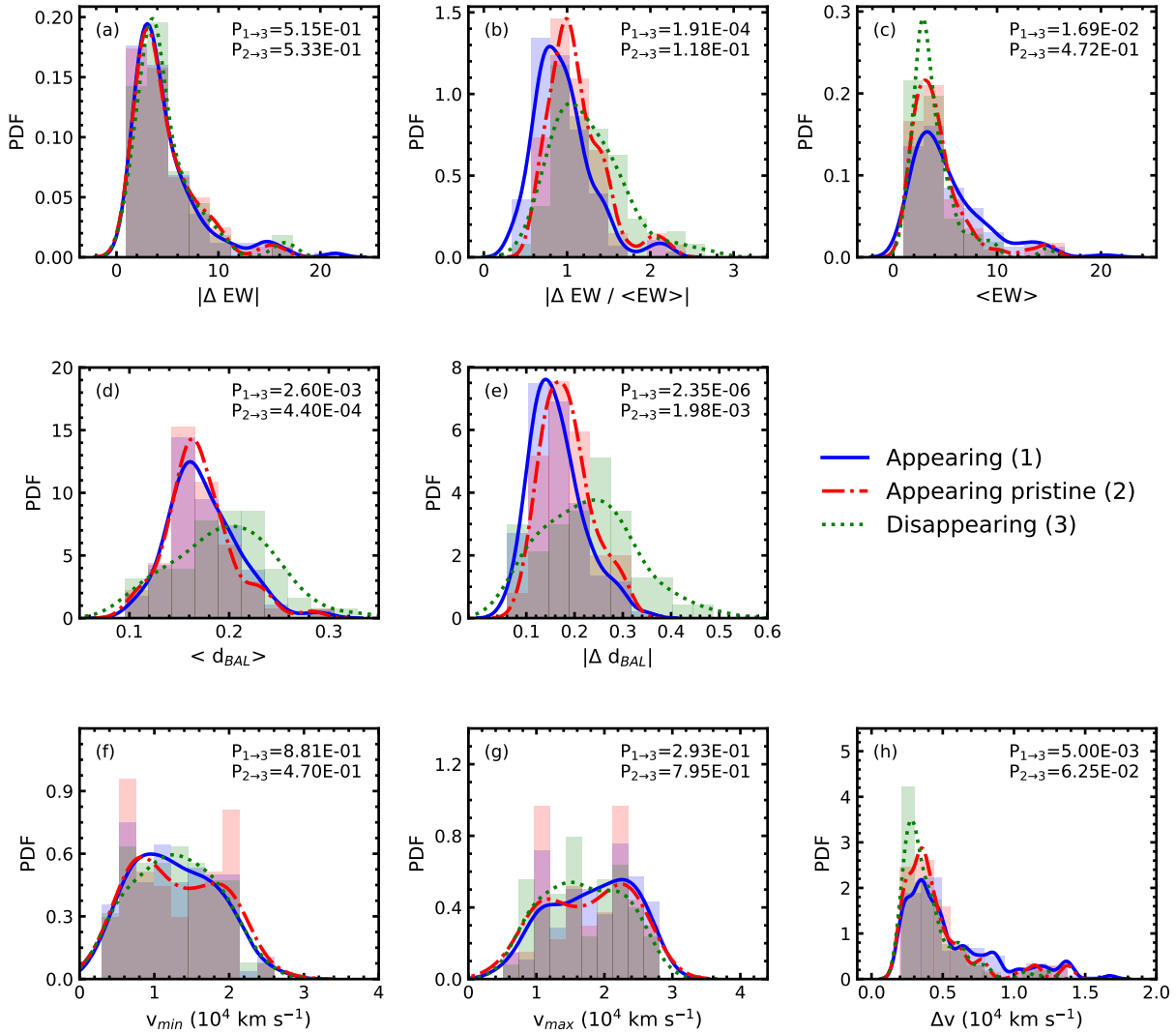


Figure 4.5: Distribution of (a) absolute change in EW, (b) absolute fractional change in EW, (c) average EW, (d) average normalized BAL depth, (e) absolute change in normalized BAL depth, (f) minimum outflow velocity, (g) maximum outflow velocity, and (h) width of BAL trough for Appearing (blue), Appearing pristine (red) and Disappearing (green) BAL complexes. On top of each distribution in each panel are the PDFs derived with Gaussian kernel KDE of similar bandwidth for Appearing (solid blue), Appearing pristine (dashed red) and Disappearing (dotted green) samples. The p-values derived from the K-S test between Appearing and Disappearing ($P_{1 \rightarrow 3}$), and Appearing pristine and Disappearing ($P_{2 \rightarrow 3}$) are mentioned at the top right corner of each panel.

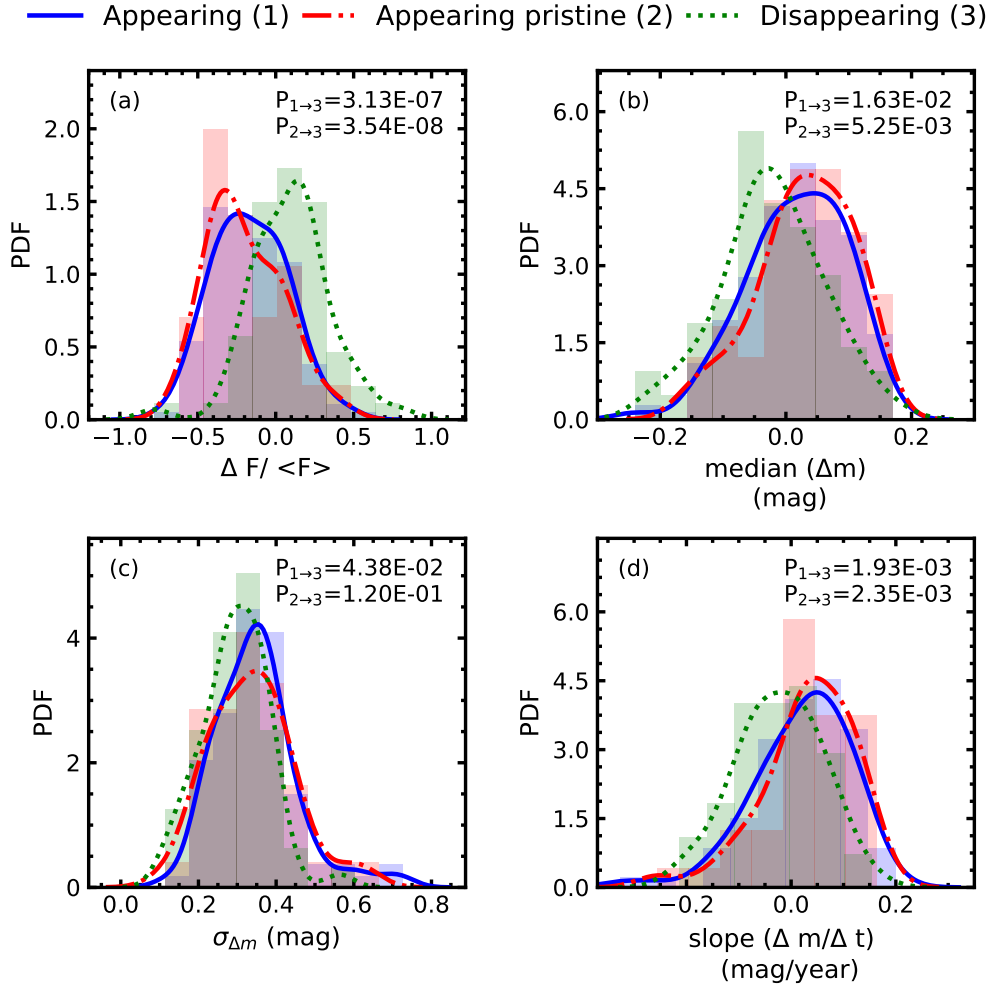


Figure 4.6: Distribution of (a) change in continuum flux at 1700 \AA (b) median of change in V-band magnitudes, (c) standard deviation of change in V-band magnitudes and (d) slope of change in V-band magnitude with time for Appearing (blue), Appearing pristine (red) and Disappearing (green) samples. Overlaid on the three distributions are the PDFs constructed with KDE using Gaussian kernels of same bandwidth for Appearing (solid blue), Appearing pristine (dashed red) and Disappearing (dotted green) samples. The p -values of the K-S test applied on Appearing and Disappearing ($P_{1 \rightarrow 3}$), and Appearing pristine and Disappearing ($P_{2 \rightarrow 3}$) are labeled at the top right corner of each panel.

are accompanied by the dimming and brightening of the continuum. The authors suggested that in such an extreme scenario where the variability amplitude of the BAL trough is very high, the ionic column density is highly sensitive to ionizing radiation. Similarly, He et al. (2017) found that in 80 percent of BAL QSOs, the trough variabilities are governed by the change in the ionizing continuum. However, the trends of BAL variabilities, whether it decreases or increases in response to the change in the continuum, depends on the ionization parameter of the absorbers. The study of Vivek (2019) revealed that the correlation between the continuum radiation and fractional EW variation strengthen when line saturation effects in BAL troughs are eliminated.

To probe whether the appearance or disappearance of BAL troughs is caused by the fluctuations produced in the continuum emission coming from the central environment, we used the variation of the continuum flux at 1700 Å ($\Delta F/\langle F \rangle_{1700}$) as a proxy for the ionizing continuum fluctuations from one epoch to another. Also, to further confirm the effect of fluctuating ionizing continuum on the appearance and disappearance of BAL troughs, we searched for the Johnson’s V magnitude light curves from the Catalina Real-Time Transient Survey (CRTS; Drake et al. 2009) for our appearing and disappearing samples (see Vivek et al. 2014; Welling et al. 2014; Vivek et al. 2016). The light curves obtained for our sources were taken between April 2005 to December 2013, and each object necessarily has at least one spectroscopic epoch intercepting the photometric time-span over which the light curve is obtained. To quantify the continuum variation from the CRTS light curves, we adopted the procedure used in the study of Vivek et al. (2014). On a given night, CRTS provides four observing frames 10 min. apart for each object. Since we are dealing with long term continuum variations, similar to Vivek et al. (2014), we averaged the V band magnitudes of these four frames to eliminate the large dispersion in the light curves. We measured the V-band magnitude difference (Δm) among all possible photometric MJD pairs (Δt) available in each source’s light curve. We fitted an error-weighted least-square straight line in Δm – Δt space and obtained the slope ($\Delta m/\Delta t$). To mark the amplitude of continuum variation, we used the median and standard deviation ($\sigma_{\Delta m}$) of Δm values, and slope of Δm – Δt plane ($\Delta m/\Delta t$) from all light curves.

Fig. 4.6 gives the distribution of $\Delta F/\langle F \rangle_{1700}$, median (Δm), $\sigma_{\Delta m}$ and $\Delta m/\Delta t$ for *Appearing*, *Appearing pristine* and *Disappearing* samples. The p-values of the K-S test applied between *Appearing* and *Disappearing* ($P_{1 \rightarrow 3}$), *Appearing pristine* and *Disappearing* ($P_{2 \rightarrow 3}$) samples are marked on the top right of each panel. The distributions of $\Delta F/\langle F \rangle_{1700}$, median (Δm), and $\Delta m/\Delta t$ for the *Appearing* and *Disappearing* samples are clearly separated and are distributed on either side of zero

(Fig. 4.6 a, b, and d). However, the distributions of $\sigma_{\Delta m}$ in Fig. 4.6 (c) for *Appearing*, *Appearing pristine*, and *Disappearing* samples show no considerable difference implying that the amplitude of magnitude variations for the BAL appearance and disappearance are similar. The distributions of $\Delta F/\langle F \rangle_{1700}$ for *Appearing* and *Appearing pristine* samples significantly differ from the *Disappearing* sample (Fig. 4.6 a). From the overlaid PDF curves to each distribution, it is evident that the appearance of BAL troughs is more likely to be accompanied by a decrease in continuum flux, whereas the disappearance of BAL troughs is accompanied by an increase in continuum flux. This is in agreement with the study of (Wang et al. 2015). Also, the significant difference in Fig. 4.6 (b and d) for median (Δm) and $\Delta m/\Delta t$ distributions of *Appearing*, *Appearing pristine* and *Disappearing* samples further supports the anti-correlation between continuum changes and BAL trough changes. The PDF curves in Fig. 4.6 (b and d) show that the increase in V-band magnitude facilitates the appearance of BAL troughs while a decrease in V-band magnitude supports the disappearance of BAL troughs. It is interesting to note that the distributions of $\Delta F/\langle F \rangle_{1700}$ are markedly different and well separated among the *Appearing*, *Appearing pristine*, and *Disappearing* samples compared to the distributions of median (Δm), and $\Delta m/\Delta t$. The $\Delta F/\langle F \rangle_{1700}$ were estimated from the same spectra that were used to measure the $\Delta EW/\langle EW \rangle$ and hence span the same time interval for the continuum and BAL trough measurements. On the other hand, the values of median (Δm), and $\Delta m/\Delta t$ are measured using CRTS light curves that do not span the same time interval of observations over which transitions in the BAL troughs have occurred. Additionally, as magnitudes are defined in the logarithmic unit of flux values, median (Δm), and $\Delta m/\Delta t$ distributions for the *Appearing* and *Disappearing* samples are not as detached as the $\Delta F/\langle F \rangle_{1700}$ distribution.

To investigate in what manner and amount do the fluctuation in the ionizing parameters correlates with the fractional variation of EW, we searched for the correlations using the Spearman correlation test between the $\Delta EW/\langle EW \rangle$ and these continuum parameters. We did not find any significant correlation between $\Delta F/\langle F \rangle_{1700}$ and $\Delta EW/\langle EW \rangle$ for either of our subsamples. The absence of correlation between the $\Delta EW/\langle EW \rangle$ and the fluctuating continuum is possibly expected since we are only dealing with the extreme cases, unlike the previous studies.

We also investigated the nature of variation of spectral index estimated from the reddened power law fitting (See Section 4.1.2.1) on each spectrum of appearing and disappearing BAL quasars. In Fig. 4.7, we present the distribution of change in spectral index ($\Delta\alpha$) from one epoch to another for *Appearing*, *Appearing pristine* and *Disappearing* samples. Interestingly, we found $\Delta\alpha$ distribution of *Disappearing* sample is remarkably different from *Appearing* and *Appearing*

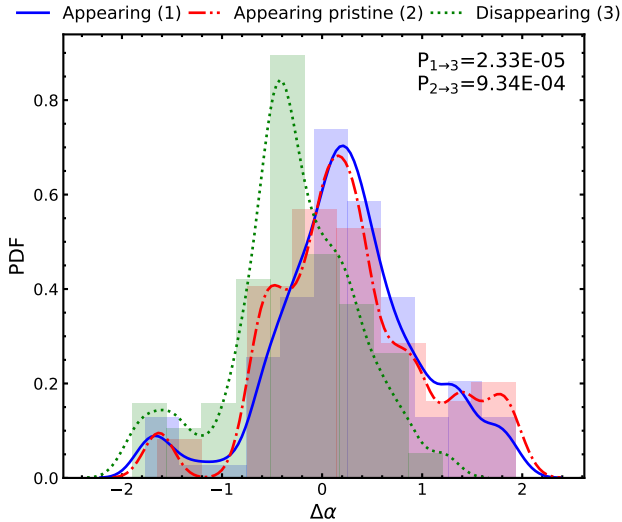


Figure 4.7: Distribution of change in spectral index for *Appearing* (blue), *Appearing pristine* (red) and *Disappearing* (green) samples. On top of these three distributions in each panel are the PDFs generated with KDE taking Gaussian kernels of similar bandwidth for *Appearing* (solid blue), *Appearing pristine* (dashed red) and *Disappearing* (dotted green) samples. The p -values of the K-S test estimated for *Appearing* and *Disappearing* ($P_{1\rightarrow3}$), and *Appearing pristine* and *Disappearing* ($P_{2\rightarrow3}$) are given at the top right corner.

pristine samples (note $P_{1\rightarrow3}$ and $P_{2\rightarrow3}$ of Fig. 4.7). It is clear from Fig. 4.7 that the $\Delta\alpha$ values for the *Disappearing* BAL quasars are distributed below zero (i.e., $\Delta\alpha < 0$ and spectral hardening), while for the *Appearing* and *Appearing pristine* BAL quasars, they are distributed above zero (i.e., $\Delta\alpha > 0$ and spectral softening). This result, together with the previous observation that BAL disappearance/appearance is accompanied by continuum brightening/dimming, implies that the quasars considered in this study follow the "bluer when brighter" trend for continuum variations. The bluer-when-brighter trend for continuum in quasars has been extensively explored in the past studies (Schmidt et al. 2012; Sun et al. 2014; Guo & Gu 2016) and the changing mass accretion rate around the central object could possibly be accountable for this trend (Sakata et al. 2011; Ruan et al. 2014).

Clearly, the trends observed for different continuum variability parameters and spectral index changes are consistent with each other. The clear separation in the distribution of these parameters between the *Appearing* and *Disappearing* samples points to the significant role of ionization in BAL emergence/disappearance.

4.1.3.4 Comparison of reddening parameters

Using a sample of 2099 SDSS BAL quasars, the study of Zhang et al. (2014) revealed that the outflow velocity and strength moderately correlate with the slope of the infrared continuum (β_{NIR}) which acts as a good indicator of hot dust emission. They suggested a BAL-dust scenario where dust being intrinsic to BAL outflows may contribute to the acceleration when subjected to the

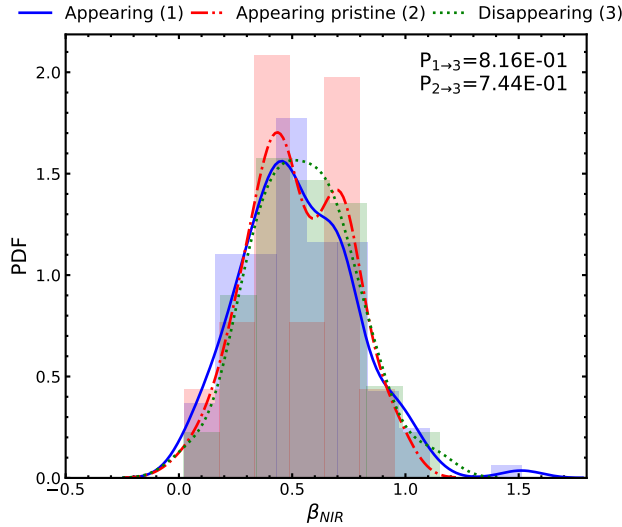


Figure 4.8: Distribution of slope of IR continuum for Appearing (blue), Appearing pristine (red) and Disappearing (green) samples. On top of these three distributions in each panel are the PDFs generated with KDE taking Gaussian kernels of similar bandwidth for Appearing (solid blue), Appearing pristine (dashed red) and Disappearing (dotted green) samples. The p -values derived from the K - S test between Appearing and Disappearing ($P_{1\rightarrow 3}$), and Appearing pristine and Disappearing ($P_{2\rightarrow 3}$) are mentioned at the top right corner.

central radiation field. Besides, the study of Gaskell et al. (2016) showed that the SED of BAL and non-BAL quasar do not intrinsically differ but apparently differ due to the dust.

In this section, to probe whether dust is intrinsic to the BAL outflows, we investigate the nature of variation of the infrared fluxes between the *Appearing* and *Disappearing* samples (Vivek et al. 2016; Tuccillo et al. 2017). These sources, having undergone an extreme transition of BAL troughs, provide an ideal opportunity to verify the role of dust associated with the BAL outflows. We used the Wide-field Infrared Survey Explorer (WISE; Wright et al. 2010) catalog to search for the infrared counterparts of our BAL samples within $3''$ from the optical position of our appearing and disappearing BAL quasars. WISE survey maps the sky in four bands W1, W2, W3, and W4 with center wavelengths at 3.4, 4.6, 12, and $22 \mu\text{m}$ respectively. In this study, we only used reliable measurements of W1, W2, and W3 magnitudes as the errors on W4 magnitudes for a majority of the sources were not available. The median redshifts of our BAL quasar samples are close to 2, hence covers a near-infrared (NIR) range of $1 - 4 \mu\text{m}$ in the rest-frame wavelengths of W1, W2, and W3 bands. For a typical quasar SED, the emission from the dust dominates beyond $3 \mu\text{m}$. To characterize the hot dust emission, several studies have used SDSS r -WISE W4 for high redshifts objects (Vivek et al. 2016). Since for the majority of quasars in our sample, reliable measurements of W4 magnitudes were not available, and W1, W2, and W3 magnitudes were not good representatives of hot dust emissions, we did not use SDSS r -WISE W4 to measure the excess of hot far-infrared emission relative to the UV emissions.

Similar to Zhang et al. (2014), we used the β_{NIR} parameter to confirm the role of dust in BAL

quasars that have undergone a complete appearance or disappearance of their BAL troughs. We converted the WISE W1, W2, and W3 magnitudes to monochromatic luminosities and fitted a power law ($L_\lambda \propto \lambda^{\beta_{\text{NIR}}}$) in the rest-frame NIR SED of each BAL quasar in *Appearing*, *Appearing pristine* and *Disappearing* samples. The distributions β_{NIR} are shown in Fig. 4.8 for *Appearing*, *Appearing pristine*, and *Disappearing* samples. It is evident from the figure that the β_{NIR} distribution is the same for appearing and disappearing BAL quasars implying that dust does not have any significant role in causing the extreme variations of BAL troughs. Note that Vivek et al. (2016) also did not find any difference in the r–W4 distributions of the parent radio-detected BAL sample of 60 objects compared to a sub-sample of 6 radio-detected transient BAL quasars hinting no clear role of dust in the transient BAL quasars.

4.1.4 Discussion

The ionization state and covering fraction of the absorbing gas are the two parameters that determine the strength of absorption lines in quasars. Any variation in these parameters can result in changes in the absorption line profile. The BAL variability caused by changes in these two key parameters can be described by the following two scenarios: (i) change in the number of ionizing photons impinging on the absorbing clouds (IC scenario), and/or (ii) transverse motion of the gas cloud along the LOS of the observer (TM scenario).

Many previous studies on BAL variability, based on the (i) lack of correlation between the changes in ionizing continuum and absorption strength and (ii) variation in only a portion of BAL trough profile, support TM scenario (Lundgren et al. 2007; Gibson et al. 2008; Hamann et al. 2008; Capellupo et al. 2011, 2013; Vivek et al. 2014; Yi et al. 2019). On the other hand, with an anti-correlation between the varying continuum and absorption strength, many previous studies support IC scenario (Barlow 1994; Capellupo et al. 2012; He et al. 2015; Wang et al. 2015; He et al. 2017; Rogerson et al. 2018; Lu et al. 2018; Huang et al. 2019; Lu & Lin 2019; Vivek 2019). The coordinated variation of different velocity BAL troughs of same species, or the coordinated variation of same velocity BAL troughs of different species point to the IC scenario as the main driver of BAL variations (Filiz Ak et al. 2013; Wang et al. 2015; Rogerson et al. 2018). By definition, BAL appearance and disappearance mean a coordinated variation of BAL troughs over a range of velocities, and it is expected that the IC scenario has a significant role in driving these variations. There are also many cases where both the IC and TM scenarios are held responsible for BAL trough variations (Capellupo et al. 2011, 2012, 2013; Filiz Ak et al. 2012, 2013; McGraw

et al. 2017).

In this study, we contrasted the properties of two samples of BAL quasars that have shown either appearance or disappearance of BAL troughs between two spectroscopic observations. The three main results from our analysis are the following: (i) the *Appearing* sample of BAL quasars is found to be more luminous as compared to the *Disappearing* sample of BAL quasars (Fig. 4.4 a and d), (ii) the distribution of BAL trough depths for the *Appearing* and *Disappearing* samples are different with the *Disappearing* BAL sample having deeper troughs as compared to the *Appearing* BAL sample (Fig. 4.5 d), and (iii) the quasar continuum brightened in the case of *Disappearing* sample of BAL quasars whereas it dimmed in the case of *Appearing* sample of BAL quasars (Fig. 4.6). We also rule out the role of dust intrinsic to the BAL clouds in causing the observed BAL variability.

The ionization parameter ($\log U$) is the key parameter that controls the ionic response of any ion (Wang et al. 2015). Fig. 4 of Hamann et al. (2001) shows the ion fraction of several ions as a function of the ionization parameter. The fraction of C iv first increases, then reaches a peak, and decreases later as the ionization parameter increases. Depending on the ionization parameter, the ionic response to a change in ionization parameter can be both positive and negative. The negative ionic response (i.e., BAL disappearance accompanied by continuum brightening and vice versa) found in this study shows that the ionization parameter of these outflows is towards the right side of the peak ionization parameter (i.e., $\log U = -2$). BAL appearance can be understood as the case where the C iv column density in the first epoch is too low to be detected (i.e., high U), but as the continuum dims (i.e., a decrease in U), recombination of C v to C iv increases the C iv column density resulting in the BAL appearance. Similarly, BAL disappearance occurs as a gas cloud in the low U regime is pushed to the high U regime due to an increase in the continuum. If we assume that the density of these absorbers is similar on average, our finding that the *Appearing* BAL quasars are brighter than the *Disappearing* BAL quasars during their earlier epochs supports the fact that the ionization parameter of the *Appearing* BAL quasars is higher compared to the *Disappearing* BAL quasars before the BAL transition event. It is known that a minimum threshold of C iv column density is required for the BAL to be detected. For a particular total hydrogen column density, Fig. 11 of Wang et al. (2015) shows that we can define two ionization parameters corresponding to the peak and the threshold ionic column densities. In the case of disappearing BALs, the ionization parameter in the earlier epoch can only be distributed between these two ionization parameters. However, in the case of appearing BALs, the ionization parameter in the earlier epoch

can be anywhere beyond the threshold ionization parameter. If we assume that the continuum changes between the two epochs are similar for the *Appearing* and *Disappearing* BAL samples (a valid assumption as we have similar distributions of $\sigma_{\Delta m}$), the difference in the distribution of initial ionization parameters around the threshold ionization parameter may explain the difference in the distribution of $\langle d_{\text{BAL}} \rangle$ and Δd_{BAL} distributions.

The changing ionizing continuum has a negligible effect on the variabilities of saturated BAL troughs. The role of change in covering fraction in response to the varying BAL strength is critical in such cases (Hamann et al. 2008; Capellupo et al. 2014; McGraw et al. 2017; Vivek 2019). Since the average depth of our BAL troughs for both the appearing and disappearing BAL samples are less than 0.4 (see Fig. 4.5 d), it is reasonable to say that the effect of line saturation may be insignificant in our study (see Vivek 2019).

If BAL variability is driven by variations in the intrinsic dust content of the absorbing gas, we expect a difference in the distribution of the hot dust emission properties between the *Appearing* and *Disappearing* samples. As we do not see any difference in the distribution of β_{NIR} parameter between the two samples, we conclude that dust emission is similar for the *Appearing* and the *Disappearing* samples. Consequently, the dust driven BAL variability scenario can be ruled out.

Conversely, it is possible that the entire BAL cloud could have moved into our LOS between the two spectroscopic epochs (TM scenario). In such a scenario, it is impossible to explain the observed connection between the BAL appearance/disappearance and continuum variations. Therefore, based on our findings presented in this study, we conclude that changes in the ionization state of the absorbing gas are the primary driver of extreme variations in BAL troughs.

4.1.5 Conclusions

Below are the point-wise conclusions of our analysis based on the three subclasses of extreme variable BAL quasars:

1. We have isolated a set of 94 appearing broad absorption line quasars based on the comparison of SDSSDR-7, SDSSDR-12, and SDSSDR-14 quasar catalogs.
2. The *Appearing pristine* and *Disappearing* BAL quasars are predominately observed on similar timescales (Fig. 4.3).

3. Our analysis shows that the *Appearing* and *Appearing pristine* BAL quasars are brighter compared to *Disappearing* BAL quasars (Fig. 4.4 a and d).
4. The distributions ΔEW , $\langle EW \rangle$, v_{min} , v_{max} and Δv are similar for *Appearing*, *Appearing pristine* and *Disappearing* BAL quasars, while *Disappearing* BAL troughs are deeper compared to *Appearing*, *Appearing pristine* BAL troughs (see Fig. 4.5)
5. Based on the distributions of $\Delta F/\langle F \rangle_{1700}$, median (Δm), and $\Delta m/\Delta t$, our analysis shows the appearance of BAL troughs is accompanied by the dimming of the continuum flux while the disappearance of BAL troughs is accompanied by the brightening of the continuum flux (see Fig. 4.6 a, b, and d). The amount of continuum variation in appearance and disappearance of BAL troughs is similar as can be inferred from the similar distribution of $\sigma_{\Delta m}$ in *Appearing*, *Appearing pristine*, and *Disappearing* samples (Fig. 4.6 c).
6. We report a significant difference in the distribution of change in spectral index of *Appearing* and *Appearing pristine* compared to *Disappearing* BAL quasars, with the distribution of appearing samples (i.e., *Appearing* and *Appearing pristine*) shifted towards the spectral softening as compared to *Disappearing* sample which show spectral hardening (Fig. 4.7). The continuum variations are in agreement with the well known bluer-when-brighter trend seen in normal quasars, which hints to the fluctuations of the ionizing radiations are caused due to changes in the central accretion processes.
7. Our analysis also reveals that the distributions of slope of IR continuum are similar for the appearing and the disappearing samples (Fig. 4.8), ruling out the dust outflow scenario proposed by Zhang et al. (2014).
8. Our findings support the scenario where changes in the ionizing conditions of the absorbing gas are the primary driver of extreme variations of BAL troughs.

Additional spectra for our sample of appearing BAL quasars are currently being obtained in our ongoing spectral variability campaign using 2m class telescopes. Future spectroscopic monitoring of these objects will help to put further constraints on the exact nature of variability in these sources and understand the dynamical evolution of BAL outflowing clouds.

Chapter 5

The relative role of kinetic-mode and radiative-mode of AGN feedback

The rapid intensity fluctuation on hour-to-minute-like time-scales on the entire range of the electromagnetic spectrum is a ubiquitous feature of active galactic nuclei (AGNs). The measurement of intra-night optical variability (INOV) or microvariability is a unique, powerful tool for constraining the physical parameters such as the size of the central region, black hole mass of the AGNs (Urry & Padovani 1995). This tool has been extensively applied in literature in the optical waveband to probe the nature and physical cause of such variations explicitly in RQ, RL, and blazar subclass of the AGNs (Carini et al. 1990, 1992; Gopal-Krishna et al. 1995; Stalin et al. 2004; Gupta & Joshi 2005; Gopal-Krishna et al. 2011; Joshi et al. 2011; Goyal et al. 2012, 2013; Joshi & Chand 2013; Kumar et al. 2016, 2017; Ojha et al. 2020). The major outcome of all these studies suggests that the typical INOV duty cycle (DC) of the RQ AGNs is $\sim 10\%$ (Romero et al. 2002; Gopal-Krishna et al. 2003; Stalin et al. 2004; Gupta & Joshi 2005; Joshi et al. 2011; Kumar et al. 2017), while in case of the RL AGNs, the INOV DC is $\sim 30\text{--}40\%$ (Sagar et al. 2004; Stalin et al. 2005; Goyal et al. 2012, 2013; Gopal-Krishna & Wiita 2018). In the RL AGNs and blazars, the strong INOV can be produced due to the fluctuations caused by the shock accelerated turbulence in the jets (Wagner & Witzel 1995; Gopal-Krishna et al. 2011). However, in RQ AGNs, the mild fluctuations in the intensity can arise from the hot spots and flaring in the accretion disk (Mangalam & Wiita 1993). Interestingly, the blazar subclass of the AGNs is characterized with strong, radio sources exhibiting flat radio spectrum, rapid flux variability with strong INOV (Gopal-Krishna & Wiita 2018, and references therein), bright, compact radio cores with aligned one-sided parsec-

scale jets. In this chapter, using INOV as a tool, we first investigate in Section 5.1 the blazar nature of 10 rare RL BAL quasars exhibiting blazar-type signatures, namely a flat/inverted radio spectrum and a large radio polarization. Secondly, we contrast the INOV properties of this blazar-like BAL quasar sample with a controlled (matching in magnitude and redshift) sample of normal blazars in Section 5.2 to probe whether or not the BAL quasars with outflows closely aligned along the relativistic jet axis are regarded as blazars' manifestations? The results and conclusions presented in the first part of this chapter (Section 5.1) are published in MNRAS Letters (Mishra et al. 2019).

5.1 Are there broad absorption-line blazars?

Blue-shifted broad absorption-lines seen in the optical/UV spectra (Weymann et al. 1991) of $\sim 20\%$ of quasi-stellar objects (QSOs) are interpreted as the covering factor of the BAL outflow in the orientation based models, or as the duration of BAL phase, in a QSOs life in the evolutionary models (e.g., Pâris et al. 2012, and references therein). The outflow speed is found to be as high as $0.3c$ (e.g., Hamann et al. 2018). In $\sim 1/7$ th of BALQSOs, the thermal plasma outflow is accompanied by ejection of a pair of relativistic plasma jets which can extend to kpc scale (Becker et al. 2000). Inferring the orientation of the jet axis from the spectral/structural radio properties as a statistical indicator has revealed no preference between the postulated equatorial (Cohen et al. 1995; Goodrich & Miller 1995; Murray et al. 1995; Elvis 2000; Proga et al. 2000) and polar (Punsly 1999a; Becker et al. 2000; Zhou et al. 2006; Ghosh & Punsly 2007; Doi et al. 2009) configurations for the BAL outflows (see, e.g., Jiang & Wang 2003; Brotherton et al. 2006; Gregg et al. 2006; Bruni et al. 2013; Kunert-Bajraszewska et al. 2015).

Although, both configurations may conceivably exist in a single BALQSO (e.g., Brotherton et al. 2006; Yang et al. 2012), the polar configuration would have a more direct bearing on the relativistic jet, given the likelihood of a physical interaction between the outflowing BAL clouds and the jet on the inner parsec scale. Since the radio flux of such compact relativistic jets, when pointed near the line of sight, would appear strongly Doppler boosted, the polar outflows of absorbers should be frequently observed in those BALQSOs whose radio spectrum is flat or inverted, and this indicator has been employed in several studies (Becker et al. 2000; Montenegro-Montes et al. 2008; Bruni et al. 2012). Additional examples of such BALQSOs with aligned jets have been found through radio flux variability (Zhou et al. 2006; Ghosh & Punsly 2007; Montenegro-Montes et al. 2008; Doi et al. 2009).

Interestingly, Fanaroff-Riley type II radio morphology is ~ 10 times rarer among BAL quasars, compared to normal quasars in the SDSS (see [Gregg et al. 2006](#)). The core dominated flat-spectrum subpopulation of RL quasars, called FSRQs, has a subset, namely blazars, which is characterised by parsec-scale relativistic jets of strongly Doppler boosted nonthermal radiation often showing superluminal motion, in addition to rapid flux variability and a strong ($p_{opt} > 3\%$) optical polarization which is highly variable (e.g., [Fugmann 1988](#); [Lister & Smith 2000](#)). Another well established exceptionality to blazars is their strong INOV, of amplitude $\psi > 3\text{-}4\%$ with a DC of around 40-50% ([Gopal-Krishna & Wiita 2018](#), and references therein). This opens up the possibility to confirm the blazar nature of the BAL quasars which are known to exhibit at least some radio properties that are commonly associated with blazars and hence may be regarded as manifestations of the polar model of the BAL phenomenon mentioned above. Here we shall apply the INOV test to a well-defined sample of 10 RL BALQSOs exhibiting blazar signatures, namely a flat/inverted radio spectrum and a large radio polarization that locates them in the high polarisation tail for BAL quasars (optical polarimetric data on RL BALQSOs being even scarcer, at present). This selection process makes our sample particularly suited for making a search for ‘BAL-blazars’, in contrast to a previous INOV search which was focussed on BAL quasars selected on the criterion of radio loudness alone and was found to show only a muted INOV (unlike blazars, e.g., see, [Joshi & Chand 2013](#)).

5.1.1 The sample of BAL–blazar candidates

Our sample of 10 BAL–blazar candidates for intranight optical monitoring was derived from 6 publications reporting 56 radio detected BALQSOs (Table 5.1). Out of these, we have selected all 10 sources which have a positive declination, an SDSS-r band apparent magnitude, $m_r < 19$, a flat or inverted radio spectrum (i.e., $\alpha > -0.5$, [Becker et al. 2000](#)) and a radio (linear) polarization $p_{rad} > 3\%$ (Table 5.1). The choice of the $p_{rad} = 3\%$ threshold is based on the distribution of median fractional polarization of the radio core, measured for 387 AGNs, by multi-epoch VLBI at 15 GHz (figure 1 in [Hodge et al. 2018](#)). This distribution consists of a single large bump peaking at $p_{rad}(15 \text{ GHz}) = 1.5\%$, followed by a sharp drop setting in at $p_{rad}(15 \text{ GHz}) \sim 3.0\%$, and finally culminating in a low-amplitude tail which extends up to $p_{rad}(15 \text{ GHz}) = 9\%$. This high polarization tail of FSRQs is strikingly similar to the distribution of $p_{rad}(15 \text{ GHz})$ found for BL Lacs, which is plotted in the same figure 1 ([Hodge et al. 2018](#)) and for which the median value of $p_{rad}(15 \text{ GHz}) = 3.5\%$. Hence, it seems reasonable to expect that at least some of the flat-spectrum BAL quasars

Table 5.1: *The sample of 10 BAL–blazar candidates monitored for intranight optical variability (INOV).*

Source name	RA (J2000)	DEC (J2000)	z_{em}	AI	m_r	$S_{1.4GHz}$	S_{150MHz}	L_{150MHz}	α_{radio}	Log(R)	Fractional polarisation	Ref. codes
SDSS	hh:mm:ss	°:':"		(kms^{-1})		mJy	mJy	erg/s/Hz			% (at GHz)	
(1)	(2)	(3)	(4)	(5)	(6)	(7)	(8)	(9)	(10)	(11)	(12)	(13)
J090552.41+025931.5	09:05:52.41	+02:59:31.5	1.82	130	16.91	35.6	46.80	1.07×10^{34}	0.12	1.76	7.7 ± 3.8 (1.4)	d,f
J092824.13+444604.7	09:28:24.13	+44:46:04.7	1.90	293	18.31	166.5	73.60	1.89×10^{34}	-0.36	2.80	4.6 ± 0.7 (1.7)	c,e
J092913.97+375743.0	09:29:13.97	+37:57:43.0	1.91	2170	18.04	42.7	125.30	3.24×10^{34}	0.48	2.20	6.1 ± 0.9 (1.4)	d,f
J105416.51+512326.1	10:54:16.51	+51:23:26.1	2.34	2220	18.73	34.8	74.10	3.14×10^{34}	0.34	2.38	4.2 ± 1.1 (1.4)	d,f
J115944.82+011206.9	11:59:44.82	+01:12:06.9	2.00	2887	17.27	271.1	331.10	9.57×10^{34}	0.09	2.60	6.5 ± 1.7 (1.4)	c,b,e
J123717.44+470807.0	12:37:17.44	+47:08:07.0	2.27	1300	18.58	89.2	50.30	1.98×10^{34}	-0.26	2.47	5.9 ± 2.6 (8.46)	d,f
J131213.57+231958.6	13:12:13.57	+23:19:58.6	1.51	-	17.32	45.8	67.90	0.98×10^{34}	0.18	1.88	3.6 ± 2.3 (22)	b
J140653.84+343337.3	14:06:53.84	+34:33:37.3	2.56	350	18.72	165.3	150.00	7.91×10^{34}	-0.04	2.83	3.5 ± 0.2 (8.46)	d,f
J162453.47+375806.6	16:24:53.47	+37:58:06.6	3.38	1020	18.45	54.6	35.60	3.67×10^{34}	-0.19	2.41	11.3 ± 1.5 (22.46)	a,b,d,f
J162559.90+485817.5	16:25:59.90	+48:58:17.5	2.72	-	18.09	25.8	<7.00	0.55×10^{34}	-0.47	1.90	17.6 ± 14.0 (43)	b

Notes. Col. 1: source name; Col. 2,3: coordinates; Col. 4: emission redshift; Col. 5: absorption index (Hall et al. 2002); Col. 6: r-band magnitude from SDSS; Col. 7: peak flux density at 1.4 GHz; Col. 8,9: peak flux density and luminosity at 150 MHz; Col. 10: spectral index ($f_\nu \propto \nu^\alpha$) between 150 MHz and 1.4 GHz; Col. 11: radio loudness parameter $R = f_{5GHz}/f_{2500\text{\AA}}$; Col. 12: fractional polarization (frequency); Col. 13: reference code(s). References: (a) Benn et al. (2005); (b) Montenegro-Montes et al. (2008); (c) Doi et al. (2009); (d) Bruni et al. (2012); (e) Hayashi et al. (2013); (f) Bruni et al. (2015).

falling within the high polarization tail would turn out to be the putative BAL–blazars.

5.1.2 Intranight photometric monitoring

Photometric observations of our sample of 10 BAL–blazar candidates were performed on a total of 30 nights (3 monitoring sessions per source). The majority of our observing sessions (25 out of 30) were carried out using the 1.3-m DFOT (Sagar et al. 2011) in SDSS-r band filter operated by the ARIES, Nainital, India. DFOT has the Ritchey-Chretien (RC) optics with f/4 Cassegrain focus, yielding a plate scale of $40 \text{ arcsec-mm}^{-1}$ and a pointing accuracy better than ten arcsec (rms). The data were recorded on a Peltier-cooled Andor CCD camera having 2048×2048 pixels of $13.5 \mu\text{m}$ size and covering an 18 arcmin field-of-view (FoV) on the sky. The CCD detector has a gain of $0.7, 2 e^-$ per analog-to-digital unit (ADU) and readout noise of $2.5, 7 e^-$ when it is read out at speeds of 31 and 1000 kHz, respectively. The camera is cooled thermoelectrically down to -85°C . Monitoring of 3 sessions were performed in R-band filter with 1.04-m ST (Sagar 1999), functioned by ARIES, Nainital. The telescope is an equatorially mounted, f/13 RC reflector with Cassegrain focus. The data were recorded on 1340×1300 liquid-nitrogenically cooled PyLoN CCD of 20-micron pixel size. The detector is capable of covering 6.8×6.5 arcmin area of the sky. The readout speed of the CCD covers a range of 50 kHz to 5 MHz with a corresponding gain of 1, 2, 4, 6 and $16 e^-/\text{ADU}$. In addition, 2 session were observed in R-band filter using 2.0m HCT

at IAO (Prabhu & Anupama 2010). It is also an RC designed an f/9 telescope with Cassegrain focus. The telescope is equipped with 2148×2048 cryogenically cooled detector covering a 10×10 arcmin FoV in the sky. The plate scale of the detector is 0.296 arcsec/pixel. The CCD has readout noise of 5.75 e^{-1} per pixel, and gain is $0.28 \text{ e}^{-1} / \text{ADU}$ (for a comprehensive detail of the telescopes see Table 2.2)

The continuous monitoring of our sources was done for a minimum duration of 3 hours. Typically, the exposure time for each data sample was between 5-10 min. The FWHM of the seeing disk during our monitoring sessions was typically between 2-4 arcsec. The centering of the FoV for each source was slightly adjusted to ensure that at least 2-3 comparison stars similar in brightness to the target quasar were also recorded on each CCD frame. The details of the comparison stars used for deriving the LC of each BAL-blazar in our sample are presented in Table 5.2.

5.1.3 The Data Reduction

Preliminary image processing (such as bias subtraction, flat correction, and removal of cosmic ray) of each observing session was performed using the standard packages in IRAF software (see Section 2.2.2). Aperture photometric techniques were employed using general tasks under DAOPHOT II to determine the instrumental magnitudes of the target source and the comparison stars in each frame. In order to probe the effect of seeing fluctuations on the observations in a particular night, we carried out the aperture photometry taking four aperture radii, i.e., for 1, 2, 3, and 4 times the FWHM of the seeing disk. To determine this value for each CCD frame, we took an average of the measured FWHMs of the images of five reasonably bright stars in that frame. Typically, the best SNR for the differential light curves (DLCs) was achieved when the aperture radius was set at $\sim 2 \times \text{FWHM}$ of the seeing disk.

We derived the DLCs of the target blazar for each monitoring session relative to two comparison stars present in each CCD frame and being close to the target quasar both in brightness and location. Relevant information on the chosen pair of comparison stars is provided in Table 5.2. The DLCs of all the 30 monitoring sessions are shown in Fig. 5.1 and 5.2. It may be noted that the absolute value of $g-r$ color for all the ‘quasar–star’ and ‘star–star’ pairs is always <1.5 . The studies by Carini et al. (1992) and Stalin et al. (2004) have shown that for such relatively small color difference, brightness changes caused by the varying atmospheric attenuation during the course of monitoring have a negligible effect on the DLCs. Further, the steadiness of all the star–star DLCs in Fig. 5.1 and 5.2 assures us that the chosen comparison stars are indeed non-varying.

Table 5.2: *Parameters of comparison stars selected for the 10 BAL-blazars.*

Object	Date(s) of obs. yyyy-mm-dd	R.A.(J2000) hh:mm:ss	Dec.(J2000) °:':"	<i>g</i> mag	<i>r</i> mag	<i>g-r</i> mag
(1)	(2)	(3)	(4)	(5)	(6)	(7)
J090552.41+025931.5	2018-04-14,2018-12-30,2019-01-28	09:05:52.41	+02:59:31.5	17.31	16.91	0.40
S1	2018-04-14,2018-12-30,2019-01-28	09:05:23.93	+03:05:10.9	16.80	16.36	0.44
S2	2018-04-14,2018-12-30,2019-01-28	09:06:09.52	+02:51:22.7	17.22	16.25	0.97
J092824.13+444604.7	2016-11-28,2016-12-27,2017-12-16	09:28:24.13	+44:46:04.7	18.33	18.31	0.02
S1	2016-11-28,2016-12-27,2017-12-16	09:27:46.65	+44:43:36.0	18.76	17.50	1.26
S2	2016-11-28,2016-12-27,2017-12-16	09:28:07.06	+44:45:10.1	18.89	17.43	1.46
J092913.97+375743.0	2012-02-23,2018-12-31,2019-01-07	09:29:13.97	+37:57:43.0	18.24	18.05	0.19
S1	2012-02-23,2018-12-31,2019-01-07	09:29:53.59	+37:57:07.9	17.74	17.25	0.49
S2	2012-02-23	09:28:38.73	+37:58:43.9	18.37	16.95	1.42
S3	2018-12-31,2019-01-07	09:29:59.63	+37:56:04.3	17.60	17.17	0.43
J105416.51+512326.1	2018-12-14,2019-02-09,2019-03-07	10:54:16.51	+51:23:26.1	18.83	18.75	0.08
S1	2018-12-14,2019-02-09,2019-03-07	10:54:53.73	+51:26:34.1	18.56	17.31	1.25
S2	2018-12-14,2019-02-09,2019-03-07	10:54:52.02	+51:29:09.2	17.98	17.14	0.65
J115944.82+011206.9	2017-02-26,2017-04-24,2017-12-25	11:59:44.82	+01:12:06.9	17.59	17.26	0.33
S1	2017-02-26,2017-04-24,2017-12-25	11:59:18.51	+01:07:21.9	17.37	16.56	0.81
S2	2017-02-26	12:00:03.48	+01:05:26.1	17.46	16.43	1.03
S3	2017-04-24,2017-12-25	11:59:20.32	+01:12:57.9	19.31	17.91	1.40
J123717.44+470807.0	2019-01-07,2019-01-15,2019-02-09	12:37:17.44	+47:08:07.0	19.06	18.63	0.43
S1	2019-01-07,2019-01-15,2019-02-09	12:37:21.26	+47:03:45.2	17.50	17.14	0.36
S2	2019-01-07,2019-01-15,2019-02-09	12:36:36.51	+47:03:15.2	18.34	17.71	0.63
J131213.57+231958.6	2019-03-06,2019-03-07,2019-03-08	13:12:13.57	+23:19:58.6	17.49	17.30	0.19
S1	2019-03-06	13:12:24.70	+23:21:13.6	17.69	16.97	0.72
S2	2019-03-06,2019-03-07,2019-03-08	13:12:12.80	+23:17:50.7	16.12	15.36	0.76
S3	2019-03-07,2019-03-08	13:12:31.37	+23:17:44.2	17.88	16.94	0.93
J140653.84+343337.3	2017-03-21,2017-03-30,2018-15-02	14:06:53.84	+34:33:37.3	18.97	18.69	0.28
S1	2017-03-21,2017-03-30,2018-15-02	14:06:54.07	+34:27:48.0	18.37	17.07	1.30
S2	2017-03-21,2017-03-30,2018-15-02	14:07:20.38	+34:40:40.6	18.82	17.63	1.19
J162453.47+375806.6	2017-03-29,2017-04-24,2018-03-17	16:24:53.47	+37:58:06.7	19.14	18.46	0.68
S1	2017-03-29,2017-04-24,2018-03-17	16:24:28.43	+37:58:23.9	17.85	17.34	0.51
S2	2017-03-29,2017-04-24,2018-03-17	16:24:42.55	+38:01:48.1	17.96	17.51	0.45
J162559.90+485817.5	2018-04-14,2018-04-15,2019-03-07	16:25:59.90	+48:58:17.5	18.09	17.94	0.15
S1	2018-04-14,2018-04-15,2019-03-07	16:26:03.63	+49:05:33.4	19.02	17.66	1.36
S2	2018-04-14,2018-04-15	16:25:55.89	+49:02:48.6	17.82	17.29	0.53
S3	2019-03-07	16:25:39.76	+49:00:02.4	17.86	17.35	0.51

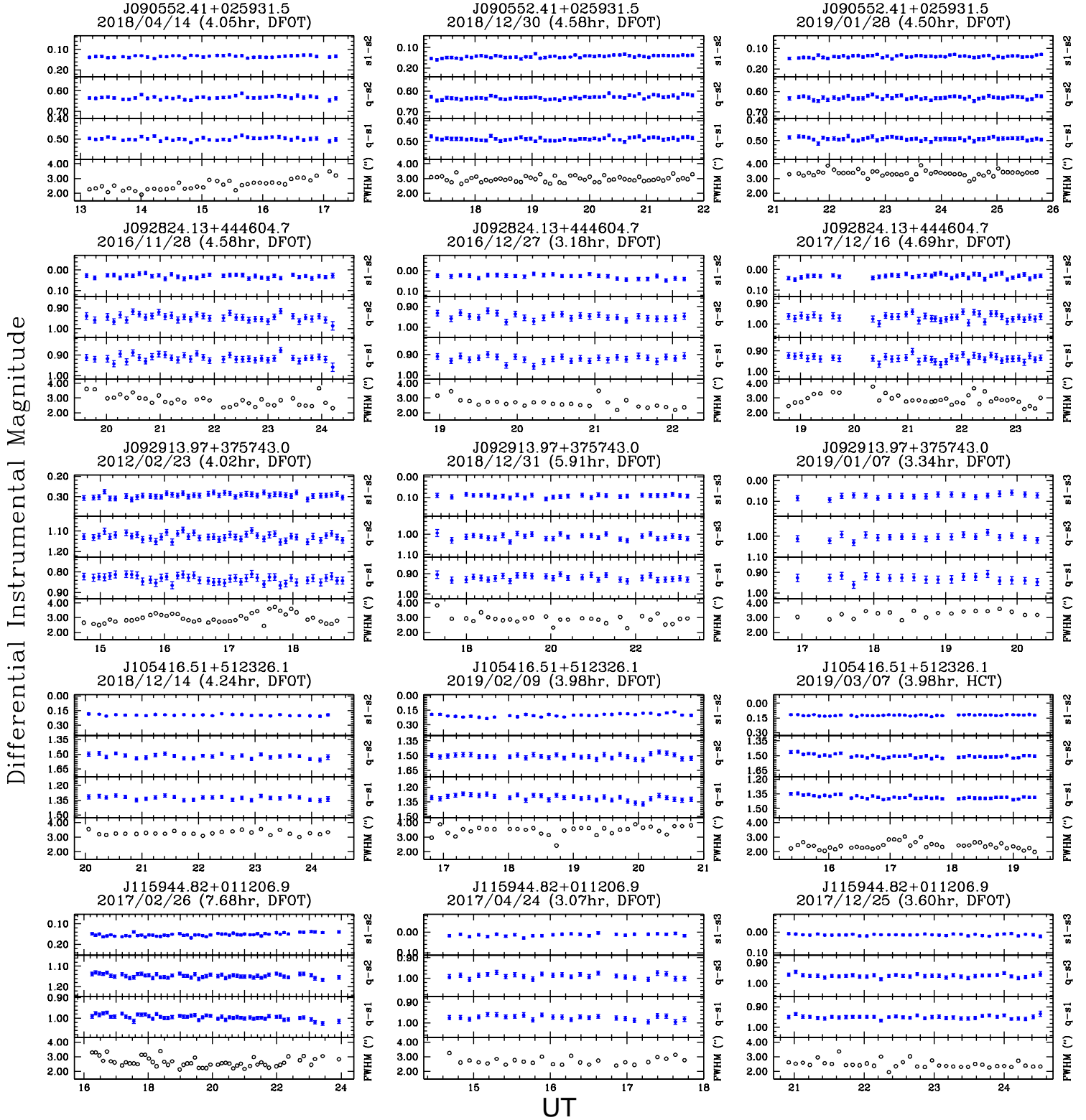


Figure 5.1: DLCs for the 10 BAL-blazar candidates (30 monitoring sessions). The name of the AGN, date, duration, and the telescope used are mentioned at the top of the panels for individual sessions. In each panel, the upper curve in blue is the DLC of the chosen two comparison stars ("star-star" DLC). The two middle blue curves display the DLCs of the target AGN relative to the two comparison stars, as defined in the labels on the right side. The lowest profile in each panel (black stars) shows the variation of the FWHM through the monitoring session.

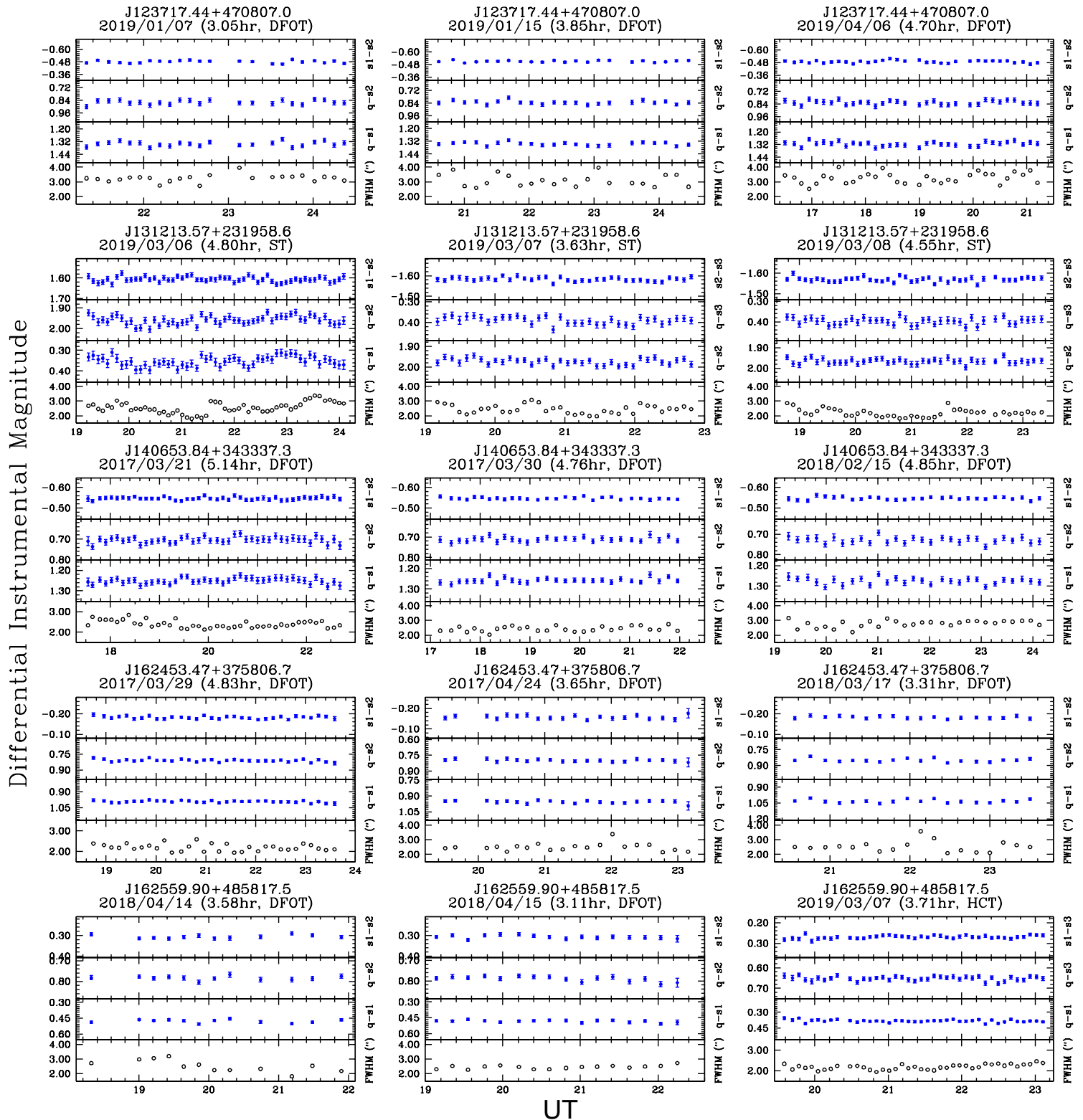


Figure 5.2: Same as Fig. 5.1

5.1.4 Statistical analysis and results

For examining the INOV of a target blazar in each DLC, we subjected the corresponding DLC (relative to the two comparison stars) to F^η test. This statistical test has been extensively employed in many studies (Gopal-Krishna et al. 2013; Goyal et al. 2013; Kumar et al. 2016, 2017). In several independent studies, the photometric errors returned by the DAOPHOT algorithm were found to be smaller by a factor η with a value ranging between 1.30 and 1.75 (Gopal-Krishna et al. 1995; Garcia et al. 1999; Bachev et al. 2005). Using a large data set, Goyal et al. (2013) found a best-fit value of η to be 1.5, which is adopted here.

The parameter F^η for the DLCs relative to two comparison stars is defined as:

$$F_1^\eta = \frac{Var(q-s1)}{\eta^2 \sum_{i=1}^N \sigma_{i,err}^2 (q-s1)/N}, \quad F_2^\eta = \frac{Var(q-s2)}{\eta^2 \sum_{i=1}^N \sigma_{i,err}^2 (q-s2)/N} \quad (5.1)$$

Where $Var(q-s1)$, $Var(q-s2)$, and $Var(s1-s2)$ are the q-s1, q-s2 and s1-s2 DLC variances, respectively. And $\sigma_{i,err}(q-s1)$ and $\sigma_{i,err}(q-s2)$ are the DAOPHOT errors of the q-s and s1-s2 DLCs on individual points, respectively. N is the number of observational data points (Column 5 of Table 5.3) and the $\eta = 1.5$ is the scaling factor, as stated above.

For each DLC, Table 5.3 compares the estimated values of F^η (relative to the two stars) with the critical value of F (F_c^α) for $\alpha = 0.05$ and 0.01 , corresponding to 95% and 99% confidence levels of INOV detection. If the F^η value exceeds F_c^α , the null hypothesis of no variability is discarded. We thus classify a target AGN with $F^\eta = F_c(0.99)$ as variable ('V') at confidence level = 0.99; probably variable ('PV') for F^η between $F_c(0.95)$ and $F_c(0.99)$, and non-variable ('NV') for F^η value less than $F_c(0.95)$. For a given session, we designate the target AGN as variable ('V') if F^η values for both q-s1 and quasar-star2 DLCs exceed the value $F_c(0.99)$; non-variable (i.e., 'NV') if F^η value of at least one q-s DLC is less than the $F_c(0.95)$; and probably variable (i.e., 'PV') in remaining cases (i.e., combination of V, PV or PV, PV) (see, Goyal et al. 2013). Column 10 in Table 5.3 lists the mean photometric accuracy $\sqrt{\langle \sigma_{i,err}^2 \rangle}$ estimated for a monitoring sessions using the two quasar-star DLCs; mostly it is better than 3% (median = 2.0%).

Table 5.3: *Observation log of the 30 monitoring sessions of the 10 BAL–blazar.*

AGN	Obs. date yyyy/mm/dd	Tel.	Filter	N	T hr	F-test		$\sqrt{\eta^2 \langle \sigma_{err}^2 \rangle}$ (q-s)	
						Computed F_1^η, F_2^η	Threshold values $F_c(0.95) \quad F_c(0.99)$		
(1)	(2)	(3)	(4)	(5)	(6)	(7)	(8)	(9)	(10)
J090552.41+025931.5	2018/04/14	DFOT	r	39	4.05	0.57,0.55	1.72	2.16	0.010
	2018/12/30	DFOT	r	54	4.58	0.48,0.77	1.58	1.91	0.010
	2019/01/28	DFOT	r	52	4.50	0.42,0.49	1.59	1.94	0.011
J092824.13+444604.7	2016/11/28	DFOT	r	36	4.58	0.53,0.49	1.76	2.23	0.021
	2016/12/27	DFOT	r	27	3.18	0.44,0.41	1.93	2.55	0.020
	2017/12/16	DFOT	r	38	4.69	0.38,0.43	1.73	2.18	0.022
J092913.97+375743.0	2012/02/23	DFOT	r	44	4.02	0.38,0.50	1.66	2.06	0.023
	2018/12/31	DFOT	r	29	5.91	0.27,0.45	1.88	2.46	0.018
	2019/01/07	DFOT	r	19	3.34	0.22,0.31	2.22	3.13	0.023
J105416.51+512326.1	2018/12/14	DFOT	r	26	4.24	0.34,0.52	1.96	2.60	0.026
	2019/02/09	DFOT	r	33	3.98	0.65,0.38	1.80	2.32	0.031
	2019/03/07	HCT	R	43	3.98	0.86,0.89	1.67	2.08	0.017
J105416.51+512326.1	2017/02/26	DFOT	r	54	7.68	0.85,0.47	1.58	1.91	0.012
	2017/04/24	DFOT	r	25	3.07	0.42,0.43	1.98	2.66	0.015
	2017/12/25	DFOT	r	36	3.60	0.33,0.35	1.76	2.23	0.011
J123717.44+470807.0	2019/01/07	DFOT	r	23	3.05	0.61,0.42	2.05	2.78	0.028
	2019/01/15	DFOT	r	22	3.85	0.45,0.44	2.08	2.86	0.024
	2019/04/06	DFOT	r	33	4.70	0.50,0.37	1.80	2.32	0.029
J131213.57+231958.6	2019/03/06	ST	R	55	4.80	0.75,0.82	1.57	1.90	0.024
	2019/03/07	ST	R	36	3.63	0.59,0.56	1.76	2.23	0.021
	2019/03/08	ST	R	42	4.55	0.37,0.44	1.68	2.09	0.021
J140653.84+343337.3	2017/03/21	DFOT	r	44	5.14	0.39,0.41	1.66	2.06	0.021
	2017/03/30	DFOT	r	28	4.76	0.44,0.33	1.90	2.51	0.017
	2018/02/15	DFOT	r	29	4.85	0.57,0.44	1.88	2.46	0.021
J162453.47+375806.6	2017/03/29	DFOT	r	32	4.83	0.32,0.49	1.82	2.35	0.017
	2017/04/24	DFOT	r	20	3.65	0.28,0.19	2.17	3.03	0.025
	2018/03/17	DFOT	r	19	3.31	0.69,0.73	2.22	3.13	0.019
J162559.90+485817.5	2018/04/14	DFOT	r	12	3.58	0.80,0.41	2.82	4.46	0.016
	2018/04/15	DFOT	r	16	3.11	0.32,0.53	2.40	3.52	0.018
	2019/03/07	HCT	R	40	3.71	0.68,0.49	1.70	2.14	0.015

Notes. Col. 1: name of the AGN; Col. 2: date of monitoring; Col 3: telescope used; Col. 4: filter used; Col. 5: number of exposures/frames; Col. 6: duration of monitoring (T); Col. 7: F-value found for the q–s1 and q–s2 DLCs; Col. 8: critical F value for 95% confidence level; Col. 9: critical F value for 99% confidence level; Col. 10: average photometric accuracy.

5.1.5 Discussion and Conclusion

The main result from this study (Table 5.3) is the non-detection of INOV in any of the 30 sessions devoted to the present representative sample of 10 BAL–blazar candidates, selected on the basis of a flat/inverted spectrum and high linear polarization at centimeter/decimeter wavelengths (Table 5.1). We shall now compare this result with the INOV results reported in Goyal et al. (2013) for a sample of 24 ‘normal’ (i.e., non-BAL) blazars that were monitored in 85 sessions, also in red filter and subjected to the same F^{η} test. For this, we first need to extract an appropriate comparison sample out of those 85 sessions, in order to minimise the difference in sensitivity achieved for that and the present sample of DLCs. The monitoring for the present sample has been almost entirely performed using the 1.3-m DFOT (Sect. 5.1.2), whereas the 24 normal blazars were mostly monitored with the 1.04-m ST.

Considering this, we adopt the premise that a proper comparison sample of DLCs of the normal blazars should be formed by matching in terms of the rms error found for the (non-varying) ‘star-star’ DLC for a given session. Thus, for the present sample of 30 DLCs of the 10 BAL–blazar candidates, we have built a comparison sample of 28 DLCs pertaining to 15 normal blazars, out of the Goyal et al. (2013) sample, adopting a tolerance of $\pm 0.5\%$ in the rms error mentioned above.

Using the data provided in table 1 of Goyal et al. (2013) we have computed the INOV DC for the sample of ‘n’ DLCs of normal blazars, as:

$$DC = 100 \frac{\sum_{i=1}^n K^i (1/T_{int}^i)}{\sum_{i=1}^n (1/T_{int}^i)} \text{percent} \quad (5.2)$$

where $T_{int}^i = T_{obs}^i (1 + z_{em})^{-1}$ is the intrinsic rest frame monitoring duration corrected for the cosmological redshift, z_{em} . K^i was taken as 1 for a positive detection of INOV in the i^{th} session, otherwise, it was set to zero. We thus find, the INOV DC to be 41.2% for the comparison sample (28 sessions devoted to 15 normal blazars). This high value is in striking contrast to the non-detection of INOV in any of the 30 sessions devoted to our sample of 10 BAL–blazar candidates.

We now examine the possibility that the strong contrast between the INOV DCs found here between the samples of BAL–blazar candidates and normal blazars might arise from the systematic difference between their optical luminosities and/or redshifts (Fig. 5.3 a, Fig. 5.3 b). To check the possible role of luminosity, we turn to the Goyal et al. (2013) sample of 85 DLCs of 24 normal blazars and divide it into two luminosity bins separated in absolute magnitude in B-band

(M_B) at $M_B = -25.0$. The higher luminosity (high-L) bin contains 8 normal blazars monitored in 40 sessions and the lower luminosity (low-L) bin contains 16 normal blazars (45 sessions). For a proper comparison between these two sets of sessions, we again apply the afore-mentioned filter of rms matching to within a tolerance of $\pm 0.5\%$. This led to 37 sessions (8 blazars) from the high-L bin matching in the rms error with 37 sessions (16 blazars) of the low-L bin. The corresponding median M_B for these two luminosity bins are -25.4 and -23.7 , respectively. Following Eq. 5.4 we have computed the INOV DCs and find them to be 44.5% and 52.0% for the high and low luminosity bins, respectively. Based on this, any decrement of DC with luminosity appears to be marginal.

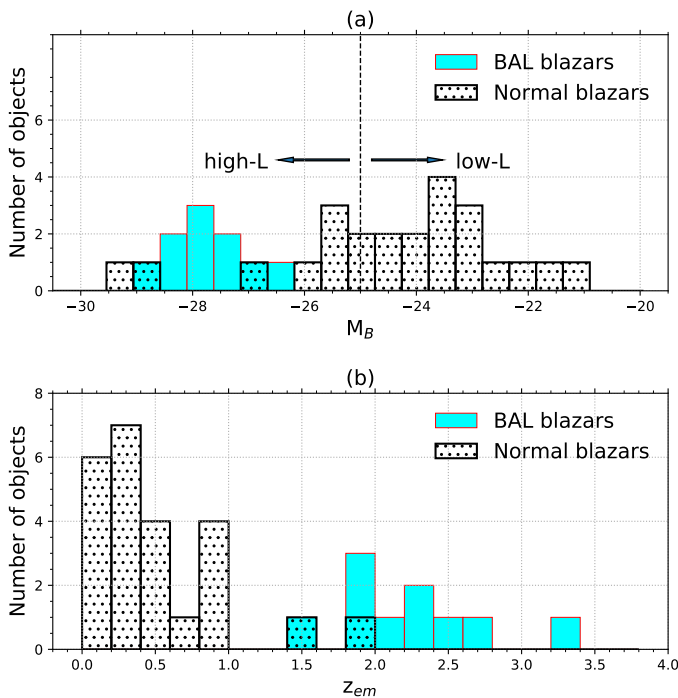


Figure 5.3: Distribution of absolute magnitude in B-band (M_B , upper panel) and emission redshift (lower panel) for the present sample of 10 BAL-blazar candidates (cyan filled) and for the sample of 24 normal blazars from Goyal et al. (2013) (black dotted). The dotted vertical in the upper panel corresponds to $M_B = -25.0$

Could the marked contrast between the INOV of the BAL-blazar candidates and normal blazars then be because of the redshifts of the BAL-blazar candidates being systematically higher than those of the comparison sample of normal blazars described above (median redshifts of the two samples are 2.13 and 0.42)? An important consequence of this difference is that, when translated to the rest-frame, the intranight monitoring durations (T_{int}) are substantially shorter for the sample of BAL-blazar candidates. To seek a clue on this point, we again turn to the afore-mentioned Goyal et al. (2013) sample of 85 intranight monitoring sessions devoted to 24 normal blazars. We divide this dataset into 4 bins of T_{int} , each containing close to 20 sessions. Median values of T_{int}

for these bins are 3.0, 4.0, 4.8 and 5.6 hr (Fig. 5.4). Computation of INOV DC for these 4 bins (Eq. 5.4) gives INOV DCs of 44.9%, 47.4%, 50.2%, and 56.5%, respectively (note that each of these estimates is the average of the DCs calculated for the two DLCs of a given AGN, derived relative to the two comparison stars). It is seen that even for the shortest bin of T_{int} (median = 3.0 hr) the INOV DC is 44.9%, which is only marginally lower than the DCs found for the 3 bins of longer duration. Furthermore, there is little evidence that strong INOV is a rarer occurrence in sessions of shorter intrinsic duration (at least over this range of T_{int}). From Fig. 5.4 it is seen that for the shortest bin (with median = 3.0 hr), strong INOV with amplitude $\psi \gtrsim 10\%$ was detected in 5 out of 22 sessions, which is evidently not smaller than the corresponding value (7/63) found for the aggregate of the 3 bins of longer sessions.

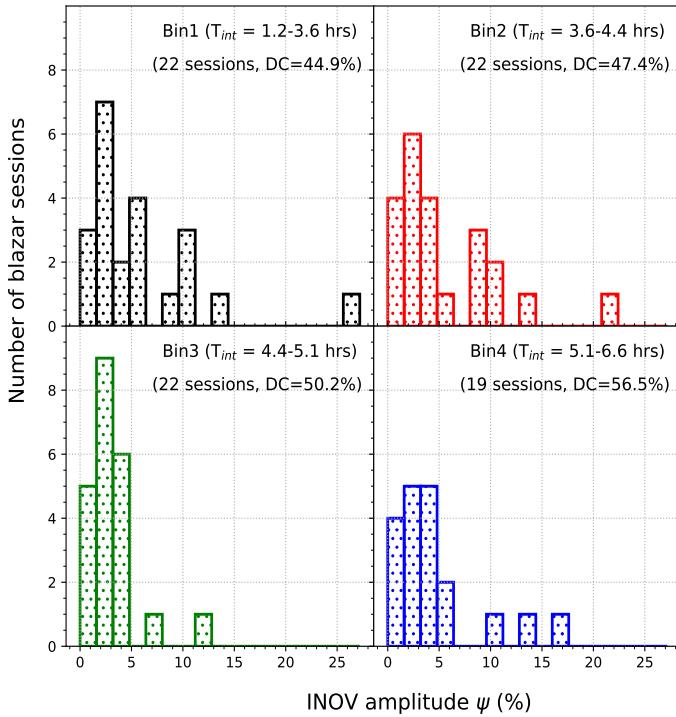


Figure 5.4: Distribution of INOV amplitude (ψ) for the 4 bins of T_{int} , derived using the comparison sample of 24 normal blazars monitored in 85 sessions (see text).

Thus, in order to reconcile the foregoing analysis with the present non-detection of INOV for the BAL-blazar candidates in any of the 30 sessions (median $T_{int} = 1.2$ hr) one might postulate a drastic drop in INOV strength for $T_{int} \lesssim 1-2$ hrs. Although, such a hypothesis cannot be ruled out at present (see, e.g., Romero et al. 2002; Gopal-Krishna et al. 2011; Gopal-Krishna & Wiita 2018), and it remains observationally verifiable, the alternative possibility that the non-detection of INOV for the BAL-blazar candidates could either undermine the polar model for the BAL

outflows (Sect. 5.1), or be traceable to some other physical effect associated with that model. For instance, could it be that, as compared to normal blazars, physical conditions in the relativistic jets of BAL quasars are less conducive for strong INOV (as, for example, is their propensity to be incapable of developing FR II radio structures, e.g., see, [Gregg et al. 2006](#)). Origin of INOV has been associated with a zone of turbulence within a parsec-scale jet, just upstream of a relativistic shock, as sketched in [Marscher et al. \(2008\)](#) (see, also, [Goyal et al. 2012](#); [Pollack et al. 2016](#)). Conceivably, the shock induced turbulence in the jets of BAL quasars is not strong enough to accelerate relativistic particles to the high energies needed for the emission of optical synchrotron radiation. Such a scenario would call for a more refined understanding of the physics of interaction of the inner relativistic jet with the rapidly outflowing BAL clouds of much denser thermal plasma, as envisioned in the polar model of BAL quasars (e.g., [Ghosh & Punsly 2007](#)). In parallel to such theoretical studies, it would also be worthwhile to intensify intranight optical monitoring of BAL–blazar candidates in sessions of longer durations.

5.2 Intra-night optical monitoring of blazar counter parts of BAL quasars

This work is in continuation of our previous work (Section 5.1), where to investigate the blazar nature of the BAL quasars, we performed the INOV study for a sample of 10 RL BAL quasars exhibiting blazar signatures (BAL–blazar), namely a flat/inverted radio spectrum and a large radio polarization that locates them in the high polarisation tail for BAL quasars ([Mishra et al. 2019](#), hereafter M19). This first INOV study focused on BALQSOs, involved 30 intra-night optical monitoring sessions devoted to the sample of 10 BAL–blazars. An unexpected outcome of M19 was that no INOV was detected in any of the 30 sessions, even though a reasonably high radio polarization ($> 3\%$) has been reported for all these BAL quasars, which qualifies them as Blazars. This total lack of INOV detection is highly abnormal for blazars (for which an INOV DC of $60\pm 20\%$ is typical). Hence, this unexpected result led us to pose the question, “Are there broad absorption-line blazars?” (see M19). We also compared the INOV DC for our BAL–blazar candidates (with DC = 0), with the INOV DC reported in the literature for normal blazars (i.e., without BAL). Our main comparison sample was derived from the extensive INOV database of 85 DLCs devoted to 24 normal blazars published by [Goyal et al. \(2013, hereafter G13\)](#). We found INOV DC to be 41.2% for the comparison sample which was in striking contrast to the non-detection of INOV in

any of the 30 sessions devoted to our sample of 10 BAL–blazar candidates (see M19).

However, the comparison sample was not entirely satisfactory, primarily due to a mismatch in the absolute magnitude and redshift distributions, compared to the sample of 10 BAL–blazars (see Fig. 5.3). The median redshifts of the BAL–blazar sample and the comparison sample of normal blazars in M19 were 2.13 and 0.42, respectively. This redshift mismatch between the two samples led to a mismatch in the intrinsic duration of monitoring ($T_{int} = T_{obs}/(1+z_{em})$; median value of T_{int} in the two samples are 1.23 hrs and 4.21 hrs), rendering substantially shorter intra-night monitoring durations for the sample of BAL–blazars as discussed in M19. Since the chance of detecting INOV DC increases with increasing the monitoring duration (see Romero et al. 2002), it becomes crucial to revisit the INOV comparison analysis of BAL–blazar candidates with the normal blazars matching in magnitudes and redshifts. Besides, the INOV study of this new sample of high redshift blazars would extend the blazar INOV analysis to a high redshift regime, which lacks so far. Hence, it would be extremely useful in ensuring an appropriate comparison of the INOV properties of various AGN subclasses at high redshift with that of blazars (Joshi et al. 2011; Gopal-Krishna et al. 2013; Joshi et al. 2013; Kumar et al. 2017; Ojha et al. 2020).

5.2.1 Sample

A blazar sample employed in this analysis is procured from the blazar catalog published by Massaro et al. (2009, ROMA-BZCAT). The ROMA-BZCAT catalog comprises 3561 objects. We limited our search to only those objects classified either as ‘RL_FSRQ’ or ‘BLLac’, resulting in a set of 2487 confirmed blazars.

From among these 2478 confirmed

blazars, we only considered objects with positive declination and magnitude less than 18.5 to perform their intranight monitoring with 2-m class northern sky telescopes. This resulted in a set of 885 blazars from the ROMA-BZCAT catalog. From among these 885 blazars, we searched for a normal blazar matching in redshift (within $\Delta z = \pm 0.1$) and apparent magnitude in R filter (within $\Delta m = \pm 0.5$ mag) for each of the 10 BAL–blazars presented in M19 (see Table 5.4). For nine out

Table 5.4: *Properties of our $m-z$ matched blazar sample.*

Name	RA	DEC	z_{em}	R_{mag}	$S_{1.4GHz}$ mJy	α_{radio}
5BZQJ0231+1322	02:31:45.89	+13:22:54.69	2.07	17.50	1560.0	0.72
5BZQJ0249+0619	02:49:18.01	+06:19:51.88	1.88	18.00	499.0	0.67
5BZQJ0646+4451	06:46:32.03	+44:51:16.59	3.39	18.30	452.0	0.63
5BZQJ0750+4814	07:50:20.44	+48:14:53.59	1.96	18.40	716.0	0.74
5BZQJ1017+6116	10:17:25.88	+61:16:27.51	2.81	18.10	404.0	0.64
5BZQJ1035+3756	10:35:51.17	+37:56:41.71	1.51	17.00	53.0	0.40
5BZQJ1125+2610	11:25:53.70	+26:10:19.99	2.34	18.20	921.0	0.76
5BZQJ1126+4516	11:26:57.65	+45:16:06.31	1.81	17.20	404.0	0.61
5BZQJ1306+4741	13:06:29.94	+47:41:32.49	2.52	18.30	54.0	0.52

[†] spectral index.

of 10 BAL–blazars, we obtained a matching normal blazar well within the considered redshift and apparent magnitude search radius. However, for J1054+5123 from the list of M19, we could not find any match. We refer to this sample of 9 blazars as ‘*m–z matched*’ blazar sample and present their properties in Table 5.4.

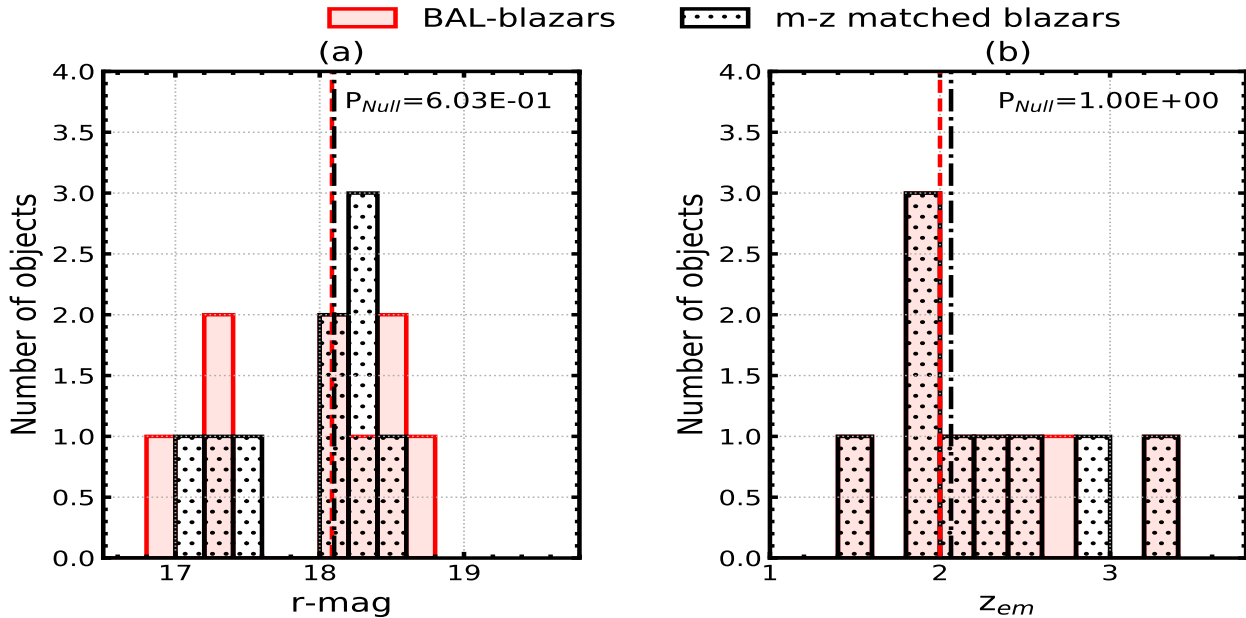


Figure 5.5: Distribution of R-band magnitude (left) and redshift (right) for BAL–blazar sample of M19 (red-filled) and our *m–z matched* blazar sample (black-hatched). The *p*-value of the K-S test is mentioned at the top right corner of each panel. The two vertical lines in each panel correspond to the parameters’ median values in BAL–blazar sample (red dashed) and *m–z matched* blazar sample (black dashed).

In Fig. 5.5, we present the R-band magnitude (Fig. 5.5 a) and the redshift (Fig. 5.5 b) distributions for the BAL–blazar sample of M19 and our *m–z matched* blazar sample. We carried out the K-S test on these distributions, and the *p*-values of the K-S test are shown in the top right corner of each panel; where the P_{null} value of the K-S test returns the null probability for the two distributions being indistinguishable. From Fig. 5.5 (a and b), it can be inferred that the magnitude and redshift distributions of BAL–blazar and our *m–z matched* blazar samples are similar with $P_{null} > 5\%$.

5.2.2 Photometric observation

Photometric monitoring of each of the 9 $m-z$ matched blazars was performed on 2 nights, adding up to a total of 18 intra-night monitoring sessions (details in the Table 5.5). For 12 of the 18 sessions, we used the 1.3-m DFOT, equipped with a Peltier-cooled Andor CCD camera which has 2048×2048 pixels of $13.5 \mu\text{m}$ size, providing 18 arcmin FoV on the sky (Sagar et al. 2011). Monitoring of 5 sessions were carried out with the 2.0-m HCT equipped with a 2148×2048 cryogenically cooled CCD detector covering a 10×10 arcmin FoV (Prabhu & Anupama 2010). For another remaining one session, the 1.04 m ST was used, which is equipped with a 1340×1300 pixel liquid-nitrogen cooled PyLoN CCD of 20-micron pixel size, providing a 6.8×6.5 arcmin FoV (Sagar 1999).

Each target AGN ($m-z$ matched blazar) was monitored in 2 separate sessions continuously for a minimum duration of 3-hours, in a sequence of 5-10 minute long exposures. At least 2 or 3 comparison stars were also recorded on each CCD frame, enabling differential photometry of the target AGN relative to the comparison stars which were chosen *a priori* on the basis of their proximity to the AGN, both in apparent magnitude and the location on the CCD chip (Table 5.5). In Fig. 5.6, we show the distributions of T_{int} of the 27 sessions devoted to 9 BAL-blazar candidates in M19 and 18 sessions dedicated to 9 $m-z$ matched blazars in this study. From the null probability of the K-S test at the top left corner of Fig. 5.6, it is inferable that the T_{int} of the DLCs devoted to the two samples are similar.

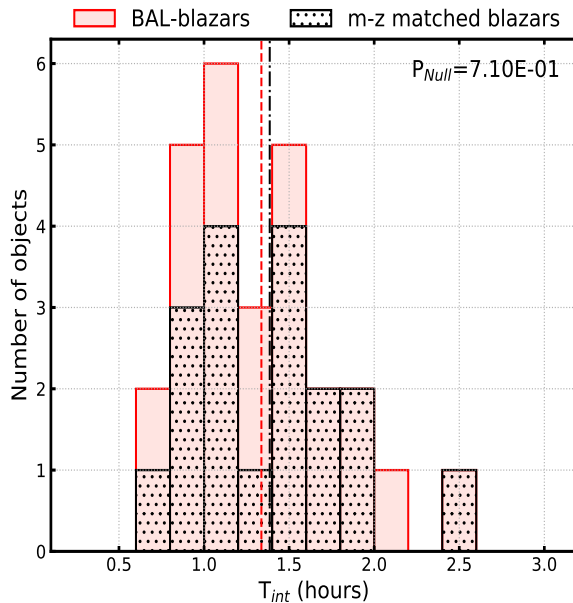


Figure 5.6: Distribution of the intrinsic duration of 27 monitoring sessions devoted to 9 BAL-blazars of M19 (red filled) and 18 sessions dedicated to 9 $m-z$ matched blazars in the present study (black hatched). The two dashed vertical lines in red and black show the median value of T_{int} of the BAL-blazar and $m-z$ matched blazar samples, respectively. The p -value of the K-S test estimated for these two samples is mentioned at the top right corner.

Table 5.5: *Parameters of comparison stars selected for the 9 m–z matched blazars.*

Object	Date(s) of obs. yyyy-mm-dd	R.A.(J2000) hh:mm:ss	Dec.(J2000) °:':"	<i>g</i> mag	<i>r</i> mag	<i>g-r</i> mag
(1)	(2)	(3)	(4)	(5)	(6)	(7)
5BZQJ0231+1322	2019-12-03,2019-12-17	02:31:45.89	+13:22:54.69	17.91	17.34	0.57
S1	2019-12-03,2019-12-17	02:31:29.93	+13:18:36.63	18.49	17.37	1.12
S2	2019-12-03	02:32:16.15	+13:24:43.07	18.98	16.84	2.14
S3	2019-12-17	02:31:54.89	+13:21:03.92	18.65	16.73	1.92
5BZQJ0249+0619	2019-11-30,2019-12-27	02:49:18.01	+06:19:51.88	18.38	17.95	0.42
S1	2019-11-30	02:49:07.37	+06:20:10.75	21.77	21.39	0.38
S2	2019-11-30,2019-12-27	02:49:41.14	+06:23:20.33	18.69	17.17	1.52
S3	2019-12-27	02:49:42.54	+06:22:34.27	17.92	17.19	0.73
5BZQJ0646+4451	2019-11-30,2019-12-24	06:46:32.03	+44:51:16.59	19.95	18.33	1.62
S1	2019-11-30	06:46:46.29	+44:53:24.73	19.54	17.93	1.61
S2	2019-11-30	06:46:33.18	+44:52:32.99	19.97	17.63	2.34
S3	2019-12-24	06:45:56.50	+44:44:43.40	18.43	17.16	1.27
S4	2019-12-24	06:46:21.97	+44:59:00.15	19.44	17.31	2.13
5BZQJ0750+4814	2019-12-04,2019-12-27	07:50:20.44	+48:14:53.59	18.42	18.34	0.07
S1	2019-12-04,2019-12-27	07:49:40.50	+48:10:45.26	18.26	17.74	0.52
S2	2019-12-04,2019-12-27	07:49:38.34	+48:11:15.33	17.99	17.70	0.28
5BZQJ1017+6116	2020-03-22,2020-04-15	10:17:25.88	+61:16:27.51	18.30	18.07	0.23
S1	2020-03-22	10:16:58.66	+61:12:59.36	19.26	17.98	1.28
S2	2020-03-22	10:17:33.81	+61:19:36.42	19.04	17.62	1.42
S3	2020-04-15	10:16:11.59	+61:14:45.95	17.44	17.14	0.30
S4	2020-04-15	10:16:15.14	+61:15:20.87	17.41	17.11	0.29
5BZQJ1035+3756	2020-01-05,2020-04-12	10:35:51.17	+37:56:41.71	17.21	16.99	0.21
S1	2020-01-05	10:35:13.14	+37:48:02.31	17.00	16.06	0.94
S2	2020-01-05	10:35:46.60	+37:50:33.61	16.80	15.79	1.01
S3	2020-04-12	10:36:15.04	+37:54:13.48	16.69	16.08	0.61
S4	2020-04-12	10:35:59.41	+37:55:21.47	17.32	16.07	1.25
5BZQJ1125+2610	2020-03-23,2020-06-23	11:25:53.70	+26:10:19.99	18.16	18.24	-0.08
S1	2020-03-23,2020-06-23	11:26:08.30	+26:12:07.99	18.77	18.45	0.32
S2	2020-03-23,2020-06-23	11:25:45.46	+26:11:41.18	19.99	18.67	1.32
5BZQJ1126+4516	2020-01-26,2020-03-16	11:26:57.65	+45:16:06.31	17.18	17.19	-0.01
S1	2020-01-26,2020-03-16	11:26:20.03	+45:13:42.01	17.44	16.77	0.67
S2	2020-01-26,2020-03-16	11:26:17.81	+45:11:43.90	16.66	16.18	0.48
5BZQJ1306+4741	2020-03-22,2020-06-22	13:06:29.94	+47:41:32.49	18.54	18.26	0.28
S1	2020-03-22,2020-06-22	13:06:16.61	+47:42:16.79	20.00	18.56	1.44
S2	2020-03-22,2020-06-22	13:06:26.82	+47:44:32.80	19.71	18.26	1.45

5.2.3 The Data Reduction

Preliminary image processing tasks (see Section 5.1.3) were performed using the standard packages in IRAF. Aperture photometry was carried out using the task DAOPHOT II. SNR was found to peak for a photometric aperture radius nearly 2 times the seeing disc whose FWHM was determined by averaging the profiles of 5 fairly bright, unsaturated stars recorded in the same CCD frame. The measured instrumental magnitudes were then used to derive the DLCs of the target AGN relative to two (steady) comparison stars, as well as the star–star DLC for the session (see Section 5.1.3). In Fig. 5.7 and 5.8, we show the DLCs obtained for the 18 sessions.

5.2.4 Statistical analysis and Result

Following M19, we applied the widely used F^η test to the DLCs of the target AGN relative to the two comparison stars (s_1, s_2). Besides, this choice ensures an appropriate comparison of the INOV properties of the $m-z$ matched blazar sample with the BAL–blazar sample in M19, where we used the same F^η test for estimating INOV results (see Section 5.1.4). The parameter F^η computed for the two AGN DLCs, is defined as:

$$F_j^\eta = \frac{\text{Var}(q - s_j)}{\eta^2 \langle \sigma_{err}^2 \rangle}; \langle \sigma_{err}^2 \rangle = \sum_{i=1}^N \sigma_{i,err}^2 (q - s_j) / N \quad (5.3)$$

$\text{Var}(q - s_j)$: variance of the ‘ q - j^{th} comparison star’ DLC, with $j=1,2$; $\sigma_{i,err}(q - s_j)$: photometric error of the individual N observational data points in the DLC (which DAOPHOT routine has returned). For both DLCs, $i=1$ to N , and $\eta = 1.5$ (see Goyal et al. 2012).

Table 5.6 (Column 7) compares the measured values of F^η with the F ($= F_c^\alpha$) for each of the two DLCs of the target AGN. The values of α are set at 0.05 and 0.01, corresponding to 95% and 99% confidence levels for INOV detection. If the computed F^η for a DLC exceeds F_c^α , the null hypothesis (i.e., no variability) is rejected at the corresponding confidence level. We thus classify a DLC as ‘V’ if its computed $F^\eta > F_c(0.99)$; ‘PV’ if the F^η lies between $F_c(0.95)$ and $F_c(0.99)$, and ‘NV’ in case $F^\eta < F_c(0.95)$ (see Section 5.1.4). Column 11 in Table 5.6 lists the session averaged photometric accuracy of the measured differential magnitudes $\sqrt{\eta^2 \langle \sigma_{err}^2 \rangle}$. It is estimated using the two AGN-star DLCs and is nearly always better than 4% (median = 2.0%).

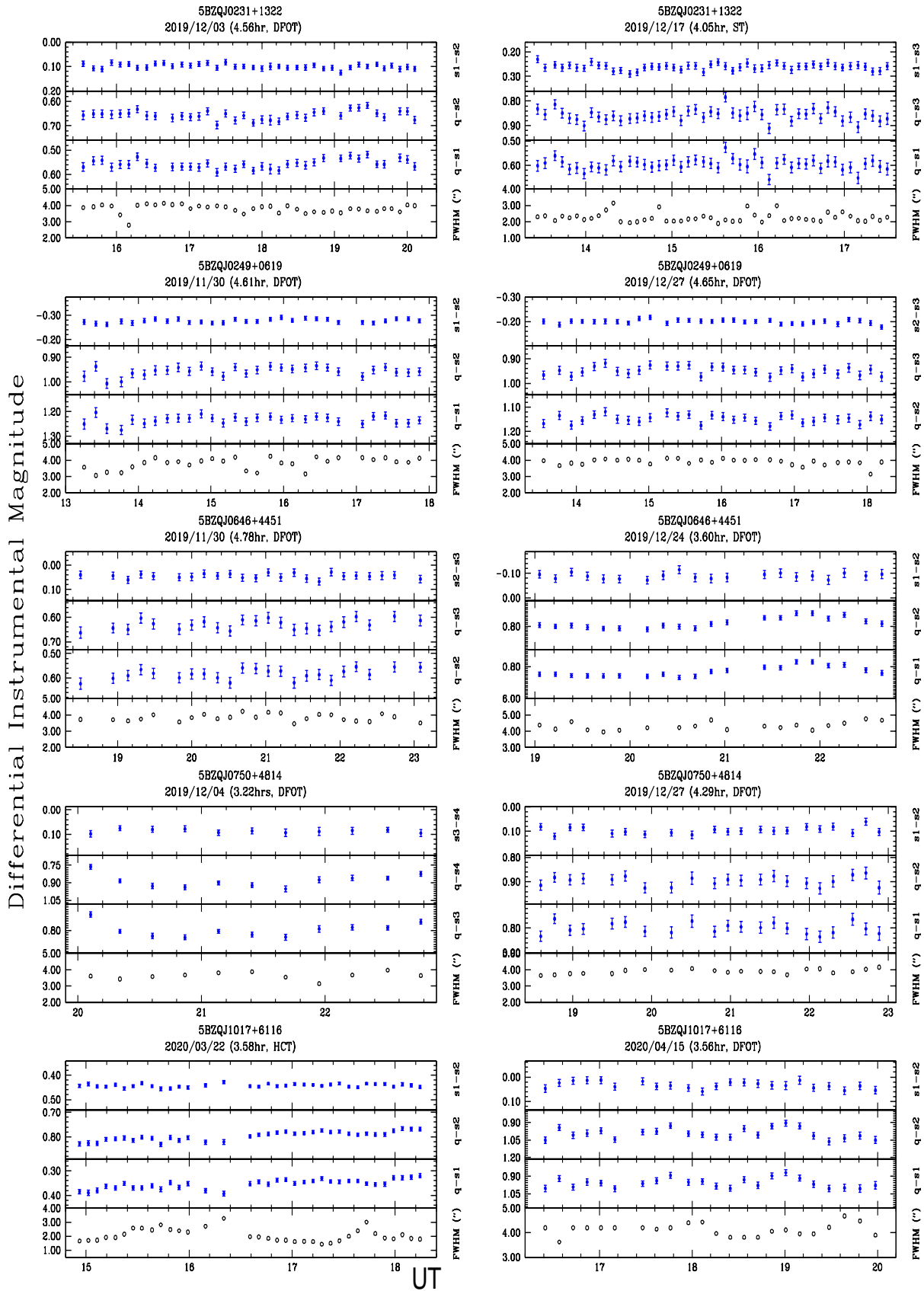


Figure 5.7: Same as Fig. 5.1 but for the $m-z$ matched blazar sample.

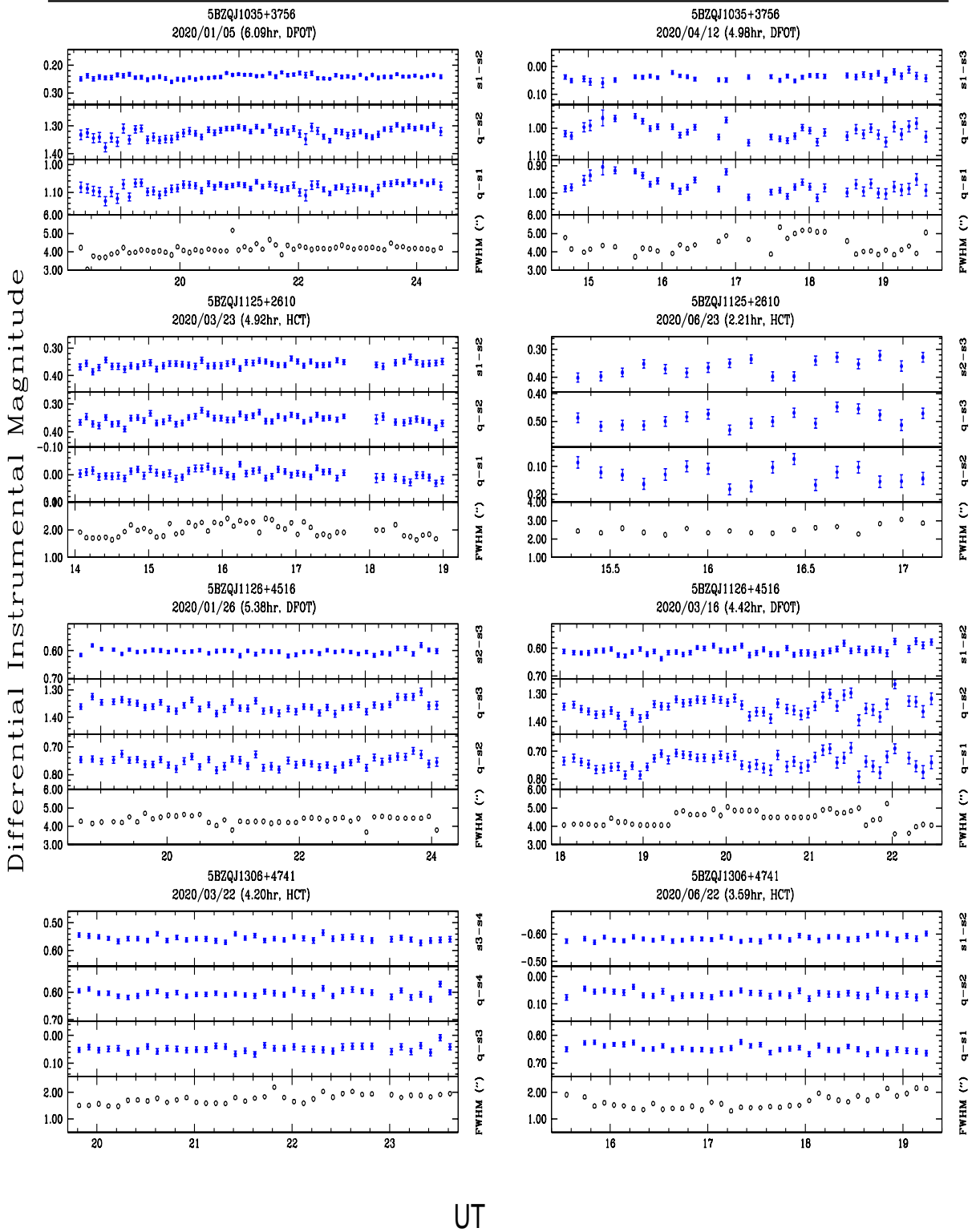


Figure 5.8: Same as Figure 5.7

Table 5.6: *Observation log and INOV results for the sample of 9 m-z matched blazars.*

AGN	Obs. date yyyy/mm/dd	Tel.	Filter	N	T hr	F-test		Variability [†] (q-s) F ⁿ	$\sqrt{\eta^2 \langle \sigma_{err}^2 \rangle}$	
						Computed F ₁ ⁿ , F ₂ ⁿ	Threshold values F _c (0.95) F _c (0.99)			
(1)	(2)	(3)	(4)	(5)	(6)	(7)	(8)	(9)	(10)	(11)
5BZQJ0231+1322	2019/12/03	DFOT	r	38	4.56	16.42 , 17.21	1.73	2.18	V ,V	0.02
5BZQJ0231+1322	2019/12/17	ST	R	48	4.06	0.48 , 0.58	1.62	1.99	NV ,NV	0.03
5BZQJ0249+0619	2019/11/30	DFOT	r	29	4.61	0.44 , 0.54	1.88	2.46	NV ,NV	0.03
5BZQJ0249+0619	2019/12/27	DFOT	r	30	4.65	0.43 , 0.46	1.86	2.42	NV ,NV	0.02
5BZQJ0646+4451	2019/11/30	DFOT	r	24	4.58	13.06 , 12.99	2.01	2.72	V ,V	0.03
5BZQJ0646+4451	2019/12/24	DFOT	r	20	3.60	2.38 , 2.14	2.17	3.03	PV ,NV	0.04
5BZQJ0750+4814	2019/12/04	DFOT	r	13	3.22	2.77 , 2.61	2.69	4.16	PV ,NV	0.04
5BZQJ0750+4814	2019/12/27	DFOT	r	21	4.29	0.42 , 0.31	2.12	2.94	NV ,NV	0.03
5BZQJ1017+6116	2020/03/22	HCT	R	35	3.31	2.24 , 2.53	1.77	2.26	PV ,V	0.01
5BZQJ1017+6116	2020/04/15	DFOT	r	23	3.56	1.05 , 1.32	2.05	2.78	NV ,NV	0.04
5BZQJ1035+3756	2020/01/05	DFOT	r	60	6.09	0.77 , 1.01	1.54	1.85	NV ,NV	0.02
5BZQJ1035+3756	2020/04/12	DFOT	r	36	4.90	1.61 , 1.46	1.76	2.23	NV ,NV	0.02
5BZQJ1125+2610	2020/03/23	HCT	R	52	4.92	0.73 , 0.85	1.59	1.94	NV ,NV	0.02
5BZQJ1125+2610	2020/06/23	HCT	R	21	2.21	0.95 , 0.71	2.12	2.94	NV ,NV	0.03
5BZQJ1126+4516	2020/01/26	DFOT	r	45	5.38	0.88 , 1.2	1.65	2.04	NV ,NV	0.02
5BZQJ1126+4516	2020/03/16	DFOT	r	50	4.42	1.05 , 1.56	1.61	1.96	NV ,NV	0.02
5BZQJ1306+4741	2020/03/22	HCT	R	42	4.20	0.44 , 0.64	1.68	2.09	NV ,NV	0.01
5BZQJ1306+4741	2020/06/22	HCT	R	37	3.69	0.88 , 0.44	1.74	2.21	NV ,NV	0.01

Notes. Col. 1: name of the AGN; Col. 2: date of monitoring; Col 3: telescope used; Col. 4: filter used; Col. 5: number of exposures/frames; Col. 6: duration of monitoring (T); Col. 7: F-value found for the q-s1 and q-s2 DLCs; Col. 8: critical F value for 95% confidence level; Col. 9: critical F value for 99% confidence level; Col. 10: Variability status; Col. 11: average photometric accuracy.

[†] V = variable at ≥ 0.99 confidence level; PV = probable variable at 0.95 – 0.99 confidence level; NV = non-variable at < 0.95 confidence level. Variability status values based on q-s1 and q-s2 pairs are separated by a comma.

5.2.5 Estimation of INOV DC

Similar to M19, we used the definition of [Romero et al. \(1999\)](#) for computing the DC of INOV, which is given by:

$$DC = 100 \frac{\sum_{i=1}^n K^i (1/T_{int}^i)}{\sum_{i=1}^n (1/T_{int}^i)} \text{percent} \quad (5.4)$$

where $T_{int}^i = T_{obs}^i (1 + z_{em})^{-1}$ is the intrinsic duration of monitoring corrected for the cosmological redshift, z_{em} and T_{obs}^i is the observed monitoring duration (Column 6 in Table 5.6) for the i^{th} night. K^i was taken as 1 in case of positive INOV detection, otherwise K^i was set to zero. The INOV DC for our sample of 18 sessions devoted to 9 $m-z$ matched blazars was found to be 11% when treating ‘PV’ cases as ‘NV’, while 19% when treating ‘PV’ cases as ‘V’.

5.2.6 Discussion and Conclusion

Numerous studies have been performed for characterizing the optical microvariability of RQ, RL, and blazar subclass of AGNs ([Carini et al. 1990, 1992](#); [Gopal-Krishna et al. 1995](#); [Stalin et al. 2004](#); [Gupta & Joshi 2005](#); [Gopal-Krishna et al. 2011](#); [Joshi et al. 2011](#); [Goyal et al. 2012, 2013](#); [Joshi & Chand 2013](#); [Kumar et al. 2016, 2017](#); [Ojha et al. 2020](#)). These studies on an average agree that the INOV DC for the blazars, being $\sim 60-70\%$, largely exceeds the typical INOV DC values reported for the other subclasses of AGNs (i.e., RL or RQ). The strong INOV detection in the blazars is invoked from the shock accelerated turbulence in the relativistic plasma jets, which gets enhanced due to the relativistic beaming effect in blazars ([Wagner & Witzel 1995](#)). On the other hand, the study of [Goyal et al. \(2012\)](#) revealed that the relativistic beaming is not sufficient for producing strong INOV, while high optical polarization is necessary.

However, in our recent study of M19, none of the 30 sessions of the representative sample of 10 BAL-blazars showed positive INOV. The blazar classification of our sources was mainly based on the flat/inverted radio spectrum and a large radio polarization. Such an absolute lack of INOV detection is exceptionally unusual for blazars. Just to assess how atypical the observed INOV behavior of BAL-blazars is, we may recall the INOV DC ($\sim 45\%$) reported in G13 for a large sample of 24 ‘normal’ blazars with 85 sessions (see Section 7 of G13), also based on the F^7 test. We also compared in M19 the INOV DC of our BAL-blazar sample with a comparison sample of 28 sessions devoted to 15 ‘normal’ (i.e., non-BAL) blazars from G13 matching in the rms error of the non-varying ‘star–star’ DLCs. The INOV DC of the comparison sample was found to be

41.2%. The explanation for the striking difference between the INOV DCs for normal and BAL blazars could potentially lie in their different luminosity and/or redshift distributions. The typical redshift for the BAL–blazar sample being considerably higher has resulted in their monitoring sessions being systematically shorter when measured in the rest-frames, and, conceivably, the likelihood of INOV detection might depend sensitively on the intrinsic (rest-frame) length of the monitoring session.

In order to overcome the effect of magnitude and redshift mismatch in the INOV results of the BAL–blazar and normal blazar samples of M19, we made an appropriate comparison sample of 9 normal blazars from the ROMA-BZCAT catalog matching in magnitude and redshift from that of BAL–blazars (see Fig. 5.5). Each blazar from the *m–z matched* blazar sample was observed twice using similar telescopes and in similar filters as of the M19 sample. We subjected the DLCs of the *m–z matched* blazar sample to the same INOV detection F^n test and presented their detailed INOV properties in Table 5.6. The INOV DC computed for this comparison sample was found to be 11% if considering ‘PV’ cases as ‘NV’, while 19% when treating ‘PV’ cases as ‘V’. Our results suggest that indeed the strong INOV detection of blazars correlates with the intrinsic duration of monitoring. However, based on the INOV DC of 11% for the *m–z matched* blazars in contrast to the complete absence of INOV for the BAL–blazar sample, we infer that the alternate possibility highlighted in M19 (see Section 5.1.5) is more likely to be a favorable scenario in explaining the INOV differences of two samples. In that scenario, the physical conditions in the relativistic jets of BAL blazars are less conducive for INOV generation, as compared to normal blazars in which INOV is generally thought to arise in a turbulent wake of a relativistic shock (e.g., Hughes et al. 1991; Marscher et al. 1992; Goyal et al. 2013). Conceivably, the shocks in the jets of BAL blazars are just not strong enough to accelerate relativistic particles to the high energies needed for optical synchrotron radiation, in spite of these sources being intrinsically powerful, as measured in terms of their radio luminosities at a low frequency of 150 MHz (see Table 5.1) where any relativistic Doppler boost is unlikely to be important (Miller et al. 1993).

Chapter 6

Summary, Conclusions and Future Prospects

6.1 Summary and Conclusions

Feedback is a ubiquitous signature of the AGNs. The feedback study of AGNs offers important insights into circum-galactic as well as inter-galactic environments. This thesis explores the impact of feedback processes in the form of radio jets and radiative winds at different length scales in different AGN sub-classes.

The first part of the thesis (Chapter 3) deals with the recently raised tension on the demarcating limit of the offset velocity (i.e., $\beta c \sim 5000 \text{ km s}^{-1}$) between the associated (with $\beta c < 5000 \text{ km s}^{-1}$) and intervening (with $\beta c > 5000 \text{ km s}^{-1}$) absorption line systems relative to the background quasar. In this context, it may be recalled that Bergeron et al. (2011, hereinafter BBM) has found that the value of dN/dz of intervening Mg II absorbers towards the 45 blazars is nearly two times the dN/dz value expected towards normal QSOs. In order to solve this puzzling finding of BBM on the excess incidence of Mg II absorbers along blazar sightlines, we have assembled a large sample of 191 blazars from archives of SDSS, ESO, and KECK (including the BBM sample of blazars). Based on our analysis of 23 weak ($0.3 \leq W_r < 1.0 \text{ \AA}$) and 20 strong ($W_r \geq 1 \text{ \AA}$) Mg II absorption systems, we conclude that (i) our independent analysis of the spectral data used by BBM for their blazar sample has reproduced the factor two excess claimed by them in dN/dz for Mg II absorbers seen towards blazars, vis-a-vis normal QSO; (ii) by using a ~ 3 times larger blazar sample (albeit, mostly with a moderate SNR) which includes the BBM sample as well, we

have arrived at a statistically more robust and independent estimate of dN/dz of Mg II absorbers along blazar sightlines. The present analysis does not show a significant difference from the dN/dz known for the sightlines towards normal QSOs; (iii) the agreement improves further when we limit the comparison to offset velocities above 60000 km s^{-1} . As a result, our work has confirmed the possibility that associated Mg II absorbers remain a significant contributor to dN/dz up to $\beta = 0.2c$ measured relative to the background QSO (Mishra et al. 2018).

In the second part of the thesis (Chapter 4), we extended our work of associated systems to examine the physical scenarios giving rise to an extreme variation of the C IV BAL troughs. First, we present a new set of 94 BAL quasars ($1.7 < z_{\text{em}} < 4.4$) exhibiting an appearance of C IV BAL troughs over 0.3–4.8 rest-frame years by comparing the SDSSDR-7, SDSSDR-12, and SDSSDR-14 quasar catalogs. Secondly, we contrast the nature of BAL variability in this appearing BAL quasar sample with disappearing BAL quasar sample studied in literature by comparing the quasar's intrinsic, BAL trough and continuum parameters between the two samples. We find that the appearing BAL quasars are brighter compared to the disappearing BAL quasars. The appearing BAL sample is also found to have shallower BAL troughs compared to the disappearing BAL sample. The distribution of quasar continuum variability parameters between the two samples is clearly separated with the appearance of the BAL troughs being accompanied by the dimming of the continuum and vice versa. Spectral index variations in the two samples also point to the anti-correlation between the BAL trough and continuum variations consistent with the "bluer when brighter" trend in quasars. We show that the intrinsic dust model is less likely to be a favorable scenario in explaining BAL appearance/disappearance. Our analysis suggests that the extreme variations of BAL troughs like BAL appearance/disappearance are mainly driven by changes in the ionization conditions of the absorbing gas.

In the last part of the thesis, we probe the similarity of the BAL quasars viewed nearly pole on with the blazar subclass of AGNs where jets are aligned within an angle of 10° relative to the observer (Mishra et al. 2019, Chapter 5.1). Since the later population of AGNs show rapid INOV on diverse time scales with $\text{DC} > 50\%$, one expects the polar BAL quasars with flat spectra and high radio polarization would also show the variability pattern in a similar way. Therefore, we probe for the INOV in the 30 monitoring sessions devoted to the 10 representative polar BAL quasars, and we found strikingly non-detection of INOV with zero DC in contrast to the normal blazar class. We comprehend this with one possible situation that the shocks induced turbulence in the jets of BAL quasars is not strong enough to accelerate relativistic particles to the high energies

needed for the emission of optical synchrotron radiation. Further, to observationally verify whether this marked contrast between the INOV of the BAL–blazars and the normal blazars has a physical origin, or it is due to the higher redshifts in case of the BAL–blazar rendering to shorter rest-frame intra-night monitoring durations compare to the normal blazars, we derive a comparison sample of 9 blazars (non-BAL) matching in magnitude and redshift with that of BAL–Blazars (Chapter 5.2). The intra-night optical monitoring of these 9 blazars over 18 monitoring sessions yielded an INOV DC of 11% (Mishra et al. 2020 to be submitted). Our results suggest that indeed the strong INOV detection of blazars correlates with the intrinsic duration of monitoring. However, the non-zero value of the INOV DC for our ‘m-z matched’ blazars in contrast to the lack of INOV for BAL–blazars, suggests that the alternate possibility highlighted in our recent work (Mishra et al. 2019, Chapter 5.1), where the relativistic jets of BAL blazars are less conducive for INOV generation is more likely to be a favorable scenario in explaining the INOV differences of the two samples.

In summary the main results presented in this thesis are as follows:

- Our study rule out the puzzling excess rate of incidence of intervening Mg II galaxies (i.e., dN/dz) towards the blazars as compared to normal QSOs. However, we show a possibility that the associated Mg II absorbers remain a significant contributor to dN/dz up to a velocity offset of $0.2c$ measured relative to the background QSOs (Mishra et al. 2018).
- Our analysis suggests that the extreme variations of BAL troughs like BAL appearance and disappearance are mainly driven by changes in the ionization conditions of the absorbing gas (Mishra et al. 2020, submitted in MNRAS).
- Our photometric analysis of 10 jet-aligned blazar-like BAL quasars shows no INOV detection, suggesting that the physical conditions in the relativistic jets of BAL quasars are less conducive for strong INOV (Mishra et al. 2019). Evidence in support of this scenario has been inferred based on our recent INOV study of a comparison sample of 9 blazars (non-BAL) matching in magnitude and redshift with that of BAL–Blazars (Mishra et al. 2020, to be submitted).

6.2 Future Prospects

Based on the detailed optical photometric and spectroscopic analysis, this thesis solves the various exciting puzzles of the AGNs using their radiative and kinetic feedbacks. However, promising future aspects which can be pursued as an extension of this research contribution are described below:

- Particularly in radio sources, the presence of powerful relativistic jets can plow out the ambient medium, resulting in the accumulation of material of large column density entrained at high velocity, which can be detected as an associated absorption system of many resonant lines such as Mg II and C IV. Our recent statistical computation of the incidence rate (dN/dz) of such absorption systems towards a large blazar sample compared to the normal quasars has indeed revealed an excess of the associated system towards the blazars up to an offset velocity of $0.2c$, similar to the ultra-fast outflows. In this regard, it would be fascinating to extend our previous analysis to compare the dN/dz of the associated systems among the steep spectrum radio quasars (SSRQs) and flat-spectrum radio quasars (FSRQs). The former subclass of quasar i.e., SSRQs being well evolved, is expected to have more time to interact with the surrounding material present in the CGM and the IGM. On the other hand, in the case of FSRQs, the jets are more aligned relative to our optical LOS. Hence, a systematic comparison of the dN/dz explicitly towards these two radio subclasses of quasars would unfold the relative role of the age and alignment of the relativistic jets on its encompassing medium.
- Our analysis presented a new set of 43 pristine BAL quasars exhibiting no-BAL to BAL transitions of C IV BAL troughs by comparing the SDSSDR-7, SDSSDR-12, and SDSSDR-14 quasar catalogs. Additional spectra for our sample of pristine appearing BAL quasars are currently being obtained in our ongoing spectral variability campaign using 2m class telescopes. Future spectroscopic monitoring of these objects will help to put further constraints on the exact nature of variability in these sources and to understand the dynamical evolution the outflowing BAL clouds.
- The BALs seen in the RL quasars offer a unique advantage by allowing the possibility to disentangle the relative roles of jet-dominated and disc-dominated acceleration mechanisms responsible for the BAL outflows. Dust in the fast-moving clouds of BAL quasars also affects their variability (Scoville & Norman 1995; Zhang et al. 2014; Gaskell et al.

2016; Tuccillo et al. 2017); hence in this context, the comparison of the spectral energy distribution of various sub-classes (e.g., RQ, RL, and blazar like) of BAL quasars would be crucial. Our continuum variability analysis isolates a rare population of BAL quasars, exhibiting blazar-like signatures. As a result, the SED comparison of this blazar-like BAL with a controlled sample of the relatively more abundant RQ, and RL population of BAL quasar would be a novel and exciting approach in ascertaining the dust scenario among these population of the BAL quasars. In our ongoing observing campaign, we have started a monitoring program for our BAL–blazar candidates in the J, H, K NIR band using 4-m class telescopes. The detailed monitoring of our entire sample would be crucial for the aforementioned goals.

Appendix A

Table A.1: Basic properties of our sample of 191 blazars.

Target	z_{em}	Data archive	Δz_{strong}^d	SNR	Target	z_{em}	Data archive	Δz_{strong}^d	SNR
J001937+202146	0.858	LRIS/KECK	0.393	6.4	J082324+222303	0.951	SDSS	0.626	20.4
J003808+001336	0.740	FORS/ESO	0.439	91.8	J082601-223027	0.910	FORS/ESO	0.520	211.4
J004054-091525	5.030	FORS/ESO	0.572	66.2	J083357+472652	0.494	SDSS	0.101	13.2
J010009-333730	0.875	FORS/ESO	0.486	58.8	J084225+025252	0.425	SDSS	0.036	13.3
J012031-270125	0.558	UVES/ESO	0.186	37.0	J084908+020622	1.174	SDSS	0.669	14.4
J014125-092843	0.730	SDSS	0.334	56.5	J090139+375246	0.477	SDSS	0.086	17.9
J020344+304237	0.761	SDSS	0.330	11.4	J090910+012135	1.022	FORS/ESO	0.630	111.8
J021046-510101	1.003	FORS/ESO	0.611	145.7	J092638+541126	0.841	SDSS	0.316	14.2
J021748+014449	1.715	FORS/ESO	0.924	180.2	J093807+371751	0.560	SDSS	0.021	13.3
J022048-084250	0.525	SDSS	0.132	29.1	J094257-004705	1.362	FORS/ESO	0.690	101.4
J023405-301519	1.690	FORS/ESO	0.924	130.8	J094827+083940	1.489	FORS/ESO	0.814	58.9
J023733-360329	0.411	Xsho/ESO	0.287	31.9	J095011+455320	0.399	SDSS	0.058	18.5
J023832-311658	0.233	Xsho/ESO	0.118	84.9	J095501+083342	0.727	SDSS	0.244	8.1
J023838+163659	0.940	FORS/ESO	0.550	68.7	J100040+531912	0.679	SDSS	0.201	8.3
J024156+004351	0.989	FORS/ESO	0.598	48.8	J100110+291137	0.558	SDSS	0.251	31.1
J025018-212940	0.498	FORS/ESO	0.070	41.9	J100656+345445	0.612	SDSS	0.216	8.9
J025927+074739	0.893	FORS/ESO	0.504	37.7	J100800+062121	0.650	SDSS	0.347	54.8
J030326-240710	0.266	Xsho/ESO	0.160	239.5	J100959+014533	1.080	FORS/ESO	0.413	37.5
J031712-075850	2.699	SDSS	1.510	11.7	J101115+010642	1.275	FORS/ESO	0.604	68.8
J033413-400825	1.351	FORS/ESO	0.658	102.5	J101213+063057	0.727	SDSS	0.412	31.7
J034923-115929	0.188	Xsho/ESO	0.062	46.2	J102339+300057	0.433	SDSS	0.113	21.8
J035700-495548	0.643	FORS/ESO	0.351	92.6	J102724+631753	0.672	SDSS	0.346	24.9
J042315-012033	0.915	FORS/ESO	0.525	149.2	J103118+505335	0.361	SDSS	0.043	49.9
J042840-375619	1.110	FORS/ESO	0.716	269.1	J103240+373826	0.528	SDSS	0.224	28.6
J043337+290555	0.970	KECK	0.551	7.3	J103607+015659	1.860	SDSS	1.445	11.4
J045703-232452	1.003	FORS/ESO	0.611	252.6	J104309+240835	0.560	SDSS	0.253	17.2
J050534+041551	0.424	Xsho/ESO	0.296	59.8	J104939+154837	0.327	SDSS	0.026	48.3
J053850-440508	0.890	FORS/ESO	0.501	303.3	J105125+394325	0.498	SDSS	0.183	21.3
J054357-553204	0.273	Xsho/ESO	0.154	71.1	J105431+385521	1.363	SDSS	1.043	38.3
J072659+373423	0.872	SDSS	0.451	13.1	J110124+410847	0.438	SDSS	0.044	13.4
J073346+411120	1.899	SDSS	1.473	18.5	J110704+501038	0.706	SDSS	0.200	9.4
J073807+174219	0.424	FORS/ESO	0.137	334.9	J110735+022224	1.074	SDSS	0.564	8.8
J074054+322600	0.946	SDSS	0.547	15.5	J110748+150210	0.664	SDSS	0.356	32.0
J074554-004417	0.994	FORS/ESO	0.602	217.3	J111224+175121	0.421	SDSS	0.020	14.4
J075445+482350	0.889	SDSS	0.571	61.4	J111757+535554	0.720	SDSS	0.395	35.2
J080115+133642	1.042	SDSS	0.540	16.5	J112903+375656	1.211	SDSS	0.778	13.5
J080323+481618	0.503	SDSS	0.009	12.1	J113115+023450	0.653	SDSS	0.178	17.7
J081126+014652	1.145	FORS/ESO	0.751	87.8	J113118+580858	0.360	SDSS	0.020	33.3
J081627-131151	0.189	Xsho/ESO	0.072	65.6	J113245+003427	1.234	FORS/ESO	0.564	92.5
J081751+324340	0.796	SDSS	0.393	12.4	J113900-020140	0.610	SDSS	0.051	7.7
J081815+422245	0.530	SDSS	0.214	34.0	J114153+021924	3.598	SDSS	1.263	12.2
J082051+235345	0.402	SDSS	0.022	26.0	J114701-381211	1.049	FORS/ESO	0.657	71.4

Table A.1: (continued)

Target	z_{em}	Data archive	Δz_{strong}^a	SNR	Target	z_{em}	Data archive	Δz_{strong}^a	SNR
J114926+624332	0.762	SDSS	0.248	10.5	J153925+421728	1.256	SDSS	0.814	12.4
J115342+382305	0.410	SDSS	0.014	10.5	J154049+144745	0.605	SDSS	0.271	30.5
J120257+385147	0.801	SDSS	0.326	21.4	J154515+003235	1.051	FORS/ESO	0.385	72.6
J120658+052952	0.841	SDSS	0.272	8.6	J154604+081913	0.513	SDSS	0.195	45.7
J121158+224232	0.453	SDSS	0.051	12.3	J154623+181715	1.006	SDSS	0.672	29.9
J121221+534127	3.190	SDSS	1.787	18.2	J155203+085047	1.016	SDSS	0.623	24.8
J121300+512935	0.796	SDSS	0.247	9.4	J155500+214159	1.286	SDSS	0.956	24.9
J121348+642520	0.888	SDSS	0.409	9.9	J155848+562514	0.903	SDSS	0.574	24.6
J121944+044622	0.489	SDSS	0.041	11.0	J160339+500955	0.621	SDSS	0.116	8.6
J122008+343121	0.588	SDSS	0.283	35.3	J160436+173325	1.007	SDSS	0.372	7.1
J122451+433519	0.703	SDSS	0.026	8.1	J161415+004722	1.562	SDSS	0.851	8.2
J122518+181821	0.696	SDSS	0.297	15.9	J162259+440142	0.511	SDSS	0.171	15.9
J123132+013813	3.230	SDSS	1.739	14.0	J162625+351341	0.498	SDSS	0.089	19.3
J123437-012951	1.060	SDSS	0.657	11.4	J163124+421702	0.467	SDSS	0.054	9.1
J123743+630144	3.535	SDSS	1.330	5.9	J164220+221143	0.592	SDSS	0.077	8.8
J123922+413251	0.461	SDSS	0.042	9.8	J164301+322104	1.028	SDSS	0.434	13.3
J124312+362743	0.485	SDSS	0.095	44.8	J164557+294730	0.958	SDSS	0.433	11.7
J124510+570954	0.521	SDSS	0.198	24.1	J165248+363212	0.648	SAO	0.165	14.3
J124533+022825	1.090	FORS/ESO	0.423	76.2	J170108+395443	1.890	SDSS	1.538	14.6
J124834+512807	0.351	SDSS	0.047	28.0	J170124+395437	0.507	SDSS	0.105	43.3
J125032+021632	0.959	SDSS	0.397	11.2	J171248+293116	0.421	SDSS	0.029	29.1
J125258-331959	0.856	FORS/ESO	0.468	32.7	J174358-035004	1.054	FORS/ESO	0.662	83.1
J125311+530111	0.664	SDSS	0.338	36.9	J182406+565100	0.660	SAO	0.438	50.7
J125359+624257	0.867	SDSS	0.552	31.4	J191816-411154	1.590	FORS/ESO	1.143	100.9
J125555+384811	0.560	SDSS	0.164	11.8	J195659-322546	1.242	FORS/ESO	0.569	48.0
J125716+364714	0.531	SDSS	0.138	20.1	J201515-013732	0.940	FORS/ESO	0.551	98.4
J130145+405624	0.649	SDSS	0.260	15.5	J203155+121941	1.215	FORS/ESO	0.525	48.7
J130925+430505	0.690	SDSS	0.366	49.0	J211552+000115	0.651	SDSS	0.054	11.4
J131028+322043	0.997	SDSS	0.590	25.2	J213410-015317	1.285	FORS/ESO	0.614	129.7
J131931+140533	0.573	SDSS	0.187	24.4	J213618-444348	0.980	FORS/ESO	0.590	76.4
J132614+293330	0.431	SDSS	0.034	19.4	J214302-392924	0.429	FORS/ESO	0.158	52.8
J133219+622715	3.150	SDSS	1.499	10.2	J215650-085535	1.017	SDSS	0.494	8.8
J133859+115316	1.580	FORS/ESO	0.903	176.0	J220719+004157	1.892	FORS/ESO	0.928	47.2
J134029+441003	0.546	SDSS	0.062	15.7	J221450-293225	1.636	FORS/ESO	0.924	101.0
J135120+111453	0.620	SDSS	0.298	44.0	J222543-111341	0.997	FORS/ESO	0.332	33.7
J135738+012813	0.564	SDSS	0.171	26.4	J222547-045701	1.404	FORS/ESO	0.710	158.3
J135949-374600	0.334	FORS/ESO	0.049	149.7	J222758+003705	1.093	SDSS	0.768	27.3
J140449+655431	0.362	SDSS	0.041	17.0	J224046+132602	0.660	SDSS	0.257	10.9
J140856-075226	1.500	FORS/ESO	0.825	119.3	J224326-254431	0.774	Xsho/ESO	0.617	32.9
J141004+020306	1.253	FORS/ESO	0.583	87.0	J224749+134248	1.175	SDSS	0.773	15.6
J141029+282055	0.521	SDSS	0.206	27.1	J225515+241011	0.863	SDSS	0.550	44.9
J141536+483030	0.496	SDSS	0.127	15.4	J230734+145017	0.503	SDSS	0.089	19.2
J141927+044513	1.680	FORS/ESO	0.945	107.1	J231116-103849	1.529	FORS/ESO	0.833	81.6
J142238+580155	0.635	SDSS	0.311	23.9	J231544-501839	0.808	FORS/ESO	0.180	42.9
J142409+043452	0.666	SDSS	0.346	33.2	J232428+144324	1.410	SDSS	1.002	12.5
J142505+035336	2.248	SDSS	1.516	9.5	J235725-015215	0.812	SDSS	0.371	11.1
J142756-420619	1.522	FORS/ESO	0.846	93.3					
J143758+300207	0.757	SDSS	0.362	18.0					
J143825+120419	0.848	SDSS	0.422	13.3					
J143917+393242	0.344	SDSS	0.035	48.7					
J144052+061016	0.316	SDSS	0.017	20.1					
J144207+434836	0.673	SDSS	0.190	25.7					
J144800+360831	0.739	SDSS	0.347	35.9					
J145127+635426	0.650	SAO	0.162	8.0					
J150006+012955	0.708	SDSS	0.250	8.5					
J150347+475930	1.323	SDSS	0.873	10.3					
J150818+563611	2.052	SDSS	1.028	6.6					
J152034+554257	2.016	SDSS	1.579	23.1					
J152237-273010	1.294	FORS/ESO	0.623	108.1					
J153058+573625	1.100	SDSS	0.511	13.0					
J153324+341640	0.811	SDSS	0.500	29.8					

^aThe redshift path contribution to the strong Mg II system
($W_r(2796) \geq 1.0 \text{ \AA}$) analysis.

Table A.2: *The detected 43 Mg II absorption systems and their rest-frame equivalent widths, $W_r(\text{Mg II } \lambda 2796 \text{ \AA})$, as identified in 34 blazars belonging to our sample of 191 blazars.*

Blazar	z_{em}	z_{abs}	W_r	Associated absorptions
J001937+202146	0.858	0.69616	1.0969	FeII2344,FeII2374,FeII2383,FeII2586,FeII2600
J010009-333730	0.875	0.67996	0.5110	Fe2383
J014125-092843	0.730	0.50042	0.3641	FeII2600,FeII2586
J021748+014449	1.715	1.34428	2.0130	MgI2852,ZnII,FeII2600,FeII2586,FeII2383,FeII2374,FeII2344,MnII
J023838+163659	0.940	0.52379	2.3725	MgI2852,FeII2600,FeII2586,FeII2383,MnII
J023838+163659	0.940	0.85163	0.4180	-
J024156+004351	0.989	0.77455	1.0803	FeII2600,FeII2586,FeII2383,FeII2374,FeII2344
J033413-400825	1.351	1.20829	0.8414	MgI2852,FeII2600,FeII2586,FeII2383,FeII2344
J042315-012033	0.915	0.63241	0.6889	MgI2852,FeII2600,FeII2586,FeII2383,FeII2344
J042840-375619	1.110	0.55833	1.0337	MgI2852,FeII2600,FeII2586,FeII2383,FeII2344
J042840-375619	1.110	1.02831	0.5341	AIII,FeII2600,FeII2383
J045703-232452	1.003	0.89117	2.2241	MgI2852,FeII2600,FeII2586,FeII2383,FeII2374,FeII2344,MnII
J075445+482350	0.889	0.83570	0.5600	MgI2852,FeII2600,FeII2586,FeII2383,FeII2374,FeII2344
J090910+012135	1.022	0.53547	0.3533	FeII2600
J094257-004705	1.362	0.81908	1.3618	MgI2852,FeII2600,FeII2586,MnII
J094257-004705	1.362	1.02386	0.3800	FeII2383
J094827+083940	1.489	1.07730	0.8824	FeII2600,FeII2383
J094827+083940	1.489	1.32810	4.0417	MgI2852,FeII2600,FeII2586,FeII2383,FeII2374,FeII2344,MnII
J094827+083940	1.489	1.42493	1.0460	MgI2852,FeII2600,FeII2586,FeII2383,FeII2374,FeII2344
J102724+631753	0.671	0.58094	1.3213	MgI2852,FeII2600,FeII2586,FeII2383,FeII2374,FeII2344,CaII
J110748+150210	0.664	0.60143	0.7363	FeII2600,FeII2383,MgI2852
J114153+021924	3.598	1.99163	2.7170	MgI2852,FeII2600,FeII2586,FeII2383,FeII2374,FeII2344,AIII, SiII, AIII, CIV, Cl*1657, Cl*
J120658+052952	0.840	0.78937	1.4952	MgI2852,FeII2600,FeII2586,FeII2383,FeII2374,FeII2344
J121221+534127	3.190	2.02630	0.4116	FeII2600,FeII2383, CIV, SiIV
J123132+013813	3.230	2.00494	1.8688	FeII2600,FeII2586,FeII2383,FeII2344, AIII, SiIV
J123743+630144	3.535	1.58914	2.2646	MgI2852,FeII2600,FeII2586,FeII2383,FeII2374,FeII2344, AIII, ZnII, CrII
J124533+022825	1.090	1.01221	0.6027	MgI2852,FeII2600,FeII2586,FeII2383,FeII2374,FeII2344
J140856-075226	1.500	1.27360	2.1917	MgI2852,FeII2600,FeII2586,FeII2383,FeII2374,FeII2344,MnII, CrII, ZnII
J141004+020306	1.253	1.11275	0.8646	FeII2600,FeII2383
J141927+044513	1.680	0.89951	0.7458	MgI2852,FeII2600,FeII2586
J141927+044513	1.680	1.08576	0.5330	FeII2600,FeII2586,FeII2383
J141927+044513	1.680	1.27255	0.6028	MgI2852,FeII2600,FeII2586,FeII2383,FeII2374,FeII2344
J142756-420619	1.522	1.09158	0.6354	FeII2600,FeII2383
J143825+120419	0.848	0.44680	1.6806	MgI2852,FeII2600,FeII2586,MnII
J174358-035004	1.054	0.52780	1.0002	MgI2852,FeII2600,FeII2586,FeII2383,FeII2374,FeII2344
J174358-035004	1.054	0.90769	2.3288	MgI2852,FeII2600,FeII2586,FeII2383,FeII2374,FeII2344
J182406+565100	0.660	0.60071	0.4588	MnII
J191816-411154	1.590	1.30941	0.9761	MgI2852,FeII2600,FeII2586,FeII2383,FeII2374,FeII2344
J195659-322546	1.242	1.06671	3.6020	MgI2852,FeII2600,FeII2586,FeII2383,FeII2374,FeII2344
J203155+121941	1.215	1.11570	0.9444	MgI2852,FeII2600,FeII2586,FeII2383,FeII2374,FeII2344
J213618-444348	0.980	0.51979	0.4621	MgI2852,FeII2600,FeII2383
J222547-045701	1.404	0.84585	0.5890	MgI2852,FeII2600,FeII2586
J232428+144324	1.410	1.03849	1.7139	FeII2600,FeII2586,FeII2383,FeII2374,FeII2344

Appendix B

Table B.1: Physical parameters of Preliminary sample of 379 BAL quasars with 517 MJD pairs.

BAL quasar	MJD-pair	z_{em}	M_i (mag)	$\log L_{bol}$ (erg s^{-1})	$\log M_{BH}$ (M_{\odot})	$\log \frac{L_{bol}}{L_{Edd}}$	Δt (years)
SDSS J000448.32+185635.8	56240-56945	2.480	-27.174	-999.9±-999.9	-999.9 ±-999.9	-999.9	0.555
SDSS J002028.34-002914.9	51816-56979	1.937	-26.678	46.763±0.009	9.483 ±0.052	-0.820	4.816
SDSS J002028.34-002914.9	51816-56979	1.937	-26.678	46.763±0.009	9.483 ±0.052	-0.820	4.816
SDSS J002028.34-002914.9	51900-56979	1.937	-26.678	46.763±0.009	9.483 ±0.052	-0.820	4.738
SDSS J002028.34-002914.9	51900-56979	1.937	-26.678	46.763±0.009	9.483 ±0.052	-0.820	4.738
SDSS J002238.35+273533.2	56570-57359	2.860	-28.006	-999.9±-999.9	-999.9 ±-999.9	-999.9	0.560
SDSS J002724.32+290807.0	56550-57361	3.069	-27.640	-999.9±-999.9	-999.9 ±-999.9	-999.9	0.546
SDSS J003150.73+062901.1	53710-54714	2.345	-27.559	46.577±0.011	0.000 ±-1.000	-999.0	0.822
SDSS J003150.73+062901.1	53710-54738	2.345	-27.559	46.577±0.011	0.000 ±-1.000	-999.0	0.842
SDSS J003150.73+062901.1	53710-55862	2.345	-27.559	46.577±0.011	0.000 ±-1.000	-999.0	1.763
SDSS J003150.73+062901.1	54714-54738	2.345	-27.559	46.577±0.011	0.000 ±-1.000	-999.0	0.020
SDSS J003150.73+062901.1	54714-55862	2.345	-27.559	46.577±0.011	0.000 ±-1.000	-999.0	0.940
SDSS J003150.73+062901.1	54738-55862	2.345	-27.559	46.577±0.011	0.000 ±-1.000	-999.0	0.921
SDSS J003837.71+134620.4	51817-51884	1.973	-26.524	46.621±0.018	8.792 ±0.070	-0.272	0.062
SDSS J003837.71+134620.4	51817-56191	1.973	-26.524	46.621±0.018	8.792 ±0.070	-0.272	4.031
SDSS J003837.71+134620.4	51884-56191	1.973	-26.524	46.621±0.018	8.792 ±0.070	-0.272	3.969
SDSS J005157.24+000354.7	51812-52201	1.949	-27.866	47.265±0.003	9.726 ±0.072	-0.562	0.361
SDSS J005157.24+000354.7	51812-54800	1.949	-27.866	47.265±0.003	9.726 ±0.072	-0.562	2.776
SDSS J005157.24+000354.7	51812-55451	1.949	-27.866	47.265±0.003	9.726 ±0.072	-0.562	3.381
SDSS J005157.24+000354.7	51812-57016	1.949	-27.866	47.265±0.003	9.726 ±0.072	-0.562	4.835
SDSS J005157.24+000354.7	51876-52201	1.949	-27.866	47.265±0.003	9.726 ±0.072	-0.562	0.302
SDSS J005157.24+000354.7	51876-54800	1.949	-27.866	47.265±0.003	9.726 ±0.072	-0.562	2.717
SDSS J005157.24+000354.7	51876-55451	1.949	-27.866	47.265±0.003	9.726 ±0.072	-0.562	3.321
SDSS J005157.24+000354.7	51876-57016	1.949	-27.866	47.265±0.003	9.726 ±0.072	-0.562	4.775
SDSS J005157.24+000354.7	51913-52201	1.949	-27.866	47.265±0.003	9.726 ±0.072	-0.562	0.268
SDSS J005157.24+000354.7	51913-54800	1.949	-27.866	47.265±0.003	9.726 ±0.072	-0.562	2.682
SDSS J005157.24+000354.7	51913-55451	1.949	-27.866	47.265±0.003	9.726 ±0.072	-0.562	3.287
SDSS J005157.24+000354.7	51913-57016	1.949	-27.866	47.265±0.003	9.726 ±0.072	-0.562	4.741
SDSS J005157.24+000354.7	52201-54800	1.949	-27.866	47.265±0.003	9.726 ±0.072	-0.562	2.415
SDSS J005157.24+000354.7	52201-55451	1.949	-27.866	47.265±0.003	9.726 ±0.072	-0.562	3.019
SDSS J005157.24+000354.7	52201-57016	1.949	-27.866	47.265±0.003	9.726 ±0.072	-0.562	4.473
SDSS J005157.24+000354.7	54800-55451	1.949	-27.866	47.265±0.003	9.726 ±0.072	-0.562	0.605
SDSS J005157.24+000354.7	54800-57016	1.949	-27.866	47.265±0.003	9.726 ±0.072	-0.562	2.059
SDSS J005157.24+000354.7	55451-57016	1.949	-27.866	47.265±0.003	9.726 ±0.072	-0.562	1.454
SDSS J005455.20+042108.9	55531-57373	2.931	-26.839	-999.9±-999.9	-999.9 ±-999.9	-999.9	1.284
SDSS J005953.35+192433.2	56190-56221	2.525	-27.452	-999.9±-999.9	-999.9 ±-999.9	-999.9	0.024
SDSS J005953.35+192433.2	56190-56901	2.525	-27.452	-999.9±-999.9	-999.9 ±-999.9	-999.9	0.553
SDSS J005953.35+192433.2	56221-56901	2.525	-27.452	-999.9±-999.9	-999.9 ±-999.9	-999.9	0.529
SDSS J013655.74+225811.9	53341-55940	2.510	-27.165	46.779±0.011	9.751 ±0.165	-1.072	2.029
SDSS J013655.74+225811.9	53341-57007	2.510	-27.165	46.779±0.011	9.751 ±0.165	-1.072	2.861

Table B.1: (continued)

BAL quasar	MJD-pair	z_{em}	M_i (mag)	$\log L_{bol}$ (erg s $^{-1}$)	$\log M_{BH}$ (M_{\odot})	$\log \frac{L_{bol}}{L_{Edd}}$	Δt (years)
SDSS J013655.74+225811.9	55940-57007	2.510	-27.165	46.779±0.011	9.751 ±0.165	-1.072	0.833
SDSS J013812.07-003002.4	52203-55444	2.614	-27.254	46.723±0.019	9.148 ±0.063	-0.525	2.457
SDSS J014029.96-082039.5	52145-56605	1.932	-26.547	46.830±0.011	9.354 ±0.076	-0.625	4.168
SDSS J015030.68+005953.6	55447-57003	2.251	-26.022	46.443±0.024	8.867 ±0.229	-0.524	1.311
SDSS J020826.41+003810.5	52937-55201	2.365	-26.672	46.573±0.016	9.372 ±0.129	-0.899	1.843
SDSS J020826.41+003810.5	52937-55451	2.365	-26.672	46.573±0.016	9.372 ±0.129	-0.899	2.047
SDSS J020826.41+003810.5	55201-55451	2.365	-26.672	46.573±0.016	9.372 ±0.129	-0.899	0.204
SDSS J022605.62-005044.7	55179-55445	2.275	-26.244	46.438±0.025	8.599 ±0.233	-0.262	0.223
SDSS J022605.62-005044.7	55179-55478	2.275	-26.244	46.438±0.025	8.599 ±0.233	-0.262	0.250
SDSS J022605.62-005044.7	55179-56544	2.275	-26.244	46.438±0.025	8.599 ±0.233	-0.262	1.142
SDSS J022605.62-005044.7	55445-55478	2.275	-26.244	46.438±0.025	8.599 ±0.233	-0.262	0.028
SDSS J022605.62-005044.7	55445-56544	2.275	-26.244	46.438±0.025	8.599 ±0.233	-0.262	0.919
SDSS J022605.62-005044.7	55478-56544	2.275	-26.244	46.438±0.025	8.599 ±0.233	-0.262	0.892
SDSS J023359.08-081631.9	53738-55539	2.759	-28.499	47.199±0.004	9.562 ±0.042	-0.464	1.313
SDSS J023423.47-075939.4	51909-53738	2.543	-27.228	46.896±0.011	9.296 ±0.452	-0.501	1.414
SDSS J023423.47-075939.4	51909-55539	2.543	-27.228	46.896±0.011	9.296 ±0.452	-0.501	2.807
SDSS J023423.47-075939.4	53738-55539	2.543	-27.228	46.896±0.011	9.296 ±0.452	-0.501	1.393
SDSS J024006.11-002037.6	51821-55247	1.706	-27.504	46.954±0.004	9.588 ±0.056	-0.734	3.469
SDSS J024006.11-002037.6	51821-55458	1.706	-27.504	46.954±0.004	9.588 ±0.056	-0.734	3.682
SDSS J024006.11-002037.6	52199-55247	1.706	-27.504	46.954±0.004	9.588 ±0.056	-0.734	3.086
SDSS J024006.11-002037.6	52199-55458	1.706	-27.504	46.954±0.004	9.588 ±0.056	-0.734	3.300
SDSS J024006.11-002037.6	55247-55458	1.706	-27.504	46.954±0.004	9.588 ±0.056	-0.734	0.214
SDSS J024532.49-002737.9	56273-56572	2.139	-25.957	46.330±0.029	9.079 ±0.123	-0.849	0.261
SDSS J024532.49-002737.9	56273-56572	2.139	-25.957	46.330±0.029	9.079 ±0.123	-0.849	0.261
SDSS J072134.30+413108.8	53313-55241	2.180	-27.204	46.810±0.012	9.536 ±0.091	-0.826	1.661
SDSS J073938.18+443123.1	55209-55481	1.975	-25.650	-999.9±-999.9	-999.9 ±-999.9	-999.9	0.250
SDSS J073938.18+443123.1	55209-56210	1.975	-25.650	-999.9±-999.9	-999.9 ±-999.9	-999.9	0.922
SDSS J073938.18+443123.1	55481-56210	1.975	-25.650	-999.9±-999.9	-999.9 ±-999.9	-999.9	0.671
SDSS J075010.17+304032.3	52663-55538	1.901	-27.096	46.871±0.011	9.196 ±0.180	-0.426	2.715
SDSS J075354.34+181449.6	54419-55629	2.367	-26.736	46.758±0.010	9.435 ±0.042	-0.777	0.985
SDSS J075707.27+355910.2	52238-55501	2.364	-27.361	46.891±0.010	8.940 ±0.369	-0.149	2.657
SDSS J080105.01+345006.7	52584-55488	2.848	-26.951	46.724±0.022	8.674 ±0.162	-0.050	2.068
SDSS J080105.01+345006.7	52584-55488	2.848	-26.951	46.724±0.022	8.674 ±0.162	-0.050	2.068
SDSS J081026.42+101041.0	54153-55574	2.502	-28.955	47.366±0.004	10.283 ±0.080	-1.017	1.112
SDSS J081417.55-000455.0	53816-55889	2.587	-28.854	47.326±0.006	9.824 ±0.063	-0.598	1.583
SDSS J081750.44+372940.1	54097-55268	2.156	-26.100	46.325±0.017	9.187 ±0.070	-0.962	1.017
SDSS J081750.44+372940.1	54097-57449	2.156	-26.100	46.325±0.017	9.187 ±0.070	-0.962	2.910
SDSS J081750.44+372940.1	55268-57449	2.156	-26.100	46.325±0.017	9.187 ±0.070	-0.962	1.893
SDSS J081855.70+385949.6	54097-55269	2.411	-27.270	46.696±0.022	8.665 ±0.443	-0.069	0.941
SDSS J081929.59+232237.4	53317-55592	1.848	-28.130	47.259±0.008	9.868 ±0.055	-0.709	2.189
SDSS J082017.08+124556.9	54096-55571	2.280	-27.160	46.675±0.013	9.560 ±0.060	-0.985	1.232
SDSS J082017.08+124556.9	54096-55600	2.280	-27.160	46.675±0.013	9.560 ±0.060	-0.985	1.256
SDSS J082017.08+124556.9	55571-55600	2.280	-27.160	46.675±0.013	9.560 ±0.060	-0.985	0.024
SDSS J082913.76+415448.4	52266-54524	2.585	-27.532	46.680±0.014	8.405 ±0.078	0.174	1.726
SDSS J082913.76+415448.4	52266-54524	2.585	-27.532	46.680±0.014	8.405 ±0.078	0.174	1.726
SDSS J082913.76+415448.4	52266-55513	2.585	-27.532	46.680±0.014	8.405 ±0.078	0.174	2.481
SDSS J082913.76+415448.4	52266-55513	2.585	-27.532	46.680±0.014	8.405 ±0.078	0.174	2.481
SDSS J082913.76+415448.4	54524-55513	2.585	-27.532	46.680±0.014	8.405 ±0.078	0.174	0.756
SDSS J082913.76+415448.4	54524-55513	2.585	-27.532	46.680±0.014	8.405 ±0.078	0.174	0.756
SDSS J083212.37+530327.3	55925-57012	4.052	-28.028	47.141±0.020	9.899 ±0.113	-0.859	0.589
SDSS J083725.17+541842.0	51899-55925	2.057	-27.110	46.820±0.008	9.257 ±0.245	-0.537	3.608
SDSS J083725.17+541842.0	51899-56751	2.057	-27.110	46.820±0.008	9.257 ±0.245	-0.537	4.348
SDSS J083725.17+541842.0	51899-56751	2.057	-27.110	46.820±0.008	9.257 ±0.245	-0.537	4.348
SDSS J083725.17+541842.0	55925-56751	2.057	-27.110	46.820±0.008	9.257 ±0.245	-0.537	0.740
SDSS J083725.17+541842.0	55925-56751	2.057	-27.110	46.820±0.008	9.257 ±0.245	-0.537	0.740
SDSS J084033.84+052626.0	52650-55927	2.246	-27.078	46.863±0.010	9.009 ±0.089	-0.247	2.766
SDSS J084033.84+052626.0	52708-55927	2.246	-27.078	46.863±0.010	9.009 ±0.089	-0.247	2.717
SDSS J084048.22+202543.1	53705-55565	2.464	-27.596	46.914±0.015	9.359 ±0.105	-0.546	1.471

Table B.1: (continued)

BAL quasar	MJD-pair	z_{em}	M_i (mag)	$\log L_{bol}$ (erg s^{-1})	$\log M_{BH}$ (M_{\odot})	$\log \frac{L_{bol}}{L_{Edd}}$	Δt (years)
SDSS J084048.22+202543.1	53705-55565	2.464	-27.596	46.914±0.015	9.359 ±0.105	-0.546	1.471
SDSS J084104.49+420818.9	52592-55924	2.752	-27.310	46.753±0.017	8.554 ±0.034	0.098	2.433
SDSS J084147.86+053038.7	52708-55927	2.230	-27.568	46.958±0.012	8.718 ±0.121	0.140	2.730
SDSS J084147.86+053038.7	52708-55927	2.230	-27.568	46.958±0.012	8.718 ±0.121	0.140	2.730
SDSS J084244.39+152901.9	53799-53800	2.290	-27.639	47.093±0.008	9.655 ±0.095	-0.662	0.001
SDSS J084244.39+152901.9	53799-53815	2.290	-27.639	47.093±0.008	9.655 ±0.095	-0.662	0.013
SDSS J084244.39+152901.9	53799-56225	2.290	-27.639	47.093±0.008	9.655 ±0.095	-0.662	2.020
SDSS J084244.39+152901.9	53799-56225	2.290	-27.639	47.093±0.008	9.655 ±0.095	-0.662	2.020
SDSS J084244.39+152901.9	53800-53815	2.290	-27.639	47.093±0.008	9.655 ±0.095	-0.662	0.012
SDSS J084244.39+152901.9	53800-56225	2.290	-27.639	47.093±0.008	9.655 ±0.095	-0.662	2.019
SDSS J084244.39+152901.9	53800-56225	2.290	-27.639	47.093±0.008	9.655 ±0.095	-0.662	2.019
SDSS J084244.39+152901.9	53815-56225	2.290	-27.639	47.093±0.008	9.655 ±0.095	-0.662	2.007
SDSS J084244.39+152901.9	53815-56225	2.290	-27.639	47.093±0.008	9.655 ±0.095	-0.662	2.007
SDSS J084410.34+593330.6	54439-56220	2.210	-27.016	46.820±0.013	9.151 ±0.172	-0.431	1.520
SDSS J084611.14+115202.6	53801-55952	2.249	-27.558	46.997±0.010	8.724 ±0.048	0.173	1.814
SDSS J084837.07+151202.9	53799-55862	2.420	-28.113	47.190±0.006	9.777 ±0.028	-0.687	1.653
SDSS J085038.16+454923.7	52235-55893	2.060	-26.436	46.546±0.023	9.413 ±0.134	-0.968	3.275
SDSS J085330.69+254250.0	53381-55957	2.418	-28.327	47.319±0.006	9.547 ±0.078	-0.328	2.065
SDSS J085330.69+254250.0	53381-55957	2.418	-28.327	47.319±0.006	9.547 ±0.078	-0.328	2.065
SDSS J085509.77+593204.3	54439-56605	2.320	-27.101	46.878±0.014	9.530 ±0.061	-0.751	1.787
SDSS J085512.32+251208.5	53381-55957	2.260	-27.637	47.023±0.008	9.514 ±0.128	-0.592	2.165
SDSS J085841.93+124932.1	53820-55953	2.075	-27.023	46.854±0.009	8.804 ±0.070	-0.050	1.900
SDSS J090002.20+180404.3	53729-55955	2.880	-28.014	47.013±0.013	8.902 ±0.104	0.011	1.572
SDSS J090002.20+180404.3	53729-55955	2.880	-28.014	47.013±0.013	8.902 ±0.104	0.011	1.572
SDSS J090122.67+204446.5	53683-56009	2.093	-28.430	46.953±0.013	9.574 ±0.035	-0.722	2.060
SDSS J090744.96+543142.4	51908-56334	2.303	-27.256	46.854±0.007	9.481 ±0.061	-0.727	3.671
SDSS J090924.01+000211.0	51929-55532	1.871	-29.150	47.469±0.008	10.020 ±0.088	-0.652	3.438
SDSS J090950.53+245846.0	53401-56328	2.372	-27.590	46.965±0.011	9.448 ±0.093	-0.584	2.378
SDSS J091259.00+131910.3	54054-55980	2.056	-26.820	46.478±0.019	9.292 ±0.092	-0.914	1.727
SDSS J091259.00+131910.3	54054-55980	2.056	-26.820	46.478±0.019	9.292 ±0.092	-0.914	1.727
SDSS J091354.58+610948.8	54450-56686	1.802	-26.367	46.578±0.011	9.602 ±0.079	-1.125	2.186
SDSS J091354.58+610948.8	54450-56722	1.802	-26.367	46.578±0.011	9.602 ±0.079	-1.125	2.222
SDSS J091354.58+610948.8	56686-56722	1.802	-26.367	46.578±0.011	9.602 ±0.079	-1.125	0.035
SDSS J091427.18+582752.3	51907-56597	2.069	-26.519	46.549±0.013	9.433 ±0.079	-0.984	4.187
SDSS J091616.42+123449.4	54086-55980	1.821	-26.710	46.580±0.016	9.319 ±0.127	-0.839	1.839
SDSS J091616.42+123449.4	54086-55980	1.821	-26.710	46.580±0.016	9.319 ±0.127	-0.839	1.839
SDSS J091701.45+303808.4	53379-56304	3.021	-27.838	46.913±0.017	9.172 ±0.043	-0.359	1.993
SDSS J091701.45+303808.4	53379-56304	3.021	-27.838	46.913±0.017	9.172 ±0.043	-0.359	1.993
SDSS J091745.24+555934.9	51908-56597	1.955	-26.688	46.509±0.016	9.146 ±0.101	-0.737	4.347
SDSS J091909.82+463435.8	52620-56363	1.919	-27.073	46.502±0.016	9.896 ±0.095	-1.495	3.513
SDSS J092127.68+221120.1	53727-56011	2.064	-26.976	46.650±0.012	9.558 ±0.228	-1.009	2.042
SDSS J092301.75+332731.4	54550-56358	2.049	-25.628	46.008±0.018	9.012 ±0.091	-1.104	1.625
SDSS J092316.93+033146.9	52254-55889	2.151	-26.956	46.834±0.009	9.612 ±0.119	-0.879	3.161
SDSS J092331.00+181956.0	53728-56245	1.982	-26.588	46.545±0.022	8.860 ±0.197	-0.415	2.313
SDSS J092337.69+462100.1	52314-56363	2.227	-27.249	46.829±0.011	9.168 ±0.052	-0.439	3.438
SDSS J092504.39+561004.9	51908-56720	2.147	-26.849	46.571±0.020	9.213 ±0.208	-0.743	4.189
SDSS J092504.39+561004.9	51908-56720	2.147	-26.849	46.571±0.020	9.213 ±0.208	-0.743	4.189
SDSS J092645.89+513502.6	56739-57040	2.548	-26.840	-999.9±-999.9	-999.9 ±-999.9	-999.9	0.232
SDSS J092743.01+290734.7	53389-56272	2.249	-27.157	46.789±0.014	9.566 ±0.147	-0.878	2.431
SDSS J092905.45+340434.4	52991-56358	3.454	-28.002	46.891±0.018	9.419 ±0.037	-0.628	2.071
SDSS J092905.45+340434.4	52991-56358	3.454	-28.002	46.891±0.018	9.419 ±0.037	-0.628	2.071
SDSS J092905.45+340434.4	52991-56358	3.454	-28.002	46.891±0.018	9.419 ±0.037	-0.628	2.071
SDSS J092905.45+340434.4	52991-56358	3.454	-28.002	46.891±0.018	9.419 ±0.037	-0.628	2.071
SDSS J092915.49+351013.7	52995-55592	2.865	-27.782	46.994±0.019	9.774 ±0.102	-0.881	1.841
SDSS J092915.49+351013.7	52995-56358	2.865	-27.782	46.994±0.019	9.774 ±0.102	-0.881	2.384
SDSS J092915.49+351013.7	55592-56358	2.865	-27.782	46.994±0.019	9.774 ±0.102	-0.881	0.543
SDSS J093059.73+560229.8	51991-56720	2.975	-27.957	47.147±0.013	9.381 ±0.048	-0.334	3.259
SDSS J093422.85+142408.6	54068-55978	2.850	-27.508	46.914±0.022	9.158 ±0.085	-0.345	1.359
SDSS J093630.22+155418.2	54085-56000	2.192	-27.546	46.891±0.009	9.469 ±0.067	-0.678	1.644

Table B.1: (continued)

BAL quasar	MJD-pair	z_{em}	M_i (mag)	$\log L_{bol}$ (erg s $^{-1}$)	$\log M_{BH}$ (M_{\odot})	$\log \frac{L_{bol}}{L_{Edd}}$	Δt (years)
SDSS J093630.22+155418.2	54085-56000	2.192	-27.546	46.891±0.009	9.469 ±0.067	-0.678	1.644
SDSS J093714.78+175253.6	53733-56248	2.045	-27.133	46.823±0.010	9.657 ±0.097	-0.934	2.263
SDSS J093714.78+175253.6	53733-56248	2.045	-27.133	46.823±0.010	9.657 ±0.097	-0.934	2.263
SDSS J093739.89+334053.5	52992-56336	2.231	-26.919	46.622±0.013	9.454 ±0.119	-0.933	2.836
SDSS J093744.85+325605.1	53386-56336	2.054	-27.064	46.815±0.010	9.341 ±0.037	-0.626	2.646
SDSS J093846.82+302418.5	53415-56309	2.459	-27.599	46.993±0.010	9.082 ±0.157	-0.189	2.292
SDSS J093921.21+264756.3	53738-56255	2.017	-27.754	46.949±0.010	9.720 ±0.081	-0.871	2.286
SDSS J094043.86+134427.9	54092-55978	1.934	-26.925	46.499±0.015	9.324 ±0.086	-0.925	1.761
SDSS J094311.71+291109.9	53385-56298	2.034	-28.026	47.174±0.005	9.062 ±0.022	0.012	2.630
SDSS J094319.27+210648.2	53713-56251	1.960	-26.909	46.497±0.023	8.889 ±0.190	-0.492	2.349
SDSS J094540.23+640001.7	54468-56746	2.312	-27.262	46.592±0.026	8.782 ±0.083	-0.289	1.884
SDSS J094540.23+640001.7	54468-56746	2.312	-27.262	46.592±0.026	8.782 ±0.083	-0.289	1.884
SDSS J094554.99+230538.7	53734-56255	3.250	-28.862	47.246±0.009	10.111 ±0.053	-0.965	1.625
SDSS J094647.06+232750.6	53734-56255	2.595	-26.365	47.182±0.010	9.774 ±0.092	-0.693	1.921
SDSS J094927.88+111518.2	53054-55945	3.823	-28.527	47.309±0.010	9.768 ±0.080	-0.560	1.642
SDSS J095005.90+362455.2	52999-55587	2.245	-27.550	46.958±0.007	9.572 ±0.085	-0.715	2.185
SDSS J095005.90+362455.2	52999-57449	2.245	-27.550	46.958±0.007	9.572 ±0.085	-0.715	3.757
SDSS J095005.90+362455.2	55587-57449	2.245	-27.550	46.958±0.007	9.572 ±0.085	-0.715	1.572
SDSS J095038.50+300133.2	53432-56328	1.910	-26.846	46.754±0.010	9.864 ±0.227	-1.210	2.727
SDSS J095120.52+505348.5	56002-56709	1.809	-25.454	46.063±0.020	8.090 ±0.764	-0.128	0.690
SDSS J095217.51+534854.7	52282-56381	2.445	-27.625	46.840±0.011	8.709 ±0.050	0.031	3.260
SDSS J095217.51+534854.7	54530-56381	2.445	-27.625	46.840±0.011	8.709 ±0.050	0.031	1.472
SDSS J095258.10+195553.1	53759-56272	1.947	-28.126	46.975±0.010	9.050 ±0.026	-0.175	2.336
SDSS J095258.10+195553.1	53759-56272	1.947	-28.126	46.975±0.010	9.050 ±0.026	-0.175	2.336
SDSS J095349.60+320548.4	53433-56325	2.782	-28.106	47.123±0.009	9.685 ±0.082	-0.662	2.095
SDSS J095651.57+004508.5	54479-55539	2.481	-26.864	46.557±0.016	9.668 ±0.182	-1.211	0.834
SDSS J095728.86+165527.9	54095-56002	1.898	-27.030	46.791±0.006	9.117 ±0.147	-0.426	1.803
SDSS J095733.44+215320.9	53737-56029	2.001	-26.782	46.373±0.019	8.901 ±0.088	-0.629	2.092
SDSS J095733.44+215320.9	53737-56029	2.001	-26.782	46.373±0.019	8.901 ±0.088	-0.629	2.092
SDSS J095835.98+015157.0	51994-55630	2.932	-27.266	46.803±0.018	8.415 ±0.087	0.288	2.533
SDSS J100003.25+282628.1	53757-56309	2.075	-27.064	46.675±0.015	9.164 ±0.063	-0.589	2.274
SDSS J100003.25+282628.1	53757-56309	2.075	-27.064	46.675±0.015	9.164 ±0.063	-0.589	2.274
SDSS J100016.09+450153.1	52703-55632	3.318	-28.192	46.970±0.015	8.884 ±0.163	-0.015	1.858
SDSS J100201.38+232408.6	53737-56273	2.964	-27.600	46.734±0.023	9.462 ±0.084	-0.828	1.753
SDSS J100201.38+232408.6	53737-56273	2.964	-27.600	46.734±0.023	9.462 ±0.084	-0.828	1.753
SDSS J100201.38+232408.6	53737-56273	2.964	-27.600	46.734±0.023	9.462 ±0.084	-0.828	1.753
SDSS J100201.50+144446.4	54169-54880	2.718	-27.020	46.866±0.013	8.767 ±0.054	-0.002	0.524
SDSS J100201.50+144446.4	54169-54880	2.718	-27.020	46.866±0.013	8.767 ±0.054	-0.002	0.524
SDSS J100201.50+144446.4	54169-55980	2.718	-27.020	46.866±0.013	8.767 ±0.054	-0.002	1.334
SDSS J100201.50+144446.4	54169-55980	2.718	-27.020	46.866±0.013	8.767 ±0.054	-0.002	1.334
SDSS J100201.50+144446.4	54169-55980	2.718	-27.020	46.866±0.013	8.767 ±0.054	-0.002	1.334
SDSS J100201.50+144446.4	54880-55980	2.718	-27.020	46.866±0.013	8.767 ±0.054	-0.002	0.811
SDSS J100201.50+144446.4	54880-55980	2.718	-27.020	46.866±0.013	8.767 ±0.054	-0.002	0.811
SDSS J100201.50+144446.4	54880-55980	2.718	-27.020	46.866±0.013	8.767 ±0.054	-0.002	0.811
SDSS J100257.85+205406.1	53737-56029	2.431	-28.204	47.096±0.008	9.572 ±0.037	-0.576	1.830
SDSS J100336.90+252038.5	53740-56310	2.640	-27.457	46.630±0.017	9.292 ±0.118	-0.762	1.934
SDSS J100342.73+240622.3	53735-56273	1.864	-27.562	47.033±0.003	9.527 ±0.068	-0.594	2.428
SDSS J100421.15+260135.3	53740-56270	1.903	-28.043	47.128±0.027	9.443 ±0.055	-0.415	2.388
SDSS J100513.61+004028.3	52235-55300	2.568	-29.007	47.543±0.005	9.746 ±0.023	-0.303	2.353
SDSS J100513.61+004028.3	52235-55300	2.568	-29.007	47.543±0.005	9.746 ±0.023	-0.303	2.353
SDSS J100733.78+210945.1	53737-56034	2.404	-27.166	46.816±0.013	9.207 ±0.031	-0.491	1.849
SDSS J100755.50+211834.7	53737-56034	2.914	-26.927	46.407±0.030	8.734 ±0.216	-0.427	1.608
SDSS J100755.50+211834.7	53737-56034	2.914	-26.927	46.407±0.030	8.734 ±0.216	-0.427	1.608
SDSS J101319.80+235834.8	56274-56310	3.170	-26.916	46.256±0.023	9.305 ±0.070	-1.149	0.024
SDSS J101408.82+473150.6	52347-56364	1.901	-26.744	46.735±0.010	8.720 ±0.518	-0.086	3.794
SDSS J101408.82+473150.6	52674-56364	1.901	-26.744	46.735±0.010	8.720 ±0.518	-0.086	3.485
SDSS J101617.67+405912.3	53034-55570	2.366	-27.293	46.761±0.016	9.113 ±0.092	-0.452	2.064
SDSS J101617.67+405912.3	53034-55570	2.366	-27.293	46.761±0.016	9.113 ±0.092	-0.452	2.064
SDSS J101748.67+222659.2	53739-56027	1.989	-27.416	46.889±0.005	9.894 ±0.030	-1.106	2.097

Table B.1: (continued)

BAL quasar	MJD-pair	z_{em}	M_i (mag)	$\log L_{bol}$ (erg s^{-1})	$\log M_{BH}$ (M_{\odot})	$\log \frac{L_{bol}}{L_{Edd}}$	Δt (years)
SDSS J101748.67+222659.2	53739-56272	1.989	-27.416	46.889±0.005	9.894 ±0.030	-1.106	2.322
SDSS J101748.67+222659.2	56027-56272	1.989	-27.416	46.889±0.005	9.894 ±0.030	-1.106	0.225
SDSS J101811.39+170324.7	54174-55987	1.833	-26.928	46.712±0.006	9.822 ±0.057	-1.211	1.753
SDSS J102021.43+215850.9	53741-56027	1.867	-27.662	47.007±0.004	9.001 ±0.076	-0.094	2.185
SDSS J102059.76+292220.1	53772-53786	2.329	-27.094	46.612±0.012	9.082 ±0.053	-0.570	0.012
SDSS J102059.76+292220.1	53772-56326	2.329	-27.094	46.612±0.012	9.082 ±0.053	-0.570	2.102
SDSS J102059.76+292220.1	53772-56326	2.329	-27.094	46.612±0.012	9.082 ±0.053	-0.570	2.102
SDSS J102059.76+292220.1	53786-56326	2.329	-27.094	46.612±0.012	9.082 ±0.053	-0.570	2.090
SDSS J102059.76+292220.1	53786-56326	2.329	-27.094	46.612±0.012	9.082 ±0.053	-0.570	2.090
SDSS J102318.10+291553.8	53772-53786	1.993	-27.246	46.690±0.008	9.113 ±0.020	-0.523	0.013
SDSS J102318.10+291553.8	53772-56339	1.993	-27.246	46.690±0.008	9.113 ±0.020	-0.523	2.350
SDSS J102318.10+291553.8	53786-56339	1.993	-27.246	46.690±0.008	9.113 ±0.020	-0.523	2.337
SDSS J102510.55+260253.7	53765-56309	2.120	-27.227	46.628±0.017	9.583 ±0.068	-1.056	2.234
SDSS J102707.91+064750.7	52750-55680	1.947	-27.815	47.199±0.008	9.456 ±0.055	-0.357	2.724
SDSS J102707.91+064750.7	52750-55680	1.947	-27.815	47.199±0.008	9.456 ±0.055	-0.357	2.724
SDSS J102708.31+161038.5	54178-56003	2.963	-26.809	46.663±0.027	9.310 ±0.224	-0.748	1.262
SDSS J102708.90+300747.6	53799-56339	1.849	-26.624	46.641±0.010	9.636 ±0.181	-1.096	2.443
SDSS J103137.75+183346.2	54175-56036	1.992	-28.482	47.382±0.007	9.903 ±0.036	-0.622	1.704
SDSS J103309.99+272657.4	53794-56330	3.059	-27.676	46.905±0.017	9.333 ±0.231	-0.528	1.712
SDSS J103322.28+140756.9	53112-56010	1.803	-26.441	46.601±0.008	9.422 ±0.113	-0.922	2.833
SDSS J103619.54+442255.1	54179-55651	2.628	-27.541	46.914±0.015	9.191 ±0.056	-0.378	1.112
SDSS J103648.24+292800.0	53799-56366	1.993	-27.599	46.953±0.008	9.748 ±0.054	-0.895	2.350
SDSS J103648.24+292800.0	53799-56366	1.993	-27.599	46.953±0.008	9.748 ±0.054	-0.895	2.350
SDSS J103718.23+302509.1	53383-56366	2.267	-27.727	46.725±0.015	9.471 ±0.060	-0.847	2.502
SDSS J104148.61+253628.6	53792-56358	3.179	-28.671	47.388±0.011	9.342 ±0.029	-0.055	1.682
SDSS J104218.61+075017.9	52643-55929	2.171	-27.055	46.805±0.037	9.245 ±0.101	-0.540	2.839
SDSS J104325.04+162050.7	53851-56008	2.354	-27.835	47.100±0.008	9.531 ±0.071	-0.531	1.762
SDSS J104735.13+174928.2	54174-56269	2.058	-27.118	46.647±0.013	9.476 ±0.056	-0.930	1.877
SDSS J104801.17+193624.7	54097-56038	2.367	-27.322	46.804±0.019	9.147 ±0.113	-0.443	1.579
SDSS J104801.17+193624.7	54097-56038	2.367	-27.322	46.804±0.019	9.147 ±0.113	-0.443	1.579
SDSS J104834.52+371833.5	55623-55626	2.528	-27.736	46.575±0.020	8.596 ±0.160	-0.121	0.002
SDSS J104836.68+213843.9	54097-56328	1.856	-26.488	46.439±0.014	8.804 ±0.163	-0.465	2.140
SDSS J104841.14+212522.5	54097-56038	3.392	-27.461	46.978±0.017	8.380 ±0.026	0.498	1.211
SDSS J105101.21+153226.8	53852-56269	2.825	-28.926	47.210±0.008	9.913 ±0.029	-0.803	1.731
SDSS J105146.03+592214.3	52427-56625	2.916	-28.014	47.153±0.013	9.448 ±0.111	-0.395	2.937
SDSS J105146.39+164411.1	53852-56269	2.215	-27.024	46.712±0.011	9.259 ±0.083	-0.648	2.060
SDSS J105257.88+160348.6	53852-56269	2.971	-27.567	46.848±0.017	9.411 ±0.054	-0.664	1.668
SDSS J105257.88+160348.6	53852-56269	2.971	-27.567	46.848±0.017	9.411 ±0.054	-0.664	1.668
SDSS J105311.39+123516.6	53117-55980	2.924	-27.652	46.957±0.015	9.644 ±0.144	-0.787	1.999
SDSS J105427.92+504835.6	52346-56384	1.983	-26.221	46.457±0.017	8.784 ±0.095	-0.427	3.709
SDSS J105847.20+005656.6	51908-55302	2.324	-27.005	46.856±0.011	9.355 ±0.070	-0.599	2.797
SDSS J105945.57+094141.6	52723-55953	2.320	-27.541	47.011±0.014	9.308 ±0.043	-0.398	2.665
SDSS J110049.03+205129.7	54149-56279	2.160	-27.079	46.939±0.008	8.826 ±0.050	0.013	1.847
SDSS J110259.95+164345.2	53852-56016	2.687	-27.485	47.009±0.010	8.885 ±0.083	0.024	1.608
SDSS J110419.11+143650.8	53377-55983	1.813	-27.431	46.938±0.003	9.246 ±0.105	-0.408	2.538
SDSS J110650.41+585551.7	54526-56666	2.631	-27.194	46.903±0.008	9.036 ±0.074	-0.233	1.615
SDSS J110650.41+585551.7	54526-56666	2.631	-27.194	46.903±0.008	9.036 ±0.074	-0.233	1.615
SDSS J110735.13+230354.7	53857-56331	2.192	-26.905	46.519±0.019	9.293 ±0.104	-0.875	2.123
SDSS J110951.36+294923.5	53792-56364	3.159	-27.189	46.684±0.020	9.425 ±0.099	-0.842	1.694
SDSS J111039.65+664253.4	51929-56741	2.178	-27.410	46.905±0.008	9.456 ±0.092	-0.651	4.148
SDSS J111039.65+664253.4	51942-56741	2.178	-27.410	46.905±0.008	9.456 ±0.092	-0.651	4.137
SDSS J111208.75+085030.4	54169-55956	1.876	-26.125	46.362±0.009	9.023 ±0.117	-0.762	1.702
SDSS J111301.13+251452.9	54115-56331	2.939	-28.033	46.945±0.014	9.493 ±0.255	-0.649	1.541
SDSS J111333.68+205602.5	54178-56041	1.805	-26.440	46.603±0.008	8.894 ±0.129	-0.391	1.820
SDSS J111343.96+184002.7	54179-56038	2.053	-26.880	46.676±0.016	9.382 ±0.198	-0.807	1.668
SDSS J111343.96+184002.7	54179-56041	2.053	-26.880	46.676±0.016	9.382 ±0.198	-0.807	1.671
SDSS J111343.96+184002.7	56038-56041	2.053	-26.880	46.676±0.016	9.382 ±0.198	-0.807	0.003
SDSS J111431.20+200024.1	54179-56041	2.022	-26.940	46.732±0.012	9.195 ±0.486	-0.563	1.688
SDSS J111618.68+201654.5	54175-56274	2.149	-27.556	47.145±0.008	9.596 ±0.052	-0.552	1.826
SDSS J111618.68+201654.5	54175-56274	2.149	-27.556	47.145±0.008	9.596 ±0.052	-0.552	1.826

Table B.1: (continued)

BAL quasar	MJD-pair	z_{em}	M_i (mag)	$\log L_{bol}$ (erg s $^{-1}$)	$\log M_{BH}$ (M_{\odot})	$\log \frac{L_{bol}}{L_{Edd}}$	Δt (years)
SDSS J114550.05+113459.5	53142-55986	1.973	-26.876	46.832±0.011	8.845 ±0.109	-0.113	2.621
SDSS J114552.43+495113.9	52412-56412	3.020	-27.176	46.701±0.030	9.327 ±0.085	-0.726	2.726
SDSS J114713.98+442543.4	53083-56398	2.100	-27.153	46.775±0.018	8.431 ±0.100	0.243	2.930
SDSS J114713.98+442543.4	53083-56398	2.100	-27.153	46.775±0.018	8.431 ±0.100	0.243	2.930
SDSS J114734.40+174655.9	53875-56035	2.006	-26.856	46.705±0.011	9.424 ±0.077	-0.819	1.969
SDSS J114851.46+231340.4	53882-56328	3.083	-29.696	47.573±0.005	9.949 ±0.033	-0.477	1.641
SDSS J115216.58+281629.7	53793-56334	2.168	-26.880	46.700±0.013	9.041 ±0.103	-0.441	2.197
SDSS J115513.64+370319.2	53433-55648	2.256	-27.044	46.664±0.020	8.945 ±0.053	-0.381	1.864
SDSS J115513.64+370319.2	53433-55648	2.256	-27.044	46.664±0.020	8.945 ±0.053	-0.381	1.864
SDSS J115513.64+370319.2	53433-55672	2.256	-27.044	46.664±0.020	8.945 ±0.053	-0.381	1.884
SDSS J115513.64+370319.2	53433-55672	2.256	-27.044	46.664±0.020	8.945 ±0.053	-0.381	1.884
SDSS J115513.64+370319.2	55648-55672	2.256	-27.044	46.664±0.020	8.945 ±0.053	-0.381	0.020
SDSS J115513.64+370319.2	55648-55672	2.256	-27.044	46.664±0.020	8.945 ±0.053	-0.381	0.020
SDSS J120100.94+244446.9	54184-56330	3.357	-27.424	47.350±0.009	9.477 ±0.030	-0.227	1.349
SDSS J120100.94+244446.9	54184-56330	3.357	-27.424	47.350±0.009	9.477 ±0.030	-0.227	1.349
SDSS J120101.05+210444.9	54208-56067	1.947	-28.835	46.479±0.007	9.314 ±0.050	-0.936	1.728
SDSS J120203.30+283300.4	53819-56334	2.573	-28.899	47.412±0.004	9.731 ±0.042	-0.419	1.928
SDSS J120508.34+222626.2	54208-56069	2.167	-26.887	46.825±0.011	9.342 ±0.096	-0.617	1.610
SDSS J120634.13+455238.2	53089-56383	1.967	-26.952	46.791±0.012	9.251 ±0.068	-0.561	3.042
SDSS J120834.84+002047.7	51666-51999	2.710	-28.288	46.984±0.012	9.720 ±0.165	-0.837	0.246
SDSS J120834.84+002047.7	51666-51999	2.710	-28.288	46.984±0.012	9.720 ±0.165	-0.837	0.246
SDSS J112712.04+272205.4	53816-54862	2.717	-27.373	46.614±0.021	9.509 ±0.134	-0.996	0.771
SDSS J112712.04+272205.4	53816-56306	2.717	-27.373	46.614±0.021	9.509 ±0.134	-0.996	1.835
SDSS J112712.04+272205.4	54862-56306	2.717	-27.373	46.614±0.021	9.509 ±0.134	-0.996	1.064
SDSS J112735.21+181423.2	54176-54859	3.104	-28.219	47.059±0.011	9.675 ±0.167	-0.717	0.456
SDSS J112735.21+181423.2	54176-54907	3.104	-28.219	47.059±0.011	9.675 ±0.167	-0.717	0.488
SDSS J112735.21+181423.2	54176-56037	3.104	-28.219	47.059±0.011	9.675 ±0.167	-0.717	1.242
SDSS J112735.21+181423.2	54859-54907	3.104	-28.219	47.059±0.011	9.675 ±0.167	-0.717	0.032
SDSS J112735.21+181423.2	54859-56037	3.104	-28.219	47.059±0.011	9.675 ±0.167	-0.717	0.786
SDSS J112735.21+181423.2	54907-56037	3.104	-28.219	47.059±0.011	9.675 ±0.167	-0.717	0.754
SDSS J112845.16+502038.4	52642-56412	1.888	-26.802	46.674±0.009	9.325 ±0.110	-0.751	3.576
SDSS J113036.42+151253.1	53385-56010	2.226	-27.456	46.929±0.007	8.885 ±0.038	-0.057	2.229
SDSS J113042.59+292028.0	53794-56362	1.856	-26.643	46.632±0.007	9.735 ±0.284	-1.203	2.463
SDSS J113123.34+460408.4	53050-54861	2.030	-27.413	46.985±0.008	9.151 ±0.067	-0.266	1.638
SDSS J113123.34+460408.4	53050-54861	2.030	-27.413	46.985±0.008	9.151 ±0.067	-0.266	1.638
SDSS J113123.34+460408.4	53050-56390	2.030	-27.413	46.985±0.008	9.151 ±0.067	-0.266	3.020
SDSS J113123.34+460408.4	53050-56390	2.030	-27.413	46.985±0.008	9.151 ±0.067	-0.266	3.020
SDSS J113123.34+460408.4	54861-56390	2.030	-27.413	46.985±0.008	9.151 ±0.067	-0.266	1.383
SDSS J113123.34+460408.4	54861-56390	2.030	-27.413	46.985±0.008	9.151 ±0.067	-0.266	1.383
SDSS J113123.34+460408.4	54861-56390	2.030	-27.413	46.985±0.008	9.151 ±0.067	-0.266	1.383
SDSS J11937.52+242600.3	54154-56304	3.247	-28.006	47.156±0.012	9.459 ±0.050	-0.403	1.387
SDSS J112446.07+353615.6	53468-55600	2.820	-27.411	46.842±0.017	8.630 ±0.051	0.112	1.529
SDSS J112446.07+353615.6	53468-55600	2.820	-27.411	46.842±0.017	8.630 ±0.051	0.112	1.529
SDSS J113226.12+205717.5	54179-56047	2.179	-28.058	47.195±0.007	10.044 ±0.102	-0.950	1.610
SDSS J113602.84+193557.7	54180-56047	3.013	-27.153	46.604±0.028	9.113 ±0.166	-0.610	1.275
SDSS J113608.22+184908.1	54179-56047	2.176	-27.023	46.697±0.017	9.020 ±0.038	-0.423	1.611
SDSS J113941.27+525233.1	52367-56416	1.867	-27.319	46.827±0.013	9.965 ±0.328	-1.238	3.869
SDSS J114015.68+300654.3	53799-56339	3.840	-28.046	46.901±0.014	10.015 ±0.229	-1.214	1.438
SDSS J114307.22+475101.7	53054-56401	2.591	-27.559	46.953±0.012	9.695 ±0.070	-0.843	2.554
SDSS J114359.13+274440.1	53792-56330	1.969	-26.792	46.229±0.029	9.016 ±0.244	-0.887	2.342
SDSS J114359.13+274440.1	53792-56330	1.969	-26.792	46.229±0.029	9.016 ±0.244	-0.887	2.342
SDSS J114408.82+532412.4	52367-56419	2.125	-27.385	46.928±0.006	9.790 ±0.073	-0.962	3.552
SDSS J120834.84+002047.7	51666-54922	2.710	-28.288	46.984±0.012	9.720 ±0.165	-0.837	2.404
SDSS J120834.84+002047.7	51666-54922	2.710	-28.288	46.984±0.012	9.720 ±0.165	-0.837	2.404
SDSS J120834.84+002047.7	51666-55321	2.710	-28.288	46.984±0.012	9.720 ±0.165	-0.837	2.699
SDSS J120834.84+002047.7	51666-55321	2.710	-28.288	46.984±0.012	9.720 ±0.165	-0.837	2.699
SDSS J120834.84+002047.7	51999-54922	2.710	-28.288	46.984±0.012	9.720 ±0.165	-0.837	2.159
SDSS J120834.84+002047.7	51999-54922	2.710	-28.288	46.984±0.012	9.720 ±0.165	-0.837	2.159
SDSS J120834.84+002047.7	51999-55321	2.710	-28.288	46.984±0.012	9.720 ±0.165	-0.837	2.453
SDSS J120834.84+002047.7	51999-55321	2.710	-28.288	46.984±0.012	9.720 ±0.165	-0.837	2.453
SDSS J120834.84+002047.7	54922-55321	2.710	-28.288	46.984±0.012	9.720 ±0.165	-0.837	0.295

Table B.1: (continued)

BAL quasar	MJD-pair	z_{em}	M_i (mag)	$\log L_{bol}$ (erg s^{-1})	$\log M_{BH}$ (M_{\odot})	$\log \frac{L_{bol}}{L_{Edd}}$	Δt (years)
SDSS J120834.84+002047.7	54922-55321	2.710	-28.288	46.984±0.012	9.720 ±0.165	-0.837	0.295
SDSS J121113.56+044946.2	52376-55633	2.310	-27.294	46.731±0.013	9.082 ±0.249	-0.451	2.696
SDSS J121221.14+202150.9	54476-56029	2.841	-27.744	46.952±0.007	9.107 ±0.021	-0.255	1.108
SDSS J121407.42+565108.7	53050-56429	1.854	-27.257	46.874±0.015	9.281 ±0.088	-0.507	3.244
SDSS J121545.71+264814.7	53816-56064	2.887	-27.294	46.767±0.018	9.550 ±0.097	-0.883	1.584
SDSS J121729.60+174332.3	54207-56033	2.051	-27.111	46.932±0.012	9.547 ±0.097	-0.715	1.640
SDSS J122131.53+100627.5	52672-55947	1.967	-27.103	46.726±0.014	8.520 ±0.083	0.106	3.024
SDSS J122135.30+230858.0	54477-56329	3.065	-27.675	47.005±0.014	9.680 ±0.057	-0.776	1.248
SDSS J122204.62+303901.6	53827-56365	1.839	-27.562	46.963±0.004	9.621 ±0.039	-0.758	2.449
SDSS J122213.41+235833.7	54502-56329	2.077	-26.987	46.637±0.012	9.558 ±0.091	-1.022	1.627
SDSS J122228.06+240017.6	54502-56329	3.540	-27.609	46.977±0.018	8.943 ±0.065	-0.066	1.103
SDSS J122513.05+081331.9	53472-55944	1.888	-26.901	46.666±0.040	8.141 ±1.115	0.425	2.345
SDSS J122651.40+312309.0	56364-56365	3.081	-26.830	46.648±0.037	8.946 ±0.166	-0.399	0.001
SDSS J122651.40+312309.0	56364-56365	3.081	-26.830	46.648±0.037	8.946 ±0.166	-0.399	0.001
SDSS J123056.65+165438.2	54232-54234	1.820	-26.430	46.479±0.015	8.219 ±1.200	0.160	0.002
SDSS J123056.65+165438.2	54232-56034	1.820	-26.430	46.479±0.015	8.219 ±1.200	0.160	1.751
SDSS J123056.65+165438.2	54234-56034	1.820	-26.430	46.479±0.015	8.219 ±1.200	0.160	1.749
SDSS J123110.28+335218.5	53819-55571	1.767	-27.783	47.109±0.003	9.419 ±0.070	-0.411	1.735
SDSS J123144.42+112115.5	53166-55979	1.885	-26.627	46.649±0.010	8.855 ±0.142	-0.306	2.671
SDSS J123329.18+285017.7	53823-56340	1.958	-26.813	46.569±0.013	9.108 ±0.066	-0.639	2.331
SDSS J123329.18+285017.7	53823-56340	1.958	-26.813	46.569±0.013	9.108 ±0.066	-0.639	2.331
SDSS J123341.29+230302.5	54495-56310	2.971	-28.520	47.247±0.008	9.549 ±0.059	-0.402	1.252
SDSS J123517.70+133018.4	53169-56010	3.098	-27.727	46.935±0.013	10.196 ±0.087	-1.361	1.899
SDSS J123542.11+440114.5	53062-56365	2.258	-26.997	46.768±0.013	9.243 ±0.103	-0.576	2.778
SDSS J123717.36+113844.5	53169-55979	2.091	-26.878	46.473±0.020	8.682 ±1.148	-0.310	2.491
SDSS J123930.24+501512.2	52735-56389	2.372	-27.266	46.889±0.016	9.217 ±0.208	-0.429	2.969
SDSS J124031.68+103129.5	52734-55955	2.154	-26.975	46.682±0.025	9.367 ±0.127	-0.785	2.798
SDSS J124103.97+260549.6	54504-56337	2.625	-27.586	46.857±0.010	9.026 ±0.051	-0.269	1.385
SDSS J124312.93+144812.0	53171-56038	1.860	-28.107	47.203±0.005	9.461 ±0.065	-0.359	2.746
SDSS J124329.42+220741.2	54485-56089	2.806	-27.388	46.636±0.022	9.320 ±0.131	-0.784	1.155
SDSS J124329.42+220741.2	54485-56089	2.806	-27.388	46.636±0.022	9.320 ±0.131	-0.784	1.155
SDSS J124345.92+185343.0	54481-56088	2.330	-26.075	46.768±0.014	9.362 ±0.121	-0.694	1.322
SDSS J124353.95+072015.4	53876-55926	3.186	-28.032	47.155±0.010	9.423 ±0.027	-0.368	1.342
SDSS J124353.95+072015.4	53876-55926	3.186	-28.032	47.155±0.010	9.423 ±0.027	-0.368	1.342
SDSS J124510.98+071055.6	53876-55926	1.934	-26.724	46.694±0.006	10.074 ±0.137	-1.480	1.914
SDSS J124526.80+172053.2	54243-56090	1.861	-27.772	47.064±0.012	9.653 ±0.061	-0.690	1.769
SDSS J124543.07+183427.2	54481-56088	2.060	-27.395	46.845±0.010	9.272 ±0.083	-0.528	1.439
SDSS J124543.07+183427.2	54481-56088	2.060	-27.395	46.845±0.010	9.272 ±0.083	-0.528	1.439
SDSS J124558.32-015857.2	54612-55222	2.495	-27.095	46.837±0.006	9.319 ±0.109	-0.583	0.478
SDSS J124634.36+083656.7	54259-55953	2.037	-27.213	46.791±0.012	9.453 ±0.104	-0.762	1.528
SDSS J124634.36+083656.7	54259-55953	2.037	-27.213	46.791±0.012	9.453 ±0.104	-0.762	1.528
SDSS J124656.95+184926.8	54481-56090	3.969	-29.441	47.768±0.008	9.694 ±0.034	-0.026	0.887
SDSS J124725.08+493042.8	52736-56413	2.379	-27.421	46.736±0.020	0.000 ±-1.000	-999.0	2.981
SDSS J124940.23-012824.9	51997-55214	2.973	-27.439	46.568±0.040	8.614 ±0.363	-0.146	2.218
SDSS J125121.39+301528.8	54175-56363	2.529	-27.110	46.736±0.014	9.619 ±0.135	-0.983	1.699
SDSS J125150.65+263900.0	54205-56339	1.913	-28.419	47.098±0.008	9.851 ±0.131	-0.854	2.007
SDSS J125157.23+124842.0	53473-55981	1.958	-26.691	46.848±0.011	9.100 ±0.131	-0.352	2.323
SDSS J125157.23+124842.0	53473-55981	1.958	-26.691	46.848±0.011	9.100 ±0.131	-0.352	2.323
SDSS J125634.98+183854.4	54582-56065	2.155	-26.252	46.180±0.020	9.194 ±0.121	-1.115	1.288
SDSS J125634.98+183854.4	54582-56065	2.155	-26.252	46.180±0.020	9.194 ±0.121	-1.115	1.288
SDSS J125650.35+041323.9	52669-55682	3.132	-27.195	46.798±0.023	9.408 ±0.127	-0.711	1.998
SDSS J125650.35+041323.9	52669-55682	3.132	-27.195	46.798±0.023	9.408 ±0.127	-0.711	1.998
SDSS J125659.00+193942.7	54483-56065	3.024	-27.200	46.789±0.018	9.066 ±0.142	-0.377	1.077
SDSS J125906.79+342529.9	53476-55320	2.758	-27.109	46.729±0.017	8.595 ±0.088	0.033	1.344
SDSS J125957.92+561334.6	52781-56426	2.139	-27.164	46.820±0.015	8.455 ±0.081	0.264	3.181
SDSS J130148.58+361515.8	53799-55335	2.155	-26.893	46.685±0.016	9.038 ±0.157	-0.453	1.334
SDSS J130203.25+601456.4	54570-56447	2.692	-26.368	46.463±0.017	8.923 ±0.091	-0.560	1.393
SDSS J130203.25+601456.4	54570-56447	2.692	-26.368	46.463±0.017	8.923 ±0.091	-0.560	1.393
SDSS J130439.13+210559.9	54505-56046	2.013	-26.974	46.227±0.016	9.765 ±0.115	-1.638	1.401
SDSS J130527.88+262522.7	54153-56334	2.158	-27.047	46.501±0.028	9.150 ±0.061	-0.750	1.892

Table B.1: (continued)

BAL quasar	MJD-pair	z_{em}	M_i (mag)	$\log L_{bol}$ (erg s $^{-1}$)	$\log M_{BH}$ (M_{\odot})	$\log \frac{L_{bol}}{L_{Edd}}$	Δt (years)
SDSS J130652.14+204315.3	54505-54880	2.028	-28.208	46.988±0.008	9.805 ±0.039	-0.917	0.339
SDSS J130652.14+204315.3	54505-56046	2.028	-28.208	46.988±0.008	9.805 ±0.039	-0.917	1.394
SDSS J130652.14+204315.3	54505-56046	2.028	-28.208	46.988±0.008	9.805 ±0.039	-0.917	1.394
SDSS J130652.14+204315.3	54880-56046	2.028	-28.208	46.988±0.008	9.805 ±0.039	-0.917	1.055
SDSS J130652.14+204315.3	54880-56046	2.028	-28.208	46.988±0.008	9.805 ±0.039	-0.917	1.055
SDSS J130809.37+191117.4	54502-54880	2.401	-27.508	46.767±0.009	9.949 ±0.041	-1.282	0.305
SDSS J130809.37+191117.4	54502-56042	2.401	-27.508	46.767±0.009	9.949 ±0.041	-1.282	1.241
SDSS J130809.37+191117.4	54880-56042	2.401	-27.508	46.767±0.009	9.949 ±0.041	-1.282	0.936
SDSS J130825.74+204707.2	54502-56046	2.039	-27.479	46.899±0.007	8.764 ±0.030	0.035	1.392
SDSS J130825.74+204707.2	54502-56046	2.039	-27.479	46.899±0.007	8.764 ±0.030	0.035	1.392
SDSS J130825.74+204707.2	54502-56047	2.039	-27.479	46.899±0.007	8.764 ±0.030	0.035	1.393
SDSS J130825.74+204707.2	56046-56047	2.039	-27.479	46.899±0.007	8.764 ±0.030	0.035	0.001
SDSS J130825.74+204707.2	56046-56047	2.039	-27.479	46.899±0.007	8.764 ±0.030	0.035	0.001
SDSS J130841.19+133130.5	53089-56009	1.959	-27.125	46.565±0.019	9.016 ±0.313	-0.551	2.704
SDSS J130841.85+162615.7	54479-56033	1.927	-26.509	46.733±0.012	8.956 ±0.332	-0.323	1.455
SDSS J130851.74+090102.6	53884-55980	2.922	-28.144	47.028±0.012	9.607 ±0.037	-0.679	1.464
SDSS J131255.45+133032.4	55986-56003	2.955	-28.102	-999.9±-999.9	-999.9 ±-999.9	-999.9	0.012
SDSS J131346.72+393604.7	53493-55603	3.442	-28.407	47.192±0.014	8.933 ±0.150	0.158	1.301
SDSS J131556.44+302042.2	53852-56328	2.416	-27.889	47.072±0.011	8.693 ±0.041	0.279	1.986
SDSS J131556.44+302042.2	53852-56330	2.416	-27.889	47.072±0.011	8.693 ±0.041	0.279	1.987
SDSS J131556.44+302042.2	56328-56330	2.416	-27.889	47.072±0.011	8.693 ±0.041	0.279	0.002
SDSS J131702.87+190458.9	54506-56034	2.634	-28.247	47.240±0.004	8.969 ±0.035	0.171	1.152
SDSS J131737.87+295627.6	53471-56328	1.770	-27.730	47.057±0.004	9.507 ±0.079	-0.550	2.826
SDSS J131737.87+295627.6	53471-56329	1.770	-27.730	47.057±0.004	9.507 ±0.079	-0.550	2.827
SDSS J131737.87+295627.6	56328-56329	1.770	-27.730	47.057±0.004	9.507 ±0.079	-0.550	0.001
SDSS J131854.87+194840.5	54506-56034	2.137	-27.048	46.737±0.011	9.202 ±0.078	-0.565	1.334
SDSS J132004.70+363830.1	53851-55597	2.771	-27.286	46.508±0.026	9.393 ±0.073	-0.985	1.269
SDSS J132115.66+495546.3	52759-56385	2.444	-27.968	47.148±0.011	9.730 ±0.071	-0.682	2.885
SDSS J132213.08+245035.6	54524-54950	1.907	-26.847	46.758±0.011	9.320 ±0.100	-0.662	0.401
SDSS J132213.08+245035.6	54524-56096	1.907	-26.847	46.758±0.011	9.320 ±0.100	-0.662	1.482
SDSS J132213.08+245035.6	54950-56096	1.907	-26.847	46.758±0.011	9.320 ±0.100	-0.662	1.080
SDSS J132246.82+272633.0	53795-56309	2.017	-26.977	46.523±0.014	8.974 ±0.671	-0.552	2.283
SDSS J132415.50+351650.8	53851-55603	3.584	-28.727	47.175±0.012	10.042 ±0.135	-0.967	1.047
SDSS J133028.14+070717.6	53556-55703	3.117	-28.220	47.140±0.009	9.671 ±0.138	-0.632	1.429
SDSS J133418.99+240011.5	54232-56087	2.537	-27.612	47.003±0.010	9.057 ±0.035	-0.155	1.437
SDSS J133418.99+240011.5	54232-56087	2.537	-27.612	47.003±0.010	9.057 ±0.035	-0.155	1.437
SDSS J133541.38+483530.0	52762-56385	2.749	-27.313	46.758±0.017	9.035 ±0.066	-0.377	2.648
SDSS J133639.28+251842.7	54208-56089	3.098	-27.553	46.558±0.030	0.000 ±-1.000	-999.0	1.258
SDSS J133727.10+081734.3	54156-55973	3.236	-27.757	46.907±0.013	9.600 ±0.075	-0.793	1.175
SDSS J133727.10+081734.3	54156-55973	3.236	-27.757	46.907±0.013	9.600 ±0.075	-0.793	1.175
SDSS J133828.47+395922.5	53091-55704	2.338	-28.042	47.058±0.010	9.655 ±0.056	-0.697	2.145
SDSS J133905.39+240751.0	54232-56087	2.003	-26.682	46.567±0.017	8.566 ±0.139	-0.099	1.692
SDSS J133937.11+313129.5	53851-56363	2.073	-27.083	47.121±0.006	9.434 ±0.033	-0.413	2.240
SDSS J133937.22+235521.9	54230-56087	2.046	-27.666	46.614±0.015	9.017 ±0.085	-0.503	1.670
SDSS J133959.98+203757.8	54231-56075	3.033	-27.620	46.744±0.024	9.388 ±0.203	-0.745	1.253
SDSS J133959.98+203757.8	54231-56075	3.033	-27.620	46.744±0.024	9.388 ±0.203	-0.745	1.253
SDSS J134005.84+224304.2	54230-56087	2.033	-27.026	46.714±0.011	9.284 ±0.057	-0.670	1.677
SDSS J134027.41+660348.2	51989-56717	2.391	-27.169	46.745±0.015	9.031 ±0.074	-0.387	3.820
SDSS J134108.93+242916.2	54230-56087	3.126	-27.926	47.012±0.010	9.303 ±0.110	-0.391	1.233
SDSS J134210.95+301521.4	53851-56363	2.176	-26.966	46.689±0.013	9.029 ±0.099	-0.440	2.167
SDSS J134339.59+301558.1	53851-56363	3.238	-27.619	46.700±0.017	8.615 ±0.567	-0.016	1.624
SDSS J134339.59+301558.1	53851-56363	3.238	-27.619	46.700±0.017	8.615 ±0.567	-0.016	1.624
SDSS J134503.64+333513.5	53818-55269	2.910	-27.568	46.504±0.024	10.127 ±0.179	-1.723	1.017
SDSS J134544.74+343255.6	53818-55268	3.220	-27.717	46.546±0.009	9.908 ±0.157	-1.462	0.941
SDSS J134825.14+270616.1	53848-56105	2.199	-28.145	47.173±0.007	9.434 ±0.052	-0.361	1.933
SDSS J135027.56+415731.5	52814-54977	2.540	-27.354	46.798±0.020	9.100 ±0.124	-0.403	1.674
SDSS J135027.56+415731.5	52814-56364	2.540	-27.354	46.798±0.020	9.100 ±0.124	-0.403	2.747
SDSS J135027.56+415731.5	54977-56364	2.540	-27.354	46.798±0.020	9.100 ±0.124	-0.403	1.073
SDSS J135633.04+233420.8	54524-56066	1.855	-27.148	46.619±0.009	9.927 ±0.026	-1.409	1.480
SDSS J140022.65+484433.7	54553-56425	3.083	-27.343	46.741±0.034	8.530 ±0.081	0.110	1.256

Table B.1: (continued)

BAL quasar	MJD-pair	z_{em}	M_i (mag)	$\log L_{bol}$ (erg s^{-1})	$\log M_{BH}$ (M_{\odot})	$\log \frac{L_{bol}}{L_{Edd}}$	Δt (years)
SDSS J140022.78+395030.8	53061-56358	3.790	-28.302	47.317±0.014	9.612 ±0.087	-0.395	1.886
SDSS J140048.01+264218.4	53793-56093	2.142	-27.068	46.803±0.011	8.756 ±0.075	-0.053	2.006
SDSS J140106.03+312829.6	54180-55276	2.163	-27.743	46.820±0.008	9.561 ±0.117	-0.841	0.949
SDSS J140106.03+312829.6	54180-55276	2.163	-27.743	46.820±0.008	9.561 ±0.117	-0.841	0.949
SDSS J140217.56+445211.1	53115-56102	2.256	-27.337	46.927±0.009	9.440 ±0.048	-0.613	2.513
SDSS J140217.56+445211.1	53115-56102	2.256	-27.337	46.927±0.009	9.440 ±0.048	-0.613	2.513
SDSS J140246.83+252317.0	53770-56093	1.944	-26.875	46.513±0.017	9.352 ±0.064	-0.939	2.162
SDSS J140317.06+191811.0	54509-56039	1.983	-27.091	46.874±0.010	9.290 ±0.063	-0.516	1.405
SDSS J140326.50+092043.8	53792-55958	2.977	-27.873	47.189±0.015	9.103 ±0.173	-0.014	1.492
SDSS J140326.50+092043.8	53792-55958	2.977	-27.873	47.189±0.015	9.103 ±0.173	-0.014	1.492
SDSS J140341.68+613933.0	52353-56419	2.206	-26.914	46.684±0.014	9.017 ±0.058	-0.433	3.475
SDSS J140651.09+650613.2	51984-56717	1.875	-27.022	46.709±0.010	9.672 ±0.056	-1.063	4.510
SDSS J140707.55+335506.7	53471-55273	2.957	-27.357	46.681±0.021	9.796 ±0.142	-1.216	1.248
SDSS J140802.52+162059.0	54231-56010	1.894	-26.787	46.385±0.032	9.677 ±0.044	-1.392	1.684
SDSS J141018.41+200610.7	54527-56046	2.765	-26.723	46.452±0.025	9.250 ±0.261	-0.899	1.105
SDSS J141304.26+164741.1	54231-56015	2.224	-27.661	46.940±0.009	9.378 ±0.107	-0.539	1.516
SDSS J141407.13+270610.3	53859-56097	2.056	-27.034	46.765±0.014	9.485 ±0.068	-0.821	2.006
SDSS J14165.436+221419.2	54537-56047	2.950	-27.098	46.781±0.021	8.558 ±0.608	0.122	1.047
SDSS J141723.73+285522.6	53794-56101	1.817	-26.747	46.739±0.006	9.490 ±0.152	-0.852	2.244
SDSS J141724.48+202752.8	54533-56046	3.250	-27.368	46.891±0.015	9.277 ±0.071	-0.487	0.975
SDSS J141724.48+202752.8	54533-56046	3.250	-27.368	46.891±0.015	9.277 ±0.071	-0.487	0.975
SDSS J141915.98+163504.5	54232-56035	2.049	-26.751	46.647±0.013	9.412 ±0.074	-0.865	1.620
SDSS J141956.96+010652.6	51609-55604	2.189	-27.012	46.833±0.010	9.487 ±0.183	-0.755	3.432
SDSS J141956.96+010652.6	51609-55634	2.189	-27.012	46.833±0.010	9.487 ±0.183	-0.755	3.458
SDSS J141956.96+010652.6	51957-55604	2.189	-27.012	46.833±0.010	9.487 ±0.183	-0.755	3.133
SDSS J141956.96+010652.6	51957-55634	2.189	-27.012	46.833±0.010	9.487 ±0.183	-0.755	3.159
SDSS J141956.96+010652.6	51997-55604	2.189	-27.012	46.833±0.010	9.487 ±0.183	-0.755	3.099
SDSS J141956.96+010652.6	51997-55634	2.189	-27.012	46.833±0.010	9.487 ±0.183	-0.755	3.125
SDSS J141956.96+010652.6	55604-55634	2.189	-27.012	46.833±0.010	9.487 ±0.183	-0.755	0.026
SDSS J142033.94+161228.3	54534-56035	2.138	-27.142	46.822±0.011	9.608 ±0.190	-0.886	1.310
SDSS J142154.86+171307.0	54534-56035	1.809	-26.961	46.764±0.013	9.078 ±0.111	-0.415	1.464
SDSS J142211.80+584249.3	52342-56429	1.710	-27.531	46.959±0.008	9.134 ±0.208	-0.275	4.132
SDSS J142221.21+265816.3	53819-54967	2.046	-26.914	46.197±0.012	9.357 ±0.300	-1.261	1.033
SDSS J142221.21+265816.3	53819-56096	2.046	-26.914	46.197±0.012	9.357 ±0.300	-1.261	2.048
SDSS J142221.21+265816.3	53819-56101	2.046	-26.914	46.197±0.012	9.357 ±0.300	-1.261	2.053
SDSS J142221.21+265816.3	54967-56096	2.046	-26.914	46.197±0.012	9.357 ±0.300	-1.261	1.015
SDSS J142221.21+265816.3	54967-56101	2.046	-26.914	46.197±0.012	9.357 ±0.300	-1.261	1.020
SDSS J142221.21+265816.3	56096-56101	2.046	-26.914	46.197±0.012	9.357 ±0.300	-1.261	0.004
SDSS J142408.10+520622.8	52764-56449	1.942	-26.858	46.736±0.015	9.273 ±0.145	-0.637	3.432
SDSS J142519.45+113925.6	53885-56000	2.326	-27.681	47.066±0.012	9.710 ±0.043	-0.745	1.742
SDSS J142519.45+113925.6	53885-56003	2.326	-27.681	47.066±0.012	9.710 ±0.043	-0.745	1.745
SDSS J142519.45+113925.6	56000-56003	2.326	-27.681	47.066±0.012	9.710 ±0.043	-0.745	0.002
SDSS J142555.22+373900.7	53089-56044	2.703	-27.404	46.746±0.017	9.628 ±0.177	-0.982	2.186
SDSS J142659.95+161003.3	54506-56018	1.971	-27.233	46.598±0.014	9.881 ±0.049	-1.384	1.394
SDSS J142734.03+182208.8	54534-56035	1.805	-27.453	46.950±0.013	9.126 ±0.158	-0.277	1.466
SDSS J142734.03+182208.8	56035-56042	1.805	-27.453	46.950±0.013	9.126 ±0.158	-0.277	0.007
SDSS J142819.48+160813.7	54233-56033	1.915	-27.563	46.842±0.007	9.686 ±0.138	-0.945	1.692
SDSS J142906.93+221001.6	54552-56043	1.950	-26.893	46.503±0.018	8.726 ±0.416	-0.324	1.385
SDSS J142906.93+221001.6	54552-56043	1.950	-26.893	46.503±0.018	8.726 ±0.416	-0.324	1.385
SDSS J143057.16+625113.1	51988-56720	2.513	-27.459	46.973±0.011	9.466 ±0.115	-0.593	3.690
SDSS J143212.86+113953.1	53533-55988	2.999	-29.164	47.415±0.010	9.856 ±0.102	-0.542	1.682
SDSS J143248.81+501048.7	52460-56416	2.463	-27.433	46.913±0.014	9.493 ±0.112	-0.681	3.130
SDSS J143255.09+155656.8	54534-56033	1.845	-26.399	46.569±0.009	9.291 ±0.131	-0.822	1.444
SDSS J143331.02+033523.7	52027-55682	2.896	-27.051	46.713±0.024	9.246 ±0.368	-0.633	2.570
SDSS J143558.56+252707.9	53827-56075	1.948	-26.873	46.866±0.009	9.258 ±0.074	-0.493	2.089
SDSS J143558.56+252707.9	53827-56075	1.948	-26.873	46.866±0.009	9.258 ±0.074	-0.493	2.089
SDSS J143650.06+264944.4	54206-56075	2.074	-27.174	46.674±0.011	9.489 ±0.154	-0.915	1.666
SDSS J143807.77+624409.5	54533-56720	3.062	-27.677	46.528±0.028	9.852 ±0.341	-1.425	1.475
SDSS J143810.86+173900.9	54534-56037	1.897	-27.119	46.776±0.007	9.299 ±0.172	-0.623	1.421
SDSS J143813.25+193525.8	54535-56038	2.251	-27.101	46.640±0.016	9.201 ±0.094	-0.662	1.267

Table B.1: (continued)

BAL quasar	MJD-pair	z_{em}	M_i (mag)	$\log L_{bol}$ (erg s $^{-1}$)	$\log M_{BH}$ (M_{\odot})	$\log \frac{L_{bol}}{L_{Edd}}$	Δt (years)
SDSS J143912.13+295210.0	53757-55277	2.845	-27.529	46.552±0.026	10.108 ±0.183	-1.656	1.083
SDSS J144151.83+142050.4	54241-56034	2.161	-27.046	46.732±0.010	9.186 ±0.122	-0.554	1.554
SDSS J144429.39+124906.6	53531-56033	2.999	-27.945	47.215±0.014	9.131 ±0.078	-0.016	1.714
SDSS J144508.33+135116.5	54241-56033	3.990	-27.851	46.837±0.014	0.000 ±-1.000	-999.0	0.984
SDSS J144621.83+261707.4	54208-56076	2.327	-27.394	46.896±0.010	9.524 ±0.065	-0.728	1.538
SDSS J144631.96+083451.5	54555-55976	2.955	-27.272	46.737±0.024	9.443 ±0.110	-0.807	0.984
SDSS J144631.96+083451.5	54555-55976	2.955	-27.272	46.737±0.024	9.443 ±0.110	-0.807	0.984
SDSS J144826.10+122814.7	53531-56033	2.073	-27.185	46.857±0.013	8.894 ±0.181	-0.137	2.231
SDSS J144844.69+092834.2	53827-55986	3.159	-28.054	46.912±0.015	8.751 ±0.060	0.061	1.422
SDSS J145357.38+130856.1	54242-56014	3.507	-27.913	46.929±0.014	9.218 ±0.338	-0.389	1.077
SDSS J145519.92+121645.0	53521-56014	1.906	-26.729	46.750±0.014	9.327 ±0.047	-0.678	2.350
SDSS J145526.86+132411.6	54242-56014	2.287	-27.190	46.667±0.018	9.531 ±0.116	-0.964	1.477
SDSS J145735.77+054142.9	54560-55711	2.220	-26.982	46.671±0.015	9.461 ±0.157	-0.890	0.979
SDSS J150406.23+614023.3	52055-56444	2.188	-27.064	46.723±0.013	9.299 ±0.113	-0.676	3.772
SDSS J150548.65+242706.1	53820-56074	3.155	-27.973	47.116±0.011	9.515 ±0.080	-0.500	1.486
SDSS J150609.76+444737.1	53147-56098	1.867	-27.050	46.807±0.010	9.618 ±0.080	-0.911	2.820
SDSS J150609.76+444737.1	54945-56098	1.867	-27.050	46.807±0.010	9.618 ±0.080	-0.911	1.102
SDSS J150609.76+444737.1	56098-56099	1.867	-27.050	46.807±0.010	9.618 ±0.080	-0.911	0.001
SDSS J150726.32+440649.2	53148-56099	3.077	-29.160	47.602±0.005	10.198 ±0.056	-0.696	1.983
SDSS J150810.38+005806.4	51665-51996	2.999	-28.100	46.872±0.025	9.601 ±0.046	-0.829	0.227
SDSS J150810.38+005806.4	51665-55629	2.999	-28.100	46.872±0.025	9.601 ±0.046	-0.829	2.716
SDSS J150810.38+005806.4	51996-55629	2.999	-28.100	46.872±0.025	9.601 ±0.046	-0.829	2.489
SDSS J150932.11+111313.6	53850-56063	2.109	-27.141	46.823±0.010	9.295 ±0.048	-0.572	1.950
SDSS J150932.11+111313.6	53850-56063	2.109	-27.141	46.823±0.010	9.295 ±0.048	-0.572	1.950
SDSS J150944.09+561605.2	52079-56425	3.170	-28.300	47.132±0.011	9.958 ±0.038	-0.926	2.855
SDSS J150955.64+270932.9	54539-55382	2.919	-28.568	47.019±0.004	9.828 ±0.021	-0.909	0.589
SDSS J151120.82+095718.6	53876-55982	2.890	-27.301	46.668±0.018	9.129 ±0.489	-0.561	1.483
SDSS J151120.82+095718.6	53876-56063	2.890	-27.301	46.668±0.018	9.129 ±0.489	-0.561	1.540
SDSS J151120.82+095718.6	55982-56063	2.890	-27.301	46.668±0.018	9.129 ±0.489	-0.561	0.057
SDSS J151130.46+323445.8	53171-55691	3.013	-27.306	46.837±0.030	10.276 ±0.177	-1.540	1.720
SDSS J151248.64+451213.2	52721-56099	2.014	-27.507	46.991±0.008	9.361 ±0.192	-0.470	3.071
SDSS J151248.64+451213.2	52721-56101	2.014	-27.507	46.991±0.008	9.361 ±0.192	-0.470	3.072
SDSS J151248.64+451213.2	56099-56101	2.014	-27.507	46.991±0.008	9.361 ±0.192	-0.470	0.002
SDSS J151307.20+603758.7	52345-56443	2.755	-27.496	46.937±0.014	9.288 ±0.054	-0.452	2.990
SDSS J151333.06+434422.3	53148-56072	2.291	-27.240	46.931±0.014	9.590 ±0.052	-0.759	2.434
SDSS J151333.06+434422.3	53148-56072	2.291	-27.240	46.931±0.014	9.590 ±0.052	-0.759	2.434
SDSS J151413.16+405157.9	52736-56067	1.871	-26.615	46.610±0.010	9.341 ±0.103	-0.831	3.179
SDSS J151448.87+354154.3	53083-56048	2.186	-27.128	46.781±0.014	9.560 ±0.216	-0.879	2.550
SDSS J151448.87+354154.3	53083-56048	2.186	-27.128	46.781±0.014	9.560 ±0.216	-0.879	2.550
SDSS J151448.87+354154.3	53083-56048	2.186	-27.128	46.781±0.014	9.560 ±0.216	-0.879	2.550
SDSS J151752.78+535010.5	52376-56402	2.899	-28.124	47.210±0.010	9.501 ±0.080	-0.391	2.829
SDSS J151752.78+535010.5	52376-56402	2.899	-28.124	47.210±0.010	9.501 ±0.080	-0.391	2.829
SDSS J152341.33+234922.8	54209-55680	3.111	-27.288	46.476±0.020	9.893 ±0.231	-1.518	0.980
SDSS J152625.38+014857.9	54560-55648	2.999	-27.204	46.943±0.019	9.406 ±0.130	-0.563	0.745
SDSS J152922.04+570817.3	53437-56453	2.644	-27.004	46.714±0.017	8.910 ±0.092	-0.296	2.268
SDSS J153326.74+073047.7	54208-56002	3.471	-28.075	47.120±0.013	9.253 ±0.044	-0.233	1.099
SDSS J153336.02+571835.7	52345-56429	2.303	-27.498	47.012±0.008	9.765 ±0.055	-0.854	3.388
SDSS J153336.02+571835.7	52347-56429	2.303	-27.498	47.012±0.008	9.765 ±0.055	-0.854	3.386
SDSS J153428.56+480028.7	52738-56419	2.153	-27.069	46.741±0.022	9.441 ±0.054	-0.801	3.199
SDSS J153703.95+533220.0	52374-52442	2.390	-28.370	47.197±0.010	9.360 ±0.036	-0.263	0.055
SDSS J153703.95+533220.0	52374-56452	2.390	-28.370	47.197±0.010	9.360 ±0.036	-0.263	3.296
SDSS J153703.95+533220.0	52442-56452	2.390	-28.370	47.197±0.010	9.360 ±0.036	-0.263	3.241
SDSS J153955.05+072955.6	53859-55733	3.113	-27.628	46.619±0.026	9.612 ±0.139	-1.093	1.248
SDSS J154229.49+145045.0	54567-55741	2.859	-27.054	46.789±0.016	9.007 ±0.114	-0.318	0.833
SDSS J154231.76+432251.7	52466-56101	2.626	-27.747	46.881±0.012	9.880 ±0.093	-1.100	2.747
SDSS J154620.35+113553.5	54241-55737	2.098	-26.830	46.688±0.022	9.191 ±0.165	-0.603	1.323
SDSS J155302.29+234648.4	53786-55321	2.155	-27.643	46.886±0.015	9.585 ±0.044	-0.799	1.333
SDSS J155719.27+103328.5	54584-55721	1.930	-26.663	46.281±0.032	9.608 ±0.134	-1.428	1.063
SDSS J160202.10+495904.3	52081-56453	2.033	-27.467	47.101±0.008	9.657 ±0.095	-0.657	3.949
SDSS J160202.10+495904.3	52375-56453	2.033	-27.467	47.101±0.008	9.657 ±0.095	-0.657	3.684

Table B.1: (continued)

BAL quasar	MJD-pair	z_{em}	M_i (mag)	$\log L_{bol}$ (erg s^{-1})	$\log M_{BH}$ (M_{\odot})	$\log \frac{L_{bol}}{L_{Edd}}$	Δt (years)
SDSS J160321.85+120414.8	54569-55711	2.232	-27.193	46.723±0.014	8.777 ±0.035	-0.154	0.968
SDSS J160445.92+335759.0	53142-55721	1.875	-26.474	46.573±0.010	9.571 ±0.140	-1.098	2.458
SDSS J160816.96+235148.3	53533-55331	2.201	-27.075	46.822±0.019	8.631 ±0.022	0.090	1.539
SDSS J161537.87+522328.9	54270-56487	2.538	-27.524	46.679±0.008	9.266 ±0.132	-0.687	1.717
SDSS J161605.39+111542.8	54571-56040	1.834	-26.575	46.711±0.009	9.409 ±0.108	-0.799	1.420
SDSS J161727.05+221121.1	53566-55331	2.220	-26.715	46.714±0.022	9.316 ±0.295	-0.703	1.502
SDSS J162625.70+155003.6	53880-55357	2.308	-26.614	46.689±0.017	8.777 ±0.103	-0.188	1.223
SDSS J162648.75+125124.5	53881-55361	3.060	-27.426	46.527±0.006	0.000 ±-1.000	-999.0	0.999
SDSS J162648.75+125124.5	53881-55361	3.060	-27.426	46.527±0.006	0.000 ±-1.000	-999.0	0.999
SDSS J162657.47+405848.0	52379-56072	3.048	-27.639	47.033±0.016	8.697 ±0.084	0.235	2.499
SDSS J162935.68+321009.5	53463-55750	2.033	-26.949	46.776±0.014	9.510 ±0.052	-0.834	2.066
SDSS J163212.72+360930.4	52765-56048	2.019	-26.098	46.579±0.014	9.354 ±0.156	-0.875	2.979
SDSS J163226.51+305506.4	53463-55749	2.012	-26.580	46.605±0.022	9.315 ±0.096	-0.810	2.079
SDSS J163226.51+305506.4	53463-55749	2.012	-26.580	46.605±0.022	9.315 ±0.096	-0.810	2.079
SDSS J163416.17+355812.9	52765-56048	3.060	-28.635	47.422±0.007	9.701 ±0.023	-0.380	2.215
SDSS J163638.18+211255.5	53149-55693	1.798	-26.503	46.565±0.016	9.093 ±0.079	-0.629	2.491
SDSS J163651.81+313148.0	52786-55824	1.845	-28.010	47.227±0.003	9.726 ±0.129	-0.599	2.926
SDSS J163844.79+330339.5	52786-55803	2.003	-28.634	47.396±0.006	9.262 ±0.013	0.034	2.752
SDSS J164228.52+394343.5	52381-56090	1.868	-27.383	46.920±0.009	9.473 ±0.202	-0.653	3.543
SDSS J164228.52+394343.5	52381-56090	1.868	-27.383	46.920±0.009	9.473 ±0.202	-0.653	3.543
SDSS J170459.04+354612.0	52427-55825	2.035	-26.731	46.559±0.023	9.283 ±0.137	-0.824	3.067
SDSS J220116.75+125636.4	52224-55831	2.922	-27.711	47.029±0.016	8.781 ±0.017	0.148	2.520
SDSS J220151.45+130719.9	52224-55831	2.521	-27.682	47.058±0.011	9.646 ±0.083	-0.688	2.807
SDSS J220151.45+130719.9	52224-55831	2.521	-27.682	47.058±0.011	9.646 ±0.083	-0.688	2.807
SDSS J220901.67+061303.7	54380-56105	3.355	-27.505	46.696±0.017	9.470 ±0.051	-0.874	1.085
SDSS J221509.31+132237.1	52210-55749	1.900	-27.050	46.825±0.006	9.626 ±0.173	-0.901	3.343
SDSS J221509.31+132237.1	52221-55749	1.900	-27.050	46.825±0.006	9.626 ±0.173	-0.901	3.333
SDSS J223118.34+003321.4	52162-55445	2.506	-27.350	46.899±0.016	9.348 ±0.073	-0.550	2.565
SDSS J223500.04+144556.7	52521-56235	2.355	-27.460	46.953±0.008	9.526 ±0.058	-0.674	3.033
SDSS J224511.29+003557.3	52590-55454	2.200	-27.209	46.721±0.021	8.890 ±0.068	-0.270	2.452
SDSS J225027.47+302618.0	54379-56535	2.260	-26.940	46.676±0.014	9.218 ±0.486	-0.643	1.812
SDSS J232300.06+151002.4	52258-56206	1.988	-27.734	47.062±0.013	9.468 ±0.029	-0.506	3.620
SDSS J233249.55+174817.2	56211-56954	3.066	-27.203	-999.9±-999.9	-999.9 ±-999.9	-999.9	0.501
SDSS J234414.97+004855.5	52524-55449	2.953	-27.508	46.931±0.020	8.718 ±0.448	0.113	2.027
SDSS J235351.71+212019.8	56272-56956	2.979	-27.406	-999.9±-999.9	-999.9 ±-999.9	-999.9	0.471
SDSS J235454.30-092603.2	52201-56602	1.981	-27.532	47.080±0.006	9.569 ±0.044	-0.589	4.045
SDSS J235454.30-092603.2	52201-56604	1.981	-27.532	47.080±0.006	9.569 ±0.044	-0.589	4.047
SDSS J235454.30-092603.2	56602-56604	1.981	-27.532	47.080±0.006	9.569 ±0.044	-0.589	0.002

Table B.2: *Details of the Appearing, Appearing pristine, and Disappearing samples of C iv BAL absorption complexes.*

BAL quasar	MJD pair	Δt year	$\Delta F/\langle F \rangle_{1700}$	Δv km s ⁻¹	v_{min} km s ⁻¹	v_{max} km s ⁻¹	ΔEW Å	$\Delta EW/\langle EW \rangle$	Type
SDSS J002028.34-002914.9	51816-56979	4.816	-0.084 ± 0.106	2462.494	-19579.232	-17116.738	1.685 ± 0.284	0.690 ± 0.148	Appearing
SDSS J002028.34-002914.9	51900-56979	4.738	-0.067 ± 0.075	2462.494	-19579.232	-17116.738	2.178 ± 0.195	0.993 ± 0.114	Appearing pristine
SDSS J004022.40+005939.6	52261-55182	2.245	0.150 ± 0.171	6453.826	-9535.714	-3081.888	-9.888 ± 0.636	-1.313 ± 0.061	Disappearing
SDSS J005157.24+000354.7	51812-52201	0.361	-0.182 ± 0.064	3483.763	-10579.552	-7095.789	1.388 ± 0.185	0.683 ± 0.089	Appearing
SDSS J005157.24+000354.7	51812-54800	2.776	-0.427 ± 0.051	3483.763	-10579.552	-7095.789	2.876 ± 0.145	1.036 ± 0.064	Appearing pristine
SDSS J005157.24+000354.7	51812-55451	3.381	-0.372 ± 0.050	3483.763	-10579.552	-7095.789	4.307 ± 0.137	1.234 ± 0.053	Appearing pristine
SDSS J005157.24+000354.7	51812-57016	4.835	-0.274 ± 0.048	3483.763	-10579.552	-7095.789	2.644 ± 0.139	0.994 ± 0.066	Appearing pristine
SDSS J005157.24+000354.7	51876-52201	0.302	-0.223 ± 0.063	3483.763	-10579.552	-7095.789	0.980 ± 0.181	0.438 ± 0.077	Appearing
SDSS J005157.24+000354.7	51876-54800	2.717	-0.466 ± 0.050	3483.763	-10579.552	-7095.789	2.468 ± 0.140	0.828 ± 0.054	Appearing pristine
SDSS J005157.24+000354.7	51876-55451	3.321	-0.411 ± 0.049	3483.763	-10579.552	-7095.789	3.899 ± 0.132	1.055 ± 0.045	Appearing pristine
SDSS J005157.24+000354.7	51876-57016	4.775	-0.314 ± 0.047	3483.763	-10579.552	-7095.789	2.236 ± 0.133	0.781 ± 0.054	Appearing pristine
SDSS J005157.24+000354.7	51913-54800	2.682	-0.565 ± 0.038	3483.763	-10579.552	-7095.789	2.095 ± 0.107	0.662 ± 0.031	Appearing pristine
SDSS J005157.24+000354.7	51913-55451	3.287	-0.512 ± 0.037	3483.763	-10579.552	-7095.789	3.526 ± 0.096	0.908 ± 0.024	Appearing pristine
SDSS J005157.24+000354.7	51913-57016	4.741	-0.417 ± 0.034	3483.763	-10579.552	-7095.789	1.863 ± 0.098	0.611 ± 0.030	Appearing pristine
SDSS J014029.96-082039.5	52145-56605	4.168	-0.622 ± 0.092	5494.332	-21802.818	-16308.486	8.737 ± 0.378	1.421 ± 0.090	Appearing pristine
SDSS J020826.41+003810.5	52937-55201	1.843	-0.560 ± 0.198	6442.992	-21367.992	-14925.000	4.062 ± 0.553	0.584 ± 0.087	Appearing
SDSS J020826.41+003810.5	52937-55451	2.047	-0.425 ± 0.181	6442.992	-21367.992	-14925.000	5.134 ± 0.517	0.685 ± 0.081	Appearing pristine
SDSS J021755.25-090140.9	52162-55828	3.020	-0.780 ± 0.097	5372.822	-21341.582	-15968.760	-4.417 ± 0.321	-0.809 ± 0.054	Disappearing
SDSS J024006.11-002037.6	51821-55247	3.469	-	2428.598	-23439.049	-21010.451	2.210 ± 0.306	1.173 ± 0.193	Appearing pristine
SDSS J024006.11-002037.6	51821-55458	3.682	-	2428.598	-23439.049	-21010.451	2.488 ± 0.246	1.230 ± 0.179	Appearing pristine
SDSS J024006.11-002037.6	52199-55247	3.086	-	2428.598	-23439.049	-21010.451	2.433 ± 0.276	1.373 ± 0.173	Appearing pristine
SDSS J024006.11-002037.6	52199-55458	3.300	-	2428.598	-23439.049	-21010.451	2.712 ± 0.206	1.419 ± 0.160	Appearing pristine
SDSS J030004.75-063224.7	51929-56577	4.002	0.280 ± 0.126	2881.721	-23111.867	-20230.146	-2.942 ± 0.311	-1.009 ± 0.071	Disappearing
SDSS J075010.17+304032.3	52663-55538	2.715	-0.342 ± 0.075	5037.403	-18184.609	-13147.206	7.439 ± 0.262	1.114 ± 0.045	Appearing pristine
SDSS J081102.91+500724.2	51912-55517	3.475	0.315 ± 0.138	2130.952	-11629.625	-9498.673	-3.920 ± 0.356	-1.480 ± 0.074	Disappearing
SDSS J081338.34+240729.1	52962-55863	2.811	-0.038 ± 0.090	2785.714	-9642.856	-6857.142	-2.567 ± 0.310	-2.659 ± 0.577	Disappearing
SDSS J083725.17+541842.0	51899-56751	4.348	-0.325 ± 0.091	2205.467	-19186.400	-16980.934	2.460 ± 0.203	1.107 ± 0.107	Appearing pristine
SDSS J084033.84+052626.0	52650-55927	2.766	-0.020 ± 0.126	7608.098	-16233.097	-8624.999	7.288 ± 0.439	1.381 ± 0.114	Appearing pristine
SDSS J084033.84+052626.0	52708-55927	2.717	0.114 ± 0.134	7608.098	-16233.097	-8624.999	5.868 ± 0.495	0.980 ± 0.107	Appearing pristine
SDSS J084147.86+053038.7	52708-55927	2.730	-0.296 ± 0.114	2639.059	-21571.414	-18932.355	2.691 ± 0.231	1.193 ± 0.132	Appearing pristine
SDSS J084147.86+053038.7	52708-55927	2.730	-0.296 ± 0.114	3346.475	-10797.697	-7451.222	4.097 ± 0.253	1.011 ± 0.077	Appearing
SDSS J084244.39+152901.9	53799-56225	2.020	-0.358 ± 0.097	2009.711	-28025.455	-26015.744	1.207 ± 0.141	0.751 ± 0.103	Appearing pristine
SDSS J084244.39+152901.9	53815-56225	2.007	-0.318 ± 0.102	2009.711	-28025.455	-26015.744	1.170 ± 0.150	0.719 ± 0.111	Appearing
SDSS J084410.34+593330.6	54439-56220	1.520	0.090 ± 0.113	4854.549	-15354.548	-10499.999	1.900 ± 0.297	0.434 ± 0.077	Appearing
SDSS J085512.32+251208.5	53381-55957	2.165	0.128 ± 0.081	5643.949	-24068.342	-18424.393	3.347 ± 0.248	0.726 ± 0.066	Appearing pristine
SDSS J085841.93+124932.1	53820-55953	1.900	-0.457 ± 0.113	5158.751	-18765.869	-13607.118	2.474 ± 0.357	0.409 ± 0.060	Appearing
SDSS J090744.96+543142.4	51908-56334	3.671	-0.187 ± 0.123	2634.143	-22087.363	-19453.221	2.226 ± 0.237	1.070 ± 0.116	Appearing pristine
SDSS J090757.38+333116.2	52989-56354	3.140	0.046 ± 0.104	4982.143	-23946.428	-18964.285	-2.626 ± 0.369	-0.702 ± 0.091	Disappearing
SDSS J090950.53+245846.0	53401-56328	2.378	0.019 ± 0.129	4018.047	-15735.873	-11717.826	3.293 ± 0.280	0.806 ± 0.085	Appearing pristine
SDSS J091159.36+442526.8	52312-56338	3.478	-0.216 ± 0.060	12491.342	-23445.195	-10953.854	-5.459 ± 0.297	-0.563 ± 0.030	Disappearing
SDSS J091427.18+582752.3	51907-56597	4.187	-0.055 ± 0.159	3645.907	-8388.417	-4742.510	3.724 ± 0.375	1.026 ± 0.134	Appearing pristine
SDSS J091808.80+005457.7	51955-55535	3.148	0.010 ± 0.155	3277.525	-24589.285	-21311.760	-7.175 ± 0.536	-1.690 ± 0.080	Disappearing
SDSS J091909.82+463435.8	52620-56363	3.513	0.005 ± 0.116	8485.785	-26920.773	-18434.988	11.224 ± 0.735	1.310 ± 0.134	Appearing
SDSS J091944.53+560243.4	51908-56625	4.621	0.084 ± 0.091	2844.731	-13906.335	-11061.604	-3.897 ± 0.254	-1.384 ± 0.088	Disappearing
SDSS J092316.93+033146.9	52254-55889	3.161	-0.188 ± 0.104	3993.155	-12751.371	-8758.216	3.119 ± 0.288	0.715 ± 0.080	Appearing
SDSS J092337.69+462100.1	52314-56363	3.438	-0.222 ± 0.117	4952.472	-15481.508	-10529.036	3.941 ± 0.339	0.798 ± 0.083	Appearing pristine
SDSS J092418.53+271851.5	53383-56273	2.502	-0.125 ± 0.093	2556.610	-8871.023	-6314.413	-3.862 ± 0.175	-1.302 ± 0.062	Disappearing
SDSS J092743.01+290734.7	53389-56272	2.431	-0.109 ± 0.141	3361.859	-15187.365	-11825.506	1.999 ± 0.366	0.649 ± 0.147	Appearing
SDSS J092851.40+311627.0	53386-56329	2.646	0.290 ± 0.084	3329.357	-22775.785	-19446.428	-3.339 ± 0.237	-1.081 ± 0.064	Disappearing
SDSS J093418.28+355508.3	52996-55590	2.066	-0.027 ± 0.113	5035.715	-25660.715	-20625.000	-3.630 ± 0.275	-1.106 ± 0.073	Disappearing
SDSS J093620.52+004649.2	52314-55563	3.271	0.526 ± 0.080	2629.749	-15597.764	-12968.015	-4.006 ± 0.254	-1.513 ± 0.072	Disappearing
SDSS J093630.22+155418.2	54085-56000	1.644	0.035 ± 0.101	6092.465	-17740.260	-10837.795	4.148 ± 0.344	0.648 ± 0.063	Appearing
SDSS J093739.89+334053.5	52992-56336	2.836	0.106 ± 0.147	6171.085	-11551.573	-5380.488	9.430 ± 0.460	2.210 ± 0.192	Appearing pristine
SDSS J094437.56+104726.8	53053-55945	2.612	-0.115 ± 0.130	6139.797	-25089.807	-18950.010	-10.739 ± 0.479	-1.385 ± 0.056	Disappearing
SDSS J094804.89+473222.9	52703-55980	3.310	-0.126 ± 0.087	4211.425	-16116.376	-11904.951	-5.768 ± 0.361	-1.129 ± 0.060	Disappearing
SDSS J095005.90+362455.2	52999-57449	3.757	-0.303 ± 0.086	2180.664	-22346.982	-20166.318	1.347 ± 0.170	0.621 ± 0.090	Appearing
SDSS J095217.51+534854.7	52282-56381	3.260	0.046 ± 0.161	3736.412	-16976.930	-13240.518	3.624 ± 0.329	0.958 ± 0.116	Appearing pristine
SDSS J100117.02+642009.4	51943-56008	3.777	0.071 ± 0.132	6076.781	-15053.571	-8976.790	-8.150 ± 0.513	-1.506 ± 0.090	Disappearing

Table B.2: (continued)

BAL quasar	MJD pair	Δt year	$\Delta F/(F)_{1700}$	Δv km s ⁻¹	v_{min} km s ⁻¹	v_{max} km s ⁻¹	ΔEW Å	$\Delta EW/(EW)$	Type
SDSS J100342.73+240622.3	53735–56273	2.428	-0.222 ±0.052	6048.916	-23340.645	-17291.729	9.976 ±0.194	1.411 ±0.039	Appearing pristine
SDSS J100607.17+625320.2	51943–56008	3.907	0.001 ±0.130	2250.000	-8089.285	-5839.285	-3.310 ±0.291	-1.525 ±0.146	Disappearing
SDSS J102250.16+483631.1	52674–56769	3.666	-0.077 ±0.098	3692.866	-15243.617	-11550.751	-2.486 ±0.270	-0.858 ±0.098	Disappearing
SDSS J102435.39+372637.0	53415–55597	2.190	-0.068 ±0.081	4297.769	-10300.402	-6002.634	-4.332 ±0.251	-1.046 ±0.056	Disappearing
SDSS J102510.55+260253.7	53765–56309	2.234	0.192 ±0.135	4602.328	-8158.657	-3556.329	2.910 ±0.399	0.805 ±0.142	Appearing
SDSS J102812.08+381132.9	52998–55597	2.525	0.315 ±0.113	2691.950	-15997.314	-13305.364	-2.960 ±0.318	-1.122 ±0.088	Disappearing
SDSS J103311.77+603146.8	52296–56659	3.412	0.163 ±0.105	6239.918	-23518.441	-17278.523	-6.172 ±0.275	-1.065 ±0.038	Disappearing
SDSS J103648.24+292800.0	53799–56366	2.350	-0.380 ±0.072	11550.536	-26840.756	-15290.220	8.932 ±0.416	0.695 ±0.039	Appearing pristine
SDSS J104325.04+162050.7	53851–56008	1.762	-0.034 ±0.092	5451.071	-17285.332	-11834.261	4.143 ±0.244	0.935 ±0.064	Appearing pristine
SDSS J104735.13+174928.2	54174–56269	1.877	-0.211 ±0.108	8635.866	-17788.648	-9152.782	3.437 ±0.505	0.371 ±0.061	Appearing
SDSS J104841.02+000042.8	51909–55570	3.314	0.148 ±0.072	2303.571	-12160.714	-9857.143	-1.327 ±0.150	-0.831 ±0.081	Disappearing
SDSS J105311.39+123516.6	53117–55980	1.999	-0.210 ±0.124	3125.578	-18561.270	-15435.691	2.260 ±0.386	0.718 ±0.142	Appearing
SDSS J105427.92+504835.6	52346–56384	3.709	-0.002 ±0.151	2830.472	-15320.615	-12490.144	2.762 ±0.376	0.783 ±0.126	Appearing
SDSS J105847.20+005656.6	51908–55302	2.797	-0.138 ±0.123	6521.829	-19809.699	-13287.870	4.451 ±0.378	0.878 ±0.096	Appearing
SDSS J110038.71+450626.2	53054–55656	2.482	0.194 ±0.142	4026.821	-19736.963	-15710.142	-4.486 ±0.458	-0.959 ±0.072	Disappearing
SDSS J110419.11+143650.8	53377–55983	2.538	-0.125 ±0.075	4850.117	-21358.164	-16508.047	4.600 ±0.293	0.934 ±0.077	Appearing
SDSS J110549.37+663457.2	51929–56741	4.343	0.163 ±0.095	2153.324	-25821.096	-23667.771	-2.113 ±0.206	-1.516 ±0.155	Disappearing
SDSS J110650.41+585551.7	54526–56666	1.615	-0.244 ±0.144	4425.103	-10813.457	-6388.354	3.573 ±0.327	0.936 ±0.084	Appearing
SDSS J110906.29+640705.2	52370–56746	4.198	0.430 ±0.052	2105.167	-15143.104	-13037.937	-0.961 ±0.117	-0.674 ±0.070	Disappearing
SDSS J111039.65+664253.4	51929–56741	4.148	0.021 ±0.088	2885.919	-9765.386	-6879.467	2.983 ±0.192	1.986 ±0.191	Appearing pristine
SDSS J111039.65+664253.4	51942–56741	4.137	0.040 ±0.081	2885.919	-9765.386	-6879.467	2.491 ±0.184	1.425 ±0.132	Appearing pristine
SDSS J111431.20+200024.1	54179–56041	1.688	-0.427 ±0.107	3673.941	-21694.334	-18020.393	3.048 ±0.350	0.822 ±0.112	Appearing
SDSS J113123.34+460408.4	53050–54861	1.638	-0.174 ±0.082	4569.349	-14460.800	-9891.451	3.103 ±0.254	0.961 ±0.103	Appearing pristine
SDSS J113438.57+091012.6	52765–55973	3.142	0.210 ±0.126	2099.897	-6671.722	-4571.825	-3.869 ±0.277	-1.497 ±0.081	Disappearing
SDSS J113608.22+184908.1	54179–56047	1.611	-0.144 ±0.134	2403.400	-26321.035	-23917.635	2.595 ±0.286	1.222 ±0.173	Appearing
SDSS J113754.91+460227.4	53050–56390	2.942	0.480 ±0.116	4242.428	-14030.722	-9788.294	-6.852 ±0.359	-1.665 ±0.064	Disappearing
SDSS J113754.91+460227.4	53054–56401	2.554	-0.069 ±0.130	4664.779	-20745.578	-16080.799	2.758 ±0.348	0.685 ±0.106	Appearing
SDSS J114408.82+532412.4	52367–56419	3.552	-0.178 ±0.104	10403.972	-26049.785	-15645.813	10.354 ±0.503	1.221 ±0.077	Appearing pristine
SDSS J115707.36+333257.9	53469–55621	1.807	0.167 ±0.117	3214.286	-14035.714	-10821.428	-2.441 ±0.265	-0.872 ±0.074	Disappearing
SDSS J120634.13+455238.2	53089–56383	3.042	-0.169 ±0.099	7949.875	-20746.973	-12797.098	5.829 ±0.451	0.845 ±0.084	Appearing pristine
SDSS J121113.56+044946.2	52376–55633	2.696	0.180 ±0.138	3995.192	-12605.667	-8610.475	4.511 ±0.338	0.957 ±0.099	Appearing pristine
SDSS J121407.42+565108.7	53050–56429	3.244	-0.342 ±0.076	4527.527	-25105.191	-20577.664	5.652 ±0.290	1.707 ±0.141	Appearing pristine
SDSS J122213.41+235833.7	54502–56329	1.627	-0.024 ±0.108	7058.033	-24645.262	-17587.229	2.917 ±0.436	0.339 ±0.058	Appearing
SDSS J123542.11+440114.5	53062–56365	2.778	-0.359 ±0.135	3520.038	-18446.033	-14925.995	3.112 ±0.337	0.862 ±0.112	Appearing pristine
SDSS J123930.24+501512.2	52735–56389	2.969	-0.200 ±0.171	2929.412	-12115.609	-9186.197	4.340 ±0.294	0.995 ±0.089	Appearing pristine
SDSS J124031.68+103129.5	52734–55955	2.798	-0.089 ±0.145	7733.159	-21417.043	-13683.884	5.488 ±0.634	0.582 ±0.082	Appearing
SDSS J124345.92+185343.0	54481–56088	1.322	-0.106 ±0.117	11175.000	-24825.000	-13650.000	6.375 ±0.585	0.744 ±0.080	Appearing
SDSS J124505.66+561430.5	52765–56426	3.221	-0.105 ±0.111	3352.616	-16959.758	-13607.142	-2.420 ±0.278	-0.874 ±0.084	Disappearing
SDSS J124526.80+172053.2	54243–56090	1.769	-0.484 ±0.061	4767.883	-22348.912	-17581.029	6.409 ±0.204	1.439 ±0.057	Appearing pristine
SDSS J124543.07+183427.2	54481–56088	1.439	-0.496 ±0.094	4784.092	-25147.828	-20363.736	3.964 ±0.328	0.729 ±0.074	Appearing
SDSS J124725.08+493042.8	52736–56413	2.981	0.022 ±0.162	13629.116	-17821.582	-4192.466	16.686 ±0.711	0.819 ±0.045	Appearing
SDSS J125150.65+263900.0	54205–56339	2.007	-0.749 ±0.059	13719.711	-25539.105	-11819.395	14.644 ±0.450	1.087 ±0.039	Appearing
SDSS J125157.23+124842.0	53473–55981	2.323	-0.603 ±0.099	4368.673	-14497.282	-10128.609	5.664 ±0.328	1.146 ±0.078	Appearing pristine
SDSS J125432.78+435228.9	53063–56371	2.866	0.066 ±0.138	2688.502	-9229.315	-6540.813	-4.490 ±0.293	-1.695 ±0.096	Disappearing
SDSS J125659.00+193942.7	54483–56065	1.077	-0.005 ±0.151	2297.778	-7421.256	-5123.478	4.088 ±0.372	2.171 ±0.318	Appearing
SDSS J125906.79+342529.9	53476–55320	1.344	0.280 ±0.154	9974.864	-14009.904	-4035.040	7.691 ±1.022	0.617 ±0.103	Appearing
SDSS J130148.58+361515.8	53799–55335	1.334	0.078 ±0.149	13182.336	-24310.467	-11128.131	8.272 ±0.814	0.692 ±0.086	Appearing
SDSS J130527.88+262522.7	54153–56334	1.892	0.106 ±0.155	7144.929	-21257.098	-14112.169	4.585 ±0.593	0.727 ±0.118	Appearing
SDSS J130542.36+462503.4	53117–56385	3.166	-0.125 ±0.121	3529.239	-12359.879	-8830.640	-5.813 ±0.361	-2.266 ±0.174	Disappearing
SDSS J130542.36+462503.4	53117–56385	3.166	-0.125 ±0.121	3235.954	-8629.612	-5393.658	-6.091 ±0.309	-2.280 ±0.148	Disappearing
SDSS J130825.74+204707.2	54502–56046	1.392	-0.312 ±0.071	2204.787	-10749.969	-8545.182	1.179 ±0.151	0.785 ±0.111	Appearing
SDSS J130825.74+204707.2	54502–56046	1.392	-0.312 ±0.071	2110.671	-5172.796	-3062.125	3.316 ±0.129	1.400 ±0.070	Appearing pristine
SDSS J130825.74+204707.2	54502–56047	1.393	-0.232 ±0.080	2110.671	-5172.796	-3062.125	2.179 ±0.159	1.210 ±0.090	Appearing pristine
SDSS J131038.17+113617.9	53116–55986	2.915	0.380 ±0.128	2873.535	-17598.844	-14725.309	-3.621 ±0.453	-1.267 ±0.102	Disappearing
SDSS J131524.71+130411.8	53142–56003	2.364	-0.231 ±0.105	4099.350	-9976.615	-5877.265	-6.351 ±0.243	-1.323 ±0.053	Disappearing
SDSS J132115.66+495546.3	52759–56385	2.885	0.173 ±0.107	16736.895	-26561.893	-9824.999	13.153 ±0.520	0.888 ±0.043	Appearing
SDSS J132216.24+052446.3	52376–55633	2.925	0.134 ±0.076	2545.699	-17569.199	-15023.500	-1.504 ±0.170	-0.847 ±0.079	Disappearing
SDSS J132216.24+052446.3	52376–55633	2.925	0.134 ±0.076	2770.400	-21377.500	-18607.100	-1.816 ±0.185	-0.964 ±0.079	Disappearing
SDSS J132246.82+272633.0	53795–56309	2.283	0.127 ±0.132	6568.117	-17813.111	-11244.994	6.701 ±0.519	0.802 ±0.082	Appearing
SDSS J132508.82+122314.2	53146–56008	2.828	0.798 ±0.058	5796.408	-9966.931	-4170.523	-15.916 ±0.210	-1.759 ±0.021	Disappearing

Table B.2: (continued)

BAL quasar	MJD pair	Δt year	$\Delta F/(F)_{1700}$	Δv km s ⁻¹	v_{min} km s ⁻¹	v_{max} km s ⁻¹	ΔEW Å	$\Delta EW/(EW)$	Type
SDSS J133211.21+392825.9	53472–55704	2.003	0.190 ± 0.124	3303.303	-20146.842	-16843.539	-3.396 ± 0.310	-0.957 ± 0.076	Disappearing
SDSS J133727.10+081734.3	54156–55973	1.175	-0.442 ± 0.138	3683.359	-15976.712	-12293.353	4.281 ± 0.460	0.969 ± 0.096	Appearing pristine
SDSS J133959.98+203757.8	54231–56075	1.253	-0.024 ± 0.114	10359.209	-16546.072	-6186.863	5.810 ± 0.805	0.619 ± 0.103	Appearing
SDSS J134027.41+660348.2	51989–56717	3.820	0.299 ± 0.153	6097.750	-14976.207	-8878.457	5.546 ± 0.433	0.801 ± 0.081	Appearing
SDSS J134210.95+301521.4	53851–56363	2.167	0.115 ± 0.118	4490.128	-10982.659	-6492.531	3.341 ± 0.313	0.600 ± 0.066	Appearing
SDSS J134544.55+002810.7	51943–55630	2.912	0.163 ± 0.101	10828.574	-14878.768	-4050.193	-17.084 ± 0.341	-1.156 ± 0.018	Disappearing
SDSS J135910.45+563617.3	52669–56487	3.218	-0.269 ± 0.067	7017.859	-26571.430	-19553.570	-3.637 ± 0.237	-0.764 ± 0.045	Disappearing
SDSS J140051.79+463530.0	52723–56367	3.361	0.054 ± 0.060	4498.080	-18921.527	-14423.447	-3.657 ± 0.182	-0.940 ± 0.039	Disappearing
SDSS J140217.56+445211.1	53115–56102	2.513	-0.462 ± 0.118	3377.906	-13830.678	-10452.771	2.369 ± 0.301	0.794 ± 0.117	Appearing
SDSS J140231.81+643610.6	51984–56717	4.454	0.185 ± 0.144	3241.602	-19852.324	-16610.723	-3.826 ± 0.457	-1.033 ± 0.085	Disappearing
SDSS J142132.01+375230.3	54509–56039	1.405	-0.539 ± 0.093	7491.569	-18123.406	-10631.837	5.606 ± 0.405	0.885 ± 0.080	Appearing
SDSS J140501.93+444759.8	53115–56102	2.545	0.203 ± 0.060	3375.000	-22714.285	-19339.285	-1.303 ± 0.146	-0.670 ± 0.067	Disappearing
SDSS J140651.09+650613.2	51984–56717	4.510	0.488 ± 0.089	8727.589	-21273.627	-12546.038	4.404 ± 0.527	0.535 ± 0.078	Appearing
SDSS J141304.26+164741.1	54231–56015	1.516	-0.071 ± 0.088	6534.416	-27523.943	-20989.527	6.342 ± 0.321	1.095 ± 0.077	Appearing pristine
SDSS J141407.25+562010.3	52674–56402	3.111	-0.032 ± 0.126	7724.580	-19296.008	-11571.428	-8.367 ± 0.456	-1.437 ± 0.089	Disappearing
SDSS J141956.96+010652.6	51997–55604	3.099	-0.323 ± 0.117	3251.163	-19030.725	-15779.562	2.513 ± 0.292	0.941 ± 0.120	Appearing
SDSS J141956.96+010652.6	51997–55634	3.125	-0.215 ± 0.112	3251.163	-19030.725	-15779.562	2.490 ± 0.261	0.937 ± 0.117	Appearing pristine
SDSS J142033.94+161228.3	54534–56035	1.310	-0.168 ± 0.107	9006.291	-26869.865	-17863.574	5.197 ± 0.484	0.741 ± 0.085	Appearing
SDSS J142132.01+375230.3	53084–56044	2.918	-0.096 ± 0.138	2559.898	-16008.180	-13448.281	-2.913 ± 0.386	-0.892 ± 0.106	Disappearing
SDSS J142211.80+584249.3	52342–56429	4.132	–	2245.422	-14083.882	-11838.460	3.131 ± 0.182	1.553 ± 0.132	Appearing pristine
SDSS J142659.95+161003.3	54506–56018	1.394	0.088 ± 0.091	8547.943	-26397.943	-17850.000	4.255 ± 0.533	0.513 ± 0.071	Appearing
SDSS J142813.72+233742.8	53494–56072	2.403	0.227 ± 0.104	2666.059	-11657.197	-8991.139	-2.749 ± 0.255	-1.090 ± 0.078	Disappearing
SDSS J143057.16+625113.1	51988–56720	3.690	-0.459 ± 0.149	12251.377	-16709.145	-4457.768	14.542 ± 0.577	1.081 ± 0.046	Appearing
SDSS J143248.81+501048.7	52460–56416	3.130	0.193 ± 0.124	8261.903	-23582.018	-15320.114	2.484 ± 0.386	0.361 ± 0.063	Appearing
SDSS J143255.09+155656.8	54534–56033	1.444	-0.380 ± 0.114	3148.271	-10451.306	-7303.034	4.004 ± 0.299	1.025 ± 0.094	Appearing pristine
SDSS J143558.56+252707.9	53827–56075	2.089	-0.347 ± 0.089	6295.221	-12075.779	-5780.558	11.523 ± 0.324	1.121 ± 0.043	Appearing
SDSS J143558.56+252707.9	53827–56075	2.089	-0.347 ± 0.089	3933.934	-23883.934	-19950.000	2.373 ± 0.278	0.693 ± 0.096	Appearing pristine
SDSS J143810.86+173900.9	54534–56037	1.421	0.230 ± 0.076	2257.232	-20831.047	-18573.814	2.069 ± 0.178	0.915 ± 0.103	Appearing pristine
SDSS J143813.25+193525.8	54535–56038	1.267	0.148 ± 0.132	8566.768	-26407.004	-17840.236	4.969 ± 0.541	0.567 ± 0.074	Appearing
SDSS J143821.60+393407.2	52797–56038	2.917	0.137 ± 0.120	2088.639	-25956.436	-23867.797	-2.129 ± 0.243	-0.921 ± 0.079	Disappearing
SDSS J144621.83+261707.4	54208–56076	1.538	-0.334 ± 0.106	12157.584	-24977.965	-12820.381	7.544 ± 0.498	0.629 ± 0.048	Appearing
SDSS J144826.10+122814.7	53531–56033	2.231	-0.296 ± 0.101	11436.425	-23270.400	-11833.976	8.085 ± 0.521	0.793 ± 0.059	Appearing pristine
SDSS J145519.92+121645.0	53521–56014	2.350	-0.338 ± 0.113	4035.729	-8119.023	-4083.294	6.127 ± 0.323	2.061 ± 0.182	Appearing pristine
SDSS J150406.23+614023.3	52055–56444	3.772	-0.436 ± 0.146	4699.928	-10541.955	-5842.027	3.738 ± 0.427	0.720 ± 0.090	Appearing
SDSS J150548.65+242706.1	53820–56074	1.486	-0.208 ± 0.091	4160.319	-19558.057	-15397.737	3.662 ± 0.312	0.811 ± 0.079	Appearing
SDSS J150932.11+111313.6	53850–56063	1.950	-0.580 ± 0.090	4855.246	-24767.754	-19912.508	4.388 ± 0.341	1.030 ± 0.088	Appearing
SDSS J151248.64+451213.2	52721–56099	3.071	0.012 ± 0.079	13738.171	-22492.920	-8754.749	14.649 ± 0.468	1.005 ± 0.042	Appearing pristine
SDSS J151248.64+451213.2	52721–56101	3.072	0.029 ± 0.076	13738.171	-22492.920	-8754.749	15.800 ± 0.205	1.043 ± 0.074	Appearing pristine
SDSS J151413.16+405157.9	52736–56067	3.179	-0.071 ± 0.137	2509.847	-14191.686	-11681.839	2.223 ± 0.334	1.136 ± 0.231	Appearing
SDSS J151448.87+354154.3	53083–56048	2.550	-0.218 ± 0.112	3262.061	-6266.309	-3004.248	2.794 ± 0.264	0.988 ± 0.127	Appearing
SDSS J151448.87+354154.3	53083–56048	2.550	-0.218 ± 0.112	3741.613	-26236.141	-22494.527	3.331 ± 0.331	1.057 ± 0.143	Appearing
SDSS J151610.08+434506.8	53148–56101	2.867	-0.156 ± 0.099	2761.890	-8609.242	-5847.352	-5.756 ± 0.254	-1.883 ± 0.131	Disappearing
SDSS J151752.78+535010.5	52376–56402	2.829	-0.069 ± 0.091	5024.323	-15189.653	-10165.330	2.684 ± 0.367	0.514 ± 0.079	Appearing
SDSS J152149.78+010236.4	51673–55635	3.351	0.612 ± 0.100	4125.000	-22071.428	-17946.428	-3.623 ± 0.265	-1.183 ± 0.054	Disappearing
SDSS J152243.98+032719.8	52025–55734	3.386	-0.331 ± 0.087	4029.357	-14925.388	-10896.030	-4.330 ± 0.281	-1.578 ± 0.105	Disappearing
SDSS J153336.02+571835.7	52345–56429	3.388	0.338 ± 0.108	4390.438	-25645.230	-21254.793	3.860 ± 0.309	1.196 ± 0.143	Appearing pristine
SDSS J153336.02+571835.7	52347–56429	3.386	0.414 ± 0.089	4390.438	-25645.230	-21254.793	3.390 ± 0.258	0.979 ± 0.101	Appearing pristine
SDSS J154256.06+372746.4	52875–56042	3.162	0.204 ± 0.146	2959.932	-15602.713	-12642.781	-4.253 ± 0.460	-1.160 ± 0.094	Disappearing
SDSS J154655.55+370739.2	52875–56042	3.096	-0.168 ± 0.132	2593.778	-12255.702	-9661.924	-3.630 ± 0.333	-1.242 ± 0.097	Disappearing
SDSS J155119.14+304019.8	53145–55739	2.083	0.244 ± 0.124	8144.533	-22340.961	-14196.428	-9.096 ± 0.393	-1.332 ± 0.041	Disappearing
SDSS J160445.92+335759.0	53142–55721	2.458	0.062 ± 0.106	13881.766	-23636.430	-9754.664	21.437 ± 0.680	1.485 ± 0.075	Appearing
SDSS J163844.42+3350857.4	52767–55803	2.548	0.078 ± 0.115	3886.727	-20403.762	-16517.035	-3.921 ± 0.288	-0.958 ± 0.064	Disappearing
SDSS J164228.52+394343.5	52381–56090	3.543	-0.021 ± 0.089	5224.135	-15206.629	-9982.494	6.439 ± 0.360	1.154 ± 0.095	Appearing
SDSS J164228.52+394343.5	52381–56090	3.543	-0.021 ± 0.089	4412.039	-24297.779	-19885.740	7.227 ± 0.368	1.491 ± 0.124	Appearing pristine
SDSS J165543.23+394519.9	52079–56098	3.997	0.462 ± 0.061	4662.332	-20891.658	-16229.326	-8.121 ± 0.276	-1.883 ± 0.063	Disappearing
SDSS J221509.31+132237.1	52210–55749	3.343	-0.192 ± 0.079	2082.920	-18152.443	-16069.523	2.076 ± 0.171	0.869 ± 0.089	Appearing
SDSS J221509.31+132237.1	52221–55749	3.333	0.016 ± 0.094	2082.920	-18152.443	-16069.523	1.965 ± 0.203	0.804 ± 0.106	Appearing
SDSS J223500.04+144556.7	52521–56235	3.033	-0.102 ± 0.107	12270.462	-23925.354	-11654.892	7.065 ± 0.473	0.718 ± 0.059	Appearing
SDSS J224511.29+003557.3	52590–55454	2.452	-0.219 ± 0.092	8783.465	-21601.881	-12818.416	4.158 ± 0.397	0.625 ± 0.071	Appearing

Bibliography

- Anderson, S. F., Weymann, R. J., Foltz, C. B., & Chaffee, Jr., F. H. 1987, *AJ*, 94, 278
- Antonucci, R. 1993, *ARA&A*, 31, 473
- Bachev, R., Strigachev, A., & Semkov, E. 2005, *MNRAS*, 358, 774
- Bahcall, J. N. & Salpeter, E. E. 1966, *ApJ*, 144, 847
- Barlow, T. A. 1994, *PASP*, 106, 548
- Becker, R. H., White, R. L., Gregg, M. D., et al. 2000, *ApJ*, 538, 72
- Begelman, M. C., Blandford, R. D., & Rees, M. J. 1984, *Reviews of Modern Physics*, 56, 255
- Benn, C. R., Carballo, R., Holt, J., et al. 2005, *MNRAS*, 360, 1455
- Bergeron, J., Boissé, P., & Ménard, B. 2011, *A&A*, 525, A51
- Brotherton, M. S., De Breuck, C., & Schaefer, J. J. 2006, *MNRAS*, 372, L58
- Bruni, G., Dallacasa, D., Mack, K.-H., et al. 2013, *A&A*, 554, A94
- Bruni, G., Mack, K.-H., Montenegro-Montes, F. M., Brienza, M., & González-Serrano, J. I. 2015, *A&A*, 582, A9
- Bruni, G., Mack, K.-H., Salerno, E., et al. 2012, *A&A*, 542, A13
- Capellupo, D. M., Hamann, F., & Barlow, T. A. 2014, *MNRAS*, 444, 1893
- Capellupo, D. M., Hamann, F., Shields, J. C., Halpern, J. P., & Barlow, T. A. 2013, *MNRAS*, 429, 1872
- Capellupo, D. M., Hamann, F., Shields, J. C., Rodríguez Hidalgo, P., & Barlow, T. A. 2011, *MNRAS*, 413, 908
- Capellupo, D. M., Hamann, F., Shields, J. C., Rodríguez Hidalgo, P., & Barlow, T. A. 2012, *MNRAS*, 422, 3249
- Carini, M. T., Miller, H. R., & Goodrich, B. D. 1990, *AJ*, 100, 347
- Carini, M. T., Miller, H. R., Noble, J. C., & Goodrich, B. D. 1992, *AJ*, 104, 15

- Chand, H. & Gopal-Krishna. 2012, *ApJ*, 754, 38
- Chand, H., Srianand, R., Petitjean, P., & Aracil, B. 2004, *A&A*, 417, 853
- Cohen, M. H., Ogle, P. M., Tran, H. D., et al. 1995, *ApJ*, 448, L77
- Condon, J. J., Cotton, W. D., Greisen, E. W., et al. 1998, *AJ*, 115, 1693
- Cucchiara, A., Jones, T., Charlton, J. C., et al. 2009, *ApJ*, 697, 345
- Cucchiara, A., Prochaska, J. X., Zhu, G., et al. 2013, *ApJ*, 773, 82
- De Cicco, D., Brandt, W. N., Grier, C. J., et al. 2018, *A&A*, 616, A114
- Doi, A., Kawaguchi, N., Kono, Y., et al. 2009, *PASJ*, 61, 1389
- Drake, A. J., Djorgovski, S. G., Mahabal, A., et al. 2009, *ApJ*, 696, 870
- Elvis, M. 2000, *ApJ*, 545, 63
- Emmering, R. T., Blandford, R. D., & Shlosman, I. 1992, *ApJ*, 385, 460
- Fabian, A. 2012, *Annual Review of Astronomy and Astrophysics*, 50, 455
- Filiz Ak, N., Brandt, W. N., Hall, P. B., et al. 2012, *ApJ*, 757, 114
- Filiz Ak, N., Brandt, W. N., Hall, P. B., et al. 2013, *ApJ*, 777, 168
- Fitzpatrick, E. L. 1999, *PASP*, 111, 63
- Fugmann, W. 1988, *A&A*, 205, 86
- Ganguly, R., Brotherton, M. S., Cales, S., et al. 2007, *ApJ*, 665, 990
- Garcia, A., Sodr e, L., Jablonski, F. J., & Terlevich, R. J. 1999, *MNRAS*, 309, 803
- Gaskell, C. M. 1982, *ApJ*, 263, 79
- Gaskell, C. M., Gill, J. J. M., & Singh, J. 2016, arXiv e-prints, arXiv:1611.03733
- Gehrels, N. 1986, *ApJ*, 303, 336
- Ghosh, K. K. & Punsly, B. 2007, *ApJ*, 661, L139
- Gibson, R. R., Brandt, W. N., Gallagher, S. C., Hewett, P. C., & Schneider, D. P. 2010, *ApJ*, 713, 220
- Gibson, R. R., Brandt, W. N., Schneider, D. P., & Gallagher, S. C. 2008, *ApJ*, 675, 985
- Gibson, R. R., Jiang, L., Brandt, W. N., et al. 2009, *ApJ*, 692, 758
- Goodrich, R. W. & Miller, J. S. 1995, *ApJ*, 448, L73

- Gopal-Krishna, Goyal, A., Joshi, S., et al. 2011, MNRAS, 416, 101
- Gopal-Krishna, Joshi, R., & Chand, H. 2013, MNRAS, 430, 1302
- Gopal-Krishna, Sagar, R., & Wiita, P. J. 1995, MNRAS, 274, 701
- Gopal-Krishna, Stalin, C. S., Sagar, R., & Wiita, P. J. 2003, ApJ, 586, L25
- Gopal-Krishna & Wiita, P. J. 2018, Bulletin de la Societe Royale des Sciences de Liege, 87, 281
- Gordon, K. D., Clayton, G. C., Misselt, K. A., Landolt, A. U., & Wolff, M. J. 2003, ApJ, 594, 279
- Goyal, A., Gopal-Krishna, Wiita, P. J., et al. 2012, A&A, 544, A37
- Goyal, A., Gopal-Krishna, Paul J., W., Stalin, C. S., & Sagar, R. 2013, MNRAS, 435, 1300
- Gregg, M. D., Becker, R. H., & de Vries, W. 2006, ApJ, 641, 210
- Guo, H. & Gu, M. 2016, ApJ, 822, 26
- Gupta, A. C. & Joshi, U. C. 2005, A&A, 440, 855
- Hall, P. B., Anderson, S. F., Strauss, M. A., et al. 2002, ApJS, 141, 267
- Hamann, F., Chartas, G., Reeves, J., & Nardini, E. 2018, MNRAS, 476, 943
- Hamann, F., Kaplan, K. F., Rodríguez Hidalgo, P., Prochaska, J. X., & Herbert-Fort, S. 2008, MNRAS, 391, L39
- Hamann, F. W., Barlow, T. A., Chaffee, F. C., Foltz, C. B., & Weymann, R. J. 2001, ApJ, 550, 142
- Häring, N. & Rix, H.-W. 2004, ApJ, 604, L89
- Hayashi, T. J., Doi, A., & Nagai, H. 2013, ApJ, 772, 4
- He, Z., Wang, T., Zhou, H., et al. 2017, ApJS, 229, 22
- He, Z.-C., Bian, W.-H., Ge, X., & Jiang, X.-L. 2015, MNRAS, 454, 3962
- Hewett, P. C. & Foltz, C. B. 2003, AJ, 125, 1784
- Hewett, P. C. & Wild, V. 2010, MNRAS, 405, 2302
- Hodge, M. A., Lister, M. L., Aller, M. F., et al. 2018, ApJ, 862, 151
- Huang, H.-Y., Pan, C.-J., Lu, W.-J., et al. 2019, MNRAS, 487, 2818
- Hughes, P. A., Aller, H. D., & Aller, M. F. 1991, ApJ, 374, 57
- Jiang, D. R. & Wang, T. G. 2003, A&A, 397, L13
- Joshi, R. & Chand, H. 2013, MNRAS, 429, 1717

- Joshi, R., Chand, H., & Gopal-Krishna. 2013, *MNRAS*, 435, 346
- Joshi, R., Chand, H., Gupta, A. C., & Wiita, P. J. 2011, *MNRAS*, 412, 2717
- Kaspi, S., Brandt, W. N., George, I. M., et al. 2002, *ApJ*, 574, 643
- Khare, P., York, D. G., & Green, R. 1989, *ApJ*, 347, 627
- Komissarov, S. 2017, in *IAU Symposium*, Vol. 324, *IAU Symposium*, 141–148
- Kormendy, J. & Gebhardt, K. 2001, in *American Institute of Physics Conference Series*, Vol. 586, 20th Texas Symposium on relativistic astrophysics, ed. J. C. Wheeler & H. Martel, 363–381
- Kormendy, J. & Ho, L. C. 2013, *ARA&A*, 51, 511
- Kulkarni, V. P., Meiring, J., Som, D., et al. 2012, *ApJ*, 749, 176
- Kumar, P., Chand, H., & Gopal-Krishna. 2016, *MNRAS*, 461, 666
- Kumar, P., Gopal-Krishna, Stalin, C. S., et al. 2017, *MNRAS*, 471, 606
- Kunert-Bajraszewska, M., Cegłowski, M., Katarzyński, K., & Roskowiński, C. 2015, *A&A*, 579, A109
- Laor, A. & Brandt, W. N. 2002, *ApJ*, 569, 641
- Lister, M. L. & Smith, P. S. 2000, *ApJ*, 541, 66
- Lu, W.-J. & Lin, Y.-R. 2019, *ApJ*, 883, 30
- Lu, W.-J., Lin, Y.-R., & Qin, Y.-P. 2018, *MNRAS*, 473, L106
- Lundgren, B. F., Wilhite, B. C., Brunner, R. J., et al. 2007, *ApJ*, 656, 73
- Lynds, C. R. 1967, *ApJ*, 147, 396
- Mangalam, A. V. & Wiita, P. J. 1993, *ApJ*, 406, 420
- Marscher, A. P., Gear, W. K., & Travis, J. P. 1992, in *Variability of Blazars*, ed. E. Valtaoja & M. Valtonen, 85
- Marscher, A. P., Jorstad, S. G., D’Arcangelo, F. D., et al. 2008, , 452, 966
- Massaro, E., Giommi, P., Leto, C., et al. 2009, *A&A*, 495, 691
- Mathes, N. L., Churchill, C. W., & Murphy, M. T. 2017, *ArXiv e-prints*
- McGraw, S. M., Brandt, W. N., Grier, C. J., et al. 2017, *MNRAS*, 469, 3163
- Merritt, D., Cruz, F., & Milosavljević, M. 2001, in *Astronomical Society of the Pacific Conference Series*, Vol. 228, *Dynamics of Star Clusters and the Milky Way*, ed. S. Deiters, B. Fuchs, A. Just, R. Spurzem, & R. Wielen, 155

- Miller, P., Rawlings, S., & Saunders, R. 1993, MNRAS, 263, 425
- Mishra, S., Chand, H., Krishna, G., et al. 2018, MNRAS, 473, 5154
- Mishra, S., Gopal-Krishna, Chand, H., Chand, K., & Ojha, V. 2019, MNRAS, 489, L42
- Møller, P., Jakobsen, P., & Perryman, M. A. C. 1994, A&A, 287, 719
- Montenegro-Montes, F. M., Mack, K.-H., Vigotti, M., et al. 2008, MNRAS, 388, 1853
- Murray, N., Chiang, J., Grossman, S. A., & Voit, G. M. 1995, ApJ, 451, 498
- Nestor, D. B., Turnshek, D. A., & Rao, S. M. 2005, ApJ, 628, 637
- Ojha, V., Chand, H., Krishna, G., Mishra, S., & Chand, K. 2020, MNRAS, 493, 3642
- Padovani, P. & Giommi, P. 1995, MNRAS, 277, 1477
- Pâris, I., Petitjean, P., Aubourg, É., et al. 2012, A&A, 548, A66
- Pâris, I., Petitjean, P., Aubourg, É., et al. 2018, A&A, 613, A51
- Pâris, I., Petitjean, P., Ross, N. P., et al. 2017, A&A, 597, A79
- Pollack, M., Pauls, D., & Wiita, P. J. 2016, ApJ, 820, 12
- Prabhu, T. P. & Anupama, G. C. 2010, in Astronomical Society of India Conference Series, Vol. 1, Astronomical Society of India Conference Series
- Prochter, G. E., Prochaska, J. X., Chen, H.-W., et al. 2006, ApJ, 648, L93
- Proga, D. & Kallman, T. R. 2004, ApJ, 616, 688
- Proga, D., Stone, J. M., & Drew, J. E. 1998, MNRAS, 295, 595
- Proga, D., Stone, J. M., & Kallman, T. R. 2000, ApJ, 543, 686
- Punsly, B. 1999a, ApJ, 527, 609
- Punsly, B. 1999b, ApJ, 527, 624
- Raghunathan, S., Clowes, R. G., Campusano, L. E., et al. 2016, MNRAS, 463, 2640
- Reichard, T. A., Richards, G. T., Hall, P. B., et al. 2003, AJ, 126, 2594
- Rogerson, J. A., Hall, P. B., Ahmed, N. S., et al. 2018, ApJ, 862, 22
- Romero, G. E., Cellone, S. A., & Combi, J. A. 1999, A&AS, 135, 477
- Romero, G. E., Cellone, S. A., Combi, J. A., & Andruchow, I. 2002, A&A, 390, 431
- Ruan, J. J., Anderson, S. F., Dexter, J., & Agol, E. 2014, ApJ, 783, 105

- Sagar, R. 1999, *Current Science*, 77, 643
- Sagar, R., Omar, A., Kumar, B., et al. 2011, *Current Science*, 101, 1020
- Sagar, R., Stalin, C. S., Gopal-Krishna, & Wiita, P. J. 2004, *MNRAS*, 348, 176
- Sakata, Y., Morokuma, T., Minezaki, T., et al. 2011, *ApJ*, 731, 50
- Schlegel, D. J., Finkbeiner, D. P., & Davis, M. 1998, *ApJ*, 500, 525
- Schmidt, K. B., Rix, H.-W., Shields, J. C., et al. 2012, *ApJ*, 744, 147
- Schneider, D. P., Hall, P. B., Richards, G. T., et al. 2007, *AJ*, 134, 102
- Schneider, D. P., Richards, G. T., Hall, P. B., et al. 2010, *AJ*, 139, 2360
- Scoville, N. & Norman, C. 1995, *ApJ*, 451, 510
- Shen, Y., Richards, G. T., Strauss, M. A., et al. 2011, *ApJS*, 194, 45
- Silverman, B. W. 1986, *Density estimation for statistics and data analysis*
- Stalin, C. S., Gopal-Krishna, Sagar, R., & Wiita, P. J. 2004, *MNRAS*, 350, 175
- Stalin, C. S., Gupta, A. C., Gopal-Krishna, Wiita, P. J., & Sagar, R. 2005, *MNRAS*, 356, 607
- Stetson, P. B. 1987, *PASP*, 99, 191
- Stocke, J. T. & Rector, T. A. 1997, *ApJ*, 489, L17
- Sudilovsky, V., Savaglio, S., Vreeswijk, P., et al. 2007, *ApJ*, 669, 741
- Sun, Y.-H., Wang, J.-X., Chen, X.-Y., & Zheng, Z.-Y. 2014, *ApJ*, 792, 54
- Tejos, N., Lopez, S., Prochaska, J. X., et al. 2009, *ApJ*, 706, 1309
- Tombesi, F., Cappi, M., Reeves, J. N., et al. 2011, *ApJ*, 742, 44
- Tuccillo, D., Bruni, G., DiPompeo, M. A., et al. 2017, *MNRAS*, 467, 4763
- Urry, C. M. & Padovani, P. 1995, *PASP*, 107, 803
- van Dokkum, P. G. 2001, *PASP*, 113, 1420
- Vanden Berk, D. E., Richards, G. T., Bauer, A., et al. 2001, *AJ*, 122, 549
- Vergani, S. D., Petitjean, P., Ledoux, C., et al. 2009, *A&A*, 503, 771
- Véron-Cetty, M.-P. & Véron, P. 2010, *A&A*, 518, A10
- Vivek, M. 2019, *MNRAS*, 486, 2379
- Vivek, M., Srianand, R., & Gupta, N. 2016, *MNRAS*, 455, 136

- Vivek, M., Srianand, R., Petitjean, P., et al. 2014, MNRAS, 440, 799
- Voit, G. M., Weymann, R. J., & Korista, K. T. 1993, ApJ, 413, 95
- Wagner, S. J. & Witzel, A. 1995, ARA&A, 33, 163
- Wang, T., Yang, C., Wang, H., & Ferland, G. 2015, ApJ, 814, 150
- Welling, C. A., Miller, B. P., Brandt, W. N., Capellupo, D. M., & Gibson, R. R. 2014, MNRAS, 440, 2474
- Weymann, R. J., Morris, S. L., Foltz, C. B., & Hewett, P. C. 1991, ApJ, 373, 23
- Wolfe, A. M., Gawiser, E., & Prochaska, J. X. 2005, ARA&A, 43, 861
- Wright, E. L., Eisenhardt, P. R. M., Mainzer, A. K., et al. 2010, AJ, 140, 1868
- Yang, J., Wu, F., Paragi, Z., & An, T. 2012, MNRAS, 419, L74
- Yi, W., Vivek, M., Brandt, W. N., et al. 2019, ApJ, 870, L25
- Zhang, S., Wang, H., Wang, T., et al. 2014, ApJ, 786, 42
- Zhou, H., Wang, T., Wang, H., et al. 2006, ApJ, 639, 716
- Zhu, G. & Ménard, B. 2013, ApJ, 770, 130